

## Electronic States near Surfaces –

- a) Analysis of calculation methods using semi-infinite boundary conditions;
- b) Sensitive detection using laser photoelectron spectroscopy

by

Yonas Beyene Abraham

A Dissertation Submitted to the Graduate Faculty of

WAKE FOREST UNIVERSITY

in Partial Fulfillment of the Requirements

for the Degree of

Doctor of Philosophy

in the Department of Physics

December 2004

Winston-Salem, North Carolina

Approved by:

Dr. N. A. W. Holzwarth, Adviser \_\_\_\_\_

Examining Committee:

Dr. Robert Plemmons, Chairman \_\_\_\_\_

Dr. Richard T. Williams \_\_\_\_\_

Dr. G. Eric Matthews \_\_\_\_\_

Dr. Keith D. Bonin \_\_\_\_\_

# Contents

<b>List of Figures</b>	<b>iv</b>
<b>List of Tables</b>	<b>vii</b>
<b>1 Introduction</b>	<b>1</b>
1.1 Simulation and physics . . . . .	1
1.2 Previous work . . . . .	3
<b>2 Background</b>	<b>5</b>
2.1 Defects/Impurities . . . . .	5
2.1.1 Point defects . . . . .	5
2.1.2 Line defects . . . . .	6
2.1.3 Plane defects . . . . .	6
2.1.4 Surface defects . . . . .	6
2.2 Density functional theory . . . . .	7
2.2.1 Schrödinger equation . . . . .	8
2.2.2 Hartree-Fock theory . . . . .	10
2.2.3 Variational principle . . . . .	12
2.2.4 Hohenberg and Kohn theorems . . . . .	13
2.2.5 Kohn-Sham theorems . . . . .	16
2.3 The pseudopotential approximation . . . . .	18
<b>3 Experimental motivation</b>	<b>23</b>
3.1 Foundations of our experiment . . . . .	23
3.1.1 Photoelectron spectroscopy . . . . .	23
3.1.2 Recording of photoelectron spectra . . . . .	24
3.1.3 Two-photon photoemission . . . . .	24
3.1.4 AES basics . . . . .	26
3.1.5 Low energy electron diffraction (LEED) basics . . . . .	27
3.2 Experimental setup . . . . .	27
3.2.1 PES . . . . .	27
3.2.2 Interpretation of PES spectra . . . . .	40

3.3	Photoelectron spectra from band states . . . . .	43
3.3.1	Comparison of PES to band structure . . . . .	45
3.3.2	Theoretical band structure of CdSe (11 $\bar{2}$ 0) . . . . .	51
3.4	Surface defects . . . . .	54
3.4.1	Background . . . . .	54
3.4.2	Quality of the cleaved surface . . . . .	54
3.4.3	Damaging the surface . . . . .	58
<b>4</b>	<b>The semi-infinite surface formalism</b>	<b>64</b>
4.1	General equations from PAW formalism . . . . .	64
4.2	Bulk and surface states . . . . .	65
4.2.1	Surface geometry . . . . .	67
4.3	Treatment of the bulk-surface boundary . . . . .	72
4.3.1	Appelbaum and Hamann approach . . . . .	72
4.3.2	Alternative approach . . . . .	73
4.3.3	Alternative method II . . . . .	74
4.3.4	Alternative method III . . . . .	75
4.3.5	Alternative method IV . . . . .	75
4.4	Generalized minimum residual method . . . . .	75
4.5	Surface states . . . . .	79
4.5.1	Region II states . . . . .	79
4.5.2	Region III states . . . . .	80
4.5.3	Match conditions . . . . .	80
4.6	Numerical detail of surface state calculation . . . . .	80
4.7	Self-consistency loop . . . . .	86
4.8	Convergence of interface charge density toward bulk region . . . . .	91
4.9	Convergence of wave function . . . . .	92
<b>5</b>	<b>Analysis</b>	<b>98</b>
5.1	Explanation of the failed method . . . . .	99
5.1.1	Basic equations for energies within bulk bands . . . . .	99
5.1.2	For energies in bulk band gaps (surface states) . . . . .	101
5.1.3	Detailed equations . . . . .	102
5.2	Methods of integration . . . . .	105
5.2.1	Predictor-corrector . . . . .	105
5.2.2	Green's function method . . . . .	107
5.3	Some results . . . . .	107
<b>6</b>	<b>User guide</b>	<b>113</b>
6.1	How to run . . . . .	113
6.1.1	Bulk input . . . . .	113
6.1.2	Surface input . . . . .	115

6.2 Smear plot . . . . .	119
<b>7 Concluding Remarks and Future Work</b>	<b>124</b>
<b>Bibliography</b>	<b>128</b>
<b>A Related publication by the author</b>	<b>136</b>
<b>B Useful programs</b>	<b>157</b>
B.1 Order $n$ calculation (nphoton.f) . . . . .	157
B.2 Photovoltage calculation (readdata.f) . . . . .	159
B.3 IDL smear plot program (SmearPlot2000.pro) . . . . .	161

# List of Figures

2.1	Basic self consistent field loop for solving Kohn-Sham equations. . . .	19
2.2	A plot of true potential (red solid line in (a)) and its corresponding pseudopotential (green dashed line in (a)) for Cd. Diagram (b) shows the 4s all electron (red solid line) and pseudowavefunction (green dashed line) for Cd atom. These were generated in the the PAW formulation using ATOMPAW. . . . .	21
3.1	PES setup for second and fourth harmonic generation . . . . .	29
3.2	PES setup for third harmonic generation . . . . .	30
3.3	Ultrahigh vacuum chambers . . . . .	32
3.4	Energy diagram representing the sample and CMA . . . . .	34
3.5	Voltage bias correction calculation for CdSe 1120 . . . . .	37
3.6	Linear plot of PES from Gold surface using FH beam. The arrow indicates where we we choose the $E_{kmax} - eV_{Bias}$ . . . . .	39
3.7	Transmission coefficient of of the density filters as a function of wave length. (a) for OD labeled 0.2, (b) for OD=0.4 (c)for OD=0.6 and (d) for OD=1.0 . . . . .	41
3.8	Linear energy distribution curve for photoelectrons excited from CdSe (11 $\bar{2}$ 0) excited by 4.5 eV pulse showing the position of the threshold energy. . . . .	43
3.9	Energy distribution curve for photoelectrons exited from CdSe (11 $\bar{2}$ 0) by 4.5 eV TH beam (Red solid line). The number of photons corresponding to this curve is shown in dotted line (Green) with respect to the right-hand ordinate order $n$ . . . . .	44
3.10	CdS 11 $\bar{2}$ 0 band structure adjusted to CdSe band gap in Ref. [44]. The experimental points are from an inverse photoemission from Ref [44]. The 4.5 eV arrows show the possible transitions that correspond to our TH phonon excitation. . . . .	48

3.11	Theoretical CdSe (11 $\bar{2}$ 0) band structure calculated using our PWPAAW code. The conduction bands are shifted to compensate for the under estimation of the band gap. The experimental points are from an inverse photoemission from Ref [44] indicated with $\times$ . . . . .	49
3.12	Schematic diagram for n-type semiconductor showing the effect of illumination on band edges. . . . .	50
3.13	Total energy as a function of planewave cutoff reciprocal vector $\mathbf{G}$ of CdSe. . . . .	52
3.14	Total energy of CdSe as a function of lattice vectors $a$ and $c$ . The dark dots are calculated values and the mesh is extrapolated values. . . . .	53
3.15	Energy distribution curve for photoelectrons exited from CdSe (11 $\bar{2}$ 0) by the 5.9 eV FH beam showing the relative position of threshold and vacuum energy levels. . . . .	55
3.16	Energy distribution curve for photoelectrons exited from CdSe (11 $\bar{2}$ 0) by 5.9 eV FH beam (Red solid line). The number of photons corresponding to this curve is shown in dotted line (Green) with respect to the right-hand ordinate photoelectron counts. . . . .	56
3.17	AES result for CdSe (11 $\bar{2}$ 0). The plot is a derivative of number of electrons as a function of Energy ( $\frac{dn}{dE}$ ). . . . .	57
3.18	LEED pattern obtained from CdSe (11 $\bar{2}$ 0) surface. The bright spots represent the diffraction patterns of an atom. . . . .	59
3.19	Flow chart showing the process of introducing defect and their measurements . . . . .	60
3.20	Different PES spectra after we apply more defects . . . . .	61
3.21	Difference in PES spectra relative to each AES application. That is the effect of AES on the density of states from the previous sputtering or fresh cleave. This will remove the effect of sputtering. If the AES does not have an effect, we would have gotten a flat curve. . . . .	62
3.22	Difference in PES spectra relative to each AES application relative to the cleaved surface. In contrast to Figure (3.21) is that, here the deference is relative to the original cleaved spectra and it also includes the effect of sputtering. . . . .	63
4.1	Diagram showing surface geometry. . . . .	67
4.2	Flow chart for GMRES. . . . .	78
4.3	Initialization scheme for the surface states in region II . . . . .	81
4.4	Initial condition for region II for different surface states. Different colors represents different initial contions. . . . .	82
4.5	Shows general surface state wave function indexing and augmentation sphere of an atom. . . . .	83
4.6	Theoretical charge fluctuation as a function of $k_{\perp}$ and $z$ . . . . .	92

4.7	Convergence of $\rho(\mathbf{0}, z)$ for Li (001) 16-layer interface region for different k-point sampling noted in the form $\lambda \times \mu \times \nu$ , where $\lambda$ and $\mu$ refer to the number of $\mathbf{k}_{\parallel}$ points in the 2 distinct surface directions and $\nu$ refers to the number of $\mathbf{k}_{\perp}$ points. . . . .	93
4.8	Comparison of 4 and 8-layered diamond (001) interface wave functions for the energy labeled as “1” in Figure 4.10. The z-axis is shifted to match the vacuum layer from both cases. . . . .	95
4.9	Comparison of 4 and 8-layered diamond (001) interface wave functions for the energy labeled as “2” in Figure 4.10. . . . .	96
4.10	Band structure for diamond (001) structure at $k_{\parallel} = (0.25, 0.25)$ . The vertical dotted lines represent the $k_{\perp}$ values used to calculate the surface wave functions. . . . .	97
5.1	Predictor corrector results for the region II for Li in bcc structure . . .	100
5.2	Wave function for $\mathbf{G}_{\parallel} = 0$ in the “Alternative Approach II” for Li in bcc structure. . . . .	100
5.3	Region II effective potential used for Li in bcc structure . . . . .	108
5.4	Region II $f_0$ solutions for Li in bcc structure using PC method . . . .	109
5.5	Region II $f^{ai}$ solutions for Li in bcc structure using PC method . . . .	110
5.6	Region II $f_0 + \sum_{ai} C_{ai} f^{ai}$ solutions for Li in bcc structure using PC method . . . . .	111
5.7	Region II $f_0 + \sum_{ai} C_{ai} f^{ai}$ solutions for Li in bcc structure using PC and Greens function method . . . . .	112
6.1	Smear diagram of CdSe $11\bar{2}0$ . . . . .	120
6.2	Diagram of the Brillouin zones for CdSe $(11\bar{2}0)[30]$ . . . . .	121
6.3	Smear diagram for diamond (001)[53] . . . . .	122
6.4	Diagram of the Brillouin zones for diamond (001) . . . . .	123
7.1	A Graphical User Interface showing the input output control tab for PWPAW/SIPAW . . . . .	126
7.2	A Graphical User Interface showing the memory control tab for PWPAW/SIPAW . . . . .	127

# List of Tables

3.1	Properties of the second, third and fourth harmonics of the Ti:sapphire fundamentals. † Note that we used 840 nm Fundamental when we generate FH beam and 820 for the TH generation as explained above.	31
3.2	Measurement of peak position as a function of $B(\text{eV}_{Bias}(\text{volts}))$ for CdSe $11\bar{2}0$ . . . . .	36
3.3	OD as a function of wave length ( $\lambda$ ) . . . . .	41
3.4	List of parameters used to construct basis and projector functions . .	51
3.5	Values used in setting the LEED pattern for CdSe ( $11\bar{2}0$ ) . . . . .	58



## Acknowledgments

I would like to gratefully acknowledge the enthusiastic supervisions of Dr. N. A. W. Holzwarth and Dr. Richard T. Williams during this work.

Dr. N. A. W. Holzwarth, my advisor for the theoretical part of this dissertation, has been an enormous help not only in my research work but also in mine and my families social life. I will not forget all her hard work in trying to make me a better researcher.

Dr. Richard T. Williams, my advisor for the experimental part of this dissertation, was a very understandable person as I was a more theoretical than experimentalist when I first joined his lab. He showed all the patience on teaching me how to be a good experimentalist. I learned a very valuable lesson on how to interpret experimentally measured values.

Dr. G. Eric Matthews was also there for me to encourage me and give me advise on how to improve and solve some of the problem I was facing thorough out my stay in wake.

I would like to thank also Dr. Robert Plemmons and Dr. Keith D. Bonin for their work in reading and correcting my thesis work.

I have enjoyed tremendous help from Dr. K. Burak Ucer who helped me with all the laser and optics setup for my photoelectron spectroscopy experiment.

I am in debt to all previous students in the research group i worked with, Specially, Dr. J. L. Lopresti and Dr. Alan Tackett for their solid foundation they left for me to continue on their work.

My deepest thanks goes to My wife Azeb , my two sons (BenHur and Siem) and my sister-in-law Luchea for being there for me and encouraging me to go forward.

# Abstract

Photoelectron spectroscopy with pulsed laser excitation can provide a low-background, sensitive view of electronic states in the band gap and photo-populated states above the Fermi level. Measurements of photoelectron emission for ultra-high vacuum cleaved surfaces of CdSe, excited by 4.5 and 5.9 eV Ti:sapphire laser pulses of 150 femtosecond duration are reported. One- and two-photon excitation processes are observed and analyzed in terms of features of the electronic structure. In order to distinguish defect and surface contributions from the bulk properties of these systems, computer modeling methods are needed.

The “SI-PAW” method is designed to solve the Kohn-Sham equations within the projector augmented wave “PAW” formalism with boundary conditions appropriate for the semi-infinite geometry of material surfaces. This method, which directly distinguishes between bulk, surface, and defect states, is an extension of the very successful Appelbaum-Hamann method, modified to accommodate non-local potential terms in the PAW formalism. In the bulk region, the wave functions are composed of linear combinations of Bloch waves of the converged self-consistent periodic lattice. In the vacuum region, the wave functions are composed of functions which decay or propagate into the vacuum. In the interface region, the wavefunctions are composed of extensions of the Bloch wavefunctions or surface states which decay into the material. The interface wavefunctions are determined by putting the Kohn-Sham equations in the form of boundary value problems, using the Numerov algorithm to approximate the differential equations and the GMRES algorithm to solve them efficiently.

# Chapter 1

## Introduction

### 1.1 Simulation and physics

Many aspects of computational modelling make it a worthy partner of experimental science. The chemist studying a particular reaction can reach into the computer simulation, alter bond lengths or angles, and then observe the effect of such changes on the process taking place. The geophysicist interested in phase transitions occurring deep inside the earth can model pressures and temperatures which could never be reached in a laboratory. All of this can be achieved with a single piece of apparatus - the computer itself.

Quantum-mechanical calculations stand out because they are by design *ab initio* i.e. from first-principles, calculations. They do not depend upon any external parameters except the atomic numbers of the constituent atoms to be modelled and cannot therefore be biased by preconceptions about the final result. Such calculations are reliable and can be used with confidence to predict the behavior of nature.

Nevertheless, the same complexity which bars exact analytical solution also results in the highly unfavorable scaling of computational effort and resources required. The computational demands of “exact” (most accurate) calculations grow exponentially with the size of the system being studied, so that they are too costly to be of significant practical use. Despite the relentless progress of computer technology, this scaling makes this approach inviable for some time yet.

Well-controlled approximations can be employed to enable the equations to be solved much more efficiently without sacrificing the predictive power or parameter-free nature of quantum-mechanical calculations. Much progress has been made in recent years in developing methods which exhibit polynomial rather than exponential scaling. One such method, that of density-functional theory, coupled with a simple description of the quantum-mechanical effects of exchange and correlation and the pseudopotential approximation, has proved to be remarkably successful and is currently applied worldwide by scientists in a wide range of disciplines. Even this method, however, requires a computational effort which scales with the cube of the system-size i.e. is  $\mathcal{O}(N^3)$ , and so is limited in the scale of simulation which can be realistically attempted.

There is a renewed interest in studying the detailed properties of interfaces and surfaces of materials for both fundamental and technological reasons. For example quantum oscillations have recently been observed and modeled in thin metallic films [71, 11]. These oscillations have been shown to affect the stability of structures at the nano scale. Similarly, extended systems with a single planar surface will also have oscillatory behavior near the surface which can have significant effects on the properties of intrinsic surfaces as well as of adsorbates and defects on surfaces. There are a lot of technologies which depend upon or are affected by the detailed properties of the electronic states on the surfaces of materials such as catalysis, chemical sensors, the manufacture of electronic devices, and substrates for materials of interest in the National Nanotechnology Initiative

Here at Wake Forest university, R. T. Williams and his collaborators and students [43, 58, 65, 72] have shown that sub-photoelectron-threshold (from valence band) laser photoelectron spectroscopy is a particularly sensitive probe of surface defects in a comparison with conventional photoemission spectroscopy. Specially Thoma *et.al.*[65] have found high density of states in the band gap in most of the II-VI and III-V group semiconductors. Laser photoemission has high power and low background noise comparing to the conventional photoelectron emission. This makes it surface specific and excellent for studying surface defects in the gap [40].

A crucial parameter in many applications and experiments is the energy of intrinsic

and defect surface states relative to the bulk band edge and to the Fermi level. For full understanding and predictive theory, it is important to be able to calculate bulk and surface electronic states within the same theoretical framework. The main aim of this project was to develop that capability. The experimental portion illustrates one kind of data that we believe can be compared well to the theory in future work. The computational methods can improve the means for calculating of surface states properly referenced to bulk bands in a wide range of materials.

## 1.2 Previous work

In the large literature of surface simulations, the vast majority of the results have been obtained using a supercell approach in the slab geometry. While this work has been very successful in studying surface properties of materials, formulation of the problem in the semi-infinite geometry has several advantages.

- The full computational effort can be focused on the interface region itself using knowledge of the bulk calculation as input.
- Interference effects from the additional boundary of the slab are avoided,
- The semi-infinite geometry more closely represents the physical system and we expect this to allow us to model details of surface physics which may not be so readily apparent in other approaches.

There have been a relatively smaller number of the surface treatments based on the semi infinite geometry. Some of these include the pioneering work of Lang and Kohn [35, 36] on the self-consistent jellium surface, later extended by Lang and William [37, 38] to treat an atomic adsorbate on a jellium surface. Appelbaum and Hamman [3, 4] developed a method based on the local pseudopotential formalism and on numerical integration of the Schrodinger equation in the surface region, matching to a linear combination of Bloch waves in the interior of the solid. In order to treat energetic electrons in low energy electron emission [28, 51] or in photoemission [24, 41] ,

Green's function methods using a muffin-tin potential approximation have been successful. Unfortunately, it would be difficult to extend this formalism to self consistent calculations. Stiles and Hamann[62] developed a method based on constructing a Green's function from generalized Bloch states in a linearized augmented plane wave (LAPW) basis for treating electron transmission through interfaces [63]. In this case, the self-consistency of the system was treated separately. In order to self-consistently determine the electronic and structural ground state of semiconductor surfaces, Krüger and Pollmann developed a method based on a Green's functions expressed in a Gaussian basis. [33] This approach has been quite successful for studying the lattice relaxation and surface state structure of several semiconductor surfaces[54, 55]. However, since the perturbing potential of this method is the difference between the surface potential and the potential of two semi-infinite perfect crystals, it is difficult to treat the effects of longer range interactions such as the image potential or to represent states which carry photocurrent. Recently, there is an interest of using the semi infinite method in quantum wires. Choi *et.al* [8], calculated the low temperature conductance of (10,10) carbon nanotubes with defects.

This report is organized as follows. In Chapter 2, we present a fundamental introduction to density functional theory, since it is the basis of our method. In Chapter 3, we present results of our laser photoelectron spectroscopy study on CdSe  $11\bar{2}0$  crystal surface to identify the surface states. Detailed explanations of our semi-infinite calculation method are shown in Chapter 4. Chapter 5 presents an analysis of our theoretical method compared to our "unsuccessful" methods. Chapter 6 gives a user guide to our surface pwpaw code. Chapter 7 contains some concluding remarks and a list of future work.

# Chapter 2

## Background

### 2.1 Defects/Impurities

It is useful to think about solids in terms of a regular repeating pattern of planes of particles. Few crystals are perfect in that all unit cells consist of the ideal arrangement of atoms or molecules and all cells line up in a three dimensional space with no distortion. Some cells may have one or more atoms less whereas others may have one or more atoms than the ideal unit cell. The imperfection of crystals are called crystal defects. Crystal defects can be classified as point, line, or plane defects.

#### 2.1.1 Point defects

There are four types of point defects. When a particle is missing at one or more lattice sites we get a vacancy. When a particle forces its way between lattice sites, we get an interstitial impurity<sup>1</sup>. Substitutional impurities result from replacing the particle that should occupy a lattice site with a different particle. Dislocations are one-dimensional defects caused by holes that are not large enough to be a vacancy.

Point defects (vacancies or interstitial defects) are common in crystals with large anions. In some cases, these ions have some freedom to move about in crystals, making them relatively good conductors. So this shows that point defects are not

---

<sup>1</sup>We have done some oxygen interstitial defect studies in  $\text{PbWO}_4$  and  $\text{CaMoO}_4$  crystals[1]

always bad, they can be useful if they are well engineered.

### 2.1.2 Line defects

Line defects are mostly due to misalignment of ions or presence of vacancies along a line. The hammering and stretching of materials often involve the movement of edge dislocation. Movements of dislocations give rise to their plastic behavior. Line dislocations usually do not end inside the crystal, and they either form loops or end at the surface of a single crystal.

### 2.1.3 Plane defects

Plane defects occur along a 2-dimensional surface. Surface atoms are different from those deep in the crystals. One of the common plane defect is the stacking fault defect. For example, in the perfect crystal, the adjacent layers may have an ordered relationship, such as ABAB or ABCABC.... A plane defect could be described by one of the layers occurring out of sequence such as ABAAB ... or ABABCABC.....

### 2.1.4 Surface defects

Surfaces are created by cutting a periodic bulk crystal along a certain plane. This breaks the periodicity along the direction perpendicular to the surface. This break in periodicity creates surface defects. Atoms at the surface experience a different bonding environment than the ones deep inside the bulk. This causes the layers at near the surface to relax and reconstruct.

The phenomena of relaxation and reconstruction involve rearrangements of surface atoms, this process is driven by the energetics of the system i.e. the desire to reduce the surface free energy. The arrangement of atoms at a free surface differs slightly from the interior structure because the surface atoms do not have neighboring atoms on one side.

Relaxation is a small and subtle rearrangement of the surface layers. It involves adjustments in the layer spacings perpendicular to the surface, there is no change



either in the periodicity parallel to the surface or to the symmetry of the surface. So in principle if one take a low energy electron diffraction<sup>2</sup> of a relaxed surface only, the pattern should look similar to the unrelaxed surface.

Unlike relaxation, the phenomenon of reconstruction involves a change in the periodicity of the surface structure along the surface plane.

## 2.2 Density functional theory

Over the past four decades, our ability to treat materials properties at a fundamental, quantum level has improved tremendously, in large part because advances in computer power has allowed us to actually solve hard equations and try things out. Today it is possible, for instance, to calculate the unit cell dimensions of a crystalline solid from first principles with a reliability in the range of a few percent. A wide variety of geometric and structural behaviors, such as the location of impurities, the structures of defects, dislocations, grain boundaries, and surfaces can similarly be calculated from first principles. Once the geometry has been determined, a range of properties—electronic, optical, and magnetic can also be calculated with varying degrees of reliability.

The advances that made this possible were largely incremental and are described in various contexts in terms of one-electron theory, band theory or self-consistent-field theory. From the late 1960s onwards, these terms found some formal legitimacy in a theory of energy and force in electronic systems called density functional theory.

In principle, all knowledge about a system can be obtained from the quantum mechanical wave function. This is obtained (non-relativistically) by solving the Schrödinger equation of the complete many electron system. However in practice solving such an N-body problem proves to be impossible. This chapter will give a brief description of earlier approximations made to solve this many-body problem and a description of the important physical features omitted from these theories. For these reasons it is necessary to use density functional theory developed by Kohn and

---

<sup>2</sup>More discussion about low energy electron diffraction will appear in Chapter 3.

Sham [31] based on the theory of Hohenberg and Kohn [22] which, in principle, is an exact ground state theory. As the name suggests, the fundamental variational parameter is the electron charge density rather than the electronic wavefunctions. In this formalism, the N-electron problem is expressed as N one-electron equations where each electron interacts with all other electrons via an effective Coulomb and exchange-correlation potential. These interactions are then calculated using the local density approximation to exchange and correlation. Plane wave basis sets and total energy pseudopotential techniques are then used to solve the Kohn-Sham one electron equations.

There are now many articles on this subject which review the topics involved in total energy calculations in depth such as those in references [46, 47, 50] . Therefore in this chapter only a brief description of the methods used for the total energy calculations used in later chapters will be discussed.

### **2.2.1 Schrödinger equation**

Until the end of the nineteenth century, it was thought that atomic and subatomic particles behaved in the same way as much larger objects. Newton's laws of classical mechanics accurately described the motion of everyday objects and planets and it was assumed that the same laws governed the motion of particles such as atoms and electrons.

However, experimental evidence was accumulating to suggest that this was not the case. Inconsistencies were observed by scientists studying black body radiation, heat capacities, atomic and molecular spectra and electromagnetic radiation which suggested that only certain discrete values for the energy of a system are possible [13]. This was in complete contrast to classical mechanics which predicts that there should be no restrictions on the energy which a system can take. This phenomenon is known as quantization and these observations led to the birth of Quantum Mechanics. The discovery of quantization forced scientists to change the way in which they described matter. Classical physics described matter as particles which travel along definite paths but quantum mechanics requires matter to be described as particles distributed

through space like a wave.

This wave is called the wavefunction,  $\Psi$ . It is a mathematical expression which contains all the information known about the particle. The wavefunction can be found by solving the Schrodinger Equation [13]. The time-independent Schrödinger equation is:

$$H\Psi = E\Psi \quad (2.1)$$

Where,

$$H = -\frac{\hbar^2}{2m} \sum_i \nabla_i^2 - \sum_{i,a} \frac{Z_a e^2}{|\mathbf{r}_i - \mathbf{R}_a|} + \frac{1}{2} \sum_{i \neq j} \frac{e^2}{|\mathbf{r}_i - \mathbf{r}_j|}. \quad (2.2)$$

Where  $Z_a$  is the atomic number of ion  $a$ ,  $e$  is the charge of an electron,  $\mathbf{R}_a$  is the position of the  $a$ th ion,  $\mathbf{r}_i$  and  $\mathbf{r}_j$  are the positions of the  $i$ th and  $j$ th electrons,  $m$  is the mass of an electron,  $\hbar$  is the Plank's constant.

By including all the forces acting on the particle, its position in space relative to the other particles with which it is interacting and other boundary conditions, such as the space in which the particle is confined, the Schrödinger equation calculates the particle's allowed wavefunctions and corresponding energy levels. Each energy level is defined in terms of a set of quantum numbers. The Born Interpretation of the wavefunction relates to the probability of finding the particle at different positions in space.

If the wavefunction of a particle has the value  $\Psi$  at some point  $r$ , the probability of finding the particle between  $r$  and  $r + dr$  is proportional to  $|\Psi|^2 dr$ .  $\Psi$  is called the probability amplitude and  $|\Psi|^2$  is called the probability density

The probability of finding the particle at a given position is not the only information contained in the wavefunction. The wavefunction carries all the information known about the particle. Properties such as the particle's kinetic energy can also be found from the wavefunction.

## 2.2.2 Hartree-Fock theory

Schrödinger equation rarely solved exactly. In most cases, one has to use approximations. The first successful attempt to derive approximate wave functions for atoms was devised by Hartree (1928) [20]. In this approach the many-electron wave function  $\Psi$  is approximated by the product of one-electron functions  $\psi$  for each of the  $N$  electrons:

$$\Psi(r_1, r_2, \dots, r_N) = \psi_1(r_1)\psi_2(r_2), \dots, \psi_N(r_N) \quad (2.3)$$

where  $r_i$ , are the positional coordinates for the  $i$ -th electron. For the sake of clarity the spin variables are not shown. The individual one-electron functions  $\psi_i$  are called orbitals and describe each electron in the atom. This approximation have some shortcomings:

- It assumes that electrons in the atom can be described independently, that is, their movements do not depend upon each other and their interaction is not pairwise, but each electron interacts with some averaged field of other electrons. This is a neat idea, the problem is that it is not true. Electrons have to avoid each another or correlate their movements, since the Coulomb interaction causes them to repel each other.
- The Hartree function does not have a proper symmetry for interchanging particle indices for fermions. The Pauli principle states that the many electron wave function has to be antisymmetric to the exchange of neighboring indices, that is, change sign:

$$\Psi(\mathbf{r}_1, \mathbf{r}_2, \dots, \mathbf{r}_i, \mathbf{r}_{i+1}, \dots, \mathbf{r}_N) = -\Psi(\mathbf{r}_1, \mathbf{r}_2, \dots, \mathbf{r}_{i+1}, \mathbf{r}_i, \dots, \mathbf{r}_N) \quad (2.4)$$

The Hartree wavefunction (2.3) is in violation of the Pauli principle, which in general imposes a change of sign of the total wavefunction when two electrons are switched.

Their next level of theory beyond the Hartree approximation is Hartree-Fock theory. The many body electronic wavefunction is also constructed from one-electron functions. The total wave function for the system was not a simple product of orbitals, but an antisymmetrized sum of all the products which can be obtained by

interchanging electron labels. It is conveniently represented as a determinant called Slater determinant:

$$\Psi(r_1, r_2, \dots, r_N) = \frac{1}{\sqrt{N!}} \begin{vmatrix} \psi_1(r_1) & \psi_2(r_1) & \cdots & \psi_N(r_1) \\ \psi_1(r_2) & \psi_2(r_2) & \cdots & \psi_N(r_2) \\ \psi_1(r_3) & \psi_2(r_3) & \cdots & \psi_N(r_3) \\ \vdots & \vdots & \vdots & \vdots \\ \psi_1(r_N) & \psi_2(r_N) & \cdots & \psi_N(r_N) \end{vmatrix} \quad (2.5)$$

The Pauli principle approximated in the independent electron approximation described above, does not allow more than one electron to occupy a given state. This wavefunction can be inserted into the Hamiltonian, equation 2.2, and an expression for the total energy derived. Applying the theorem that the value of a determinant is unchanged by any non-singular linear transformation, we may choose the  $\psi_i$  to be an orthonormal set. We now introduce a Lagrange multiplier  $\epsilon_i$  to impose the condition that the  $\psi_i$  are normalized, and minimize with respect to the  $\psi_i$  functions.

$$\frac{\delta}{\delta\psi} \left[ \langle \vec{H} \rangle - \sum_j \epsilon_j |\psi_j|^2 d\mathbf{r} \right] = 0 \quad (2.6)$$

An enormous simplification of the expressions for the orbitals  $\psi$  results. They reduce to a set of one-electron equations of the form

$$-\frac{1}{2}\nabla^2\psi_i(\mathbf{r}) + V_{nuc}(\mathbf{r})\psi_i(\mathbf{r}) + U(\mathbf{r})\psi_i(\mathbf{r}) = \epsilon_i\psi_i(\mathbf{r}) \quad (2.7)$$

where  $U(\mathbf{r})$  is a non-local potential and the local nuclear potential is denoted by  $V_{nuc}(\mathbf{r})$ . The one-electron equations resemble single-particle Schrödinger equations. The full Hartree-Fock equations are given by

$$\epsilon_i\psi_i(\mathbf{r}) = \left( -\frac{1}{2}\nabla^2 + V_{nuc}(\mathbf{r}) \right) \psi_i(\mathbf{r}) + \sum_j e^2 \int d\mathbf{r}' \frac{|\psi_i(\mathbf{r}')|^2}{|\mathbf{r} - \mathbf{r}'|} \psi_i(\mathbf{r}) \quad (2.8)$$

$$- e^2 \sum_j \delta_{\sigma_i\sigma_j} \int d\mathbf{r}' \frac{\psi_j^*(\mathbf{r}')\psi_i(\mathbf{r}')}{|\mathbf{r} - \mathbf{r}'|} \psi_j(\mathbf{r}) \quad (2.9)$$

The right hand side of the equations consists of four terms. The first and second give rise are the kinetic energy contribution and the electron-nuclear potential. The third term, or Hartree term, is the simply electrostatic repulsion potential arising from the charge distribution of  $N$  electrons. As written, the term includes an unphysical self-interaction of electrons when  $i = j$ . This term is cancelled in the fourth, or exchange term. The exchange term results from our inclusion of the Pauli principle and the assumed determinantal form of the wavefunction. The effect of exchange is for electrons of like-spin to avoid each other. Each electron of a given spin is consequently surrounded by an “exchange hole”, a small volume around the electron which like-spin electron avoid.

Hartree-Fock theory, by assuming a single-determinant form for the wavefunction, neglects correlation between electrons. The electrons are subject to an average non-local potential arising from the other electrons, which can lead to a poor description of the electronic structure. Although qualitatively correct in many materials and compounds, Hartree-Fock theory is often insufficiently accurate to make accurate quantitative predictions.

The Hartree-Fock equations are solved using an iterative scheme. The starting point is an approximative description of the single particle functions,  $\psi_i(r)$ . These could be hydrogen-like functions, but usually some better approximations are used. With these starting functions, the Hartree-Fock potential is constructed and the eigenvalue equation (2.8) is solved. Then a new set of single-particle functions are obtained and a new Hartree-Fock potential is constructed and again the eigenvalue equation is solved. This is done over and over again until the single particle functions  $\psi_i(r)$  as well as the energy eigenvalues  $\epsilon_i$  are stable.

### 2.2.3 Variational principle

The Variational Principle provides the starting point for almost all methods which aim to find an approximate solution to Schrödinger’s equation. It was discovered very early in the history of quantum mechanics [5]. The variational principle states that if we take some trial wave function  $\Psi$  for a system and calculate the expectation value

of energy  $E$ , this energy will be either higher, or equal to the ground state energy  $E_0$ , which is the expectation value of the system calculated using the true ground state wave function  $\Psi_0$ .

$$E = \frac{\langle \Psi | H | \Psi \rangle}{\langle \Psi | \Psi \rangle} \geq E_0 = \frac{\langle \Psi_0 | H | \Psi_0 \rangle}{\langle \Psi_0 | \Psi_0 \rangle} \quad (2.10)$$

The  $E = E_0$  occurs only if  $\Psi$  is equivalent to  $\Psi_0$ , but otherwise,  $E > E_0$ . For proof of the theorem refer to [60, 42]

What is more important however, that this theorem provides us with the prescription how to find the good wave function: try to go as low with the expectation value of energy, as you can since you cannot go lower than the true value. And the lower you go, the better you are. But be careful, the principle is true only if we are applying a true Hamiltonian in the expression for expectation energy. Of course, if your Hamiltonian does not represent a physical system, you can get whatever you wish.

## 2.2.4 Hohenberg and Kohn theorems

The basics of the rigorous density functional theory (DFT) were laid in 1964 with the publication of the Hohenberg and Kohn paper [22] in which they proved two theorems which will be formulated below. For an  $N$ -electron system, the external potential or  $V_{ext}$  (the electrostatic potential of the electrons due to nuclei) completely fixes the Hamiltonian; thus  $N$  and  $V_{ext}$  determine all properties for the ground state. We consider non-degenerate ground states only, but the theory can be extended to degenerate systems [49]. This of course is not surprising since  $V_{ext}$  defines the whole nuclear framework of a system, which together with the number of electrons  $N$ , determines all the electronic properties. Notice also that  $\rho(r)$  and  $N$  are related through the normalization condition

$$N = \int \rho(r) d^3r, \quad (2.11)$$

Instead of  $N$  and  $V_{ext}$ , the first Hohenberg-Kohn theorem legitimizes the use of electron density  $\rho(r)$  as basic variable. It states:

*The external potential  $V_{ext}$  is determined, within a trivial additive constant, by the electron density  $\rho(r)$ .*

Notice that this constant does not change anything, since the Schrödinger equation with Hamiltonians  $H$  and  $H + const$  will yield exactly the same eigenfunctions and all the energies will be simply shifted by the value of this const, which just establishes the zero energy reference.

An alternative formulation of the theorem is: Every observable of a stationary quantum mechanical system (including energy), can be calculated, in principle exactly, from the ground-state density alone, i.e., every observable can be written as a functional of the ground-state density.

The proof of this theorem is quite simple. The proof was made through contradiction.

1. Assume that we have an exact ground state density  $\rho(r)$ .
2. Assume that the ground state is nondegenerate.
3. Assume that for the density there are two possible external potentials:  $V_{ext}$  and  $V'_{ext}$ , which obviously produce two different Hamiltonians:  $H$  and  $H'$ , respectively. These produce two different wave functions for the ground state:  $\Psi$  and  $\Psi'$ , respectively. They correspond to energies  $E = \langle \Psi | H | \Psi \rangle$  and  $E' = \langle \Psi' | H' | \Psi' \rangle$ .
4. The expectation value of energy for the  $\Psi'$  with the Hamiltonian  $H$  is always larger than the ground state energy according to the variational theorem:

$$\begin{aligned} E_0 &= \langle \Psi | H | \Psi \rangle \\ &< \langle \Psi' | H | \Psi' \rangle \end{aligned} \tag{2.12}$$

$$\begin{aligned} &< \langle \Psi' | H - H' + H' | \Psi' \rangle \\ &< \langle \Psi' | H - H' | \Psi' \rangle + \langle \Psi' | H' | \Psi' \rangle \\ &< \int \rho(r) [V_{ext}(r) - V'_{ext}(r)] d\mathbf{r} + E'_0 \end{aligned} \tag{2.13}$$

5. Now let's calculate the expectation value of energy for the  $\Psi$  with the Hamiltonian  $H'$  and apply again the variational theorem:

$$E'_0 = \langle \Psi' | H' | \Psi' \rangle$$



$$< \langle \Psi | H' | \Psi \rangle \tag{2.14}$$

$$< \langle \Psi | H' - H + H | \Psi \rangle$$

$$< \langle \Psi | H' - H | \Psi \rangle + \langle \Psi | H | \Psi \rangle$$

$$< - \int \rho(r) [V_{ext}(r) - V'_{ext}(r)] d\mathbf{r} + E_0 \tag{2.15}$$

6. By adding eqs. (2.13) and eqs. (2.15) we arrive at:

$$E_0 - E'_0 < E'_0 - E_0$$

This obviously leads to a contradiction, and so there cannot be two different  $V_{ext}$  that give the same  $\rho(r)$  for their ground states. Thus,  $\rho(r)$  determines  $N$  and  $V_{ext}$  and hence all properties of the ground state. This will give us a chance to write the total energy as a functional of the density as  $E[\rho]$ .

The second Hohenberg-Kohn theorem provides the energy variational principle. It reads:

*For a trial density  $\tilde{\rho}(r)$  such that  $\tilde{\rho}(r) \geq 0$  and  $\int \tilde{\rho}(r) d^3r = N$ ,*

$$E_0 < E[\tilde{\rho}].$$

In other words, if some density represents the correct number of electrons  $N$ , the total energy calculated from this density cannot be lower than the true energy of the ground state and the ground state density can be calculated, in principle exactly, using the variational method involving only density.

To prove this theorem is straight forward by using the first theorem above. Note that the previous theorem assures that  $\tilde{\rho}(r)$  determines its own  $V_{ext}$ , Hamiltonian  $H$ , and wave function  $\tilde{\Psi}$ . Using this wave function as a trial wave function, one can calculate the expectation value of the ground state Hamiltonian, which is  $E[\tilde{\rho}]$ . But we know from variational principle that this energy should be greater than the energy of the true wave function ( $E[\rho] \equiv E_0$ ). Therefore,  $E[\tilde{\rho}] \geq E_0$ .

### 2.2.5 Kohn-Sham theorems

The total-energy functional looks like the following [31].

$$\begin{aligned}
 E[\{\psi(\mathbf{r})\}] &= \sum_i f_i \int \psi_i^*(\mathbf{r}) \left( -\frac{\hbar^2}{2m} \nabla^2 \psi_i(\mathbf{r}) \right) d^3\mathbf{r} \\
 &+ \int V_{nuc}(\mathbf{r}) \rho(\mathbf{r}) d^3\mathbf{r} \\
 &+ \frac{1}{2} \int \phi(\mathbf{r}) \rho(\mathbf{r}) d^3\mathbf{r} \\
 &+ \int f_{xc}(\rho(\mathbf{r})) d^3\mathbf{r} \\
 &+ U_{nn}
 \end{aligned} \tag{2.16}$$

for  $i = 1, 2, \dots$ , number of orbital, and where:

- $f_i$  (usually equal to two) is the number of electrons in orbital  $i$ .
- $\psi_i(\mathbf{r})$  are called the Kohn-Sham orbitals. An orbital often is described as a three-dimensional region within which there is a high probability of finding the electron [48]. These orbitals also describe the behavior of the electrons.
- $\psi_i^*(\mathbf{r})$  is the complex conjugate of  $\psi_i(\mathbf{r})$ .
- $\hbar$  is the Plank's constant.
- $m$  is the mass of an electron.
- $d^3\mathbf{r}$  is a volume element.
- $V_{nuc}(\mathbf{r}) = -Ke^2 \sum_a \frac{Z_a}{|\mathbf{r}-\mathbf{R}_a|}$  is the single electron potential at point  $\mathbf{r}$ , where  $K$  is the Coulomb's constant,  $\mathbf{R}_a$  is the distance from point  $\mathbf{r}$  to nucleus  $a$ .  $e$  is the elementary charge, and  $Z_a$  is the atomic number of nucleus  $a$ .
- $U_{nn} = \frac{1}{2}Ke^2 \sum_{a \neq b} \frac{Z_a Z_b}{\mathbf{R}_{ab}}$  is the total potential energy arising from the interactions among all the nuclei. Where  $\mathbf{R}_{ab}$  is the separation between nuclei  $a$  and  $b$ .
- $\rho(\mathbf{r}) = \sum_i f_i |\psi_i(\mathbf{r})|^2$  is the volume density (number per unit volume) of electrons.

- $\phi(\mathbf{r}) = Ke^2 \int \frac{\rho(\mathbf{r}')d^3\mathbf{r}'}{|\mathbf{r}-\mathbf{r}'|}$  is the total Coulomb potential for a single electron at position  $\mathbf{r}$  due to electronic charge density  $\rho(\mathbf{r})$ .
- $f_{xc}$  is the exchange and correlation function.

It is important to note that not all parts of the right hand side of (2.16) are known. In particular, the eXchange-Correlation (XC) part (which is the  $f_{xc}(\rho(\mathbf{r}))$  term) must be approximated. This function depends on what approximation method we are using. The orbital wave functions  $\psi_i$  can be any functions as long as they obey the following constraint of orthonormality:

$$\int \psi_i^*(\mathbf{r})\psi_j(\mathbf{r})d^3\mathbf{r} = \begin{cases} 1 & i = j \\ 0 & i \neq j \end{cases} . \quad (2.17)$$

We now have an expression for the energy in terms of the orbitals, but which orbitals are the right ones to use? The answer is quite sensible: *the correct orbitals are those which minimize the total energy  $E$  (2.16) while satisfying the orthonormality condition (2.17)*. To minimize (2.16) we need to solve  $\frac{\partial E(\{\psi_i(\mathbf{r})\})}{\partial \psi_i(\mathbf{r})^*} = 0$ . This leads to Kohn-Sham equations [31]:

To make things simpler, we can combine (2.16) and (2.17) using Lagrange multiplier  $\lambda_i$  and minimize it as follows:

$$0 = \frac{\delta}{\delta \psi_i^*(\mathbf{r})} \left( E[\{\psi(\mathbf{r})\}] - \sum_i \lambda_i \int \psi_i^*(\mathbf{r})\psi_i(\mathbf{r}) \right) \quad (2.18)$$

Now we can apply the derivative term by term. The first term (the kinetic energy of the electrons), has only one  $\psi_i^*(\mathbf{r})$  in it, so the derivative looks like :  $-f_i \frac{\hbar^2}{2m} \nabla^2 \psi_i(\mathbf{r})$ . For the electron-nuclear potential energy (second term), the only term which depends on  $\psi_i^*(\mathbf{r})$  is the charge density. But the nuclear potential,  $V_{nuc}(\mathbf{r})$ , is independent of  $\psi_i^*(\mathbf{r})$ . So its derivative takes of the form of  $f_i V_{nuc}(\mathbf{r})\psi_i(\mathbf{r})$ . The electron-electron energy, (third term), has a very similar structure and it will take of the form  $f_i \phi(\mathbf{r})\psi_i(\mathbf{r})$ . For the exchange-correlation term, (fourth term), applying chain rule will lead to  $f_i f'_{xc}(\rho(\mathbf{r}))\psi_i(\mathbf{r})$ . Where  $f'_{xc}(\rho(\mathbf{r})) \equiv \frac{\delta f_{xc}(\rho(\mathbf{r}))}{\delta \rho}$ . The final term of (2.16), the ion-ion interaction does not depend on  $\psi_i^*(\mathbf{r})$ , so there is no contribution to the derivative

term. Finally, the constraint term in (2.18) has only one  $\psi_i^*(\mathbf{r})$  and contributes to the form  $-\lambda_i\psi_i(\mathbf{r})$ .

Collecting all the terms and setting the result to zero and dividing all the terms by  $f_i$ , results in the following equation:

$$-\frac{\hbar^2}{2m}\nabla^2\psi_i(\mathbf{r}) + [V_{nuc}(\mathbf{r}) + \phi(\mathbf{r}) + f'_{xc}(\rho(\mathbf{r}))] = \frac{\lambda_i}{f_i}\psi_i(\mathbf{r}). \quad (2.19)$$

We can re-write (2.19), so as to look like the famous Schrodinger equation as follows.

$$-\frac{\hbar^2}{2m}\nabla^2\psi_i(\mathbf{r}) + V(\mathbf{r})\psi_i(\mathbf{r}) = \epsilon_i\psi_i(\mathbf{r}), \quad (2.20)$$

where,

$$V(\mathbf{r}) \equiv V_{nuc}(\mathbf{r}) + \phi(\mathbf{r}) + f'_{xc}(\rho(\mathbf{r})) \quad (2.21)$$

and  $\epsilon_i \equiv \frac{\lambda_i}{f_i}$ .

So how do we find the correct wave function? Lets see the steps needed to compute the best wave functions using the above mentioned equations of Kohn and Sham. To evaluate the various terms in (2.16), we need the correct orbitals  $\psi_i(\mathbf{r})$ , which we can find from  $V(\mathbf{r})$  using a Kohn-Sham-solver routine to solve (2.19). But to determine  $V(\mathbf{r})$  according to (2.21), we need the nuclear potential, the potential from the electrons and a simple subroutine to evaluate the functions  $f_{xc}$  and  $f'_{xc}$  for a giving starting density  $\rho(\mathbf{r})$ . The minimum of  $E$  obtains only when all of the above equations hold simultaneously. In particular, the density must be self-consistent. That is, the density  $\rho_1(\mathbf{r})$  which we input must lead to a potential  $V(\mathbf{r})$  which gives rise to a set of orbitals  $\psi_i(\mathbf{r})$  that sum to a final density  $\rho_2(\mathbf{r})$  which should equal to the input density  $\rho_1(\mathbf{r})$ . If  $\rho_1(\mathbf{r}) \neq \rho_2(\mathbf{r})$ , we generate a new input density  $\rho_1(\mathbf{r})$  from a combination of previous densities and continue the self consistent iterations. Figure (2.1), shows these process graphically. This method of solution is called Self Consistent Field theory (SCF).

## 2.3 The pseudopotential approximation

To calculate the electronic wavefunctions for a relatively large slab including all the electrons is an extremely hard task; in an element such as silicon, where the

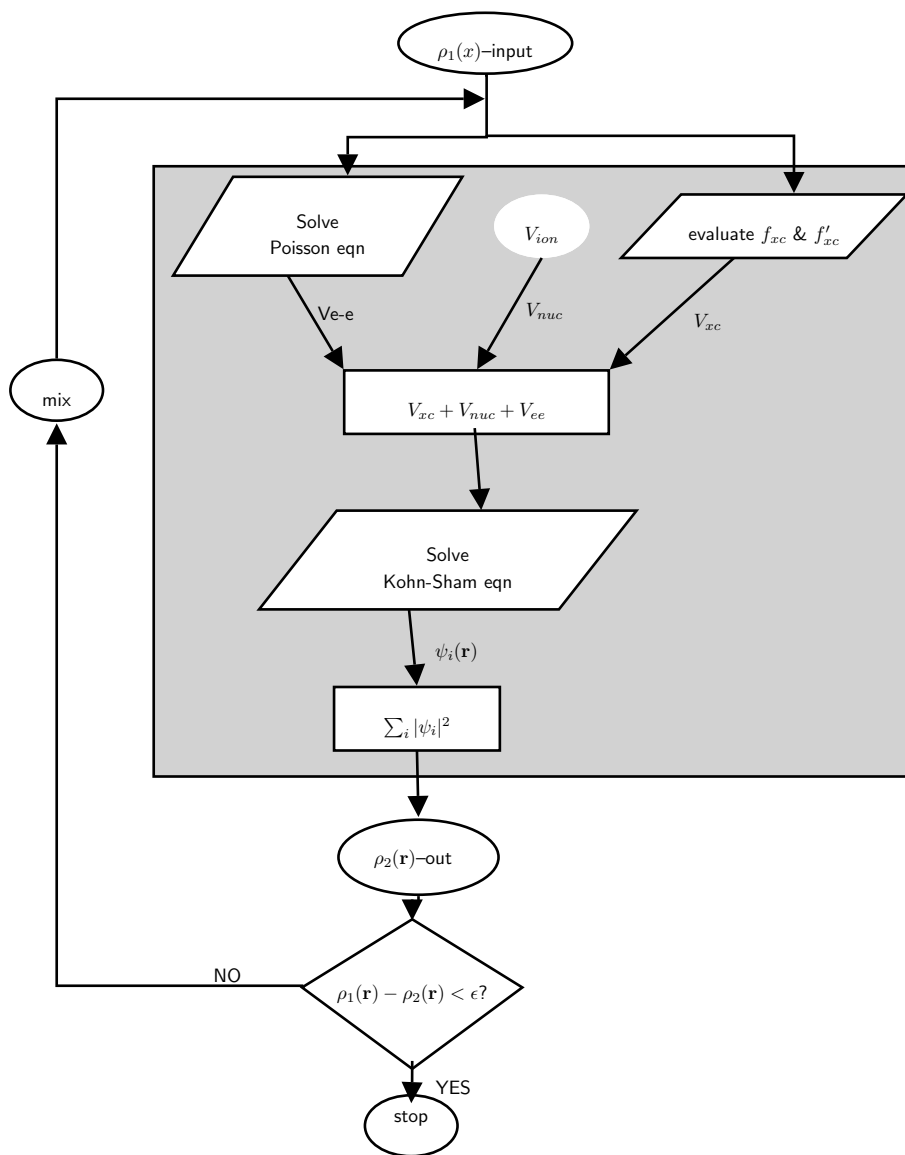


Figure 2.1: Basic self consistent field loop for solving Kohn-Sham equations.

outer, or valence, electrons are in the 3s and 3p orbitals, their wavefunctions must be orthogonal to those of the inner, core states due to the Pauli exclusion principle. This entails introducing nodes into these wavefunctions, which in turn gives them a high kinetic energy in the core region, requiring a high plane wave cutoff and increasing computational time enormously. What is done in practice to make the calculation easier is to replace both the inner electrons and potential with another potential. Because the orthogonality requirement, due to the inner, core electrons, means that the nuclear charge has less effect on the outer electrons - they are screened. There is a close cancellation between the attractive, Coulomb potential from the nucleus and the repulsive orthogonality requirement from the core electrons. This can be taken advantage of, by replacing the strong, nuclear Coulomb potential inside a certain radius with a weaker “pseudopotential”, and modelling only the valence electrons (which should now be referred to more properly as pseudoelectrons). Figure (2.2) shows an example of pseudopotential for Cd atom generated using the projector augmented wave (PAW) formulation using ATOMPAW [27].

Electrons with different angular momentum components (e.g. s or p electrons) will scatter differently from an atomic potential (or a pseudopotential). The best way to correctly represent this different scattering with a pseudopotential is to use different projectors and potentials for different angular momentum components:

$$V_{NL} = \sum_{lm} |lm\rangle V_l \langle lm| \quad (2.22)$$

where  $V_l$  is the pseudopotential for angular momentum component  $l$ . This form of pseudopotential is known as a non-local pseudopotential, and it allows the maintenance of softness of a pseudopotential (i.e. allowing the plane wave cutoff to be kept small) while correctly reproducing the scattering and phase shift of the electrons.

Another key feature of a pseudopotential is that the wavefunctions and charge density outside the core region should be identical to those produced by the genuine ionic potential. If the integral of the pseudo-charge density within the core is made to be equal to the integral of the real charge density in the core, then this condition, known as norm conservation, is fulfilled. Norm-conserving pseudopotentials were first introduced by Starkloff and Joannopoulos ([29, 61] for local pseudopotentials only, and

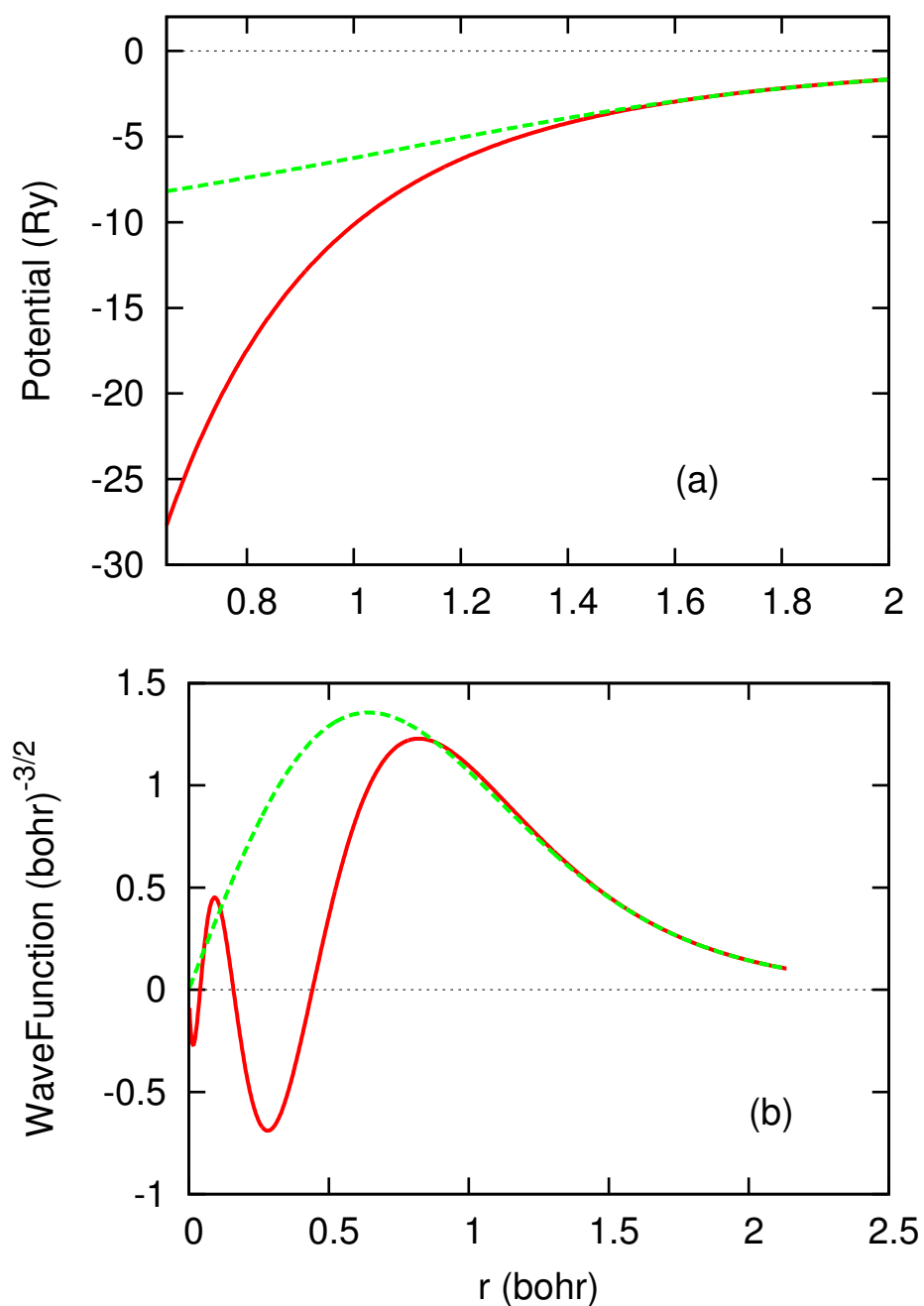


Figure 2.2: A plot of true potential (red solid line in (a)) and its corresponding pseudopotential (green dashed line in (a)) for Cd. Diagram (b) shows the 4s all electron (red solid line) and pseudowavefunction (green dashed line) for Cd atom. These were generated in the the PAW formulation using ATOMPAW.

accurately described the valence energies and wave functions of many heavy atoms accurately. The method was extended to non-local pseudopotentials by several groups [56, 19, 73, 6]. As Hamann et al. [19] observed, the matching of the real and pseudo wavefunctions outside the core guarantees that the first order energy dependence of the scattering is correct, so that the scattering is described correctly for a wide range of energies. The most recent development in pseudopotentials involves relaxing the norm conservation criterion, in order to reduce further the plane wave cutoff required (in particular for extremely hard elements such as oxygen)[68]. This in turn requires non local pseudo potentials to reproduce the energy scattering properties for the same wide range of energies. The use of Vanderbilt pseudopotentials (also known as ultrasoft pseudopotentials) can speed up calculations.

Vanderbilt's ultra-soft pseudopotential is the most widely used at this time. But there are several drawbacks that intimidate users. One of the problems is that the method to construct the pseudo potentials needs many parameters and several cutoff radii. This leads to testing the potentials extensively in order to obtain an accurate and highly transferable pseudopotential.

A very similar approach is given by Blöchl's projector augmented wave method[7] (PAW), with an additional advantage. The PAW method maps all electron (AE) wave functions (one-electron eigenfunctions of the Kohn-Sham equations) onto a pseudofunction that is smooth in the regions close to the nuclei. Unlike the ultrasoft approach, a key advantage here is that the mapping is reversible. That is, one can recover the complete nodal behavior of the all electron wave function. This is achieved without increasing computational calculation. For more derivations of this approach, readers are advised to read references [7, 25, 26].



# Chapter 3

## Experimental motivation

### 3.1 Foundations of our experiment

#### 3.1.1 Photoelectron spectroscopy

Electron spectroscopy is when electrons created by photoionization are used as carriers of information about the system they have just left behind, and the interaction mechanisms. The photoelectric effect was explored in 1887 by Heinrich Hertz. He could produce an electric current in a photocell by simply illuminating the cathode with light of sufficiently short wavelength [13]. The photoelectric law was formulated by Albert Einstein in 1905. He introduced a quantization of the radiation and in this description the radiation appears in the form of wave packets, or energy quanta. Each photon has a given wavelength  $\lambda$  and, accordingly,  $E$  is given by

$$E = h \frac{c}{\lambda} = h\nu \quad (3.1)$$

where  $h$  is Planck's constant,  $c$  is the speed of light and  $\nu$  is the frequency of the radiation.

The photoelectric law was written originally

$$h\nu = E_B + E_{kin} \quad (3.2)$$

where  $E_{kin}$  is the kinetic energy of the photoelectron,  $h\nu$  is the energy of the photon absorbed and  $E_B$  is the binding energy of the electron in the atom. This atomic

phenomenon can be modified to work for solid surfaces. In solids, the highest filled electronic state is the valence band. The electrons in this band are prevented from escaping the sample by an energy barrier called the work function. The relation in (3.2), then needs to be modified to account for the work function ( $\phi$ ) as:

$$E_{kin} = h\nu - E_B - \phi. \quad (3.3)$$

The  $E_{kin}$  is usually measured relative to vacuum energy ( $E_{vac}$ ). The vacuum level is the energy of an electron which is just outside the sample surface with zero kinetic energy.

In principle, it should be possible to put an instrument in front of the photoelectron and measure its kinetic energy, thereby gaining information about the binding energy of the electron via the photoelectric law. In fact, this is precisely what is being done and this idea forms the basis of the technique of *photoelectron spectroscopy*.

### 3.1.2 Recording of photoelectron spectra

The independent experimental variable for recording a spectrum is the voltage  $V$  applied between the cylindrical mirror analyzer. A voltage applied between two cylindrical electrodes disperses the electrons with respect to their kinetic energy. In order to record a full spectrum, the applied voltage must usually be swept. Therefore a variable voltage supply that is controlled by a computer is normally used in the place of  $V$ . In the simplest arrangement the electrons are detected by means of a single channel electron detector behind a slit. A complete spectrum is obtained by stepping the voltage between the cylindrical electrodes and counting the number of electrons per unit time reaching the detector as a function of the applied voltage. The time and voltage steps are determined by the operator depending on the requirements of statistics and resolution in the experiment.

### 3.1.3 Two-photon photoemission

Photoemission spectroscopy has established its firm position as the most versatile technique to study electronic states in solids and at surfaces as well as of adsorbates

on solid surfaces. The photoemission spectrum is almost a copy of the density of states below the Fermi level from which the electrons are excited above the vacuum level. Photoemission occurs not only by absorbing a single photon exceeding the work function (one-photon), but also by successive absorption of two (pump and probe) photons of energy  $\omega_1$  and  $\omega_2$  respectively under the conditions

$$\hbar\omega_1 < \phi \quad \text{and} \quad \hbar(\omega_1 + \omega_2) > \phi, \quad (3.4)$$

where  $\phi$  is the work function. One-photon photoemission can be used as a tool to study the population and dynamics of normally occupied surface and valence band states. In the process of two-photon photoemission the first pump photon  $\omega_1$  excites an electron from an occupied state below the Fermi level ( $E_F$ ) to an intermediate state between  $E_F$  and  $E_{vac}$ . Upon absorption of a second probe photon  $\omega_2$ , during the survival time of the electron in a transiently populated intermediate state, electrons are excited above  $E_{vac}$  to final photoelectron states, whose kinetic energy distribution curve is the two-photon photoemission spectrum.

Photoelectron spectroscopy is very sensitive to surface states. In previous experiments done here at Wake Forest University, a high density of states in the band gap was observed in most of the II-VI and III-V group semiconductors [43, 58, 65]. One- and two-photon photoemission would be a handy method to better understand these “unusual” (defect) states in the gap. Two-photon photoemission is used to excite and probe unoccupied intermediate states while one-photon photoemission is used to assess the occupied states.

The focus of our project was on using photon energies below the valence photoelectron threshold to observe surface defects in the band gap of a cleaved crystal of CdSe. These defects can be grouped into two groups: intrinsic and extrinsic. Vacancies, interstitials (atoms occupying non lattice sites) and antisite defects (atoms occupy a wrong lattice site) are considered in the intrinsic group while impurity atoms and surface step structures caused by bad cleavage are considered to be extrinsic defects. The advantage of our pulsed laser PES to that of a conventional PES is that, we use a very low photon energy and an intense laser beam. We do not excite electrons directly from the valence band with the low photon energy, and the laser beam power

( $\sim 10^{16}$  photons/second) allows high sensitivity.

### 3.1.4 AES basics

Auger Electron Spectroscopy (AES) is an analytical technique that uses a primary electron beam to probe the surface of a solid material. Secondary electrons that are emitted as a result of the Auger process are analyzed and their kinetic energy is determined. The identity and quantity of the elements are determined from the kinetic energy and intensity of the Auger peaks.

The Auger electrons start with narrow energy distribution, but they soon lose energy as they pass through materials. Auger electrons fail to emerge with their characteristic energies if they start from deeper than about 1 to 5 nm into the surface. Thus, Auger analysis is surface specific. Auger electrons that escape from deeper in the sample contribute lower energy loss tails to the spectrum background. The secondary and backscattered electrons have broad energy distributions that tail into the Auger region. The sum of these interfering signals is much greater than the Auger signals themselves. Auger display algorithms use differentiation to enhance the signal relative to the interferences.[16]

Auger electrons are emitted at discrete energies that allow the atom of origin to be identified. The Auger process involves three steps:

- atom is ionized by removing a core electron,
- upper level electron falls to lower level,
- third electron (Auger electron) is excited by the energy given off in step 2 and detected.

Note that the atom is left with two vacancies so that this technique cannot detect hydrogen or helium.

### 3.1.5 Low energy electron diffraction (LEED) basics

Electrons which have been accelerated through a potential of 30 to 500 volts (i.e., their kinetic energy is around 30 to 500 eV), have a wavelength given by the de Broglie relation which varies from 2.2 Å to 0.5 Å in this case. This fits nicely into the range of distances between atoms in solids and therefore these “low energy” electrons are diffracted by them. The recording and analysis of the diffraction pattern can tell us the arrangement of the atoms on the surface. The sharpness of the pattern is related to the extent of order of the atoms on the surface.

The experiment consists of an electron gun that forms an electron beam with a narrow kinetic energy spread. This beam scatters from the sample surface through a set of charged grids which function to energy select only the electrons which elastically scatter from the surface and are then accelerated to a fluorescent screen. When they strike the screen, they cause the phosphor to glow, revealing a pattern of dots which is the diffraction pattern.

## 3.2 Experimental setup

### 3.2.1 PES

#### Optical set up

A mode-locked Ti:sapphire laser system with 130 fs pulse width, 76 MHz repetition rate, and an average power of 700 mW has been used as a photon source. It has a tunable wavelength range in the infrared region between 770 to 900 nm. In order to overcome the work function of our crystal, our experiment was done using Second Harmonic (SH), Third Harmonic (TH) and Fourth Harmonic(FH) generated for exciting and probing the defect states.

The TH light was generated using 820 nm wave length fundamental light, while the FH was generated using 840 nm. These fundamentals gives rise to 4.5 eV and 5.9 eV TH and FH generated lights respectively. The reason we select two different fundamental wave lengths are due to wave length restrictions on the optical lens and

beta-barium borate (BBO) crystal used in the experiment.

The optical setup for second and fourth harmonic generation is shown in Figure (3.1). The fundamental (IR) light was focused by the first lens into the first BBO crystal. This produces blue light with double the frequency of the fundamental and perpendicular polarization to the fundamental. A second lens is used to focus the blue light to a second BBO crystal to generate the ultraviolet fourth harmonic light. The frequency of the fourth harmonic is double that of second harmonic and quadruple that of fundamental IR light.

In all the doubling process there is some residue of light that passes through the BBO without doubling. Therefore the final light is not only fourth harmonic light but also a combination of second harmonic and fundamental light. So a prism was used to select which beam of light to send to the sample. A prism has been used instead of a regular filter so as to gain more beam power. Regular filters decrease the power of the transmitted beam by up to 50% whereas prisms have a loss of only about 10% due to surface reflections and ultraviolet absorption.

The setup for third harmonic (THG) is shown in Figure (3.2). The first lens focuses the fundamental (IR) light into the first BBO to produce the second harmonic blue light. A second lens is used to collimate the beam. A dichroic mirror is used to separate the visible (second harmonic) from the fundamental (IR) beam. The dichroic mirror transmits IR (820 nm) and reflects SH (420 nm). The dichroic and aluminum mirror are used to rotate the polarization of the SH beam from vertical to horizontal. To generate THG, the polarization of SH and IR must both be aligned with the ordinary axes of the second BBO crystal. Please note that after the first BBO crystal the polarization of SH is  $90^\circ$  relative to the original IR beam.

The SH beam travels a fixed path while the IR travels a variable path length. This is done by mounting two mirrors on a translation stage. This is necessary because the IR and the SH must both spatially overlap and coincide in phase and time in the second BBO. This is accomplished by moving a translation stage placed in the path of the IR beam. A prism or dichroic mirror is used to filter out and send the desired beam to ward the sample in the chamber.

Table (3.1) show the wavelength, photon energy and power of of the generated

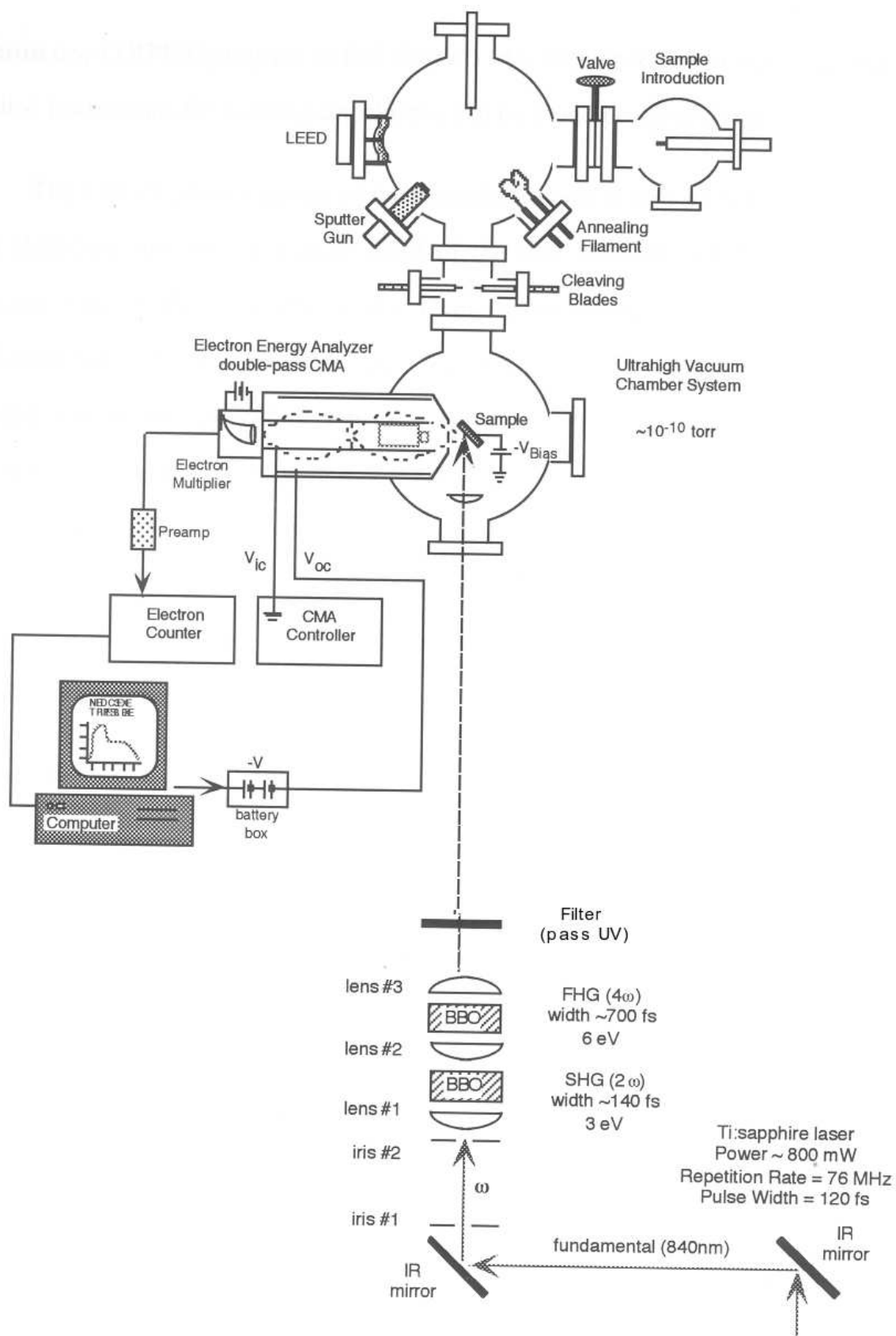


Figure 3.1: PES setup for second and fourth harmonic generation

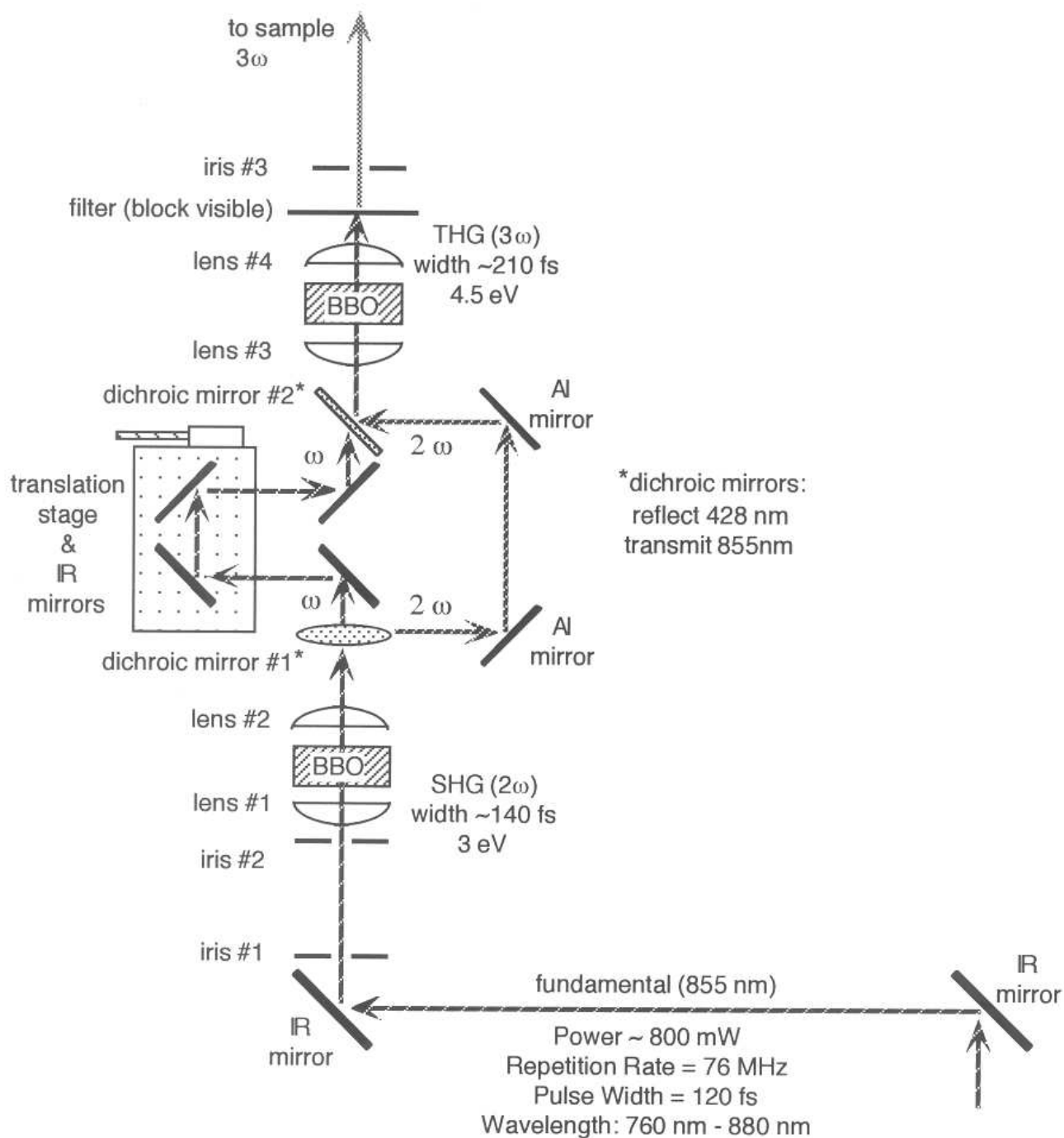


Figure 3.2: PES setup for third harmonic generation



beams.

Harmonic	Wave length (nm) †	Photon Energy (eV)	Average Power (mW)
SH	420	2.95	190
FH	210	5.90	0.5
TH	280	4.5	6

Table 3.1: Properties of the second, third and fourth harmonics of the Ti:sapphire fundamentals. † Note that we used 840 nm Fundamental when we generate FH beam and 820 for the TH generation as explained above.

## Sample preparation

Surface analysis is very sensitive to impurities and the sample surface that we want to study can easily be modified by air molecules if it is not kept in a vacuum chamber. An ultrahigh vacuum chamber is crucial for creating very clean sample surface and keeping the sample clean for a relatively long enough time till the experimental analysis is finished.

Our vacuum system consists of three interconnected chambers which I like to refer it as Side, LEED and PES chambers. Figure(3.3) shows the chambers in more detail.

Each chamber is separated by a valve to prevent any contamination when we open one of the chambers<sup>1</sup>. When a new sample is mounted, the side chamber would be opened and brought to atmospheric pressure while the side-LEED valve is closed. Once the sample is mounted on the horizontal translation arm, the side chamber is closed and the turbomolecular pump would bring the pressure to  $10^{-7}$  or  $10^{-6}$  Torr in about two to three hours.<sup>2</sup> Once the desired low pressure is reached, the side-LEED would be opened<sup>3</sup> and the sample can be moved to the LEED chamber using the horizontal translation arm. This horizontal translation arm only goes from the side chamber to the LEED chamber. So if one needs to send the sample to the main

---

<sup>1</sup>For example when we open the side chamber to load new crystal we do not want to bring the pressure in the LEED chamber to atmospheric pressure.

<sup>2</sup>The side chamber is very small in volume and that is why it takes it relatively small time to take it to a lower pressure.

<sup>3</sup>It is important to make sure the pressure on LEED chamber does not go very high. This can be checked by the pressure guage on the side of the LEED chamber. If it starts to go up, please close the valve.

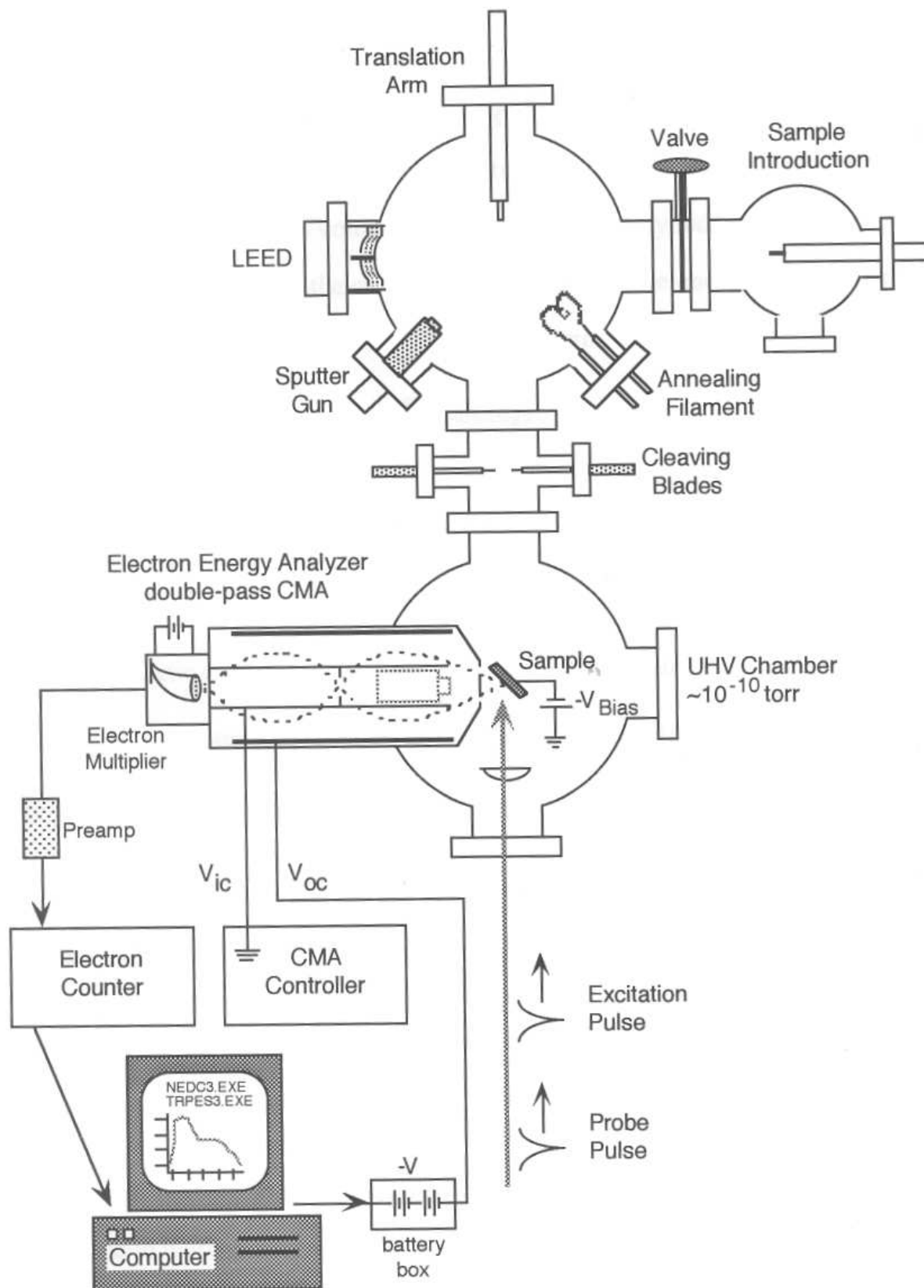


Figure 3.3: Ultrahigh vacuum chambers

chamber, the sample has to be transferred to the vertical translation arm located on the LEED chamber first. The sample is then transferred from the vertical translation to the horizontal translation arm that connects the LEED-main chamber<sup>4</sup>. It is a good idea to keep checking the pressure gauge. If the pressure does not drop down to what it was before the introduction of the sample in a few hours, you can help the ion pump by heating the chamber. The LEED chamber has internal quartz lamp which can be used to heat the chamber from inside to a temperature of 150° or greater. To get a good result, it is good to wrap the chamber with heating tapes and blankets.

After the desired temperature is reached, the quartz lamp should be turned off and the sublimator should be turned on to aid the ion pump removing water vapor from the ultrahigh vacuum system<sup>5</sup>. The normal working pressure of the LEED chamber is about  $2.5 \times 10^{-9}$  Torr.

### Energy distribution curve

The PES experiment was conducted in ultrahigh vacuum (UHV) at a working pressure of  $4 \times 10^{-10}$  Torr. The electron-energy analysis was accomplished with a double-pass cylindrical mirror analyzer (CMA). A convex lens was placed inside the vacuum chamber to focus the laser light to the sample. Minimum spot size on the sample was obtained by translating the lens along the optical axis to maximize photoelectron counts on the two-photon part of the spectrum characterized by quadratic dependence on the laser intensity. In addition to that the sample was biased to about -25 V to improve the CMA transmission efficiency.

We calculated the defect state energy (states could be occupied or unoccupied) from the measured kinetic energy. A basic program NEDC3.EXE [39] that controls voltage applied to the outer cylinder of the CMA records  $E_K - eV_{Bias}$  and the logarithm of the electron counts to an output data file. Since the detector and the sample are at two different vacuum energy levels due to the negative bias voltage, we need to relate the kinetic energy measured by the CMA to the “real” kinetic energy of

---

<sup>4</sup>At this point all the valves are closed and each chamber is isolated

<sup>5</sup>Usually the system does not need baking if one waits long enough for the turbo pump to drop the pressure to a low value before the opening of the LEED-side chamber valve

the photoelectron when it leaves the sample. Figure (3.4) shows a schematic energy diagram representation the sample and the cylindrical mirror analyzer.

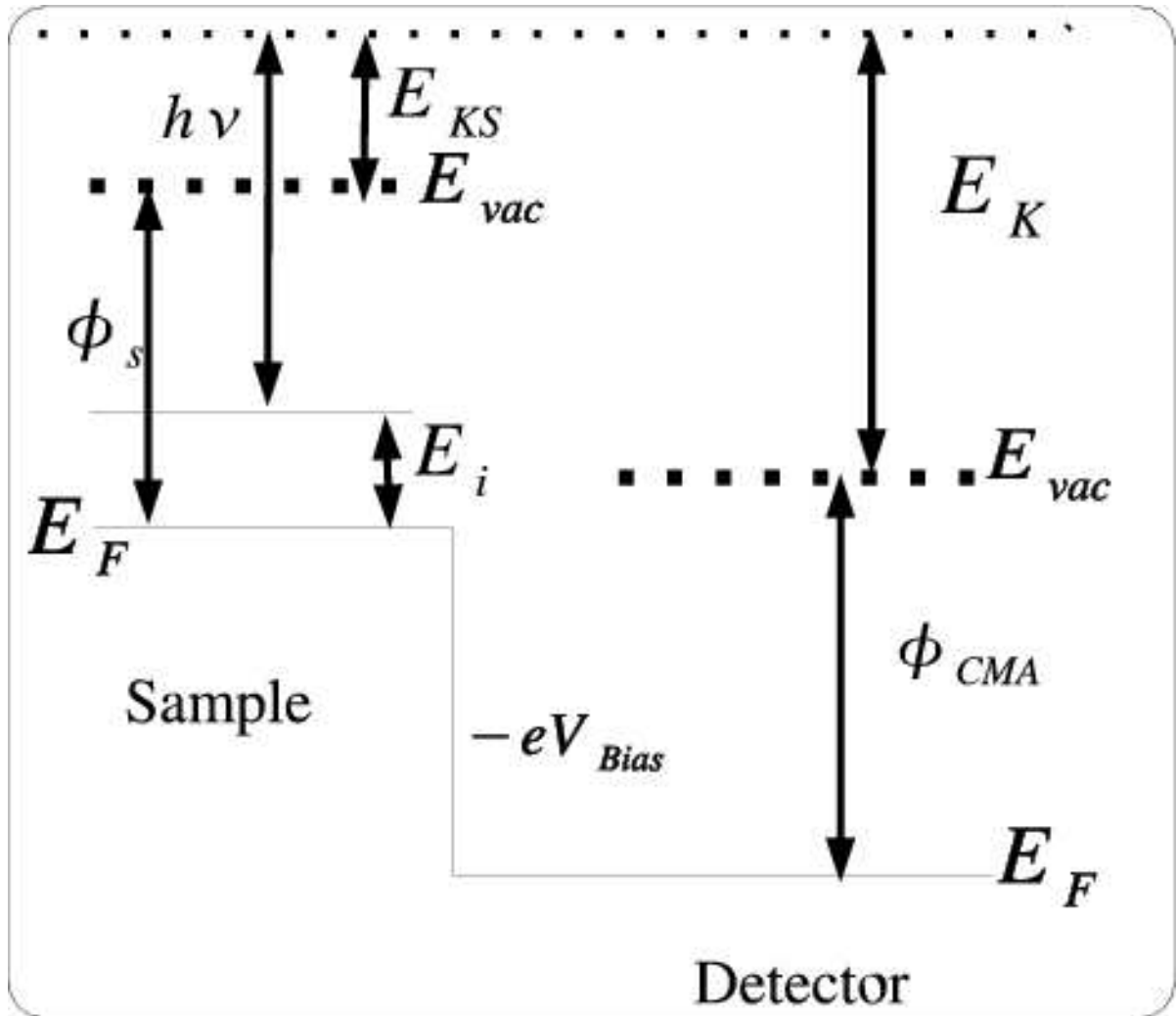


Figure 3.4: Energy diagram representing the sample and CMA

From Figure (3.4) we can derive the relationship between the sample and detector parameters as follows:

$$E_{KS} = E_i + h\nu - \phi_s \quad (3.5)$$

$$\begin{aligned} E_K &= E_{KS} + \Delta E_{vac} \\ &= E_{KS} + \phi_s - (\phi_{CMA} - eV_{Bias}) \\ &= E_{KS} + \phi_s - \phi_{CMA} + eV_{Bias} \end{aligned}$$

$$\begin{aligned}
&= E_i + h\nu - \phi_s + \phi_s - \phi_{CMA} + eV_{Bias} \\
&= E_i + h\nu - \phi_{CMA} + eV_{Bias}.
\end{aligned} \tag{3.6}$$

Where:

- $E_{KS}$  is the kinetic energy of the photoelectron as measured relative to vacuum level of the sample.
- $E_i$  is the energy of the intermediate state (for the unoccupied states and initial energy for the occupied states) the electron was occupying just before it was excited out of the material.
- $h\nu$  is the energy of the photon source.
- $\phi_s$  is the work function of the sample.
- $E_K$  is the kinetic energy of the photoexcited electron measured by the detector.
- $eV_{Bias}$  is the negative bias voltage energy applied to the sample.
- $\phi_{CMA}$  is the work function of the CMA.

Equation (3.6) is not the complete relationship between the sample and CMA properties. According to Ref.[43], there are two terms that are not included in the above equation. These are the effect of power of probe beam on band bending and the effect of bias voltage. Rearranging (3.6) to solve for the intermediate state energy and including the effect of power and bias voltage, the intermediate state energy can be written as:

$$E_i = E_K - eV_{Bias} - h\nu + \phi_{CMA} \pm E_{Photovoltage} - E_{BiasCorrection}, \tag{3.7}$$

where:

- $E_{Photovoltage}$  is the correction to the voltage shift <sup>6</sup>.
- $E_{BiasCorrection}$  is a correction for the bias voltage

---

<sup>6</sup>This term is very small for our samples. It will not be considered later. We just put it here for completeness and if one wants to use it for other materials.

### Bias correction of CdSe (11 $\bar{2}$ 0)

According to [43], the negative bias voltage applied to the sample can introduce an unwanted effect if the bias voltage is relatively large. The main reason we want to apply the negative bias voltage is to elevate the Fermi level of the sample so as to get enough counts of photoelectrons. The bad thing is that this correction not only depends on the value of the bias voltage but also on the type and shape of crystal under investigation. This means that, for every new cleaved sample one has to calculate this shift.

To calculate this correction, one needs to obtain a set of energy distribution curves for different applied sample bias voltage. Table (3.2) shows peak energy value as a function of bias voltage. The peak value was generated using a FORTRAN program (B.2), which selects the energy value that corresponds to the one that has peak photoelectron count for a given energy distribution curve.

B	peak pos	B	peak pos
-12	3.94814491	-23	4.34658194
-13	3.89833999	-24	4.3963871
-14	4.14736414	-25	4.495996
-15	4.04775381	-26	4.54580116
-17	4.19716787	-27	4.54580116
-18	4.19716787	-28	4.54580116
-19	4.24697304	-29	4.64541101
-20	4.19716787	-30	4.69521523
-21	4.34658194	-31	4.69521523
-22	4.44619179	-32	4.69521523

Table 3.2: Measurement of peak position as a function of B( $eV_{Bias}$ (volts)) for CdSe 11 $\bar{2}$ 0

When the peak position of the spectrum is plotted as a function of bias voltage, the shift can be determined from the slope of a linear fit. Figure (3.5) shows the linear fit of Table (3.2). The slope of the linear fit is  $0.039037(eV/volt)$ . The correction to the photoelectron intensity is given by:

$$E_{BiasCorrection} = slope(eV/volt) \times eV_{Bias}(volts) \quad (3.8)$$

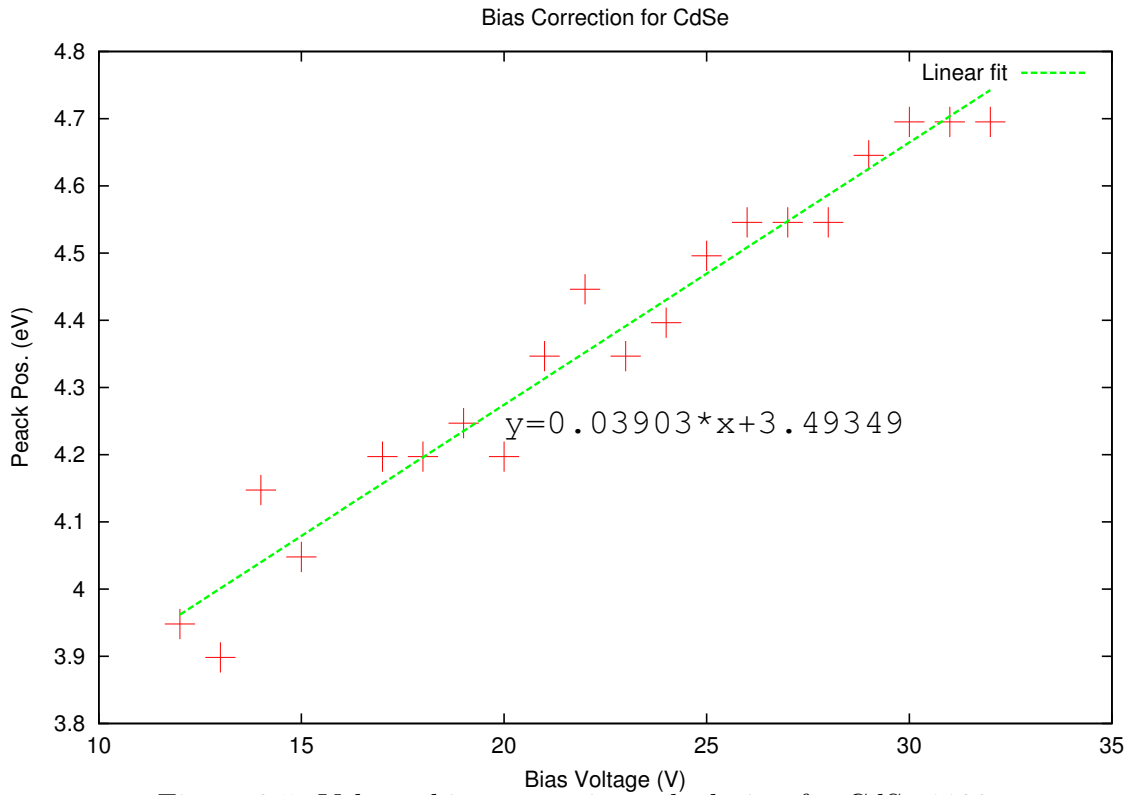


Figure 3.5: Voltage bias correction calculation for CdSe 1120

### Calculation of $\phi_{CMA}$

A Cylindrical Mirror analyzer (CMA) consists of two concentric metal cylinders arranged such that their axes are coincident. Different voltages are placed on each cylinder such that there is an electric field between the two cylinders. Electrons are injected from a point on the axis into the gap between the two cylinders. If the electrons are travelling very fast, they will impinge on the outer cylinder. If they are travelling very slowly, they will be attracted to the inner cylinder. Hence only electrons in a narrow energy region called the pass energy succeed in getting all the way along the cylinders to the detector.

The CMA detector's work function needs to be known as it is used in (3.7). Even though this work function should be a fixed value, in our experience it looks like

it fluctuates over a very long time interval. We thought that this value should be consistent with the value used by former students. The first time when we started taking PES data, we decided to reproduce the ZnTe PES curve. We had a hard time reproducing it because our curves were shifted by same constant value. That is why we decided to recalculate the work function of the CMA. The CMA was idle for a very long time (about two years) before we used it.

To calibrate the  $\phi_{CMA}$  we used a gold surface and  $h\nu = 5.9eV$  (FH). The reason we use FH is because the work function of gold is to a high ( 5.1 to 5.47 eV[70]) for SH or TH photons. Figure (3.6) shows the energy distribution curve for gold surface. Since gold is metal, the highest filled state (Fermi level) is at  $E_i = 0$ . Setting  $E_i = 0$  in (3.7), the CMA work function is then given as:

$$\begin{aligned}\phi_{CMA} &= eV_{Bias} + h\nu - E_{kmax} \\ &= h\nu - (E_{kmax} - eV_{Bias}).\end{aligned}\tag{3.9}$$

Where  $E_{kmax}$  is the maximum kinetic energy measured by the CMA. It is worth noting that this does not involve the sample (gold) work function  $\phi_s$ . Remember that in Figure (3.6), the x-axis represents  $E_k - eV_{Bias}$ . The energy used to probe ( $h\nu$ ) was 5.90eV and  $E_{kmax} - eV_{Bias}$  is about 5.0 eV.<sup>7</sup> Putting all this together in to (3.9) will get:

$$\begin{aligned}\phi_{CMA} &= h\nu - (E_{kmax} - eV_{Bias}) \\ &= 5.90 - 5.0 \\ &= 0.90eV\end{aligned}\tag{3.10}$$

It was assumed that the shoulder above 5 eV in Figure (3.6) is an artifact (due to light scattered into the CMA by the gold, eg).

---

<sup>7</sup>According to Figure (3.6),  $E_{kmax} - eV_{Bias}$  would be about 6.3 eV. But since the work function is comparable to the  $h\nu = 5.9$ , all the value above 5 eV we think it is from two-photon process. It is also clearly visible a “shoulder” that suggests a boundary between one- and two-photon processes in that Figure. The other reason is also we have to make sure that we do not get a negative work function for the CMA



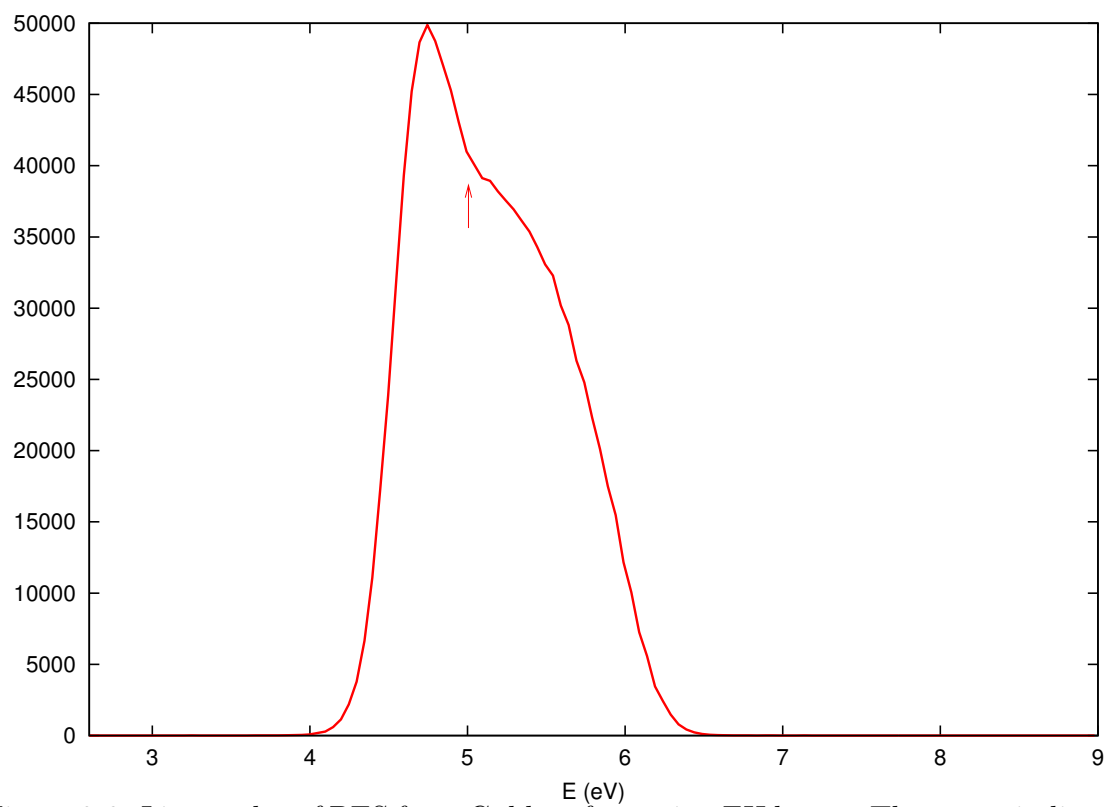


Figure 3.6: Linear plot of PES from Gold surface using FH beam. The arrow indicates where we choose the  $E_{kmax} - eV_{Bias}$ .

### 3.2.2 Interpretation of PES spectra

To interpret any energy distribution curve, one first needs to know the relative position of the band edges. The placement of the band edges, the valence band maximum (VBM) and conduction band minimum (CBM) with respect to the Fermi level requires information about the ionization threshold, electron affinity, band gap and work function of the material under investigation. The following expressions will help us relate the photoemission results with the above terminology.

- Vacuum Energy  $\equiv E_{vac}$
- Ionization Threshold  $\equiv E_{th} = E_{vac} - E_{VBM}$
- Electron Affinity  $\equiv \chi = E_{vac} - E_{CBM}$
- Work Function  $\equiv \phi_{sample} = E_{vac} - E_F$
- Band Gap  $\equiv E_{gap} = E_{CBM} - E_{VBM}$

We took measurements of PES on CdSe crystals under different conditions. These conditions were: different bias voltage, incrementally reduced beam power, and different probing photon energies. The result from these measurements provide a key ingredient for calculation the intermediate state energies, locating band edges and determining the order of the photon process.

We generated a series of Energy Distribution Curves (EDC) as a function of power. Different neutral density filters are used to change the power of the TH light. We have used six neutral optical density filters with specified optical density value of: 0.2, 0.4, 0.6, 0.8, 1.0 and 2.0. The actual values of these optical densities depend on wavelength. The Melles Griot transmission curve manual does not give the exact value for all of the filters used with in our range of wavelength. To determine the exact value we used a spectrophotometer to measure the transmission coefficients. Figure (3.7) shows the transmission values for some of the filters. Equation 3.11 was used to calculate the exact value of these filters and the results are shown in Table (3.3).

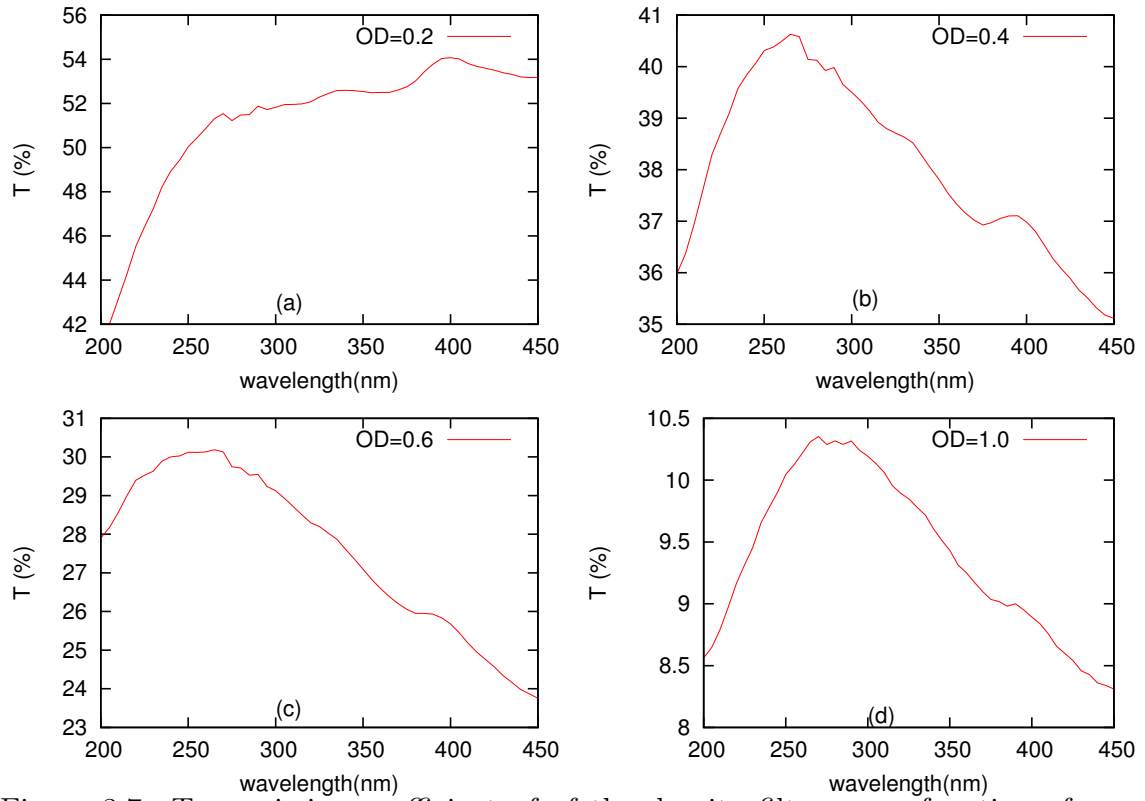


Figure 3.7: Transmission coefficient of of the density filters as a function of wave length. (a) for OD labeled 0.2, (b) for OD=0.4 (c)for OD=0.6 and (d) for OD=1.0

label	FH(210nm)	TH(280nm)	SH(420)
0.2	0.365	0.288	0.271
0.4	0.432	0.397	0.443
0.6	0.544	0.527	0.606
0.8	0.909	0.815	0.877
1	1.056	0.986	1.066
2	2.492	2.199	2.182

Table 3.3: OD as a function of wave length ( $\lambda$ )

The relationship between the Optical Density (OD) specification and intensity of the photoelectrons is the basis for finding if the photoemission was a linear, quadratic or cubic process corresponding to one-, two- or three photon processes. Knowledge of the  $n$  photon process is a key ingredient to the identification of whether or not the last state from which the photoelectron escaped was a filled state. In the following few lines, we derive the relationship between the  $n$ -photon process, the photoelectron counts and the optical density values of the filters used in the experiment.

The OD specification on the neutral density filter is defined as:[43]

$$I = I_0 \frac{1}{10^{OD}} \quad (3.11)$$

Where,  $I_0$  and  $I$  are the photon flux or beam power before and after the neutral density filter respectively.

The electron count ( $C$ ) is also defined as :

$$C = AI^n \quad (3.12)$$

Where  $C$  is Count,  $A$  is arbitrary proportionality constant,  $I$  is the photon flux and  $n$  is the number of photons ( or order  $n$  ). We can use Eqns [3.11]and [3.12] to find a linear equation of  $I$  as a function of  $OD$  as follows.

$$\begin{aligned} C &= AI^n \\ \text{Log}(C) &= \text{Log}(A) + n\text{Log}(I) \\ \text{Log}(I) &= \text{Log}(I_0) - OD \\ \text{Log}(C) &= \text{Log}(A) + n\text{Log}(I_0) - nOD \end{aligned} \quad (3.13)$$

These can also be written as:

$$y = b + ax \quad (3.14)$$

where,  $b = \text{Log}(A) + n\text{Log}(I_0)$  ,  $a = -n$  ,  $y = \text{log}(C)$  and  $x = OD$ .

The number of photons ( $n$ ) involved in the excitation of an electron with a particular energy is found by determining the slope of the best linear fit of  $\text{Log}(C)$  verses

optical density. To automate our experiment, we wrote a small FORTRAN program [B.1] that takes the output of basic program NEDC3.EXE [39] (controls voltage applied to the outer cylinder of the CMA records  $E_K - eV_{Bias}$  and the logarithm of the electron counts to file), and the set of  $OD$ 's to generate the order  $n$  automatically.

### 3.3 Photoelectron spectra from band states

The CdSe ( $11\bar{2}0$ ) crystal was probed with 4.5 eV pulses. This single crystal was cut into a rectangular rod oriented along ( $11\bar{2}0$ ) cleavage plane and cleaved in a ultrahigh vacuum. It has uniform notches of cuts on the side to help the cleaving blades align along the ( $11\bar{2}0$ ) plane to produce a better cleave surface.

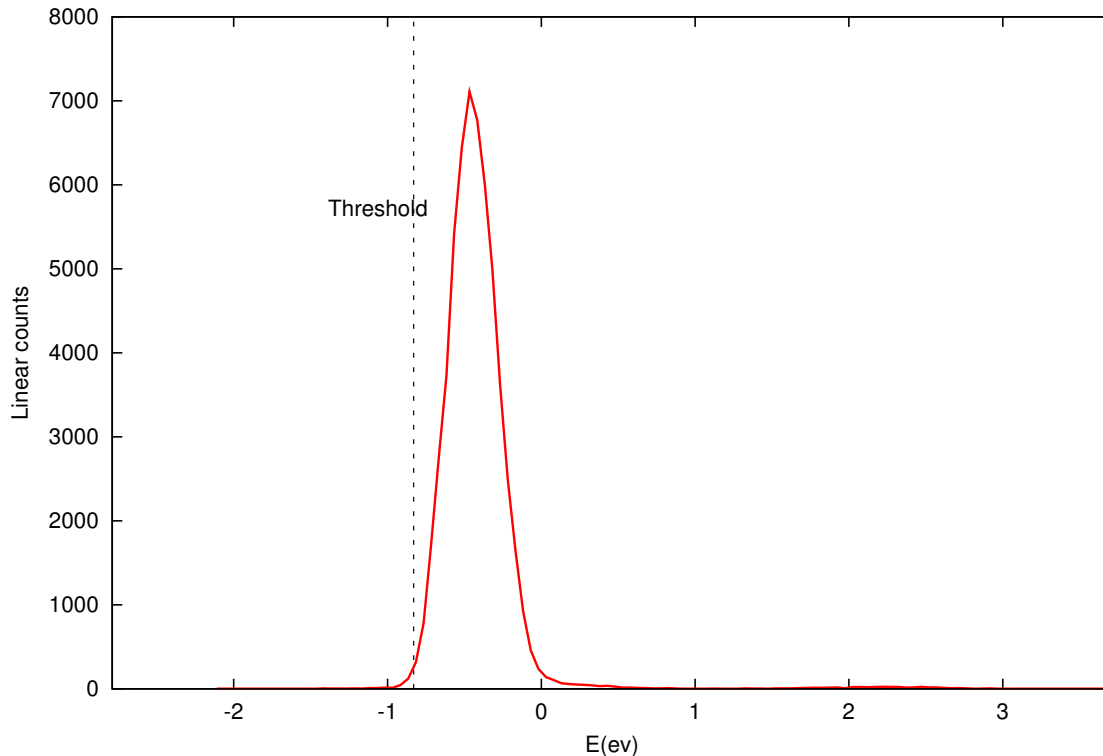


Figure 3.8: Linear energy distribution curve for photoelectrons excited from CdSe ( $11\bar{2}0$ ) excited by 4.5 eV pulse showing the position of the threshold energy.

In Figure (3.8) the energy on the x-axis is the intermediate state energy with respect to the Fermi level, which is set to be 0 eV. This intermediate energy is cal-

culated using Equation (3.7). The y-axis represents the linear photoelectron count per second. The point of interest in this figure is the energy level labeled as threshold energy. This is the lowest energy state from which a photon of energy  $h\nu = 4.5\text{eV}$  can excite an electron into the vacuum. This energy is located by looking at the plot and finding the energy value at which there exists a sharp rise in the photoelectron count. A bias voltage of  $-25\text{ eV}$  was used to improve transmission efficiency and to distinguish photoelectrons from extraneous electrons elsewhere in the vacuum chamber or analyzer.

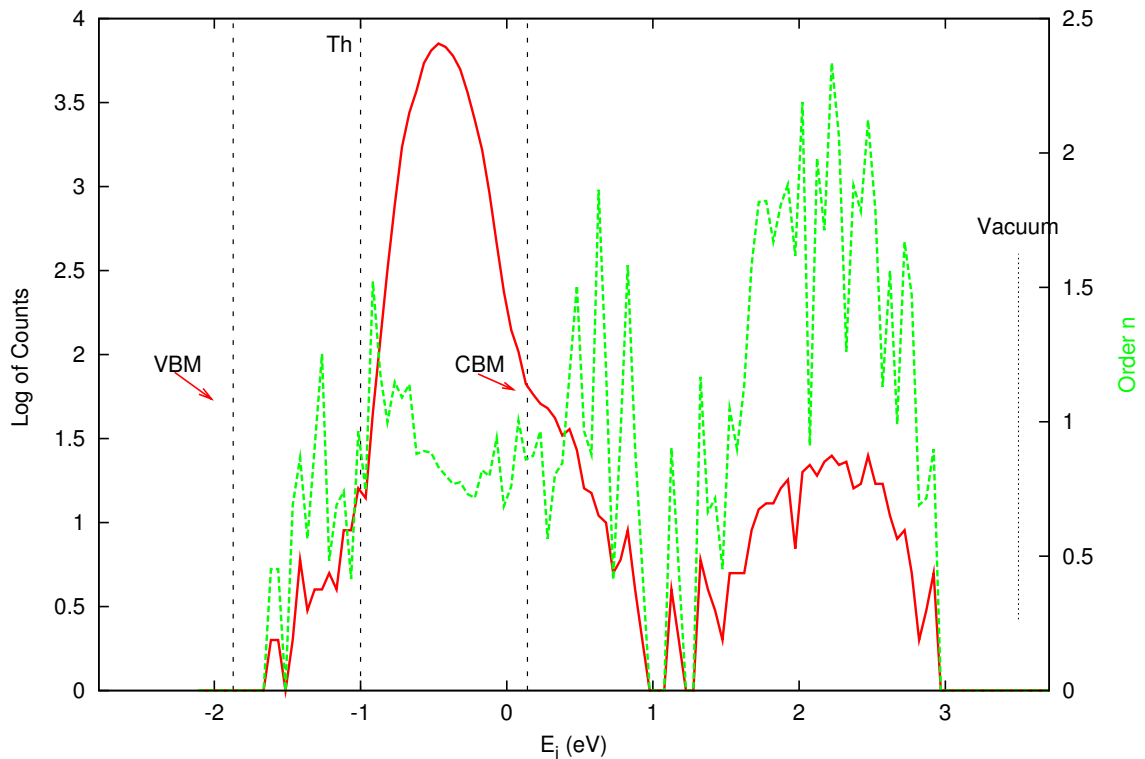


Figure 3.9: Energy distribution curve for photoelectrons exited from CdSe (11 $\bar{2}$ 0) by 4.5 eV TH beam (Red solid line). The number of photons corresponding to this curve is shown in dotted line (Green) with respect to the right-hand ordinate order  $n$ .

The left ordinate of Figure (3.9) shows the same data as in Figure (3.8) with a logarithmic photoelectron count scale. The counts data are shown in red solid line. The energy scale at the bottom is obtained from (3.7) same as above. The number of photons involved in the photoelectron process is shown in green dotted line relative

to the right-hand ordinate. The order  $n$  of the photon process was calculated using equation (3.13).

In addition to the threshold energy reference determined in Figure (3.8), Figure (3.9) also shows the relative positions of valence band maximum (VBM), conduction band minimum (CBM) and vacuum level<sup>8</sup>. These reference points usually are called band edges. The position of the vacuum level is the first to be identified after identifying the threshold initial state for photoemission. The vacuum energy thus lies  $h\nu = 4.5$  eV above the threshold initial state, which is about 0.78 eV below the Fermi energy level. This puts the position of vacuum to be about 3.72 eV above the Fermi energy level. Similarly, the work function, which is the energy difference between vacuum and the Fermi level, would be about 3.72 eV. The position of CBM was fixed by looking at the “shoulder” of the spectra above the Fermi level and by noting that our sample is an n-type semiconductor.<sup>9</sup> The Fermi level of an n-type crystal is closer to the conduction band.

Once the CBM is fixed, the VBM is then found by knowing the gap energy, which is 1.98 eV [45]. This indicates the VBM to be about 1.78 eV below the Fermi level. The electron affinity is defined as the difference in energies between the vacuum and CBM energy levels. Electron affinity is about 3.52 eV.

### 3.3.1 Comparison of PES to band structure

The spectra of Figures 3.9 and 3.16 are plotted versus  $E_i$ . It is the energy level from which the electron is removed by the last photon in  $n$ -photon photoemission.  $E_i$  is the *initial state* for one-photon PES and it is the *intermediate state* for two-photon PES. The zero of  $E_i$  is taken to be  $E_F$  (Fermi energy).

In order to explain the features of Figure (3.9) compared to measured and calculated band structures, we need to know some properties of CdSe (11 $\bar{2}$ 0). Reference [44] has an experimental electronic band structure for wavevector along the  $\Gamma - M$

---

<sup>8</sup>The vacuum level is the point at which an electron is just outside the sample surface zero kinetic energy

<sup>9</sup>To determine the doping type of our sample we ran a Hall effect experiment with the help of Mr. Gang Xiong. The direction of Hall voltage indicates whether it is an n-type or p-type crystal. For more information on the whole experiment read his dissertation.

line using angle resolved photoelectron spectroscopy and inverse photoemission for the same crystal cut. We have also calculated electronic band structure using PWPAW code. Figure (3.11) shows the calculated band structure after shifting the conduction bands to compensate the well known under-estimation of band gap energies by the density functional theory calculation.

Reference [45] has the experimental values for work function, band gap and the position of Fermi level relative to valence band maximum. Once we know these values relative to our energy distribution curve, it will be easy to see which part of the spectra belongs to surface defect states and whether or not the states were empty or occupied. The values are shown below with their relevance to locating the position of valence band maximum, conduction band minimum and Fermi level.

- Vacuum level ( $E_{vac}$ )  $\approx 6.2$  eV above  $E_{VBM} \equiv$  “photoelectron threshold”<sup>†</sup>.
- $E_{gap} = (E_{CBM} - E_{VBM}) \approx 1.98$  eV<sup>†</sup>
- Work function =  $(E_{vac} - E_F) \approx 5.35$  eV.

<sup>†</sup> Ref [45]

The 6.2 eV vacuum level is referenced from the top of the valence band. To make sure that this is really true in the case of our experiment, we can make a simple check using the width of the two-photon conduction band spectrum located at the end of Figure (3.9). It has about 1.7 eV width. Now if we use two photons each with an energy of 4.5eV (TH), starting from the top of the valence band around the wavevector at the point  $M$ , which is around -1.44eV, the photoelectrons will be thrown out to the empty conduction bands around 7.55 eV. To find the vacuum level, now we can subtract the width of our top of the conduction band spectrum in Figure 3.9. This indicates the vacuum level to be at about 5.8 eV above the valence band minimum. This will translate to about 4.07 eV above the Fermi level, which is 0.35 eV higher than what we calculated above. This is not that bad considering the very limited resolving power of the method they used to generate those results.

Our calculated band structure Figure (3.11), could also be used to verify the location of the vacuum level. If we use the same procedure as above, the initial



state would be about  $-0.75\text{eV}$ . The two photon energy of third harmonic will lift the photoelectrons to about  $8.25\text{eV}$  and this implies that the vacuum level is about  $6.75\text{eV}$ . According to Vogel *et.al.*[69], CdSe shows a strong spin-orbit interaction. But in our calculation, spin-orbit coupling is not included due to the fact that the code does not have the ability to do so.

Considering all the above parameters, we can get some picture of the EDC now. Since our sample is n-type crystal, the Fermi level is closer to the conduction band. From looking at the spectrum, we suggest that the CBM is about  $0.2\text{ eV}$  above  $E_F$ .

Now looking at the first peak (from around  $-1.6$  to  $0.2\text{eV}$ ) of Fig.3.9, it lies in the gap of the material and it should not be there for an ideal material. So these must be defect states. The order  $n$  calculation shows that it is a one-photon process. This means that the defect states in the gap must have been occupied!

The second peak (from around  $0.2\text{ eV}$  to  $1\text{ eV}$ ) in Figure 3.9 is a combination of states in the gap and in the conduction band. As we expected, they are initially unoccupied, because of the order  $n \sim 2$ , which indicates a two-photon process. We believe that it is a result of two photon excitation around the  $M$  point on the bandstructure plot on fig. 3.10.

The third group is in the range from about  $1.5\text{ eV}$  to about  $3\text{eV}$ . These entirely lay on the conduction band and it is a two photon process. It is probably excited from the  $M$  point of the conduction band.

### **Comments on the difference in some of the parameters**

On an n-type semiconductor, the band edges bend upwards with the Fermi level pinned by surface states or surface defects at equilibrium condition. Equilibrium condition is when there is no or very few photons of illumination. This is sometimes referred to as a dark condition[66]. Electron-hole pairs created under intense illumination during photoelectron spectroscopy can cause the bending of bands at the surface to change. This flattening of the bands creates a photovoltage shift. Figure (3.12) shows a schematic diagram for n-type semiconductor under different illumination and its effect on band flattening.

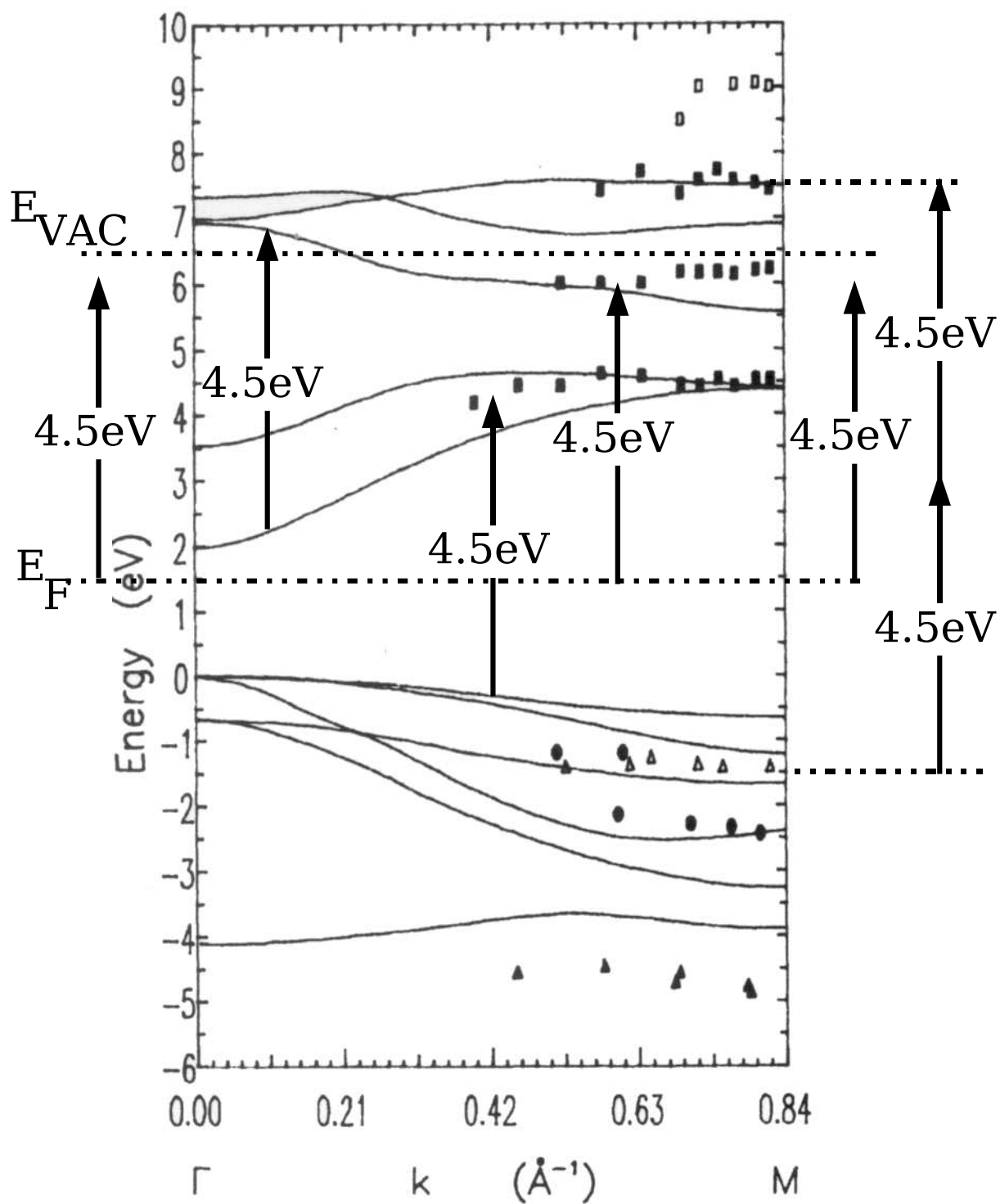


Figure 3.10: CdS  $11\bar{2}0$  band structure adjusted to CdSe band gap in Ref. [44]. The experimental points are from an inverse photoemission from Ref [44]. The 4.5 eV arrows show the possible transitions that correspond to our TH phonon excitation.

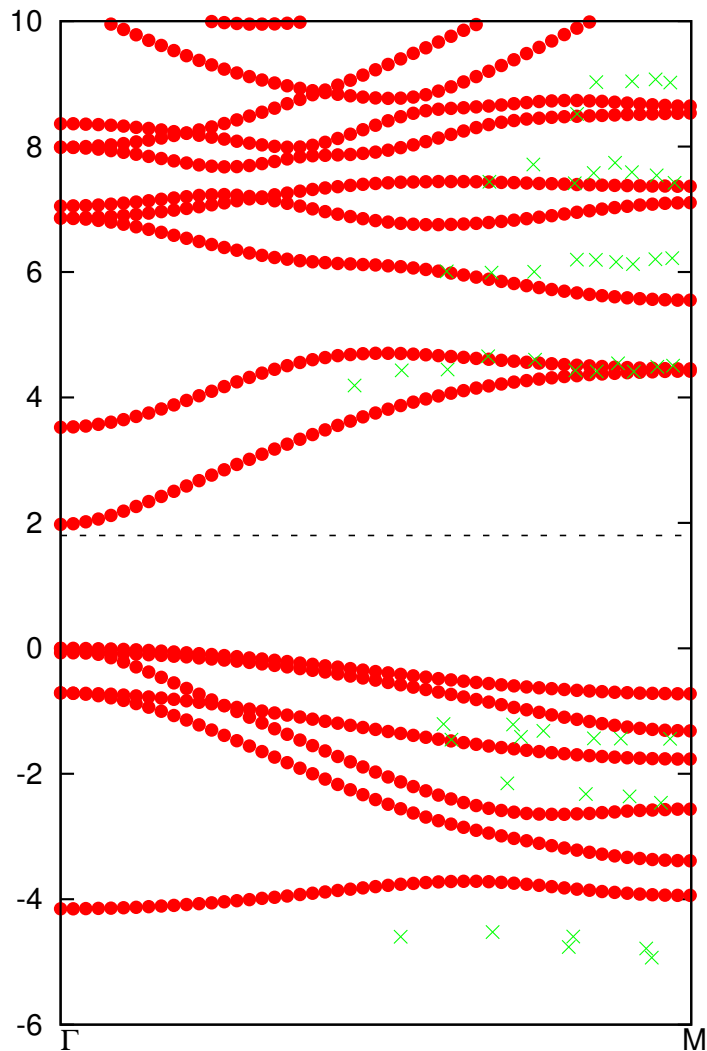


Figure 3.11: Theoretical CdSe ( $11\bar{2}0$ ) band structure calculated using our PWPAW code. The conduction bands are shifted to compensate for the under estimation of the band gap. The experimental points are from an inverse photoemission from Ref [44] indicated with  $\times$ .

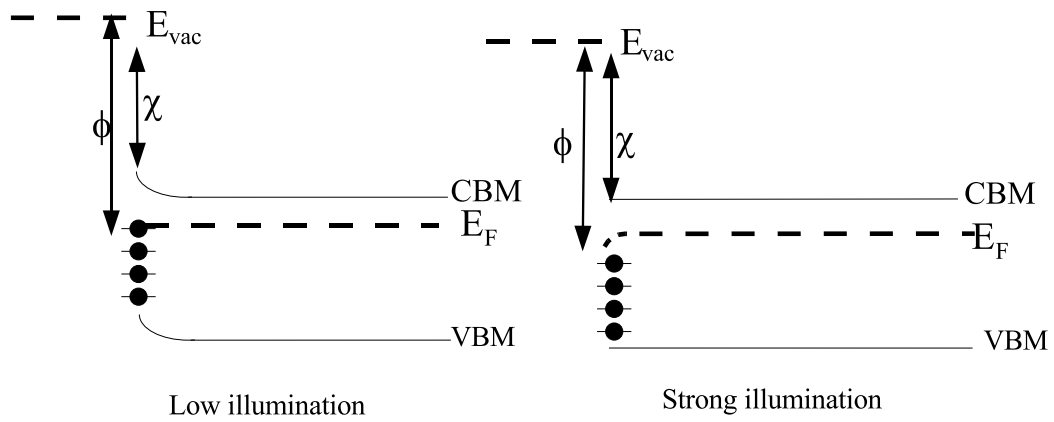


Figure 3.12: Schematic diagram for n-type semiconductor showing the effect of illumination on band edges.

As the illumination strength used by reference ([44]) is smaller than our beam power, this could have been one of the contributing factors to our slight difference in our results.

### 3.3.2 Theoretical band structure of CdSe (11 $\bar{2}$ 0)

In order to explain some features of the photoelectron spectra in Figure (3.9), we used the PWWAW code [64] based on the projector augmented wave (PAW) approach of Blöchl to [7] calculate the band diagram shown in Figure (3.11). The local density approximation (LDA) form of Perdew and Wang [52] was used to approximate the exchange-correlation interactions.

The first step of the PAW procedure is to produce the necessary projectors and basis functions. This is done using the ATOMPAW code [27]. The local potential contributions  $\tilde{v}_{loc}^a(r)$  were constructed using the squared sinc shape function.

Table (3.4) lists the parameters used in this work. In the table the notation  $\epsilon$  indicates a continuum function, where the positive energy  $\epsilon$  is chosen to insure that  $\phi_{\epsilon l}^a(r)$  basis function has the correct number of nodes in the augmentation region.

Atom	$z^a$	Core Charge	$nl$ basis	$r_c^a$ (Bohr)
Cd	48	28	4s,5s,4p, $\epsilon$ p,4d, $\epsilon$ d	2.01
Se	34	18	4s,es,4p, $\epsilon$ p,3d, $\epsilon$ d	2.41

Table 3.4: List of parameters used to construct basis and projector functions

We minimized the energy with respect to lattice constants as can be seen in Figure (3.14), and found that  $a=4.315 \text{ \AA}$  and  $c=7.096 \text{ \AA}$  and  $u=0.3748$ . The values quoted by Cohen *et.al*[10] for this crystal are  $a=4.299 \text{ \AA}$ ,  $c=7.01 \text{ \AA}$  and  $u=0.375$ . In addition to the lattice parameters, we need to find the optimal cutoff for the plane wave basis expansion. This is done by finding the minimum value of the reciprocal vector  $\mathbf{G}_0$ , that converges the total energy of the crystal. Ideally, if one uses  $\mathbf{G}$  value that is greater than  $\mathbf{G}_0$ , the total energy should remain constant within some tolerance value. Figure (3.13) shows the total energy as a function of reciprocal vector  $\mathbf{G}$ . For our calculation we use  $\mathbf{G}_0 = 8 \text{ (bohr)}^{-1}$ .

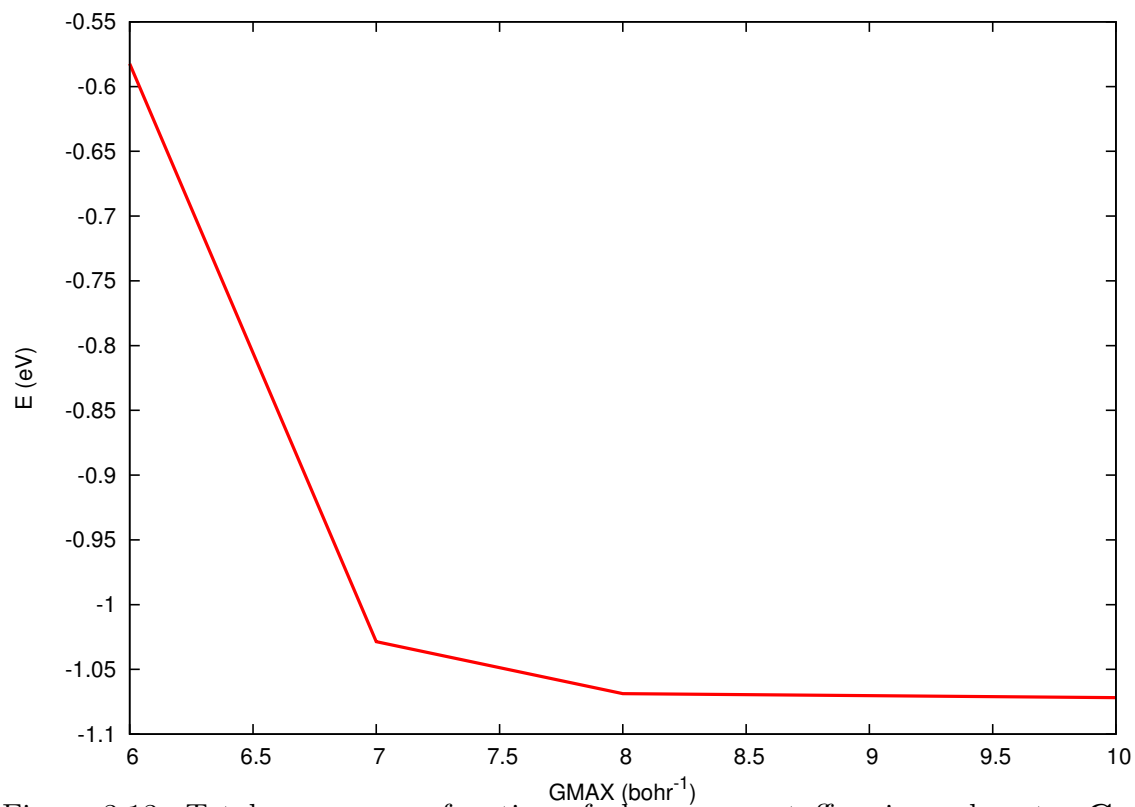


Figure 3.13: Total energy as a function of planewave cutoff reciprocal vector  $\mathbf{G}$  of CdSe.

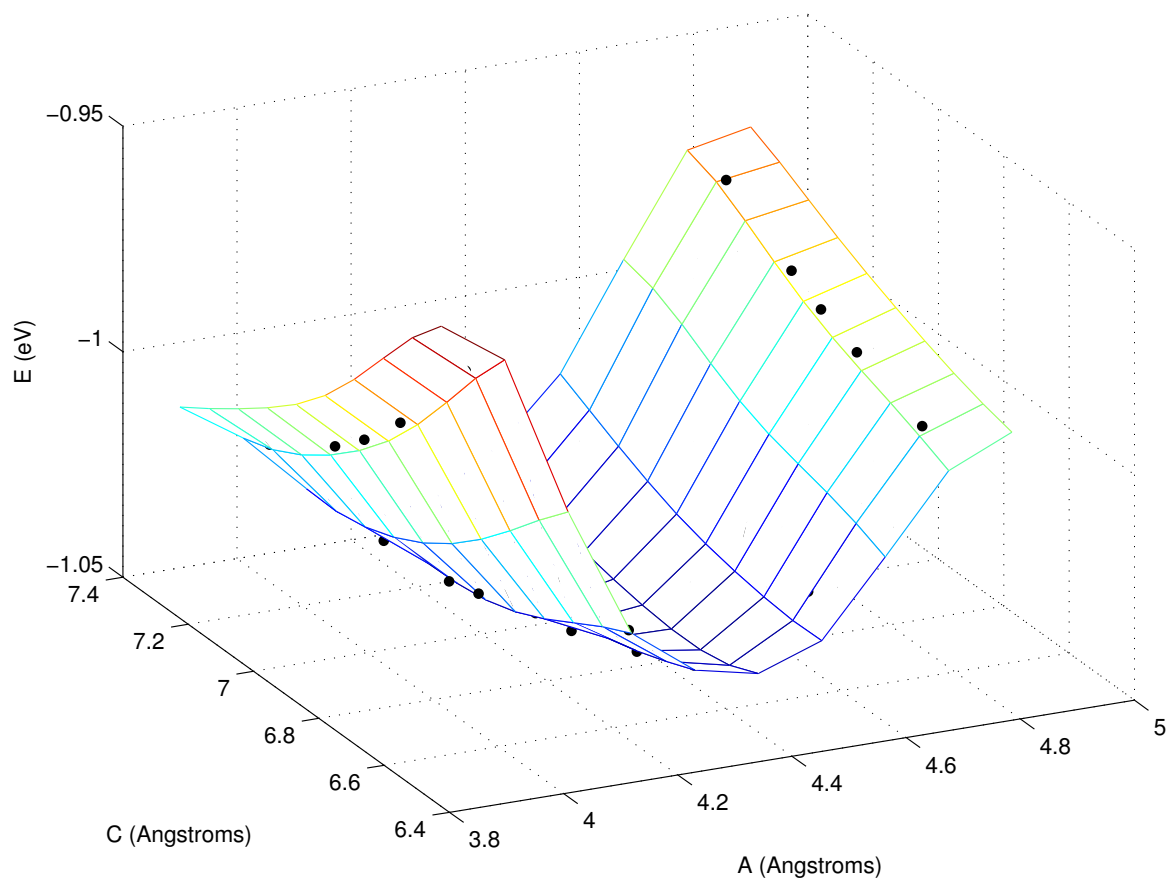


Figure 3.14: Total energy of CdSe as a function of lattice vectors  $a$  and  $c$ . The dark dots are calculated values and the mesh is extrapolated values.

### 5.9-eV excitation

For further investigation we also studied CdSe ( $11\bar{2}0$ ) using a 5.9 eV fourth harmonic pulse. The fourth harmonic pulse width is very broad compared to the 4.5 eV third harmonic pulse. This is due to the dispersion of the beam in the BBO crystal and in the optics. This decreases the power in the photon beam. As mentioned before, the two-photon process depends on power quadratically. As a result of this, the resulting peak power was insufficient to produce measurable two-photon photoemission.

Figure (3.15) shows the energy distribution curve for CdSe ( $11\bar{2}0$ ) excited by 5.9 eV FH beam. The ordinate axis is in linear scale to make it easy to identify the threshold energy. The threshold is about 2.33 eV below the Fermi level. The vacuum level is then marked at about 3.57 eV above the Fermi level. The CBM and VBM can be placed as shown in Figure (3.16) using the same hypothesis as above.

## 3.4 Surface defects

### 3.4.1 Background

The relaxation of a few top layers of a crystal due to termination of a perfect symmetry of the crystal results in surface states. Both intrinsic and extrinsic defects can occur at the surface. Intrinsic defects are due to vacancies, interstitials (atoms occupying nonlattice sites), and antisite lattice defects (when the wrong constituent atom of a compound crystal occupies the sublattice site of another).

In order to observe the population of the defect states in the energy band gap, we introduced more defects to the crystal by using 2 KeV electron beam of Auger electron spectroscopy and by sputtering with Argon ions.

### 3.4.2 Quality of the cleaved surface

Auger Electron Spectroscopy (AES) is a technique used to measure elemental surface composition. Each atom species has its own unique Auger spectrum that acts



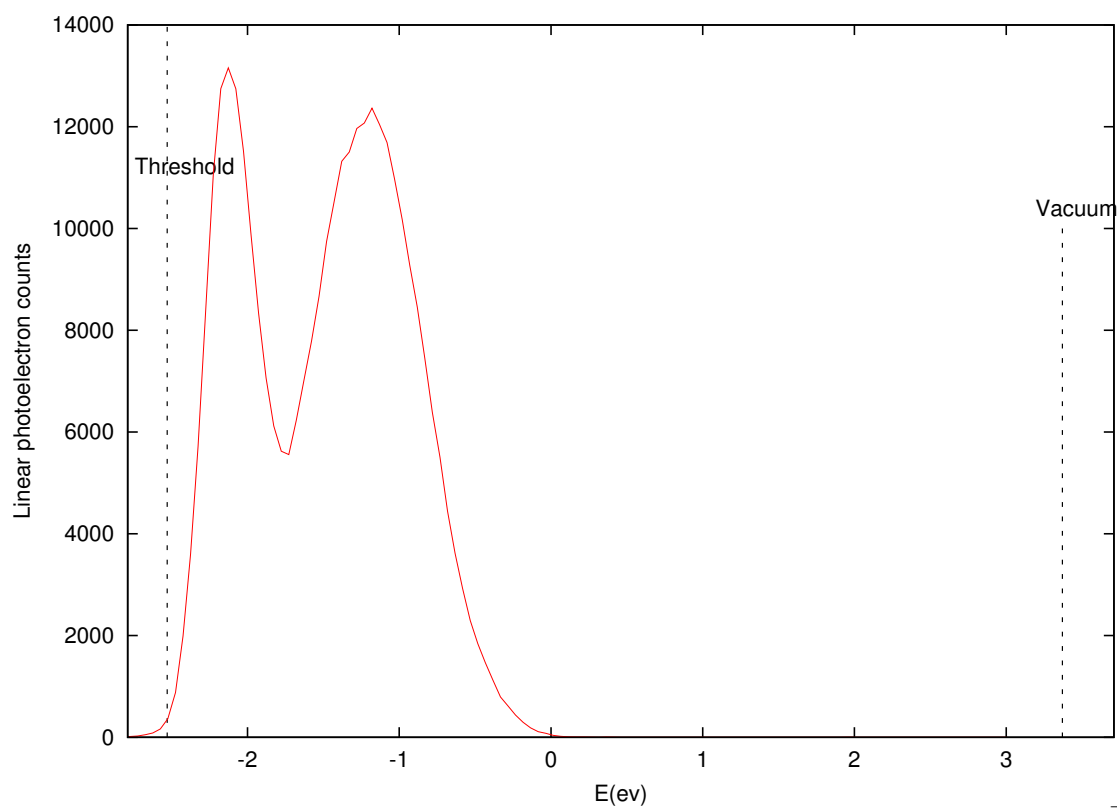


Figure 3.15: Energy distribution curve for photoelectrons exited from CdSe ( $11\bar{2}0$ ) by the 5.9 eV FH beam showing the relative position of threshold and vacuum energy levels.

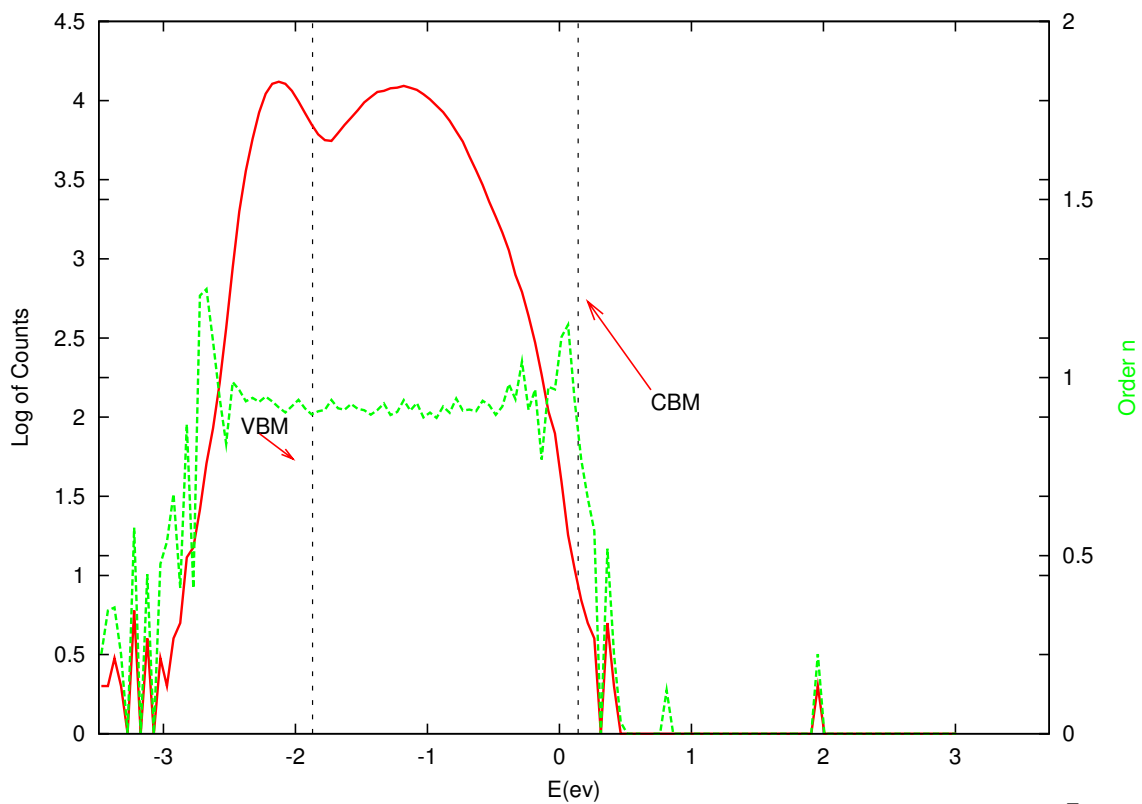


Figure 3.16: Energy distribution curve for photoelectrons exited from CdSe (11 $\bar{2}$ 0) by 5.9 eV FH beam (Red solid line). The number of photons corresponding to this curve is shown in dotted line (Green) with respect to the right-hand ordinate photoelectron counts.

as a finger print to identify the elemental components on the surface.

Auger Electronic Spectroscopy was measured to make sure the composition of our surface contains the right elements. This is also, like the PES, conducted in ultrahigh vacuum (UHV) at a working pressure of  $4 \times 10^{-9}$  Torr. The AES results of CdSe (11 $\bar{2}$ 0) are shown in Figure 3.17. According to the Handbook of AES [12] cadmium (Cd) peaks are located at 396 and 382 eV and selenium (Se) peaks are at 1315 and 1355 eV. The spectra demonstrated that our crystal has a clean composition of Cd and Se elements. But it has also some contamination with carbon (C) at around 280 eV.

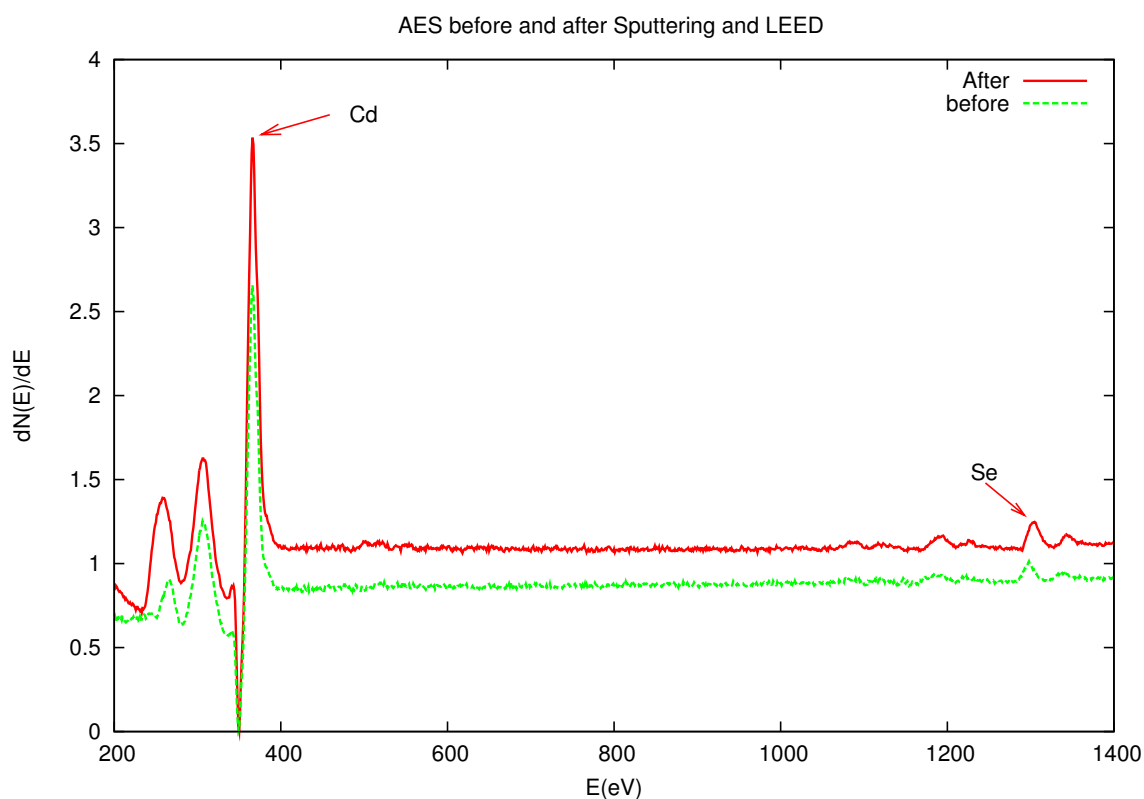


Figure 3.17: AES result for CdSe (11 $\bar{2}$ 0). The plot is a derivative of number of electrons as a function of Energy ( $\frac{dn}{dE}$ ).

In connection with AES, we also have done a LEED experiment to make sure the atoms on the surface have the correct arrangements. Figure (3.18) shows a LEED pattern obtained from CdSe (11 $\bar{2}$ 0) surface. The bright spot represents the diffraction patterns from atom. The results agrees with the proposed CdSe (11 $\bar{2}$ 0) structure in reference [9]. This assures as that we had a well reconstructed surface.

The LEED measurement was done by following the recipe in Mark Rowe's thesis[57]. The sharp patterns were generated using the parameters in Table (3.5).

Filament Current	2.67 A
Retarding Voltage	-56 V
Beam Energy	-60 V
Focus Voltage	60 V
Screen Voltage	4.03 kV
Beam Current	1.0 A

Table 3.5: Values used in setting the LEED pattern for CdSe (11 $\bar{2}$ 0)

### 3.4.3 Damaging the surface

To make sure that the states we found in the gap are really defect states, we introduced more defects by damaging the surface. If the states are really defect states, their density should increase or change when the surface gets damaged.

We followed the procedure below to create more defects and to monitor them.

1. Take photoelectron measurements.
2. Measure Auger spectroscopy.
3. Take photoelectron spectroscopy.
4. Measure low energy electron diffraction.<sup>10</sup>
5. Take photoelectron spectroscopy.

---

<sup>10</sup>LEED is only done for the first couple iterations. This is because once the surface is sputtered, no visible LEED patterns are found. The Auger electron beam also had much more effect.

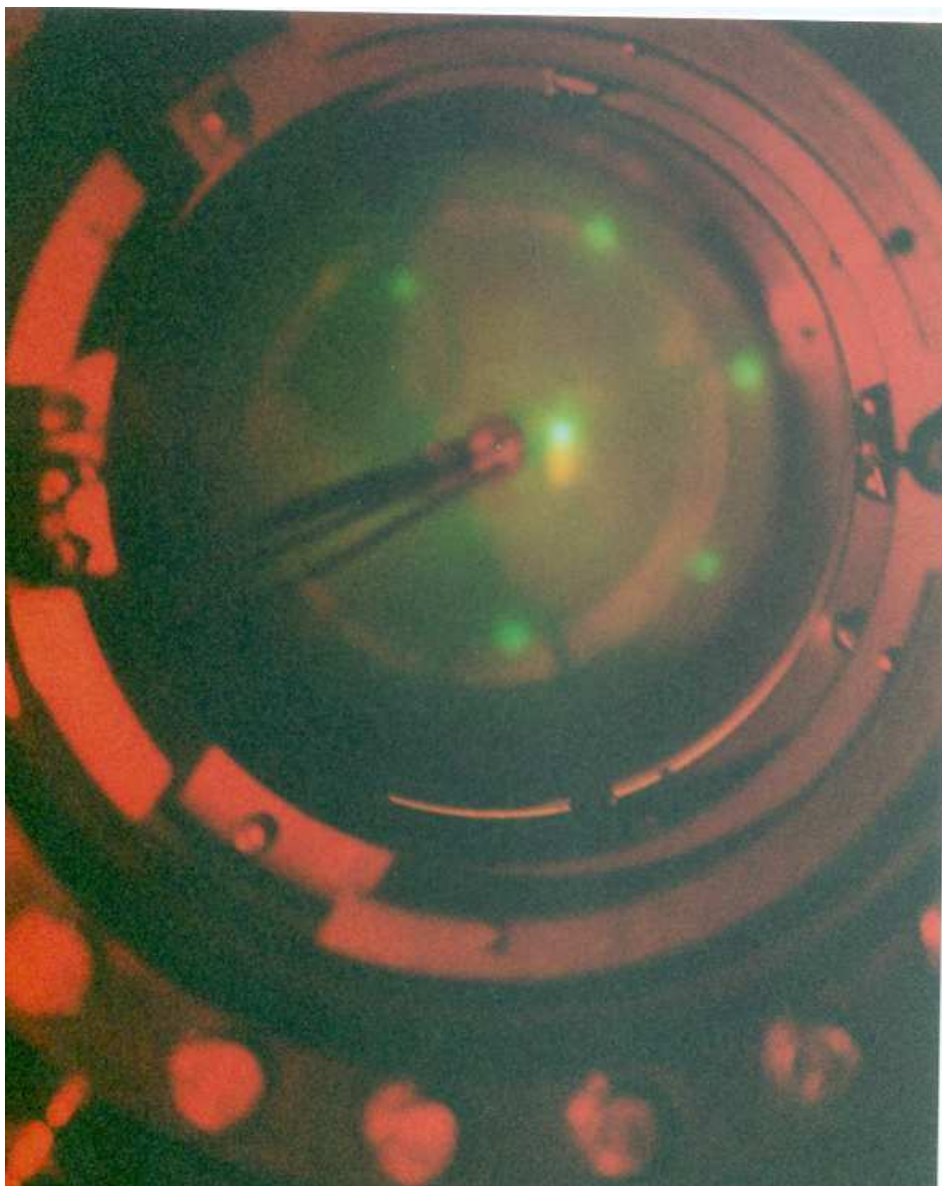


Figure 3.18: LEED pattern obtained from CdSe  $(11\bar{2}0)$  surface. The bright spots represent the diffraction patterns of an atom.

6. Do Argon sputtering.
7. Do all over again.

This process is illustrated in Figure (3.19).

We have done three cycles and the results will follow shortly.

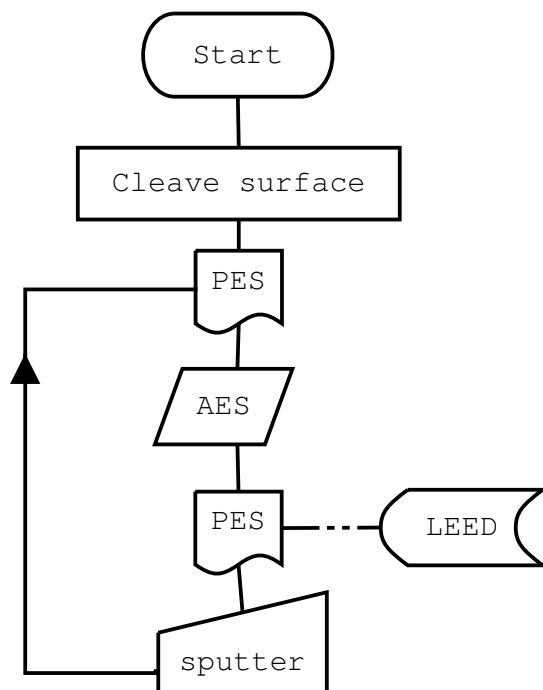


Figure 3.19: Flow chart showing the process of introducing defect and their measurements .

### Argon sputtering

Sputtering is a process in which atoms, ions, and molecular species in the surface of a target material are ejected under the action of ion-beam irradiation. Argon ion bombardment is used here to avoid unwanted chemical interactions between the ions of the beam and our sample. An incident Argon ion strikes atoms on the surface and one or more atoms may be ejected from the surface.

The detailed experimental procedure can be found in reference [43]. We sputter at each cycle for about 4 minutes using 1 keV ion beam energy. The current on the

raster scan was  $0.38 \mu\text{A}$ . Sputtering increases the vacuum pressure. It ranged between  $5 \times 10^{-5}$  and  $6.4 \times 10^{-5}$  Torr.

Figure (3.20) shows the photoelectron spectroscopy measurements after each step in Figure (3.19). The Auger spectroscopy was done using beam energy of 3 keV and current of 0.4 mA for about 10 minutes. The results show that the effects of Auger spectroscopy (electron beam) is larger than that of sputtering. This is because of the energy of the Auger beam is stronger than that of sputtering. The other main feature is that the relative density of states in the gap is higher at each step. To see this effect more clearly we plot the difference of photoelectron spectroscopy after each Auger measurement in Figure (3.21). Figure(3.22) shows the photoelectron spectroscopy measurements after each Auger measurement relative to the original cleave measurements. This clearly shows that the intensity of the defect states increases dramatically relative to the unoccupied conduction bands for each AES cycle.

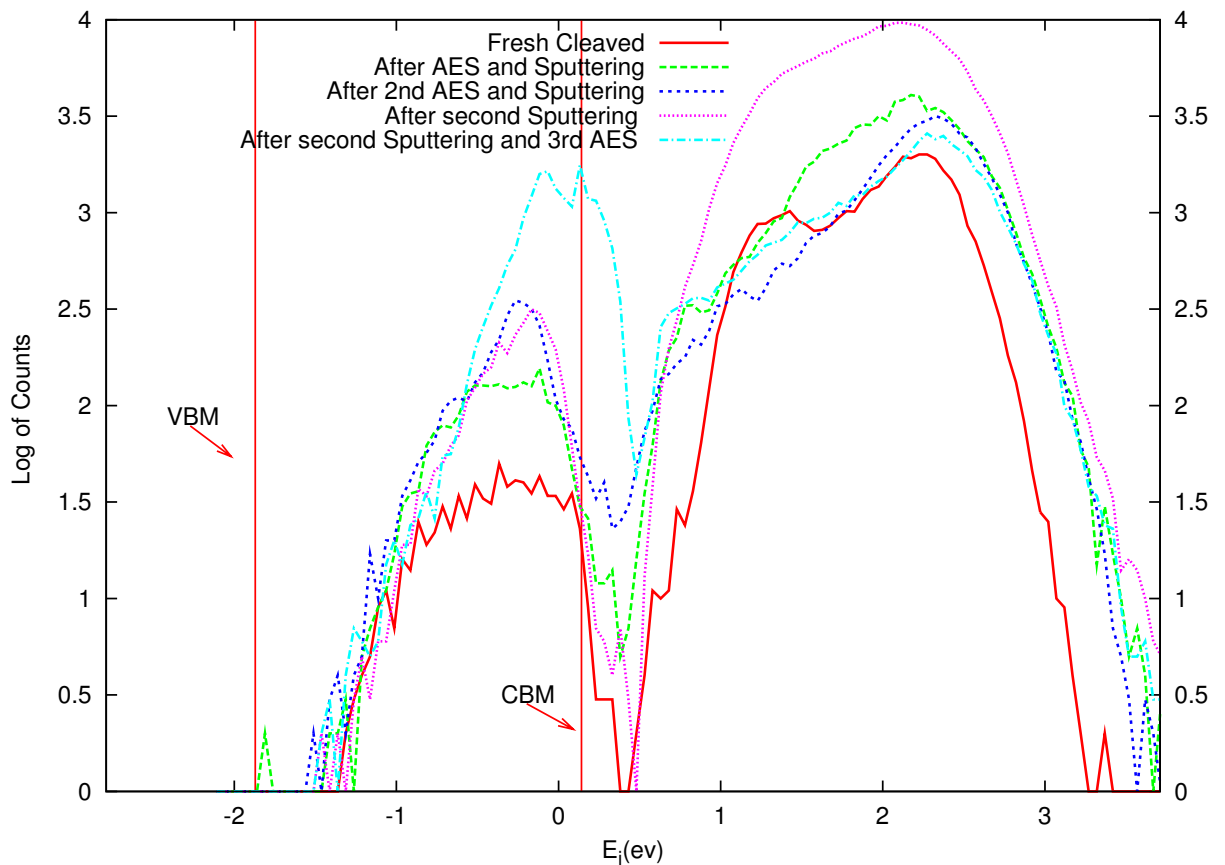


Figure 3.20: Different PES spectra after we apply more defects

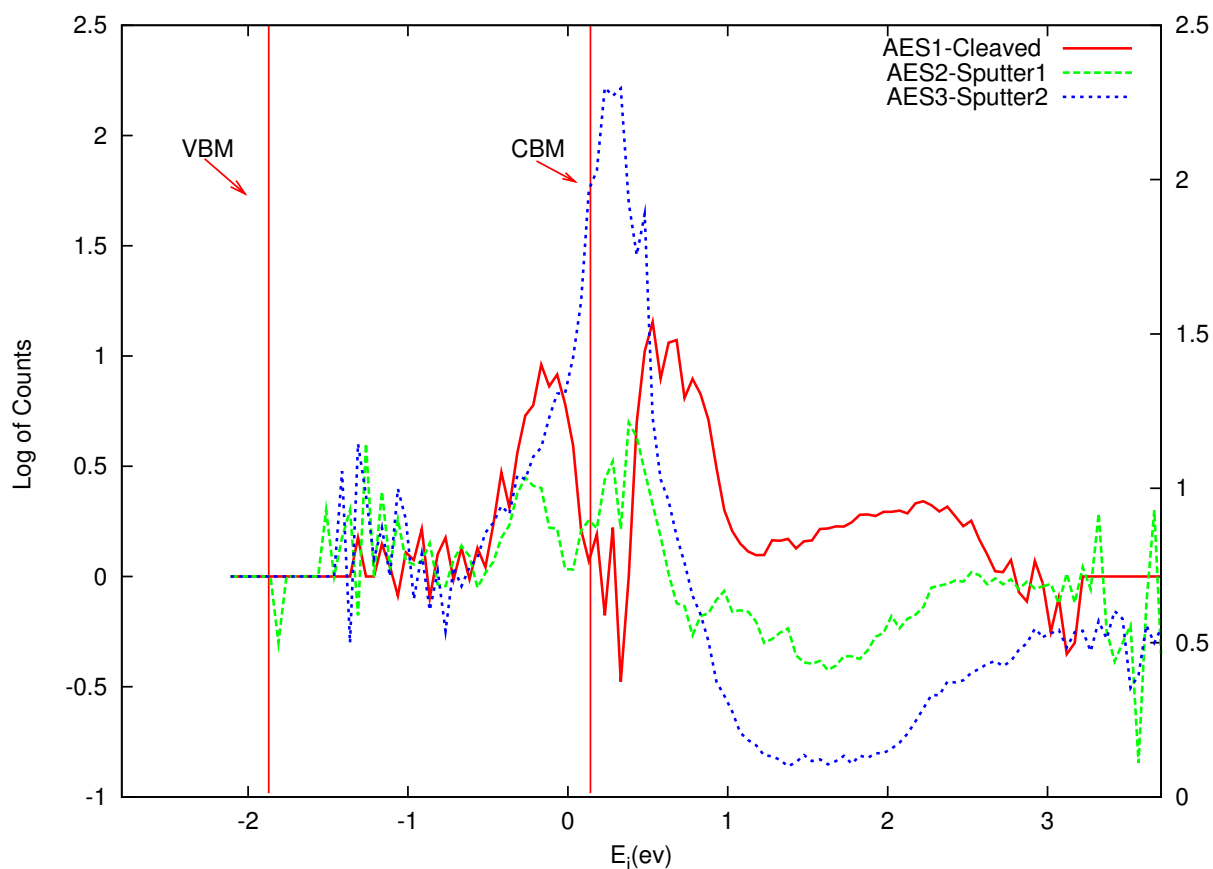


Figure 3.21: Difference in PES spectra relative to each AES application. That is the effect of AES on the density of states from the previous sputtering or fresh cleave. This will remove the effect of sputtering. If the AES does not have an effect, we would have gotten a flat curve.



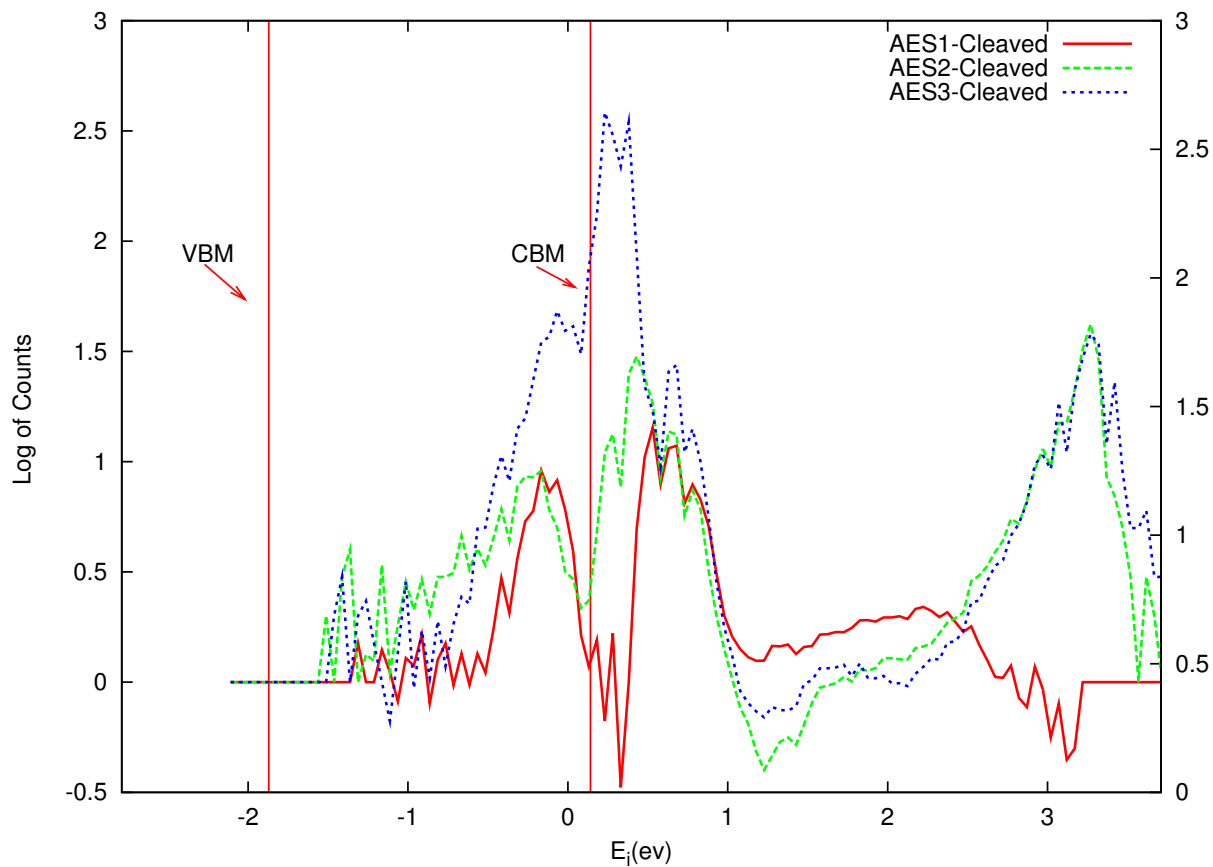


Figure 3.22: Difference in PES spectra relative to each AES application relative to the cleaved surface. In contrast to Figure (3.21) is that, here the difference is relative to the original cleaved spectra and it also includes the effect of sputtering.

# Chapter 4

## The semi-infinite surface formalism

Several researchers have done a lot of surface state investigation for II-VI group semiconductors using slab and supercell methods[32]. One of the main disadvantages of such methods is that it is very hard to distinguish the calculated slab states corresponding to bulk or surface states. Our formulation is based on the use of Semi-Infinite boundary conditions which we believe will let us understand those effects clearly. In this approach, the crystal surface is divided in to three regions in the direction perpendicular to the  $xy$  surface. These regions are known as, “bulk”, “interface” and “vacuum”. We can solve for the wave function in each of these regions, forming the complete solution by matching them on the boundaries.

### 4.1 General equations from PAW formalism

In the PAW method[7, 25, 27, 64], the Schrödinger equation takes the form

$$\{\mathbf{H}^{\text{PAW}}(\mathbf{r}) - E_{n\mathbf{k}}\mathbf{O}\} |\tilde{\Psi}_{n\mathbf{k}}(\mathbf{r})\rangle = 0, \quad (4.1)$$

where

$$\mathbf{H}^{\text{PAW}} \equiv \tilde{H}(\mathbf{r}) + \sum_{aij} |\tilde{p}_i^a\rangle D_{ij}^a \langle \tilde{p}_j^a| \quad \text{and} \quad \mathbf{O} \equiv \mathbf{1} + \sum_{aij} |\tilde{p}_i^a\rangle O_{ij}^a \langle \tilde{p}_j^a|. \quad (4.2)$$

The local term contribution to the PAW Hamiltonian is given by

$$\tilde{H}(\mathbf{r}) = -\frac{\hbar^2}{2m}\nabla^2 + \tilde{v}_{\text{eff}}(\mathbf{r}), \quad (4.3)$$

with the smooth local potential given by

$$\tilde{v}_{\text{eff}}(\mathbf{r}) = \frac{1}{\mathcal{V}} \sum_{\mathbf{G}} \bar{v}_{\text{loc}}(\mathbf{G}) e^{i\mathbf{G}\cdot\mathbf{r}} + \frac{4\pi e^2}{\mathcal{V}} \sum_{\mathbf{G}\neq 0} \frac{\bar{n}(\mathbf{G}) + \tilde{n}(\mathbf{G})}{G^2} e^{i\mathbf{G}\cdot\mathbf{r}} + \mu_{\text{xc}}[\tilde{n}(\mathbf{r})]. \quad (4.4)$$

The first term in this expression is the fixed local potential term. The second term represents the Coulomb contribution of the smooth density  $\tilde{n}$  and the compensation charge density  $\hat{n}$ , while the last term represents the exchange-correlation potential function[52]. The non-local contribution to the PAW Hamiltonian is given by

$$D_{ij}^a = K_{ij}^a + [v_{\text{at}}^a]_{ij} - [\hat{v}^a]_{ij} + [V_{\text{H}}^a]_{ij} + [v_0^a]_{ij} + [V_{\text{xc}}^a]_{ij} \quad (4.5)$$

and

$$O_{ij}^a \equiv \langle \phi_i^a | \phi_j^a \rangle - \langle \tilde{\phi}_i^a | \tilde{\phi}_j^a \rangle = O_{n_i l_i n_j l_j}^a \delta_{l_i l_j} \delta_{m_i m_j}. \quad (4.6)$$

These matrix elements will be described in more detail below.

## 4.2 Bulk and surface states

In the presence of a surface, bulk states of the material continue to exist. In addition, new surface states may also exist in at energies within the surface band gaps. In order to determine the energies for each  $\mathbf{k}_{\parallel}$  where bulk states and where band gaps exist, it is useful to construct a “smear” plot of the bulk structure. Based on this scheme we will calculate the bulk calculations in the surface geometry as follows. We will plot a diagram of bulk bands (smear plots). According to [23], if we divide the Brillouin zone in to  $\mathbf{k}_{\perp}$  and  $\mathbf{k}_{\parallel}$ , we can assign  $\mathbf{k}_{\parallel}$  along the surface Brillouin zone and  $\mathbf{k}_{\perp}$  along the surface direction. For each value of  $\mathbf{k}_{\parallel}$  distributed uniformly over special directions in the surface Brillouin zone, the band energies  $E_{n\mathbf{k}}$  and their gradients  $\nabla_{\mathbf{k}} E_{n\mathbf{k}}$  will be evaluated for a series of values of  $\mathbf{k}_{\perp}^i \equiv (i + \frac{1}{2})\delta\mathbf{k}_{\perp}$  spanning the irreducible range of  $\mathbf{k}_{\perp}$ . For each of these points, the range of bulk band energies for the given  $\mathbf{k}_{\parallel}$  could then be approximated by

$$E_{n\mathbf{k}}^i - \frac{\delta\mathbf{k}_{\perp}}{2} \cdot \nabla_{\mathbf{k}} E_{n\mathbf{k}} \leq E(\mathbf{k}_{\parallel}) \leq E_{n\mathbf{k}}^i + \frac{\delta\mathbf{k}_{\perp}}{2} \cdot \nabla_{\mathbf{k}} E_{n\mathbf{k}}. \quad (4.7)$$

Where  $\delta\mathbf{k}_\perp$  is chosen to be a small value of about  $0.039$  ( $\text{bohr}^{-1}$ )<sup>1</sup> for CdSe (11 $\bar{2}$ 0) and  $0.047$  ( $\text{bohr}^{-1}$ ) for diamond (001). The band energy  $E_{n\mathbf{k}}$  evaluated at  $\mathbf{k} = \mathbf{k}_\perp + \mathbf{k}_\parallel$ . At each  $\mathbf{k}_\parallel$ , for each  $\mathbf{k}_\perp^i$  and each band index  $n$ , a vertical line drawn from  $E_{n\mathbf{k}}^i - \frac{\delta\mathbf{k}_\perp}{2} \cdot \nabla_{\mathbf{k}} E_{n\mathbf{k}}$  to  $E_{n\mathbf{k}}^i + \frac{\delta\mathbf{k}_\perp}{2} \cdot \nabla_{\mathbf{k}} E_{n\mathbf{k}}$  contribute to the projected band structure plot (smear diagram).

Details of the calculation of  $\nabla_{\mathbf{k}} E_{n\mathbf{k}}$

$$E_{n\mathbf{k}} = \langle \tilde{\psi}_{n\mathbf{k}} | \mathcal{H}^{PAW} | \tilde{\psi}_{n\mathbf{k}} \rangle \quad (4.8)$$

$$= \sum_G |k + G|^2 |A_{n\mathbf{k}}(G)|^2 + \sum_{GG'} \tilde{V}_{eff}(G - G') A_{n\mathbf{k}}^*(G) A_{n\mathbf{k}}(G') \quad (4.9)$$

$$+ \sum_{aij} \langle \tilde{\psi}_{n\mathbf{k}} | \tilde{p}_i^a \rangle D_{ij}^a \langle \tilde{p}_j | \tilde{\psi}_{n\mathbf{k}} \rangle \quad (4.10)$$

Where

$$\langle \tilde{p}_j | \tilde{\psi}_{n\mathbf{k}} \rangle = \frac{1}{\sqrt{V}} \sum_G \left( 4\pi i^{l_i} Y_{l_i m_i}^* (\widehat{k + G}) e^{i(k+G) \cdot R^a} \tilde{p}_{n_i k_i} (|k + G|) \right) A_{n\mathbf{k}}(G).$$

Now using Hellman-Feynman theorem,  $\nabla_{\mathbf{k}} E_{n\mathbf{k}}$  will have the following form.

$$\nabla_{\mathbf{k}} E_{n\mathbf{k}} = \sum_G (k + G) |A_{n\mathbf{k}}(G)|^2 \quad (4.11)$$

$$+ \sum_{aij} D_{ij}^a \left( \left( \nabla_{\mathbf{k}} \langle \tilde{\psi}_{n\mathbf{k}} | \tilde{p}_i^a \rangle \right) \langle \tilde{p}_j | \tilde{\psi}_{n\mathbf{k}} \rangle + \langle \tilde{\psi}_{n\mathbf{k}} | \tilde{p}_i^a \rangle \left( \nabla_{\mathbf{k}} \langle \tilde{p}_j | \tilde{\psi}_{n\mathbf{k}} \rangle \right) \right), \quad (4.12)$$

where

$$\nabla_{\mathbf{k}} \langle \tilde{\psi}_{n\mathbf{k}} | \tilde{p}_i^a \rangle = \frac{4\pi i^{l_i}}{\sqrt{V}} \sum_G \nabla_{\mathbf{k}} \mathcal{J}_{n_j l_j m_j} (k + G) e^{i(k+G) \cdot R^a} A_{n\mathbf{k}}(G)$$

,

$$\nabla_{\mathbf{k}} \langle \tilde{p}_j | \tilde{\psi}_{n\mathbf{k}} \rangle = \nabla_{\mathbf{k}} \langle \tilde{\psi}_{n\mathbf{k}} | \tilde{p}_i^a \rangle^*.$$

,

and

---

<sup>1</sup>This value is calculated from the relation  $\frac{2\pi}{CN_k}$ . Where  $C$  is the unit cell dimension along the z-axis and  $N_k$  is the number of grid points.

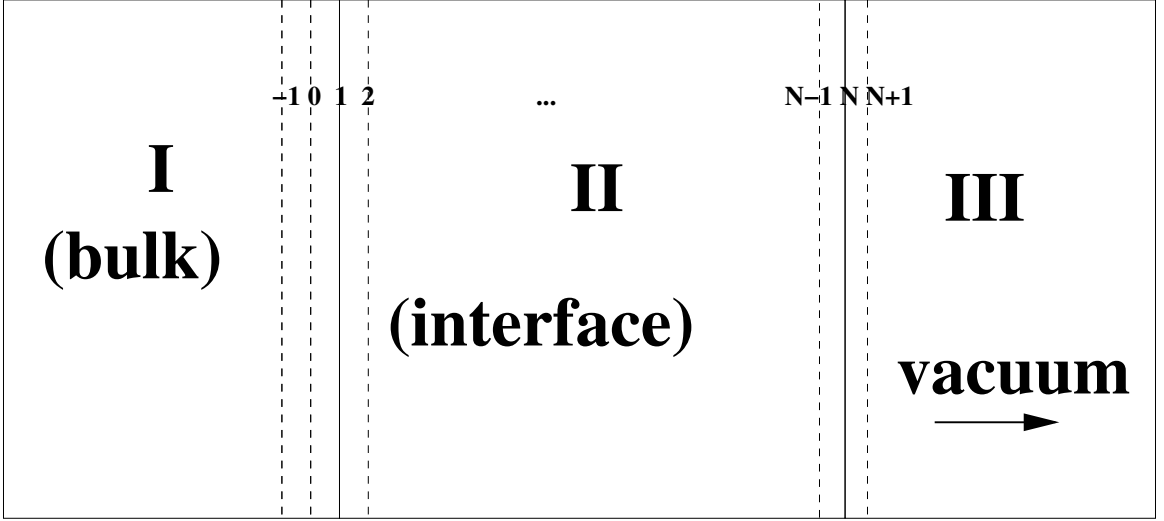


Figure 4.1: Diagram showing surface geometry.

$$\begin{aligned} \nabla_k \mathcal{J}_{nlm}(k+G) &= Y_{l_i m_i}^*(\widehat{\mathbf{k}+\mathbf{G}}) \mathcal{P}_{nl}(|\mathbf{k}+\mathbf{G}|) \frac{\mathbf{k}+\vec{\mathbf{G}}}{|\mathbf{k}+\mathbf{G}|} \\ &+ \frac{\bar{P}_{nk}(|\mathbf{k}+\mathbf{G}|)}{|\mathbf{k}+\mathbf{G}|} \left( -im \frac{Y_{lm}^*(\widehat{\mathbf{k}+\mathbf{G}})}{\sin(\theta)} \hat{\varphi} + \frac{\partial Y_{lm}^*(\widehat{\mathbf{k}+\mathbf{G}})}{\partial \theta} \hat{\theta} \right) \end{aligned} \quad (4.13)$$

An example of smear plot using the above formalism for CdSe (11 $\bar{2}$ 0) and Diamond (001) are given in Chapter 6 section 6.2.

### 4.2.1 Surface geometry

It is helpful to visualize the surface in three regions. In region I, it is assumed that the electronic wavefunctions satisfy the bulk Schrödinger equation. Region III is defined to be outside the range of all of the atoms and asymptotically merges to the vacuum. The “interface region” II is the most computationally demanding.

In the surface geometry, it will be convenient to expand the wavefunctions in two-dimensional plane waves representing the surface plane and a discrete grid along the surface ( $\hat{\mathbf{z}}$ ) direction. In the presence of the surface, the wavevector can be decomposed according to  $\mathbf{k} = \mathbf{k}_{\parallel} + k_{\perp} \hat{\mathbf{z}}$ . While  $k_{\perp}$  is no longer conserved at the surface, each bulk Bloch state corresponds to a state in the surface representation. It

is convenient to label the semi-infinite wavefunctions by  $\lambda\mathbf{k}_{\parallel}$ , where  $\lambda$  can represent the band index  $n$  and the perpendicular wavevector  $k_{\perp}$  or a surface state label. The general surface representation of the wavefunction takes the form

$$\tilde{\Psi}_{\lambda\mathbf{k}_{\parallel}}(\mathbf{r}) = \sqrt{\frac{1}{\mathcal{A}}} \sum_{\mathbf{G}_{\parallel}} f_{\lambda\mathbf{k}_{\parallel}}(\mathbf{G}_{\parallel}, z) e^{i(\mathbf{k}_{\parallel} + \mathbf{G}_{\parallel}) \cdot \mathbf{r}_{\parallel}}, \quad (4.14)$$

where the function  $f_{\lambda\mathbf{k}_{\parallel}}(\mathbf{G}_{\parallel}, z)$  must be determined in regions II and III and  $\mathcal{A}$  is the area of the surface. In particular,  $z$  will be discretized in region II with  $z_1$  located at the boundary between regions I and II and  $z_N$  located at the boundary between regions II and III. Intermediate values are given by  $z_n = z_1 + (n - 1)h_z$ .

For the surface representation (4.14), the Schrödinger equation (4.1) for  $f_{\lambda\mathbf{k}_{\parallel}}(\mathbf{G}_{\parallel}, z)$  takes the form

$$\frac{d^2 f(\mathbf{G}_{\parallel}, z)}{dz^2} = M(\mathbf{G}_{\parallel}, z), \quad (4.15)$$

where

$$M(\mathbf{G}_{\parallel}, z) \equiv M_1(\mathbf{G}_{\parallel}, z) + M_2(\mathbf{G}_{\parallel}, z), \quad (4.16)$$

with

$$\begin{aligned} M_1(\mathbf{G}_{\parallel}, z) &\equiv \left[ |\mathbf{k}_{\parallel} + \mathbf{G}_{\parallel}|^2 - \frac{2m}{\hbar^2} E_{\lambda\mathbf{k}_{\parallel}} \right] f_{\lambda\mathbf{k}_{\parallel}}(\mathbf{G}_{\parallel}, z) \\ &+ \frac{2m}{\hbar^2} \sum_{\mathbf{G}'_{\parallel}} \tilde{v}_{\text{eff}}(\mathbf{G}_{\parallel} - \mathbf{G}'_{\parallel}, z) f_{\lambda\mathbf{k}_{\parallel}}(\mathbf{G}'_{\parallel}, z), \end{aligned} \quad (4.17)$$

representing the local contributions and  $M_2(\mathbf{G}_{\parallel}, z)$  representing the non-local contributions. In order to evaluate these, we must expand the projector functions in the surface representation which take the form

$$\tilde{p}_i^a(\mathbf{r}) = \sqrt{\frac{1}{\mathcal{A}}} \sum_{\mathbf{G}_{\parallel}} e^{i(\mathbf{k}_{\parallel} + \mathbf{G}_{\parallel}) \cdot \mathbf{r}_{\parallel}} \mathcal{P}_i^a(\mathbf{G}_{\parallel}, z). \quad (4.18)$$

The two-dimensional Fourier coefficient for the projector is determined by inverting the above equation.

$$\mathcal{P}_i^a(\mathbf{G}_{\parallel}, z) \equiv \sqrt{\frac{1}{\mathcal{A}}} \int d^2 r_{\parallel} e^{-i(\mathbf{k}_{\parallel} + \mathbf{G}_{\parallel}) \cdot \mathbf{r}_{\parallel}} \tilde{p}_i^a(\mathbf{r}) \quad (4.19)$$

Writing the projector function in terms of its radial and spherical terms,

$$\tilde{p}_i^a(\mathbf{r}) \equiv \frac{p_{n_i l_i}(r)}{r} Y_{l_i m_i}(\hat{\mathbf{r}}), \quad (4.20)$$

where  $Y_{lm}(\hat{\mathbf{r}})$  denotes a spherical harmonic function, the integral becomes

$$\mathcal{P}_i^a(\mathbf{G}_{\parallel}, z) \equiv \sqrt{\frac{1}{\mathcal{A}}} \int d^2 r_{\parallel} e^{-i(\mathbf{k}_{\parallel} + \mathbf{G}_{\parallel}) \cdot r_{\parallel}} \frac{\tilde{p}_{n_i l_i}^a(|\mathbf{r} - \mathbf{R}^a|)}{|\mathbf{r} - \mathbf{R}^a|} Y_{l_i}^{m_i}(\widehat{\mathbf{r} - \mathbf{R}^a}). \quad (4.21)$$

which can be evaluated using

$$\begin{aligned} \mathcal{P}_i^a(\mathbf{G}_{\parallel}, z) &= \mathcal{N}_{l_i m_i}^a(\mathbf{k}_{\parallel} + \mathbf{G}_{\parallel}) \int_{|z - Z^a|}^{R_c^a} dr p_{n_i l_i}(r) P_{l_i}^{|m_i|} \left( \frac{z - Z^a}{r} \right) \\ &\quad \times J_{|m_i|} \left( |\mathbf{k}_{\parallel} + \mathbf{G}_{\parallel}| \sqrt{r^2 - (z - Z^a)^2} \right), \end{aligned} \quad (4.22)$$

where  $P_{l_i}^{|m_i|}(u)$  represents an Associated Legendre function,  $J_{|m_i|}(u)$  represents a Bessel function of integer order  $|m_i|$ , and

$$\begin{aligned} \mathcal{N}_{l_i m_i}^a(\mathbf{k}_{\parallel} + \mathbf{G}_{\parallel}) &\equiv e^{-i(\mathbf{k}_{\parallel} + \mathbf{G}_{\parallel}) \cdot \mathbf{R}_{\parallel}^a} \left[ \frac{(\mathbf{k}_{\parallel} + \mathbf{G}_{\parallel})_x}{|\mathbf{k}_{\parallel} + \mathbf{G}_{\parallel}|} + i \frac{(\mathbf{k}_{\parallel} + \mathbf{G}_{\parallel})_y}{|\mathbf{k}_{\parallel} + \mathbf{G}_{\parallel}|} \right]^{m_i} e^{-im_i \pi/2} \\ &\quad \times \sqrt{\frac{\pi(2l_i + 1)}{\mathcal{A}}} \sqrt{\frac{(l_i - |m_i|)!}{(l_i + |m_i|)!}}. \end{aligned} \quad (4.23)$$

The non-local contribution to equation (4.17) can then be written

$$M_2(\mathbf{G}_{\parallel}, z) = \sum_{ai} \mathcal{P}_i^a(\mathbf{G}_{\parallel}, z) \mathcal{K}_i^a \quad \text{with} \quad \mathcal{K}_i^a \equiv \sum_j \frac{2m}{\hbar^2} \left( D_{ij}^a - E_{\lambda \mathbf{k}_{\parallel}} O_{ij}^a \right) \langle \tilde{p}_j^a | \tilde{\Psi}_{\lambda \mathbf{k}_{\parallel}} \rangle. \quad (4.24)$$

The summation of the atom index  $a$  should be taken over all atoms with a non-zero contribution to the projector function  $\mathcal{P}_i^a(\mathbf{G}_{\parallel}, z)$  at the given value of  $z$ , including atoms on the boundary between regions I and II. In the surface representation, the overlap of the projector function with the smooth wavefunction can be evaluated using

$$\langle \tilde{p}_j^a | \tilde{\Psi}_{\lambda \mathbf{k}_{\parallel}} \rangle = \sum_{\mathbf{G}_{\parallel}} \int dz \mathcal{P}_i^a(\mathbf{G}_{\parallel}, z)^* f_{\lambda \mathbf{k}_{\parallel}}(\mathbf{G}_{\parallel}, z). \quad (4.25)$$

Here the integration over  $z$  can extend into Region I for atoms on the boundary.

In order to solve the surface Schrödinger equation (4.15), we can use the Numerov algorithm [21] which takes the following form in the interior of Region II:

$$\begin{aligned}
& f(\mathbf{G}_{\parallel}, z_{n-1}) - \frac{\hbar_z^2}{12} M(\mathbf{G}_{\parallel}, z_{n-1}) \\
& - 2f(\mathbf{G}_{\parallel}, z_n) - \frac{10\hbar_z^2}{12} M(\mathbf{G}_{\parallel}, z_n) \\
& + f(\mathbf{G}_{\parallel}, z_{n+1}) - \frac{\hbar_z^2}{12} M(\mathbf{G}_{\parallel}, z_{n+1}) = 0.
\end{aligned} \tag{4.26}$$

In order to solve this equation, we need to specify boundary conditions.

First, consider the boundary between Region II and Region III. In Region III, the surface Schrödinger equation is identical to (4.15), except that since there are no atoms in the region the nonlocal term  $M_2(\mathbf{G}_{\parallel}, z)$  term vanishes. Furthermore, for  $z \rightarrow \infty$ , the potential takes the asymptotic value  $\bar{v}_{\text{eff}}(\mathbf{G}_{\parallel}, z) \rightarrow V_{\infty} \delta_{\mathbf{G}_{\parallel}, \mathbf{0}}$ . It is convenient to find  $N_{\mathbf{G}_{\parallel}}$  independent solutions  $\{f_{\mathbf{G}_{\parallel}^0}^{III}(\mathbf{G}_{\parallel}, z)\}$  to the Schrödinger equation in Region III by integrating Eq. (4.15) from  $z \rightarrow \infty$  to  $z_N$ . The index  $\mathbf{G}_{\parallel}^0$  corresponds to the boundary condition

$$f_{\mathbf{G}_{\parallel}^0}^{III}(\mathbf{G}_{\parallel}, z \rightarrow \infty) = e^{-\kappa_{\mathbf{G}_{\parallel}^0} z} \delta_{\mathbf{G}_{\parallel}, \mathbf{G}_{\parallel}^0}, \tag{4.27}$$

where

$$\kappa_{\mathbf{G}_{\parallel}^0} \equiv \begin{cases} \sqrt{|\mathbf{k}_{\parallel} + \mathbf{G}_{\parallel}^0|^2 + 2m(V_{\infty} - E_{\lambda \mathbf{k}_{\parallel}})/\hbar^2} & \text{for } E_{\lambda \mathbf{k}_{\parallel}} < V_{\infty} + \hbar^2 |\mathbf{k}_{\parallel} + \mathbf{G}_{\parallel}^0|^2 / 2m \\ -i\sqrt{2m(E_{\lambda \mathbf{k}_{\parallel}} - V_{\infty})/\hbar^2 - |\mathbf{k}_{\parallel} + \mathbf{G}_{\parallel}^0|^2} & \text{for } E_{\lambda \mathbf{k}_{\parallel}} > V_{\infty} + \hbar^2 |\mathbf{k}_{\parallel} + \mathbf{G}_{\parallel}^0|^2 / 2m \end{cases}. \tag{4.28}$$

In general, we expect that for  $z \geq z_N$ ,

$$f(\mathbf{G}_{\parallel}, z) = \sum_{\mathbf{G}_{\parallel}^0} C_{\mathbf{G}_{\parallel}^0} f_{\mathbf{G}_{\parallel}^0}^{III}(\mathbf{G}_{\parallel}, z). \tag{4.29}$$

Since the potential is continuous at  $z = z_N$ , we can extend the Numerov integration to the point  $z_{N+1}$  by using Eq. (4.29) to evaluate  $f(\mathbf{G}_{\parallel}, z_{N+1})$  and  $M(\mathbf{G}_{\parallel}, z_{N+1})$ , determining the coefficients  $\{C_{\mathbf{G}_{\parallel}^0}\}$  from the matching equation at  $z_N$ . Setting the matrix  $\Lambda_{\mathbf{G}_{\parallel}, \mathbf{G}_{\parallel}^0} \equiv f_{\mathbf{G}_{\parallel}^0}^{III}(\mathbf{G}_{\parallel}, z_N)$ , we can determine

$$C_{\mathbf{G}_{\parallel}^0} = \sum_{\mathbf{G}_{\parallel}} \Lambda_{\mathbf{G}_{\parallel}, \mathbf{G}_{\parallel}^0}^{-1} f(\mathbf{G}_{\parallel}, z_N). \tag{4.30}$$



At the  $z_1$  boundary, there are several possible alternative approaches. In general we expect that for  $z \leq z_1$ , the wavefunction can be expressed as a linear combination of Bloch waves.

The Bloch wavefunctions in Region I can be expanded in a 3 dimensional Fourier expansion of the form:

$$\tilde{\Psi}_{n\mathbf{k}}^{\text{Bloch}}(\mathbf{r}) = \sqrt{\frac{1}{\mathcal{V}}} \sum_{\mathbf{G}} A_{n\mathbf{k}}(\mathbf{G}) e^{i(\mathbf{k}+\mathbf{G})\cdot\mathbf{r}}, \quad (4.31)$$

where  $\mathcal{V}$  denotes the unit cell volume.

In terms of the 3-dimensional expansion coefficients, the surface representation of the Bloch wave is given by

$$f_{n\mathbf{k}_{\parallel}k_{\perp}}^{\text{Bloch}}(\mathbf{G}_{\parallel}, z) = \sqrt{\frac{A}{\mathcal{V}}} \sum_{G_{\perp}} A_{n\mathbf{k}}(\mathbf{G}) e^{i(k_{\perp}+G_{\perp})z}. \quad (4.32)$$

For the cases of interest in this treatment, we assume that the bulk symmetry group includes the  $xyz \rightarrow xy\bar{z}$  element so that for every Bloch state  $f_{n\mathbf{k}_{\parallel}k_{\perp}}^{\text{Bloch}}$  there exists a degenerate ‘‘reflected’’ Bloch state  $f_{n\mathbf{k}_{\parallel}-k_{\perp}}^{\text{Bloch}}$  which can also be determined from the bulk calculation.

In general, we expect that for  $z \leq z_1$

$$f(\mathbf{G}_{\parallel}, z) = f_{n\mathbf{k}_{\parallel}k_{\perp}}^{\text{Bloch}}(\mathbf{G}_{\parallel}, z) + \mathcal{R} f_{n\mathbf{k}_{\parallel}-k_{\perp}}^{\text{Bloch}}(\mathbf{G}_{\parallel}, z). \quad (4.33)$$

Here the reflection coefficient  $\mathcal{R}$  is a parameter to be calculated. The Numerov equations (4.26) represent  $N_{\mathbf{G}_{\parallel}} \cdot N$  equations for  $z_n$  values  $1 \leq n \leq N$ . The corresponding wavefunction coefficients  $\{f(\mathbf{G}_{\parallel}, z_n)\}$  represent  $N_{\mathbf{G}_{\parallel}} \cdot N$  unknowns. However, the matching condition (4.33) introduces an extra unknown  $\mathcal{R}$ . In general,  $\mathcal{R}$  will be complex, but for wavefunctions with energies below the work function, which carry no current, we expect that  $\mathcal{R} = e^{i\varphi}$ , where  $\varphi$  denotes a real phase factor.

### 4.3 Treatment of the bulk-surface boundary

The basic Numerov equations in the interface region take the form:

$$\begin{aligned}
Q_1 + P_2 + \dots + \dots + \dots &= -P_0 \\
P_1 + Q_2 + P_3 + \dots + \dots &= 0 \\
\dots + P_2 + Q_3 + P_4 + \dots &= 0 \\
\vdots + \vdots + \vdots + \vdots + \vdots &= 0 \\
\dots + \dots + P_{N-1} + Q_N + P_{N+1} &= 0,
\end{aligned} \tag{4.34}$$

where

$$P_n \equiv f(\mathbf{G}_{\parallel}, z_n) - \frac{\hbar^2}{12} M(\mathbf{G}_{\parallel}, z_n), \tag{4.35}$$

and

$$Q_n \equiv -2f(\mathbf{G}_{\parallel}, z_n) - \frac{10\hbar^2}{12} M(\mathbf{G}_{\parallel}, z_n). \tag{4.36}$$

Here the functions evaluated at  $z_{N+1}$  are determined from Eq. (4.29), with the coefficients determined from a knowledge of the function at  $z_N$  according to Eq. (4.30). The function evaluated at  $z_0$  are in the bulk region and should be represented by the linear combination of Bloch functions (4.33). There are possible variations of these equations that can be solved.

#### 4.3.1 Appelbaum and Hamann approach

Our adaptation of the Appelbaum and Hamann[3] approach uses the last  $N_{\mathbf{G}_{\parallel}}(N-1)$  equations of the Numerov set (4.34). The remaining  $N_{\mathbf{G}_{\parallel}}$  equations are given by the Bloch wave matching condition (4.33) evaluated at  $z = z_1$

$$-\mathcal{R} f_{n\mathbf{k}_{\parallel}-k_{\perp}}^{\text{Bloch}}(\mathbf{G}_{\parallel}, z_1) + f(\mathbf{G}_{\parallel}, z_1) = f_{n\mathbf{k}_{\parallel}k_{\perp}}^{\text{Bloch}}(\mathbf{G}_{\parallel}, z_1). \tag{4.37}$$

One additional equation must be used to determine the unknown reflectivity coefficient  $\mathcal{R}$ . The additional equation minimizes the  $z$ -derivative of equation (4.37) relative to the choice of the reflectivity coefficient:

$$\mathcal{R} \sum_{\mathbf{G}_{\parallel}} \left| \frac{df_{n\mathbf{k}_{\parallel}-k_{\perp}}^{\text{Bloch}}(\mathbf{G}_{\parallel}, z_1)}{dz} \right|^2 = \sum_{\mathbf{G}_{\parallel}} \left( \frac{df_{n\mathbf{k}_{\parallel}-k_{\perp}}^{\text{Bloch}}(\mathbf{G}_{\parallel}, z_1)}{dz} \right)^* \left( \frac{df(\mathbf{G}_{\parallel}, z_1)}{dz} - \frac{df_{n\mathbf{k}_{\parallel}k_{\perp}}^{\text{Bloch}}(\mathbf{G}_{\parallel}, z_1)}{dz} \right), \tag{4.38}$$

where the  $z$ -derivative of the wavefunction coefficients can be determined from the forward difference formula

$$\frac{df(\mathbf{G}_{\parallel}, z_1)}{dz} = \frac{1}{h_z} \left( -\frac{25}{12}f(\mathbf{G}_{\parallel}, z_1) + 4f(\mathbf{G}_{\parallel}, z_2) - 3f(\mathbf{G}_{\parallel}, z_3) + \frac{4}{3}f(\mathbf{G}_{\parallel}, z_4) - \frac{1}{4}f(\mathbf{G}_{\parallel}, z_5) \right). \quad (4.39)$$

For states carrying no current, we could in principle calculate the reflection phase factor  $\varphi$  using the following equation instead of (4.38)

$$e^{2i\varphi} = \frac{\sum_{\mathbf{G}_{\parallel}} \left( \frac{df_{n\mathbf{k}_{\parallel}k_{\perp}}^{\text{Bloch}}(\mathbf{G}_{\parallel}, z_1)}{dz} \right)^* \left( \frac{df(\mathbf{G}_{\parallel}, z_1)}{dz} - \frac{df_{n\mathbf{k}_{\parallel}k_{\perp}}^{\text{Bloch}}(\mathbf{G}_{\parallel}, z_1)}{dz} \right)}{\sum_{\mathbf{G}_{\parallel}} \left( \frac{df_{n\mathbf{k}_{\parallel}k_{\perp}}^{\text{Bloch}}(\mathbf{G}_{\parallel}, z_1)}{dz} \right) \left( \frac{df(\mathbf{G}_{\parallel}, z_1)}{dz} - \frac{df_{n\mathbf{k}_{\parallel}k_{\perp}}^{\text{Bloch}}(\mathbf{G}_{\parallel}, z_1)}{dz} \right)^*}. \quad (4.40)$$

Thus we have  $N_{\mathbf{G}_{\parallel}} \cdot N + 1$  equations and unknowns. Unfortunately, Eq. (4.40) is nonlinear so we use the following procedure instead. For a fixed value of the reflectance  $\mathcal{R} = e^{i\phi}$ , Eqs. (4.34) and (4.37) can be written as  $N_{\mathbf{G}_{\parallel}} \cdot N$  linear equations and unknowns. For each solution, we can evaluate the mismatch

$$\Delta(\phi) \equiv \sum_{\mathbf{G}_{\parallel}} \left| \left( \frac{df_1(\mathbf{G}_{\parallel}, z)}{dz} - \frac{df_{n\mathbf{k}_{\parallel}k_{\perp}}^{\text{Bloch}}(\mathbf{G}_{\parallel}, z)}{dz} - e^{i\phi} \frac{df_{n\mathbf{k}_{\parallel}k_{\perp}}^{\text{Bloch}}(\mathbf{G}_{\parallel}, z)}{dz} \right) \right|_{z=z_1}^2. \quad (4.41)$$

Minimizing the mismatch  $\Delta(\phi)$  as a function of the  $\phi$  can be efficiently accomplished by using an surrogate function[2]  $\Delta(\phi) \approx F_K(\phi)$ , where  $F_K(\phi)$  is a spline interpolation function. After evaluating  $\Delta(\phi)$  for 4 initial values of  $\phi$ , it is very efficient to fit to the surrogate function and iteratively determine the minimum  $\Delta(\phi)$ .

### 4.3.2 Alternative approach

The Appelbaum-Hamann approach is based on the assumption that interface wavefunction takes the bulk values for  $z \leq z_1$ . If the potential is continuous at  $z_1$ , it makes sense to require that the Numerov equations (4.34) are all satisfied at  $z_1$ , representing the functions at  $z_0$  by

$$P_0 \equiv f(\mathbf{G}_{\parallel}, z_0) - \frac{h_z^2}{12}M(\mathbf{G}_{\parallel}, z_0) = \quad (4.42)$$

$$f_{n\mathbf{k}_{\parallel}k_{\perp}}^{\text{Bloch}}(\mathbf{G}_{\parallel}, z_0) + \mathcal{R}f_{n\mathbf{k}_{\parallel}k_{\perp}}^{\text{Bloch}}(\mathbf{G}_{\parallel}, z_0) - \frac{h_z^2}{12} \left( f_{n\mathbf{k}_{\parallel}k_{\perp}}^{\text{Bloch}''}(\mathbf{G}_{\parallel}, z_0) + \mathcal{R}f_{n\mathbf{k}_{\parallel}k_{\perp}}^{\text{Bloch}''}(\mathbf{G}_{\parallel}, z_0) \right), \quad (4.43)$$

where  $''$  denotes second derivative with respect to  $z$ . This approach ensures that the interface wavefunction and its second derivative satisfies Eq. (4.33) at  $z_0$ , but does not explicitly require that it be continuous at  $z_1$ . We can then added one more equation to minimize the error in satisfying Eq. (4.33) at  $z_1$  by varying the reflectivity coefficient, similar to Appelbaum-Hamann Eq. (4.38)

$$\mathcal{R} \sum_{\mathbf{G}_{\parallel}} \left| f_{n\mathbf{k}_{\parallel}-k_{\perp}}^{\text{Bloch}}(\mathbf{G}_{\parallel}, z_1) \right|^2 = \sum_{\mathbf{G}_{\parallel}} \left( f_{n\mathbf{k}_{\parallel}-k_{\perp}}^{\text{Bloch}}(\mathbf{G}_{\parallel}, z_1) \right)^* \left( f(\mathbf{G}_{\parallel}, z_1) - f_{n\mathbf{k}_{\parallel}k_{\perp}}^{\text{Bloch}}(\mathbf{G}_{\parallel}, z_1) \right). \quad (4.44)$$

Alternatively, for the no current condition we have

$$e^{2i\phi} = \frac{\sum_{\mathbf{G}_{\parallel}} \left( f_{n\mathbf{k}_{\parallel}-k_{\perp}}^{\text{Bloch}}(\mathbf{G}_{\parallel}, z_1) \right)^* \left( f(\mathbf{G}_{\parallel}, z_1) - f_{n\mathbf{k}_{\parallel}k_{\perp}}^{\text{Bloch}}(\mathbf{G}_{\parallel}, z_1) \right)}{\sum_{\mathbf{G}_{\parallel}} \left( f_{n\mathbf{k}_{\parallel}-k_{\perp}}^{\text{Bloch}}(\mathbf{G}_{\parallel}, z_1) \right) \left( f(\mathbf{G}_{\parallel}, z_1) - f_{n\mathbf{k}_{\parallel}k_{\perp}}^{\text{Bloch}}(\mathbf{G}_{\parallel}, z_1) \right)^*}. \quad (4.45)$$

Again we have  $N_{\mathbf{G}_{\parallel}} \cdot N + 1$  equations and unknowns.

Again, in practice we replace this with the minimization constraint:

$$\Delta(\phi) \equiv \sum_{\mathbf{G}_{\parallel}} \left| \left( f(\mathbf{G}_{\parallel}, z_1) - f_{n\mathbf{k}_{\parallel}k_{\perp}}^{\text{Bloch}}(\mathbf{G}_{\parallel}, z_1) - e^{i\phi} f_{n\mathbf{k}_{\parallel}-k_{\perp}}^{\text{Bloch}}(\mathbf{G}_{\parallel}, z_1) \right) \right|^2. \quad (4.46)$$

### 4.3.3 Alternative method II

Another slight variation of this is to also replace  $P_1$  in Eq. (4.34) with

$$\begin{aligned} P_1 \equiv f(\mathbf{G}_{\parallel}, z_1) - \frac{\hbar^2}{12} M(\mathbf{G}_{\parallel}, z_1) = \\ f_{n\mathbf{k}_{\parallel}k_{\perp}}^{\text{Bloch}}(\mathbf{G}_{\parallel}, z_1) + \mathcal{R} f_{n\mathbf{k}_{\parallel}-k_{\perp}}^{\text{Bloch}}(\mathbf{G}_{\parallel}, z_1) \\ - \frac{\hbar^2}{12} \left( f_{n\mathbf{k}_{\parallel}k_{\perp}}^{\text{Bloch}''}(\mathbf{G}_{\parallel}, z_1) + \mathcal{R} f_{n\mathbf{k}_{\parallel}-k_{\perp}}^{\text{Bloch}''}(\mathbf{G}_{\parallel}, z_1) \right). \end{aligned} \quad (4.47)$$

This implies that we need to replace the second line of (4.34) by the following equation:

$$Q_2 + P_3 = -(P_{1k_{\perp}}^{\text{Bloch}} + \mathcal{R} P_{1-k_{\perp}}^{\text{Bloch}}). \quad (4.48)$$

The  $\Delta(\phi)$  is defined as the sum of the norm of the function and its derivative at  $z_1$  as follows:

$$\Delta(\phi) \equiv \sum_{\mathbf{G}_{\parallel}} \left| \left( f(\mathbf{G}_{\parallel}, z_1) - f_{n\mathbf{k}_{\parallel}k_{\perp}}^{\text{Bloch}}(\mathbf{G}_{\parallel}, z_1) - e^{i\phi} f_{n\mathbf{k}_{\parallel}-k_{\perp}}^{\text{Bloch}}(\mathbf{G}_{\parallel}, z_1) \right) \right|^2 \quad (4.49)$$

$$+ \sum_{\mathbf{G}_{\parallel}} \left| \frac{d}{dz} f(\mathbf{G}_{\parallel}, z_1) - \left( \frac{d}{dz} f_{n\mathbf{k}_{\parallel}k_{\perp}}^{\text{Bloch}}(\mathbf{G}_{\parallel}, z_1) - \mathcal{R} \frac{d}{dz} f_{n\mathbf{k}_{\parallel}-k_{\perp}}^{\text{Bloch}}(\mathbf{G}_{\parallel}, z_1) \right) \right|^2 \quad (4.50)$$

### 4.3.4 Alternative method III

This method is similar to method II, in fact the GMRES equations are exactly the same. The only difference is the way the  $\Delta(\phi)$  function is defined. In this method,  $\Delta(\phi)$  does not require the derivative of the function to be matched. But instead, it requires the wave function to be matched at more than one point to the Bloch wave functions. We can also define  $\Delta(\phi)$  to include a sum over several match points  $\{z_i\}$  in the neighborhood of  $z_1$ .

$$\Delta(\phi) \equiv \sum_{\mathbf{G}_{\parallel}j} \left| \left( f(\mathbf{G}_{\parallel}, z_j) - f_{n\mathbf{k}_{\parallel}k_{\perp}}^{\text{Bloch}}(\mathbf{G}_{\parallel}, z_j) - e^{i\phi} f_{n\mathbf{k}_{\parallel}-k_{\perp}}^{\text{Bloch}}(\mathbf{G}_{\parallel}, z_j) \right) \right|^2 \quad (4.51)$$

Where  $j$  runs up to the desired matching grid points. The default is set to five points. This means if  $\Delta(\phi) = 0$  then  $f(\mathbf{G}_{\parallel}, z_1), f(\mathbf{G}_{\parallel}, z_2), \dots, f(\mathbf{G}_{\parallel}, z_5)$  matches the Bloch wavefunctions exactly.

### 4.3.5 Alternative method IV

This method treats the  $\langle \tilde{p}_j^a | \tilde{\Psi}_{\lambda\mathbf{k}_{\parallel}} \rangle$  for the boundary atoms as an unknown variables that go into the Numerov equations. This method does not need to recalculate the dot product each time there is a new guess solution of the wave function. Its accuracy should be comparable to the previous method. The  $\Delta(\phi)$  function is computed exactly as 4.51.

## 4.4 Generalized minimum residual method

The Numerov equations (4.34) are efficiently solved as a linear algebra  $Ax = b$  problem using the GMRES algorithm.[59, 17] In this case, the  $b$  vector is formed from the Bloch wave contributions. Since the non-local terms of the Hamiltonian  $M_2(\mathbf{G}_{\parallel}, z)$  include integrals over all of the augmentation spheres, all spheres which

pass through the  $z_1$  plane will contain additional contributions to the  $b$  vector. The  $b$  vector is different for each of the boundary matching schemes listed above.

Once the desired boundary condition is set using one of the methods above, equation (4.34) can be treated as a system of linear equations. One can represent it as  $AX = b$ , with  $AX$  representing the unknown terms on the left hand side of (4.34) and  $b$  representing the known right hand side terms of (4.34). The exact dimension of the system of equations depends on the choice of boundary conditions. But in most cases  $A$  has the dimension of  $N_{G_{\parallel}} * N_z \times N_{G_{\parallel}} * N_z$  and  $X$ , and  $b$  have the dimension of  $(N_{G_{\parallel}} * N_z)$ . For four layered interface diamond (001) for example  $N_{G_{\parallel}} \sim 100$  and  $N_z \sim 150$ . So storing  $A$  and  $b$  and solving for  $X$  would be very difficult specially considering that each element is a double precision complex variable.

So our aim is to solve the systems of linear questions for  $X$ . It will hold the wave function values as follows.

$$X = \begin{pmatrix} f(1, 1) \\ f(2, 1) \\ \vdots \\ f(N_{G_{\parallel}}, 1) \\ f(1, 2) \\ \vdots \\ f(N_{G_{\parallel}}, N_z) \end{pmatrix} \quad (4.52)$$

We need a solver that does not need to explicitly store values of the  $A$  matrix, although we can easily calculate the matrix-vector products  $AX$ . Even if we can come with an explicit expression for  $A$ , it would be very difficult to store it because of its size. For the above example, we need to store about  $15000 \times 15000$  complex double-precision elements.

This is where the Generalized Minimum Residual (GMRES) method comes to the rescue. GMRES method is designed to solve nonsymmetric linear systems [59]. The most popular form of GMRES is based on the notation that orthogonalized vectors of  $A^p X$ ,  $p = 1, 2, 3 \dots m$  form an efficient basis for representing the solution  $X$ . Each step of the procedure adds a new vector to the approximation, up to a chosen restart parameter  $m$ .

If no restarts are used, for an  $A$  matrix with dimension  $s$ , GMRES will converge in no more than  $s$  steps (assuming exact arithmetic). Of course this is of no practical value when  $s$  is large; moreover, the storage and computational requirements in the absence of restarts are prohibitive. Indeed, the crucial element for successful application of GMRES( $m$ ) revolves around the decision of when to restart; that is, the choice of  $m$ . Unfortunately, there exist examples for which the method stagnates and convergence takes place only at the  $s$ th step. For such systems, any choice of  $m$  less than  $s$  fails to converge.

Saad and Schultz [59] have proved several useful results. In particular, they show that if the coefficient matrix  $A$  is real and nearly positive definite, then a “reasonable” value for  $m$  may be selected. When solving large nonsymmetric systems of linear equations with the restarted GMRES algorithm, one is inclined to select a relatively large restart parameter in the hope of mimicking the full GMRES process. Surprisingly, cases exist where small values of the restart parameter yield convergence in fewer iterations than larger values[14].

The clear advantage for us was that, GMRES only asks for us to construct a procedure for calculating  $AX$  for any given  $X$ . So for our problem it is to our advantage to not have an explicit form of  $A$ . This is because one can use a function to generate  $AX$  from (4.34) and store it in an  $N_{G_{\parallel}} * N_z \times 1$  vector.

Figure (4.2) show a flow chart on how GMRES solves the system of linear equations iteratively. It starts with a initial guess value of  $X_0$  and known vector  $b$ . A function then calculates the  $AX_0$  using (4.34). The GMRES subroutine then starts to iteratively minimize the residue,  $r_0 = b - AX_0$ . The detailed algorithm is represented in the chart by the function labeled  $f(r_0)$ . The interested reader is advised to consult reference [59] for the full “guts” of the procedure which provides a better solution vector as  $X$ . The program is then run in a loop until self consistent up to some tolerance or the maximum iteration is reached. At each step, when a new  $X$  is determined, it updates the value of  $X_0$  and ask the user to provide the  $AX_0$  using the updated value.

For our implementation, we used a GMRES Fortran77 library from the European Center for Research and Advanced Training in Scientific Computation (CERFACS)

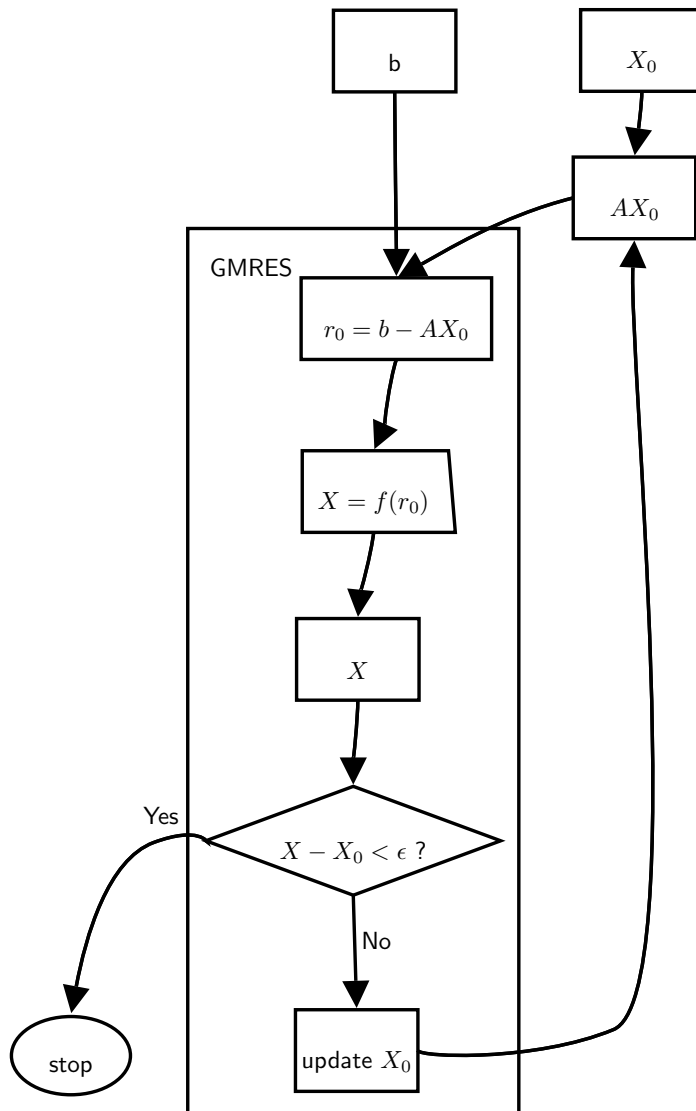


Figure 4.2: Flow chart for GMRES.



website. The library has the ability to do real and complex, single and double precision arithmetic, suitable for serial, shared memory and distributed memory computers [18].

## 4.5 Surface states

In order to calculate surface states, we need to find new solutions to the PAW within the band gap energies. From the smear plot results, we know the the possible energies from which there are no bulk states and we assume that these surface states are spatially confined to Region II and III.

### 4.5.1 Region II states

For each  $\mathbf{k}_{\parallel}$  and energy range, we guess an energy  $E_0$ . Find  $N$  decaying solutions in region II which vanish for  $z < z_0$  as described above. The Hamiltonian terms would take of the form:

$$\tilde{\mathcal{H}}^{PAW} \equiv \tilde{\mathcal{H}} + \sum_{aij} |\tilde{p}_i^a\rangle D_{ij}^a \langle p_j^a| \quad (4.53)$$

$$\tilde{O}^{PAW} \equiv 1 + \sum_{aij} |\tilde{p}_i^a\rangle O_{ij}^a \langle p_j^a|. \quad (4.54)$$

We need to solve two Schrödinger equations for the surface state wave function and its derivative with respect to its energy eigenvalue.

$$\left( \tilde{\mathcal{H}}^{PAW} - E_0 \tilde{O}^{PAW} \right) \Psi_D^{II} = 0 \quad (4.55)$$

$$\left( \tilde{\mathcal{H}}^{PAW} - E_0 \tilde{O}^{PAW} \right) \frac{\partial \Psi_D^{II}}{\partial E} = \tilde{O}^{PAW} \tilde{\Psi}_D. \quad (4.56)$$

Once we have solved (4.55) and (4.56), the total surface states would be computed using :

$$\Psi^{II} = \sum_D C_D \left( \Psi_D^{II} + [E - E_0] \frac{\partial \Psi_D^{II}}{\partial E} \right) \quad (4.57)$$

### 4.5.2 Region III states

We can make the same construction at  $E_0$  in region III. In this region, there are no atoms, so the Schrödinger equation takes the simpler form:

$$\left(\tilde{\mathcal{H}} - E_0\right) \Psi_s^{III} = 0 \quad (4.58)$$

$$\left(\tilde{\mathcal{H}} - E_0\right) \frac{\partial \Psi_s^{III}}{\partial E} = \tilde{\Psi}_s \quad (4.59)$$

$$\Psi^{III} = \sum_s C_s \left( \Psi_s^{III} + [E - E_0] \frac{\partial \Psi_s^{III}}{\partial E} \right) \quad (4.60)$$

### 4.5.3 Match conditions

We require the surface state solutions and their z-derivatives to be continuous at the II-III boundary:

$$\Psi^{II}(z_N) = \Psi^{III}(z_N) \quad (4.61)$$

$$\Psi'^{II}(z_N) = \Psi'^{III}(z_N) \quad (4.62)$$

In order for this conditions to be done easily with the same number of equations and unknowns, we must choose  $N = N_{\mathbf{G}_{\parallel}}$

$$\begin{pmatrix} \Psi_D^{II}(z_N) & -\Psi_s^{III}(z_N) \\ \frac{\partial \Psi_D^{II}(z_N)}{\partial z} & -\frac{\partial \Psi_s^{III}(z_N)}{\partial z} \end{pmatrix} \begin{pmatrix} C_D \\ C_s \end{pmatrix} = (E - E_0) \begin{pmatrix} -\frac{\partial \Psi_D^{II}(z_N)}{\partial E} & \frac{\partial \Psi_s^{III}(z_N)}{\partial E} \\ -\frac{\partial^2 \Psi_D^{II}(z_N)}{\partial E \partial z} & \frac{\partial^2 \Psi_s^{III}(z_N)}{\partial E \partial z} \end{pmatrix} \begin{pmatrix} C_D \\ C_s \end{pmatrix} \quad (4.63)$$

(4.64)

this gives us a  $2N_{\mathbf{G}_{\parallel}} \times 2N_{\mathbf{G}_{\parallel}}$  eigenvalue problem. A surface state solution would be characterized by eigenvalue  $(E - E_0)$  being real and of small magnitude. We may have to try several  $E_0$ 's for this method to work.

## 4.6 Numerical detail of surface state calculation

For an energy  $E_0$ , there are  $N_{G_{\parallel}}$  physical solutions in the vacuum region. In order to match the surface states at the vacuum boundary, we need to have  $N_{G_{\parallel}}$  unique

solutions in the intermediate region. To achieve these, we choose to evaluate (4.55)  $N_{G_{\parallel}}$  times with different initial conditions. This is done by dividing the intermediate region into  $N_{G_{\parallel}}$  equally spaced grids. The first equation was then solved by setting all the wave functions to the left of the first grid to zero with the exception of the last one, which is set to some small initial value. This is demonstrated in Figure (4.3), where it shows that  $\dots = z_{i-3} = z_{i-2} = 0$  and  $z_{i-1} = \epsilon$  are used as initial values for solving the values of  $z_i, z_{i+1}, \dots, z_N$ .

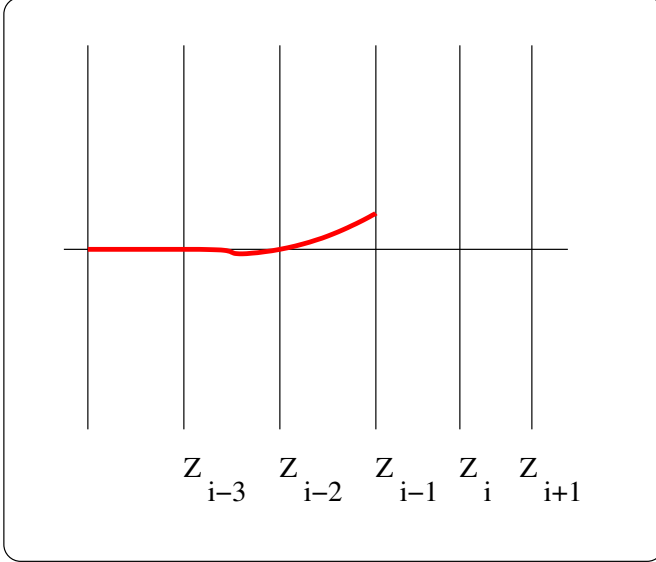


Figure 4.3: Initialization scheme for the surface states in region II

The next solution is then solved similarly except now we used  $\dots = z_{i-3} = z_{i-2} = z_{i-1} = 0$  and  $z_i = \epsilon$  as initial condition. This can be repeated  $N_{G_{\parallel}}$  times. This is demonstrated graphically in Figure (4.4)

Equation (4.55) has the same form as (4.1) so its solution takes the form of (4.15)

$$\frac{d^2}{dz^2} \Psi_D^{II}(G_{\parallel}, z) = M(G_{\parallel}, z) \quad (4.65)$$

$$= M_1(G_{\parallel}, z) + M_2(G_{\parallel}, z) \quad (4.66)$$

$$(4.67)$$

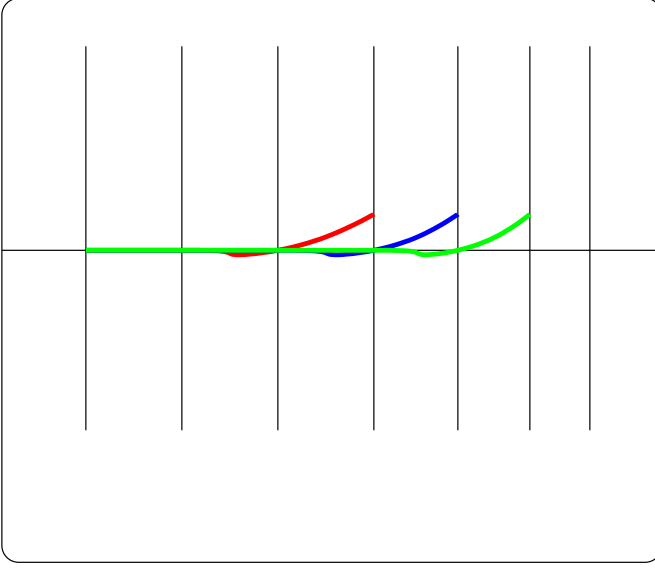


Figure 4.4: Initial condition for region II for different surface states. Different colors represents different initial conditions.

Where

$$M_1(G_{||}, z) = \left[ |k_{||} + G_{||}|^2 - \frac{2m}{\hbar^2} E_0 \right] \Psi_D^I(G_{||}, z) \quad (4.68)$$

$$+ \frac{2m}{\hbar^2} \sum_{G'_{||}} \tilde{V}_{eff}(G_{||} - G'_{||}, z) \Psi_D^I(G'_{||}, z) \quad (4.69)$$

and

$$M_2(G_{||}, z) = \sum_{ai} \mathcal{P}_i^a(G_{||}, z) \sum_j \frac{2m}{\hbar^2} (D_{ij}^a - E_0 O_{ij}^a) \langle \mathcal{P}_j^a | \Psi_D^I \rangle \quad (4.70)$$

$M_1(G_{||}, z)$  is local and easy to implement. But  $M_2(G_{||}, z)$ , has non-local contributions. In addition to this, some of the non-local parts are completely known while there rest are yet to be calculated. To make our formalism suitable for solving systems of linear equations, we need to separate these two terms. Remember that  $\langle \mathcal{P}_j^a | \Psi_D^I \rangle$  is defined as follows.

$$\langle \mathcal{P}_j^a | \Psi_D^I \rangle = \sum_{G_{||}} \int_{z_0}^{z_f} dz \mathcal{P}_i^a(G_{||}, z)^* \Psi_D^I(G_{||}, z). \quad (4.71)$$

Now Let  $z_i$  be the first index of the wave function we are evaluating. This means that all the wave function to the left of  $z_i$  (that is, ...,  $z_{i-2}, z_{i-1}$ ) are all known by design. Figure (4.5) shows the general indexing in the  $z$  direction and the augmentation sphere of an atom. Remember that outside the augmentation sphere, the projector ( $\mathcal{P}$ ) vanishes. Using all the above information, we can split (4.71) in to two parts (known and unknown parts) as follows,

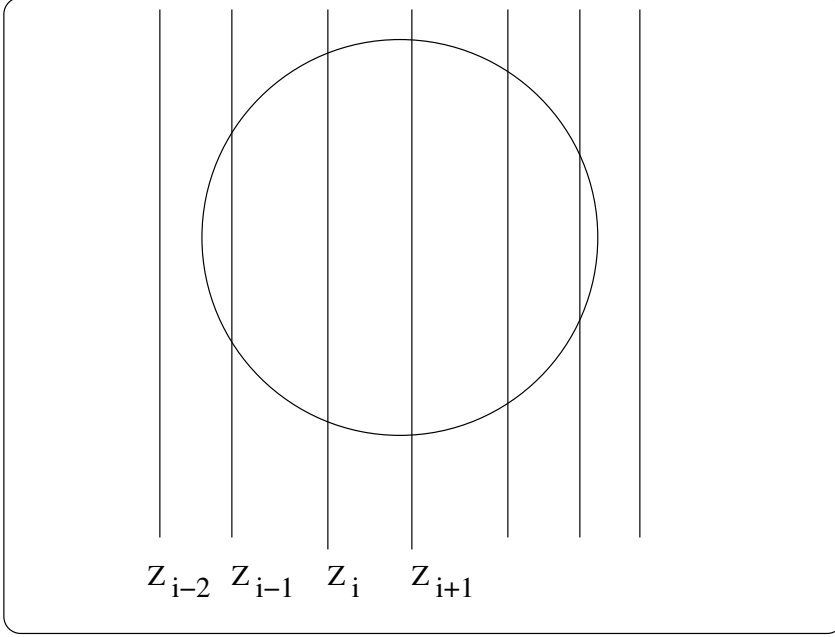


Figure 4.5: Shows general surface state wave function indexing and augmentation sphere of an atom.

$$\begin{aligned} \langle \mathcal{P}_j^a | \Psi_D^{II} \rangle &= \sum_{G_{||}} \int_{z_0}^{z_i} dz \mathcal{P}_j^a(G_{||}, z) \Psi_D^{II}(G_{||}, z) \\ &+ \sum_{G_{||}} \int_{z_i}^{z_f} dz \mathcal{P}_j^a(G_{||}, z) \Psi_D^{II}(G_{||}, z) \end{aligned} \quad (4.72)$$

Where the first term is known and the second term is unknown. The first term is also farther simplified due to the fact that only one of the wave function is non-zero, namely  $\Psi_D^{II}(1, z_{i-1})$ . We have used Simpson's integration rule to approximate it.

Simpson's rule needs three points to integrate, so we will use  $z_{i-2}, z_{i-1}, z_i$ . Equation (4.72) is then looks like the following,

$$\langle \mathcal{P}_j^a | \Psi_D^H \rangle = \frac{4}{3} h \mathcal{P}_j^a(1, z_{i-1})^* \Psi_D^H(1, z_{i-1}) \quad (4.73)$$

$$+ \frac{h}{3} \sum_{G_{||}} \mathcal{P}_j^a(G_{||}, z_i)^* \Psi_D^H(G_{||}, z_i) \quad (4.74)$$

$$+ \sum_{G_{||}} \int_{z_i}^{z_f} dz \mathcal{P}_j^a(G_{||}, z)^* \Psi_D^H(G_{||}, z)$$

Where  $h$  the uniform step size along the  $z$ -axes. Note that  $\Psi_D^H(G_{||}, z_{i-2}) = 0$  is assumed.

Now if we substitute (4.73) in to (4.70), we get

$$\begin{aligned} M_2(G_{||}, z) &= \sum_{ak} \mathcal{P}_k^a(G_{||}, z) \sum_j \frac{2m}{\hbar^2} (D_{kj}^a - E_0 O_{kj}^a) \left[ \frac{4}{3} h \mathcal{P}_j^a(1, z_{i-1}) \Psi_D^H(1, z_{i-1}) \right. \\ &+ \frac{h}{3} \sum_{G_{||}} \mathcal{P}_j^a(G_{||}, z_i) \Psi_D^H(G_{||}, z_i) \\ &+ \left. \sum_{G_{||}} \int_{z_i}^{z_f} dz \mathcal{P}_j^a(G_{||}, z) \Psi_D^H(G_{||}, z) \right] \\ &= M_{2k}(G_{||}, z) + M_{2uk}(G_{||}, z) \end{aligned}$$

Where

$$M_{2k}(G_{||}, z) = \frac{8mh}{3\hbar^2} \sum_{akj} \mathcal{P}_k^a(G_{||}, z) (D_{kj}^a - E_0 O_{kj}^a) \mathcal{P}_j^a(1, z_{i-1}) \Psi_D^H(1, z_{i-1}) \quad (4.75)$$

$$\begin{aligned} M_{2uk}(G_{||}, z) &= \frac{2mh}{3\hbar^2} \sum_{akj} \mathcal{P}_k^a(G_{||}, z) (D_{kj}^a - E_0 O_{kj}^a) \quad (4.76) \\ &\left[ \sum_{G_{||}} \mathcal{P}_j^a(G_{||}, z_i) \Psi_D^H(G_{||}, z_i) \right. \\ &+ \left. \sum_{G_{||}} \int_{z_i}^{z_f} dz \mathcal{P}_j^a(G_{||}, z) \Psi_D^H(G_{||}, z) \right]. \end{aligned}$$

The Numerov solution to the surface states looks like

$$\begin{aligned}
P_{i-2} + Q_{i-1} + P_i &= 0 \\
P_{i-1} + Q_i + P_{i+1} &= 0 \\
\vdots & \\
P_{N-2} + Q_{N-1} + P_N &= 0
\end{aligned} \tag{4.77}$$

where

$$P_i = \Psi_D^{II}(z_i) - \frac{\hbar^2}{12} (M_1(z_i) + M_{2uk}(z_i)) - \frac{\hbar^2}{12} M_{2k}(z_i) \tag{4.78}$$

$$Q_i = -2\Psi_D^{II}(z_i) - \frac{\hbar^2}{12} (M_i(z_i) + M_{2uk}(z_i)) - \frac{10\hbar^2}{12} M_{2k}(z_i). \tag{4.79}$$

Note that the  $G_{||}$  index is suppressed for clarity.

Substituting (4.75), (4.76), (4.78) and (4.79) into (4.77) and rearranging it so that it will take the following form.

$$Ax = b$$

where

$$Ax = \begin{pmatrix} f(z_i) - \frac{\hbar^2}{12} [M_A(z_{i-2}) + 10M_A(z_{i-1}) + M_A(z_i)] \\ -2f(z_i) + f(z_{i+1}) - \frac{\hbar^2}{12} [M_A(z_{i-1}) + 10M_A(z_i) + M_A(z_{i+1})] \\ \vdots \\ f(z_{N-2}) - 2f(z_{N-1}) + f(z_N) - \frac{\hbar^2}{12} [M_A(z_{N-2}) + 10M_A(z_{N-1}) + M_A(z_N)] \end{pmatrix} \tag{4.80}$$

$$b = \begin{pmatrix} -f(z_{i-2}) + 2f(z_{i-1}) + \frac{\hbar^2}{12} [M_{2k}(z_{i-2}) + 10M_{2k}(z_{i-1}) + M_{2k}(z_i)] \\ -f(z_{i-1}) + \frac{\hbar^2}{12} [M_{2k}(z_{i-1}) + 10M_{2k}(z_i) + M_{2k}(z_{i+1})] \\ \vdots \\ \frac{\hbar^2}{12} [M_{2k}(z_{N-2}) + 10M_{2k}(z_{N-1}) + M_{2k}(z_N)] \end{pmatrix}. \tag{4.81}$$

Where  $M_A(z_i) \equiv M_1(z_i) + M_{2uk}(z_i)$ .

Note that the dimension of  $Ax$  is  $N_{G_{\parallel}} * (N - i + 1)$ . where  $N_{G_{\parallel}}$  is the number of  $G_{\parallel}$ 's and  $N$  is the index number of the region II and III. The contents of vector  $b$  is completely known for a given  $z_i$ .

## 4.7 Self-consistency loop

The self-consistency process needs the smooth potential  $\tilde{v}_{\text{eff}}(\mathbf{r})$  and the atom centered Hamiltonian matrix elements  $D_{ij}^a$ .

The potential needs to be expressed in the surface form

$$\tilde{v}_{\text{eff}}(\mathbf{r}) = \sum_{\mathbf{G}_{\parallel}} \tilde{v}_{\text{eff}}(\mathbf{G}_{\parallel}, z) e^{i\mathbf{G}_{\parallel} \cdot \mathbf{r}_{\parallel}}. \quad (4.82)$$

where the contributions are given in equation (4.4).

The local potential term has the form of a sum of spherically symmetric function  $\mathcal{V}_{loc}^a(|\mathbf{r} - \mathbf{R}^a|)$ .

In order to put this term in the surface representation, we must evaluate

$$\hat{v}_{loc}(\mathbf{G}_{\parallel}, z) = \frac{2\pi}{\mathcal{A}} \sum_a e^{-i\mathbf{G}_{\parallel} \cdot \mathbf{R}^a} \int_{|z-Z^a|}^{R_c^a} dr J_0\left(\mathbf{G}_{\parallel} \sqrt{r^2 - |z - Z^a|^2}\right) r \mathcal{V}_{loc}^a(r). \quad (4.83)$$

Once the wavefunctions in Region II and III are determined, we can determine the smooth density:

$$\tilde{n}(\mathbf{r}) = \sum_{\lambda \mathbf{k}_{\parallel}} w_{\lambda \mathbf{k}_{\parallel}} |\tilde{\Psi}_{\lambda \mathbf{k}_{\parallel}}(\mathbf{r})|^2, \quad (4.84)$$

where  $w_{\lambda \mathbf{k}_{\parallel}}$  represents a weighting factor depending on surface Brillouin zone sampling and on occupancy. We can also evaluate the projected occupancy coefficients

$$W_{ij}^a \equiv \sum_{\lambda \mathbf{k}_{\parallel}} w_{\lambda \mathbf{k}_{\parallel}} \langle \tilde{\Psi}_{\lambda \mathbf{k}_{\parallel}} | \tilde{p}_i^a \rangle \langle \tilde{p}_j^a | \tilde{\Psi}_{\lambda \mathbf{k}_{\parallel}} \rangle. \quad (4.85)$$

These two results enable us to update the Hamiltonian.

$$Q_{LM}^a = (-Z^a + Q_{core}^a) \delta_{L0} \delta_{M0} + \sum_{i,j} W_{ij}^a G_{\ell_i m_i \ell_j m_j}^{LM} n_{n_i \ell_i n_j \ell_j}^{aL}. \quad (4.86)$$



Where the Gaunt coefficient is defined by:

$$G_{l_1 m_1 l_2 m_2}^{LM} \equiv \sqrt{4\pi} \int d^3 \mathbf{r} Y_{l_1 m_1}^*(\hat{\mathbf{r}}) Y_{LM}^*(\hat{\mathbf{r}}) Y_{l_2 m_2}(\hat{\mathbf{r}}).$$

From this result, we can calculate the compensation charge density

$$\hat{n}(\mathbf{r}) = \sum_{aLM} Q_{LM}^a g_{LM}^a(\mathbf{r} - \mathbf{R}^a), \quad (4.87)$$

where the functions  $g_{LM}^a(\mathbf{r})$  are defined to be

$$g_{LM}^a(\mathbf{r}) \equiv \mathcal{N}_L r^L k^a(r) Y_{LM}(\hat{\mathbf{r}}), \quad \text{where, } [\sqrt{4\pi} \mathcal{N}_L]^{-1} \equiv \int_0^{R_c^a} dr r^{2+2L} k^a(r) \quad (4.88)$$

and where the shape function  $k^a(r)$  is defined by

$$k^a(r) = \begin{cases} \left[ \frac{\sin(\pi r/R_c^a)}{(\pi r/R_c^a)} \right]^2 & \text{for } r < R_c^a \\ 0 & \text{for } r \geq R_c^a \end{cases}. \quad (4.89)$$

Writing the electron density in the surface representation, we have

$$\tilde{n}(\mathbf{r}) = \sum_{\mathbf{G}_{\parallel}} \tilde{n}(\mathbf{G}_{\parallel}, z) e^{i\mathbf{G}_{\parallel} \cdot \mathbf{r}_{\parallel}}, \quad (4.90)$$

where

$$\tilde{n}(\mathbf{G}_{\parallel}, z) \equiv \frac{1}{\mathcal{A}} \int d^2 \mathbf{r}_{\parallel} e^{-i\mathbf{G}_{\parallel} \cdot \mathbf{r}_{\parallel}} \tilde{n}(\mathbf{G}_{\parallel} \mathbf{r}) = \sum_{\mathbf{G}_{\perp}} \tilde{n}(\mathbf{G}_{\perp}) e^{i\mathbf{G}_{\perp} \cdot z}. \quad (4.91)$$

We also need to represent the compensation charge density in the surface geometry. These can be evaluated

$$\tilde{n}(\mathbf{G}_{\parallel}, z) = \sum_{aLM} Q_{LM}^a e^{-i\mathbf{G}_{\parallel} \cdot \mathbf{R}^a} K_{LM}^a(\mathbf{G}_{\parallel}, z - Z^a), \quad (4.92)$$

where

$$\begin{aligned} K_{LM}^a(\mathbf{G}_{\parallel}, z - Z^a) &\equiv \frac{\mathcal{N}_L}{\mathcal{A}} \left[ \frac{\mathbf{G}_{\parallel x}}{|\mathbf{G}_{\parallel}|} + i \frac{\mathbf{G}_{\parallel y}}{|\mathbf{G}_{\parallel}|} \right]^M \\ &\times e^{-iM\pi/2} \sqrt{\frac{\pi(2L+1)(L-|M|)!}{(L+|M|)!}} \\ &\times \int_{|z-Z^a|}^{R_c^a} dr r^{L+1} k^a(r) P_L^{|M|} \left( \frac{z - Z^a}{r} \right) \\ &\times J_{|M|} \left( |\mathbf{G}_{\parallel}| \sqrt{r^2 - (z - Z^a)^2} \right). \end{aligned} \quad (4.93)$$

$$(4.94)$$

The total pseudodensity in the surface representation  $\tilde{n}_T(\mathbf{G}_{\parallel}, z)$  should be used to calculate the Coulomb contribution to the potential as a solution to the Poisson equation

$$\left(-G_{\parallel}^2 + \frac{d^2}{dz^2}\right) \tilde{v}_{\text{Coul}}(\mathbf{G}_{\parallel}, z) = -4\pi e^2 \tilde{n}_T(\mathbf{G}_{\parallel}, z). \quad (4.95)$$

The zero potential for Eq. (4.95) is set by the solution of the 3-dimensional Poisson equation in the bulk and can be calculated from

$$\tilde{v}_{\text{Coul}}(\mathbf{G}_{\parallel}, z_1) = \frac{4\pi e^2}{\mathcal{V}} \sum_{G_{\perp}, \mathbf{G} \neq \mathbf{0}} \frac{\tilde{n}(\mathbf{G}) + \tilde{\hat{n}}(\mathbf{G})}{G_{\parallel}^2 + G_{\perp}^2} e^{iG_{\perp} z_1}. \quad (4.96)$$

The Green's function solution of (4.95) can be written as follows,

### Case 1 ( $G_{\parallel} \neq 0$ )

$$\begin{aligned} \tilde{v}_{\text{Coul}}(G_{\parallel}, z) &= \frac{2\pi e^2}{\mathbf{G}_{\parallel}} \int_{z_1}^z e^{-\mathbf{G}_{\parallel}(z-z')} \tilde{n}_T(\mathbf{G}_{\parallel}, z') dz' \\ &+ \frac{2\pi e^2}{\mathbf{G}_{\parallel}} \int_z^{\infty} e^{\mathbf{G}_{\parallel}(z-z')} \tilde{n}_T(\mathbf{G}_{\parallel}, z') dz' \\ &+ C_{G_{\parallel}} e^{-\mathbf{G}_{\parallel}(z-z_1)} \end{aligned} \quad (4.97)$$

Where  $C_{G_{\parallel}}$  is a constant. It is also assumed that  $\tilde{v}_{\text{Coul}}(G_{\parallel}, z \rightarrow \infty)$  approaches to zero exponentially. Now lets find the value of  $C_{G_{\parallel}}$ . Let  $z_{\rho}$  be the value of  $z$  where  $\tilde{n}_T(G_{\parallel}, z_{\rho}) \equiv 0$ .

For  $z = z_1$  (4.97) can be written as

$$\tilde{v}_{\text{Coul}}(\mathbf{G}_{\parallel}, z_1) = \frac{2\pi e^2}{\mathbf{G}_{\parallel}} \int_{z_1}^{z_{\rho}} e^{\mathbf{G}_{\parallel}(z_1-z')} \tilde{n}_T(\mathbf{G}_{\parallel}, z') dz' + C_{G_{\parallel}}. \quad (4.98)$$

Here it assumed that

$$\frac{2\pi e^2}{\mathbf{G}_{\parallel}} \int_{z_{\rho}}^{\infty} e^{-\mathbf{G}_{\parallel}(z-z')} \tilde{n}_T(\mathbf{G}_{\parallel}, z') dz' \equiv 0.$$

Remember that the value of the  $\bar{v}_{Coul}(\mathbf{G}_{\parallel}, z_1)$  is known from the matching condition at the bulk-intermediate boundary. Equation (4.98) can be rearranged to solve for  $C_{G_{\parallel}}$  as follows

$$C_{G_{\parallel}} = \bar{v}_{Coul}(\mathbf{G}_{\parallel}, z_1) - \frac{2\pi e^2}{\mathbf{G}_{\parallel}} \int_{z_1}^{z_p} e^{\mathbf{G}_{\parallel}(z_1-z')} \bar{n}_T(\mathbf{G}_{\parallel}, z') dz'.$$

Therefore, (4.97) can be written

$$\begin{aligned} \bar{v}_{Coul}(G_{\parallel}, z) &= \frac{2\pi e^2}{\mathbf{G}_{\parallel}} \int_{z_1}^z e^{-\mathbf{G}_{\parallel}(z-z')} \bar{n}_T(\mathbf{G}_{\parallel}, z') dz' \\ &+ \frac{2\pi e^2}{\mathbf{G}_{\parallel}} \int_z^{z_p} e^{\mathbf{G}_{\parallel}(z-z')} \bar{n}_T(\mathbf{G}_{\parallel}, z') dz' \\ &+ \left[ \bar{v}_{Coul}(\mathbf{G}_{\parallel}, z_1) - \frac{2\pi e^2}{\mathbf{G}_{\parallel}} \int_{z_1}^{z_p} e^{\mathbf{G}_{\parallel}(z_1-z')} \bar{n}_T(\mathbf{G}_{\parallel}, z') dz' \right] e^{-\mathbf{G}_{\parallel}(z-z_1)}. \end{aligned}$$

**Case 2**  $G_{\parallel} = 0$

$\bar{v}_{Coul}(\mathbf{0}, z)$  can be solved similarly

$$\bar{v}_{Coul}(\mathbf{0}, z) = \bar{v}_{Coul}(\mathbf{0}, z_1) + 4\pi e^2 \int_{z_1}^z (z' - z) \bar{n}_T(\mathbf{0}, z') dz'. \quad (4.99)$$

In order for this to have no net electric field, the system must be neutral:

$$\int_{z_1}^{\infty} \bar{n}_T(\mathbf{0}, z') dz' = 0. \quad (4.100)$$

Also, in order that this form be consistent with the bulk periodic potential,  $z_1$  must be chosen so that

$$\int_{z_1-c/2}^{z_1+c/2} (z' - z_1) \bar{n}_T^{\text{Bulk}}(\mathbf{0}, z') dz' = 0. \quad (4.101)$$

The expression for the  $G_{\parallel} = \mathbf{0}$  contribution allows us to evaluate  $V_{\infty}$  which is used in Eq. (4.28)

$$V_{\infty} = \bar{v}_{Coul}(\mathbf{0}, z_1) + 4\pi e^2 \int_{z_1}^{\infty} (z' - z_1) \bar{n}_T(\mathbf{0}, z') dz'. \quad (4.102)$$

The exchange correlation term  $\mu_{xc}[\tilde{n}(\mathbf{r})]$  can be evaluated by using a 2-dimensional FFT.

The  $D_{ij}^a$  coefficients (4.5) can be determined from a combination of matrix elements set in the *atompaw* code and the projected weight coefficients. The equations we need for updating the  $D_{ij}^a$  coefficients are for the most part, the same as for the bulk PAW formalism as described in reference [26] and are summarized below. By assumption,  $D_{ij}^a$  is taken to be the bulk value if  $Z^a \leq z_1$  and we need to update only those for  $Z^a > z_1$ .

The kinetic energy and the ionic and local potential terms are taken directly from the stored matrix elements:

$$K_{ij}^a + [v_{\text{at}}^a]_{ij} = \delta_{l_i l_j} \delta_{m_i m_j} (K_{n_i l_i n_j l_j}^a + [v_{\text{at}}]_{n_i l_i n_j l_j}). \quad (4.103)$$

The matrix element of the compensation potential is given by

$$[\hat{v}^a]_{ij} = \sum_{LM} Q_{LM}^a (-1)^M G_{l_i m_i l_j m_j}^{L-M} \hat{v}_{n_i l_i n_j l_j}^{aL}. \quad (4.104)$$

The Hartree terms can be calculated according to

$$[V_H^a]_{ij} = \sum_{LM, (k, l)} (-1)^M G_{l_i m_i l_j m_j}^{L-M} G_{l_k m_k l_l m_l}^{LM} W_{kl}^a V_{n_i l_i n_j l_j; n_k l_k n_l l_i}^{aL}. \quad (4.105)$$

In this equation, the sum over  $L$  and  $l_k$  and  $l_l$  is restricted by  $|l_k - l_l| \leq L \leq l_k + l_l$  and  $|l_i - l_j| \leq L \leq l_i + l_j$ . The sum over  $m_k$  and  $m_l$  is restricted by  $M = m_j - m_i = m_k - m_l$ .

The Coulomb shift term can be evaluated:

$$[v_0^a]_{ij} = \sum_{LM} \frac{\partial E}{\partial Q_{LM}^a} G_{l_i m_i l_j m_j}^{LM} n_{n_i l_i n_j l_j}^{aL}. \quad (4.106)$$

The coefficients  $\frac{\partial E}{\partial Q_{LM}^a}$  have several contributions which can be written:

$$\begin{aligned} \frac{\partial E}{\partial Q_{LM}^a} = & \sum_{\mathbf{G}_{\parallel}} e^{-i\mathbf{G}_{\parallel} \cdot \mathbf{R}_{\parallel}^a} \int_{Z^a - R_c^a}^{Z^a + R_c^a} \bar{v}(\mathbf{G}_{\parallel}, z)^* K_{LM}^a(\mathbf{G}_{\parallel}, z - Z^a) dz \\ & - \sum_{i, j} W_{ij}^a (-1)^M G_{l_i m_i l_j m_j}^{L-M} \hat{v}_{n_i l_i n_j l_j}^{aL} - 2Q_{LM}^{a*} \hat{E}^{aL}. \end{aligned} \quad (4.107)$$

The exchange correlation term can be calculated according to

$$[V_{XC}^a]_{ij} = \sum_{\alpha} w_{\alpha} Y_{l_i m_i}^*(\hat{\mathbf{r}}_{\alpha}) Y_{l_j m_j}(\hat{\mathbf{r}}_{\alpha})$$

$$\begin{aligned} & \times \int_0^{r_c^a} dr \left[ \mu_{xc} [n^a(\hat{\mathbf{r}}_\alpha r) + n_{core}^a(r)] \phi_{n_i l_i}^a(r) \phi_{n_j l_j}^a(r) \right. \\ & \left. - \mu_{xc} [\tilde{n}^a(\hat{\mathbf{r}}_\alpha r)] \tilde{\phi}_{n_i l_i}^a(r) \tilde{\phi}_{n_j l_j}^a(r) \right], \end{aligned} \quad (4.108)$$

where the radial integral over  $r$  is performed for each angular mesh point  $\hat{\mathbf{r}}_\alpha$ . The efficiency of evaluating (4.108), can be improved by separating the angular and radial contributions in the atomic density functions according to:

$$\begin{aligned} n^a(\hat{\mathbf{r}}_\alpha r) &= \sum_{i,j} W_{ij}^a Y_{l_i m_i}^*(\hat{\mathbf{r}}_\alpha) Y_{l_j m_j}(\hat{\mathbf{r}}_\alpha) \frac{\phi_{n_i l_i}^a(r) \phi_{n_j l_j}^a(r)}{r^2} \quad \text{and} \\ \tilde{n}^a(\hat{\mathbf{r}}_\alpha r) &= \sum_{i,j} W_{ij}^a Y_{l_i m_i}^*(\hat{\mathbf{r}}_\alpha) Y_{l_j m_j}(\hat{\mathbf{r}}_\alpha) \frac{\tilde{\phi}_{n_i l_i}^a(r) \tilde{\phi}_{n_j l_j}^a(r)}{r^2}. \end{aligned} \quad (4.109)$$

## 4.8 Convergence of interface charge density toward bulk region

The presence of an impurity in a metal is known to cause oscillations in the density profile due to the sharp Fermi surface. The decay of the density oscillations induced by a defect is a long-standing problem in solid state physics. This phenomenon, called Friedel oscillations [34, 67], is closely related to the singularity in the response function for wave-vectors close to  $2k_F$  (Fermi level), also occurs in the vicinity of the surface.

$$\text{For } z \approx z_1: \quad \tilde{\rho} = \sum_{\mathbf{k}_\parallel k_\perp} w_{\mathbf{k}_\parallel k_\perp} |\tilde{\Psi}_{\mathbf{k}_\parallel k_\perp}^{\text{Bloch}} + \mathcal{R} \tilde{\Psi}_{\mathbf{k}_\parallel -k_\perp}^{\text{Bloch}}|^2 = \tilde{\rho}^{\text{Bloch}} + \delta \tilde{\rho}_{\text{osc}}^{\text{Bloch}}.$$

Interference term  $\delta \tilde{\rho}_{\text{osc}}^{\text{Bloch}}$  decreases in amplitude as  $z$  approaches bulk region provided that  $k_\perp$  sampling is sufficiently large.

It is expected that for the surface problem, the induced density decays asymptotically as

$$\delta \tilde{\rho}_{\text{osc}}^{\text{Bloch}} \sim \frac{\cos(2k_F z - \gamma)}{z^2} \quad (4.110)$$

Where  $\gamma$  is some constant that depends on the Fermi level [34].

Figure (4.6) illustrates the effect of k-point sampling for a one-dimensional model system. The exact solution is found by analytically integrating the model density. It

is clearly shown that one needs to use enough  $k_{\perp}$  points to smooth out the Friedel oscillations for density far from the interface plane.

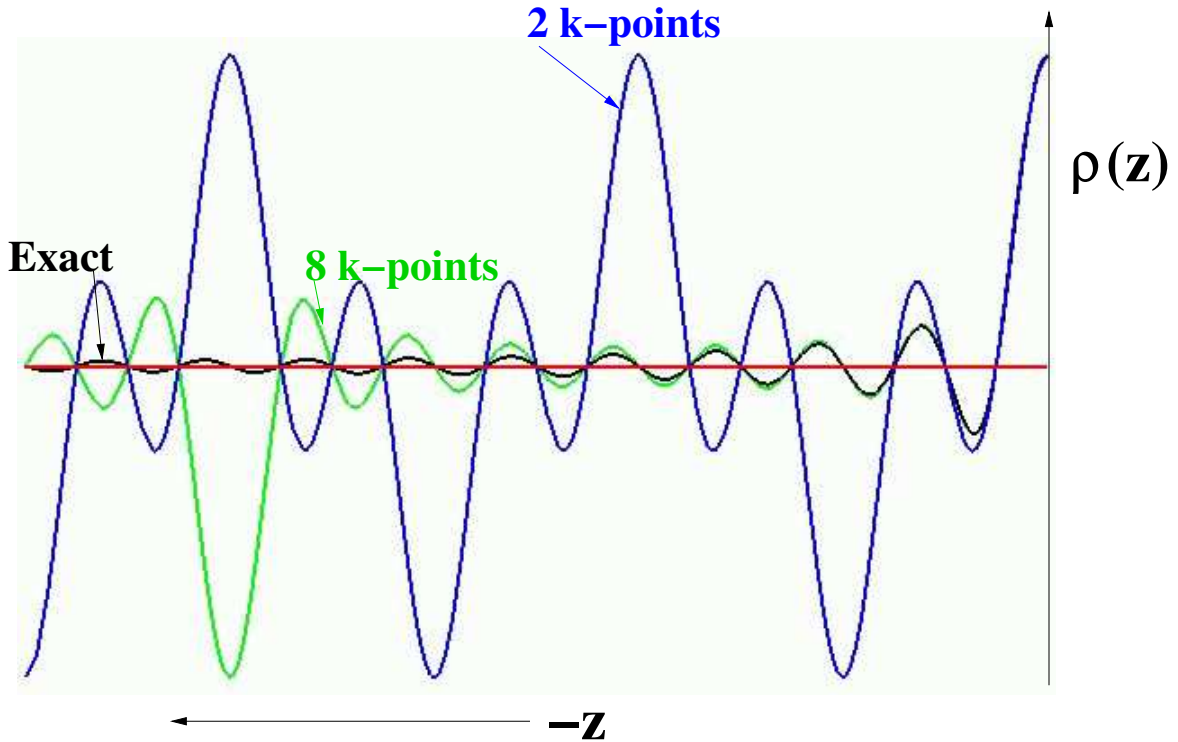


Figure 4.6: Theoretical charge fluctuation as a function of  $k_{\perp}$  and  $z$

Figure (4.7) shows convergence of the  $G_{\parallel} = 0$  charge density component of lithium (001) crystal for different  $\mathbf{k}_{\perp}$  sampling points. We used 16 layers in the interface region.

## 4.9 Convergence of wave function

The surface relaxation introduced by the abrupt lattice termination in the surface region should only affect the wave functions close to the surface. But the wave function should resemble the bulk states as one goes from the surface to the bulk region. On the other hand, if one choose different size for region II (interface region) the interface wave function should remain the same. One way to check our method is to compare the simulation results of two different sizes for region II. The results should not

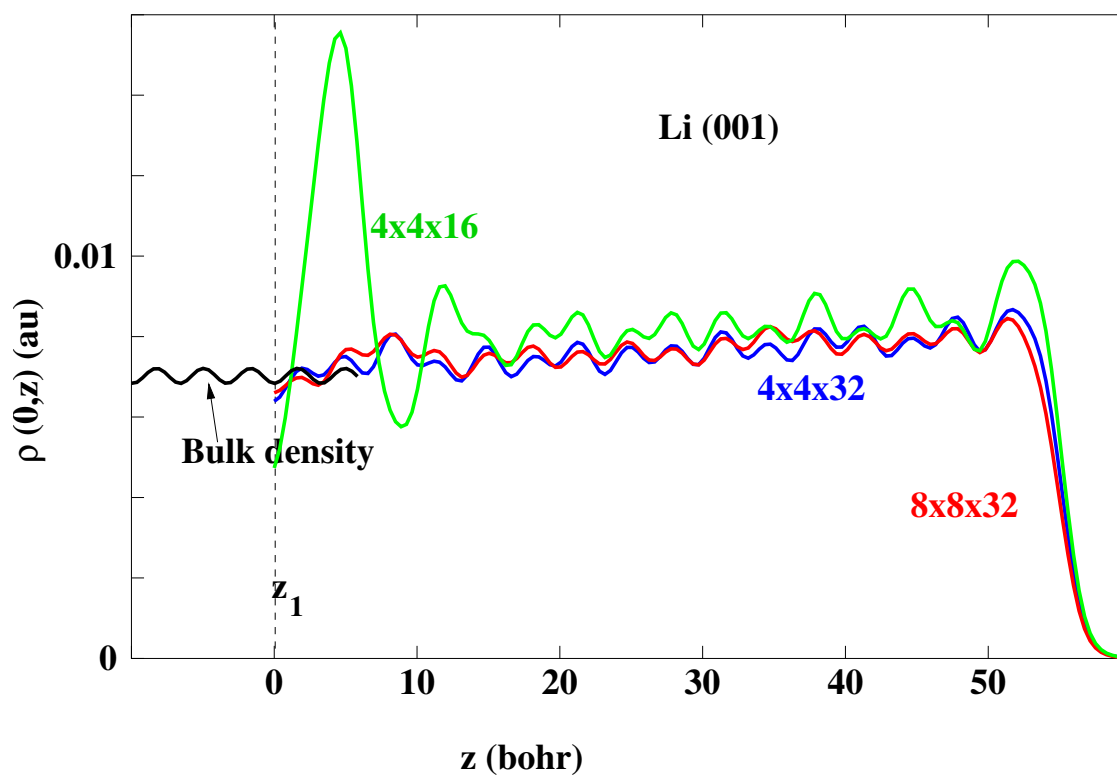


Figure 4.7: Convergence of  $\rho(\mathbf{0}, z)$  for Li (001) 16-layer interface region for different  $\mathbf{k}$ -point sampling noted in the form  $\lambda \times \mu \times \nu$ , where  $\lambda$  and  $\mu$  refer to the number of  $\mathbf{k}_{\parallel}$  points in the 2 distinct surface directions and  $\nu$  refers to the number of  $\mathbf{k}_{\perp}$  points.

depend on whether or not some of the bulk layers are treated in the interface region. Figures (4.8 and 4.9) shows a wavefunction that extends from bulk to vacuum region calculated for four interface layers and eight interface layers diamond (001). Two different energy levels are presented. Figure (4.8) was generated by using the energy labeled “1” in Figure (4.10) while Figure (4.9) generated using the energy labeled “2” in the same plot. Figure (4.10) show the band structure of diamond (001) surface as a function of  $\mathbf{k}_\perp$  for the  $\mathbf{k}_\parallel = (1/4, 1/4)$  in a fractional unit of the surface Brillouin zone.

In our implementation, we have made an assumption that for each Bloch wave traveling toward the interface at a given energy level, we have one reflected Bloch wave. This is expressed by

$$f_{n\mathbf{k}_\parallel k_\perp}^{\text{Bloch}}(\mathbf{G}_\parallel, z) + \mathcal{R}f_{n\mathbf{k}_\parallel -k_\perp}^{\text{Bloch}}(\mathbf{G}_\parallel, z). \quad (4.111)$$

This assumption is true for the case “1” because there is only one  $\mathbf{k}_\perp$  point that has the same energy as “1”. In other words, if you draw a horizontal line  $E = -0.05$  on Figure (4.10), that line intersects the band structure curve only once, that is, at point “1”. That is why the results for different lattice layers converges on Figure (4.8). This assumption would not work for the case of “2”. This is because we can have more than one  $\mathbf{k}_\perp$  for a given energy. The corresponding result shows that the wave function changes a lot for different choices of the interface region. So to fix this, we need to update our assumption to include the additional reflected wavefunctions. The reflected Bloch wavefunctions should be

$$f_{n\mathbf{k}_\parallel k_\perp}^{\text{Bloch}}(\mathbf{G}_\parallel, z) + \sum_j \mathcal{R}_j f_{n\mathbf{k}_\parallel -k_{\perp j}}^{\text{Bloch}}(\mathbf{G}_\parallel, z). \quad (4.112)$$

Where  $j$  sums over all of the degenerate  $\mathbf{k}_\perp$  points representing refelected Bloch waves.



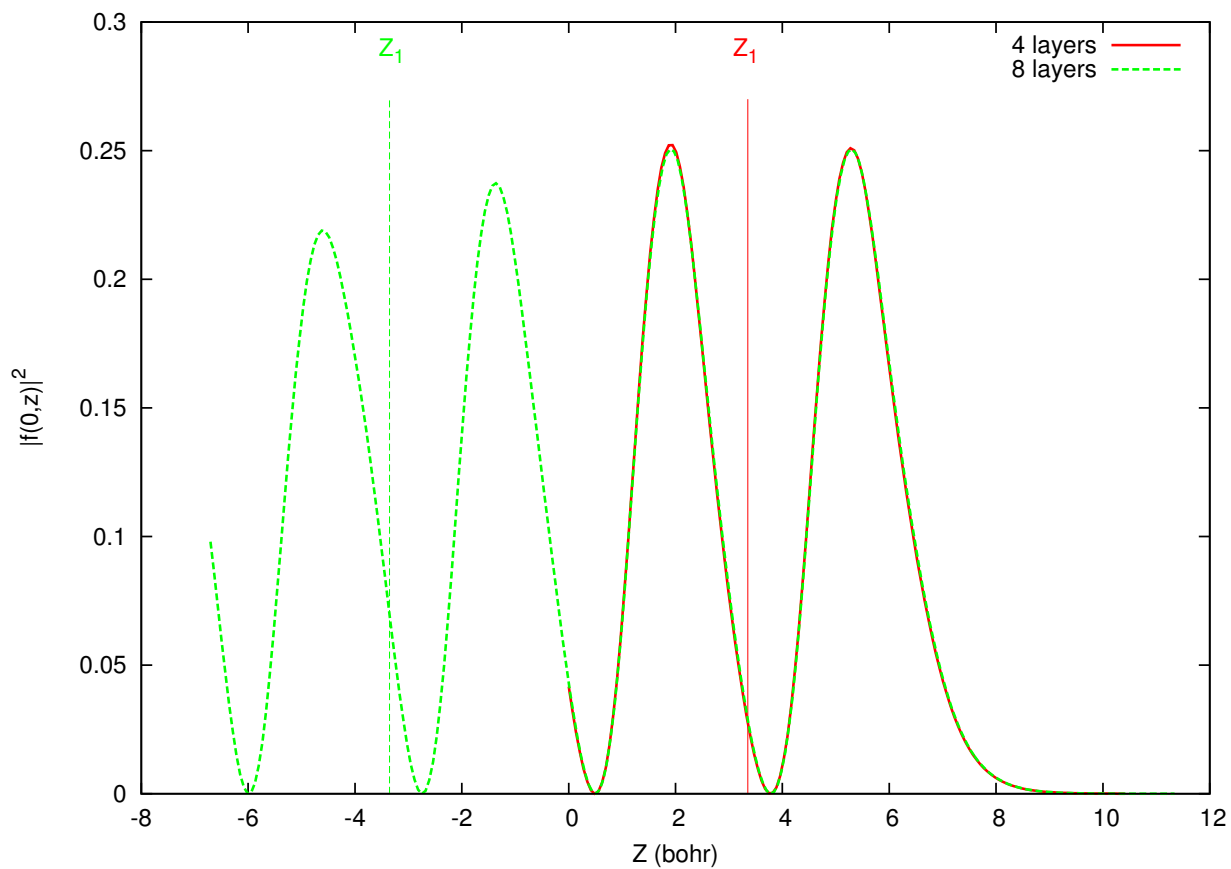


Figure 4.8: Comparison of 4 and 8-layered diamond (001) interface wave functions for the energy labeled as “1” in Figure 4.10. The  $z$ -axis is shifted to match the vacuum layer from both cases.

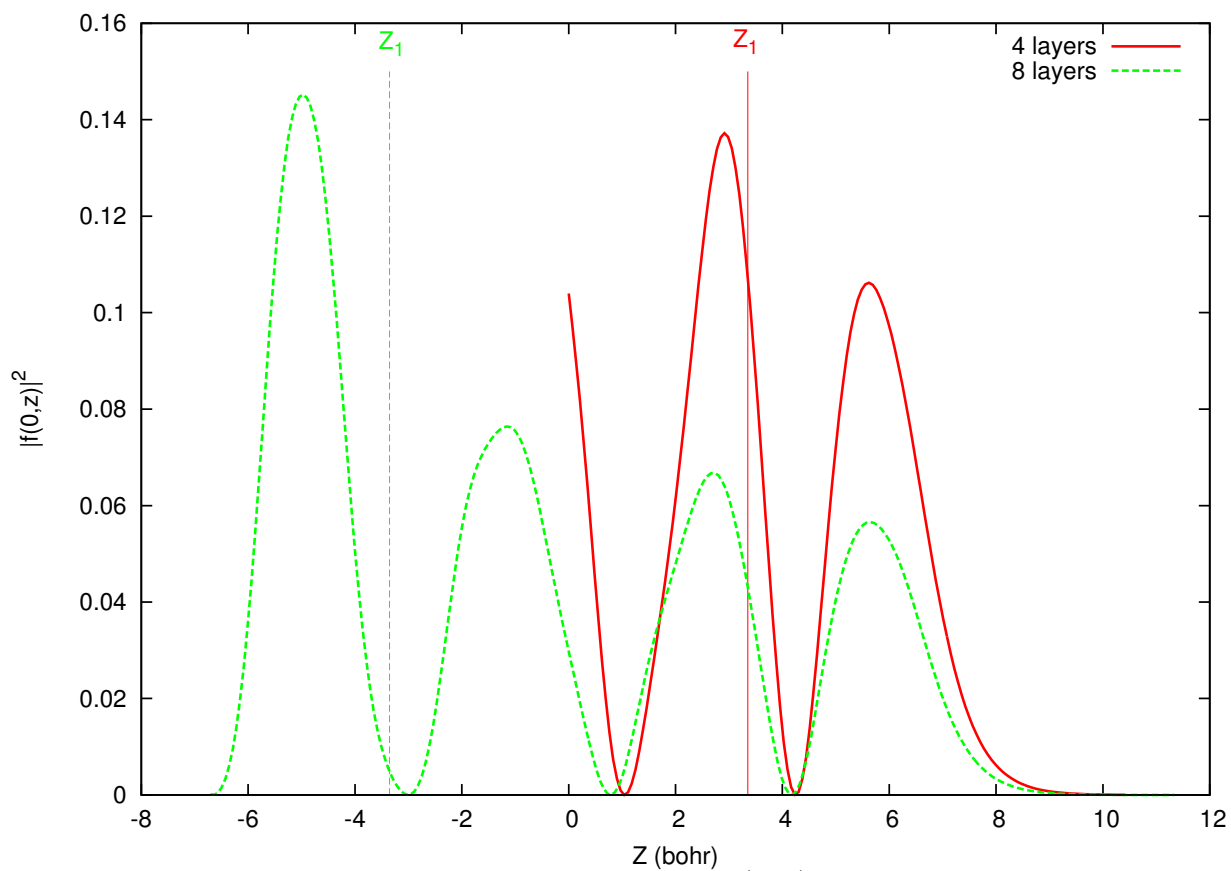


Figure 4.9: Comparison of 4 and 8-layered diamond (001) interface wave functions for the energy labeled as “2” in Figure 4.10.

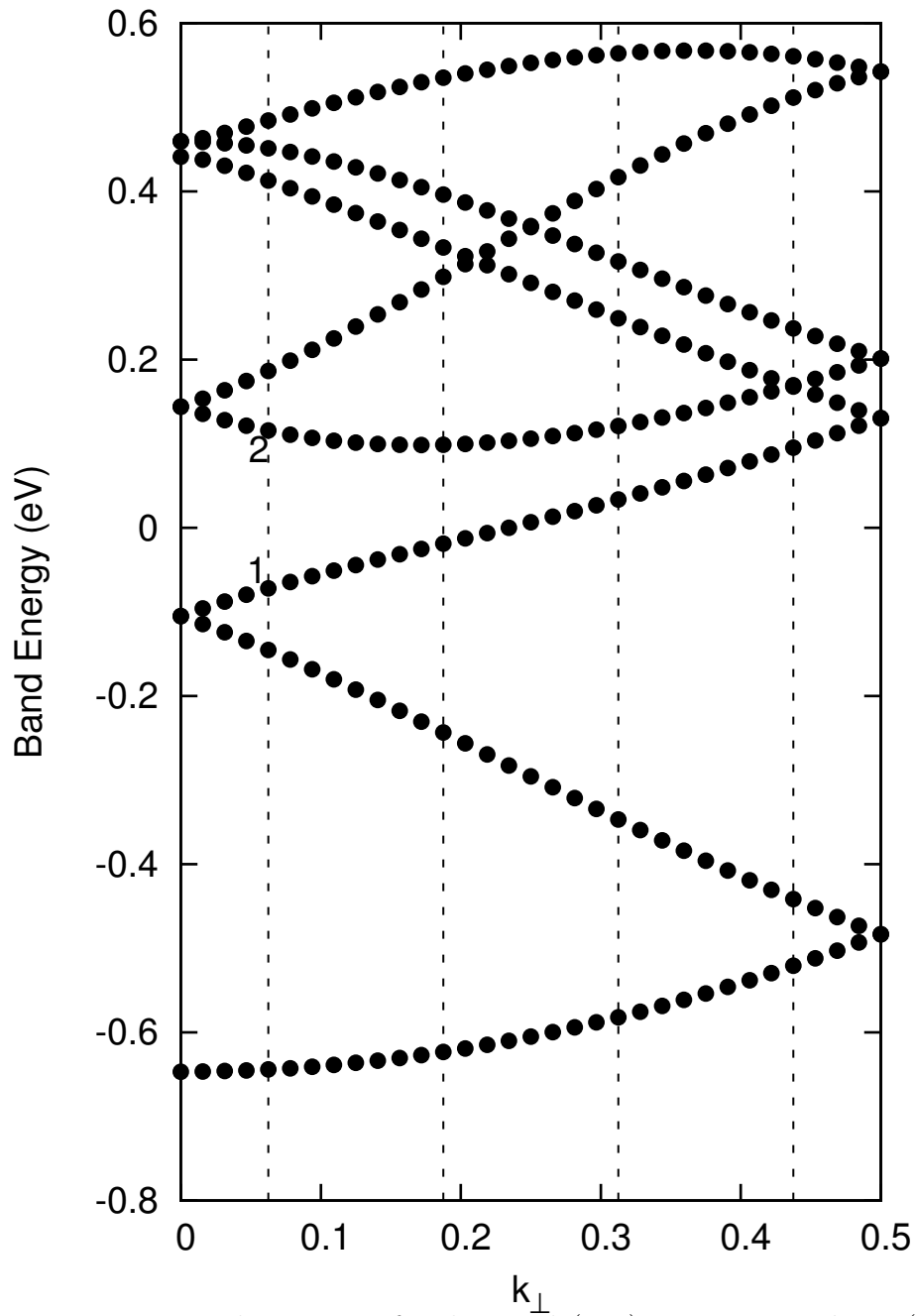


Figure 4.10: Band structure for diamond (001) structure at  $k_{\parallel} = (0.25, 0.25)$ . The vertical dotted lines represent the  $k_{\perp}$  values used to calculate the surface wave functions.

# Chapter 5

## Analysis

When we first started the project, we formulated the solution of the equation in region II (the intermediate region) (see fig 4.1 for geometry), as an initial value problem by taking the bulk wave functions to set the initial value. Since the differential equations are second order, there are two independent solutions for each equation. One of these equations is unphysical. We used the Predictor-Corrector method [15] to solve our second order equations. It turned out that Predictor-corrector had difficulty in filtering out the unphysical solution that grows exponentially. Figure (5.1), shows one such result. The result shows the region II wave functions for lithium in the body centered cubic structure. We tried to control the growing solutions by using different methods, such as by using Green's functions, by explicitly dropping the growing solution, and by changing the step size. All of these failed to correct the problem.

Why are the exponentially growing solutions bad? The reason is that we want to match the solutions in regions II and III at the vacuum interface. Since the wave function of the region III have a finite value at the interface then we would expect the same for region II.

After a long try, we abandoned solving initial value problem for the region II wave function. Instead, we have now formulated the problem as a boundary value problem. This method is explained in detailed in previous Chapter 4. The down side of the boundary value formulation is that we have to solve a very large system of equations.

The size of equation is in the order of  $(N_{\mathbf{G}_{\parallel}} \times N_z)$ . Where  $N_{\mathbf{G}_{\parallel}}$  is number of  $\mathbf{G}_{\parallel}$  wave vectors and  $N_z$  is the number of z-steps. To give you some sense of how large this is for lithium, constructing region II with 4 unit cells and by including all  $|\mathbf{G}_{\parallel}| \leq 6$  bohr<sup>-1</sup>, there are approximately 15000 equations and unknowns. This is far to big to fit in to a single processor computer.

To overcome this difficulty we use the Generalized Minimum RESidual (GMRES) method developed by Saad and Schultz in 1986 [59] in order to solve large nonsymmetric linear systems. This method does not need the  $s \times s$  coefficient matrix to be stored. instead, you can use a function to generate the right hand side of the  $AX = b$  system of equations. This way, you need only a storage for a dimension of  $s \times m$ , where  $m$  be is the “restart” parameter described in section (4.4).

So why do we need to know about the methods which have failed? There are two reasons. First is that by explaining these methods, we will help prevent repeating the same mistakes. The second reason is that our next generation method is likely to use most of the procedures discussed below. This is because, we have recently reexamined the initial value formulation and have developed a recurrence algorithm that looks very promising for future development

The results for the boundary value formulation are really encouraging. Now it is possible to solve the wave function for the complete region, i.e Region I, II and III for one energy level with out the growing solutions. Figure(5.2) shows the real and imaginary part of  $\mathbf{G}_{\parallel} = 0$  for the first occupied energy for one SCF cycle.

## 5.1 Explanation of the failed method

### 5.1.1 Basic equations for energies within bulk bands

- Assume that region *I* wave function is a sum of Bloch wave:

$$\Psi_I = \sum_{n\mathbf{k}_{\perp} (E_{n\mathbf{k}_{\parallel}\mathbf{k}_{\perp}}=E)} C_{n\mathbf{k}_{\perp}}^{\mathbf{k}_{\parallel}} \Psi_{n\mathbf{k}_{\parallel}\mathbf{k}_{\perp}}^{\text{Bloch}} \quad (5.1)$$

- Divide region *II* wave function in two parts; one that propagates from bulk the other that decay into the solid as follows:

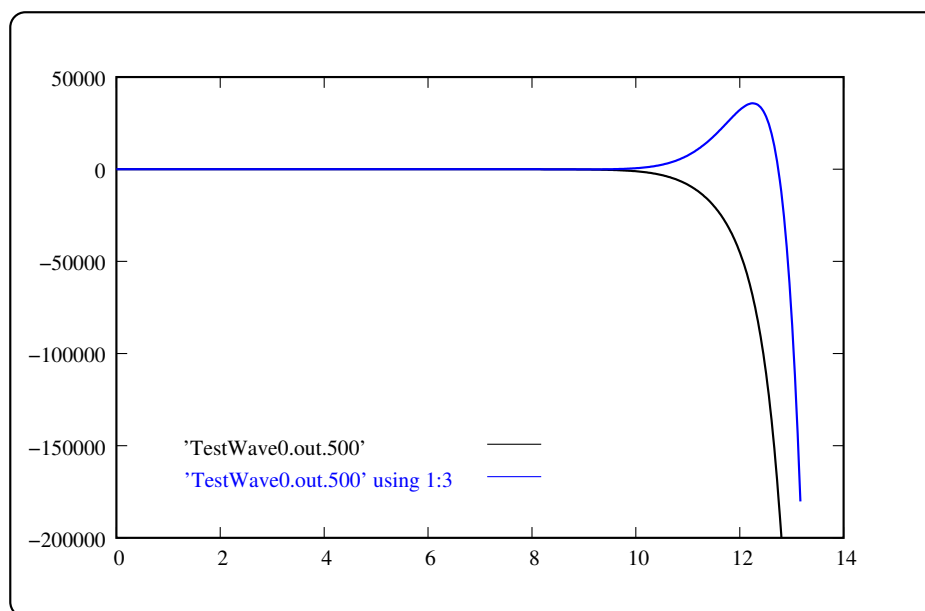


Figure 5.1: Predictor corrector results for the region II for Li in bcc structure

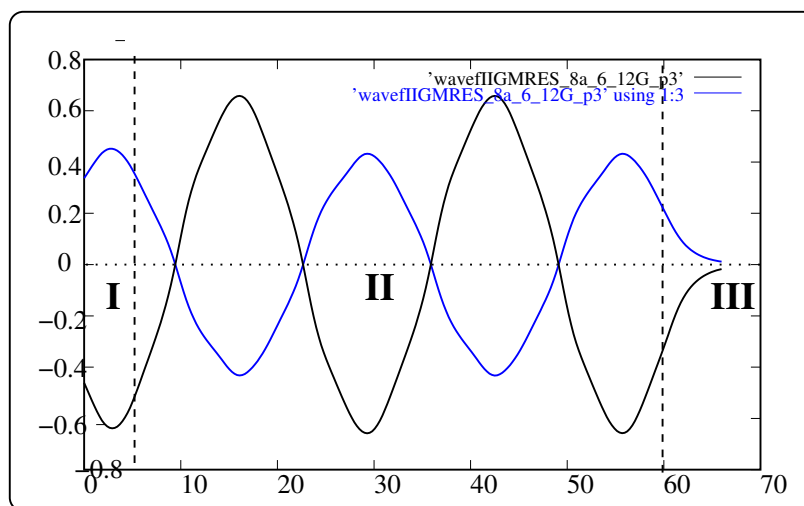


Figure 5.2: Wave function for  $\mathbf{G}_{\parallel} = 0$  in the “Alternative Approach II” for Li in bcc structure.

$$\Psi_{II} = \sum_{n\mathbf{k}_\perp} C_{n\mathbf{k}_\perp}^{\mathbf{k}_\parallel} \Psi_{n\mathbf{k}_\parallel\mathbf{k}_\perp}^{II} + \sum_d C_d \Psi_{\mathbf{k}_\parallel}^d \quad (5.2)$$

- Expand region *III* wave function as a sum of wave functions which decay or propagate into the vacuum region with dominant parallel wavevector  $\mathbf{k}_\parallel + \mathbf{G}_\parallel'$ :

$$\Psi_{III} = \sum_{\mathbf{G}_\parallel'} C_{\mathbf{G}_\parallel'}^{III} \Psi_{\mathbf{G}_\parallel'}^{III}(r) \quad (5.3)$$

- Determine unknown coefficients  $C_{n\mathbf{k}_\perp}^{\mathbf{k}_\parallel}, C_d, C_{\mathbf{G}_\parallel'}^{III}$  from matching conditions:

$$\Psi_I = \Psi_{II} |_{z=z_1} \quad \text{and} \quad \Psi_{II} = \Psi_{III} |_{z=z_N}$$

+(similar expression for matching the derivatives).

### 5.1.2 For energies in bulk band gaps (surface states)

- $\Psi_I \equiv 0$  because bulk wave functions do not exist for energies within the band gap.
- Using surface projected band diagram, guess surface state energy  $E$  within band gaps.
- Expand region *II* wave functions as a sum of  $N$  decaying functions.

$$\Psi_{II} = \sum_d C_d \Psi_{\mathbf{k}_\parallel}^d \quad (5.4)$$

- Expand region *III* wave function as a sum of wave functions which decay or propagate into the vacuum region with dominant parallel wavevector  $\mathbf{k}_\parallel + \mathbf{G}_\parallel'$

$$\Psi_{III} = \sum_{\mathbf{G}_\parallel'} C_{\mathbf{G}_\parallel'}^{III} \Psi_{\mathbf{G}_\parallel'}^{III}(r) \quad (5.5)$$

- Matching at the  $z_N$  boundary determines coefficients  $C_d, C_{\mathbf{G}_\parallel'}^{III}$  at the correct  $E$ .

$$\Psi_{II} = \Psi_{III} |_{z=z_N} \quad \text{and} \quad \frac{\partial \Psi_{II}}{\partial z} = \frac{\partial \Psi_{III}}{\partial z} |_{z=z_N} \quad (5.6)$$

- In practice, energy search is performed by linearizing matching conditions with respect to energy.

### 5.1.3 Detailed equations

#### Region I (Bloch waves)

$$\begin{aligned}
\tilde{\Psi}_{nk}^I(\vec{r}) &= \sqrt{\frac{1}{\mathcal{V}}} \sum_{\mathbf{G}} A_{nk}(\mathbf{G}) e^{i(\mathbf{k}+\mathbf{G})\cdot\vec{r}} \\
\vec{G} &= \mathbf{G}_{\parallel} + \mathbf{G}_{\perp} \\
\vec{k} &= \mathbf{k}_{\parallel} + \mathbf{k}_{\perp} \\
\tilde{\Psi}_{nk}^I(\vec{r}) &= \sqrt{\frac{1}{A}} \sum_{\mathbf{G}_{\parallel}} f_{nk\mathbf{G}_{\parallel}}^I(z) e^{i(\mathbf{k}_{\parallel}+\mathbf{G}_{\parallel})\cdot r_{\parallel}} \\
f_{nk\mathbf{G}_{\parallel}}^I(z) &= \sqrt{\frac{A}{\mathcal{V}}} e^{i\mathbf{k}_{\perp}\cdot z} \sum_{\mathbf{G}_{\perp}} A_{nk}(\mathbf{G}_{\parallel}, \mathbf{G}_{\perp}) e^{i\mathbf{G}_{\perp}\cdot z}
\end{aligned}$$

#### Region II

Similarly region II wavefunction would be represented as:

$$\Psi_{nk}^{II} = \sqrt{\frac{1}{A}} \sum_{\mathbf{k}_{\parallel}} f_{nk\mathbf{G}_{\parallel}}^{II}(z) e^{i(\mathbf{k}_{\parallel}+\mathbf{G}_{\parallel})\cdot r_{\parallel}}. \quad (5.7)$$

Its equivalent Schrödinger equation would be:

$$\begin{aligned}
\left( -\frac{\hbar^2}{2m} \frac{d^2}{dz^2} + \frac{\hbar^2(\mathbf{k}_{\parallel} + \mathbf{G}_{\parallel})^2}{2m} - E_{nk} \right) f_{nk\mathbf{G}_{\parallel}}^{II}(z) + \sum_{\mathbf{G}_{\parallel}'} V(\mathbf{G}_{\parallel} - \mathbf{G}_{\parallel}', z) f_{nk\mathbf{G}_{\parallel}'}^{II}(z) \quad (5.8) \\
+ \sum_{aij} \wp_{\mathbf{G}_{\parallel}}^{ai}(z) (D_{ij}^a - E_{nk} O_{ij}^a) \langle \tilde{p}_j^a | \tilde{\Psi}_{\alpha} \rangle = 0 \quad (5.9)
\end{aligned}$$

Where the notation are changed from the previous chapter. For reference here is the equivalence syntax.

- $\wp_{\mathbf{G}_{\parallel}}^{ai}(z) \equiv \mathcal{P}_i^a(\mathbf{G}_{\parallel}, z)$
- $f_{\mathbf{G}_{\parallel}}^{II}(z) \equiv f_{nk}^{II}(\mathbf{G}_{\parallel}, z)$



Now lets expand  $f_{\mathbf{G}_{\parallel}}^{II}(z)$  using :

$$= f_{\mathbf{G}_{\parallel}}^0(z) + \sum_{ai} C_{ai} f_{\mathbf{G}_{\parallel}}^{ai}(z). \quad (5.10)$$

The functions  $f_{\mathbf{G}_{\parallel}}^0(z)$  are solutions to the coupled equations:

$$\left( -\frac{\hbar^2}{2m} \frac{d^2}{dz^2} + \frac{\hbar^2(k_{\parallel} + \mathbf{G}_{\parallel})^2}{2m} - E_{nk} \right) f_{nk\mathbf{G}_{\parallel}}^0(z) \quad (5.11)$$

$$+ \sum_{\mathbf{G}_{\parallel}'} V_{\mathbf{G}_{\parallel} - \mathbf{G}_{\parallel}'}(z) f_{nk\mathbf{G}_{\parallel}'}^0(z) + \sum_{ai} \wp_{\mathbf{G}_{\parallel}}^{ai}(z) C_{ai}^0 = 0 \quad (5.12)$$

Where

$$C_{ai}^0 = \sum_j (D_{ij}^a - E_{nk} O_{ij}^a) \langle \tilde{p}_j^a | \tilde{\Psi}_\alpha \rangle \quad (5.13)$$

and the functions  $f_{\mathbf{G}_{\parallel}}^{ai}(z)$  are solutions to the equations

$$\left( -\frac{\hbar^2}{2m} \frac{d^2}{dz^2} + \frac{\hbar^2(k_{\parallel} + \mathbf{G}_{\parallel})^2}{2m} - E_{nk} \right) f_{nk\mathbf{G}_{\parallel}}^{ai}(z) \quad (5.14)$$

$$+ \sum_{\mathbf{G}_{\parallel}'} V_{\mathbf{G}_{\parallel} - \mathbf{G}_{\parallel}'}(z) f_{nk\mathbf{G}_{\parallel}'}^{ai}(z) = -\wp_{\mathbf{G}_{\parallel}}^{ai}(z). \quad (5.15)$$

Since outside the  $0 < z - z_a < r_c^a$  and  $|z_1 - z_a| \leq r_c^a$  region,  $\wp_{\mathbf{G}_{\parallel}}^{ai}(z) = 0$ , we assume  $f_{\mathbf{G}_{11}}^{ai}(z) \equiv 0$  for  $z < z_a - r_c^a$  for all  $a$  such that  $|z_0 - z_a| > r_c^a$ .

In order to find  $f_{\mathbf{G}_{\parallel}}^{II}(z)$ , we must find  $C_{ai}$  coefficients.

### Calculation of $C_{ai}$ coefficients

For  $b$  such that  $|z_1 - z^b| > r_c^b$ ,

$$\sum_{bi} C_{bi} (-\wp_{\mathbf{G}_{\parallel}}^{bi}(z)) + \sum_{b'jk} \wp_{\mathbf{G}_{\parallel}}^{b'j}(z) \left( D_{jk}^{b'} - E_{nk} O_{jk}^{b'} \right) \langle \wp_{\mathbf{G}_{\parallel}}^{b'k} | f_{\mathbf{G}_{\parallel}}^0 \rangle + \sum_{el} C_{el} f_{\mathbf{G}_{\parallel}}^{el} = 0$$

Suppose that we would like to ensure that the coefficient of each  $\wp_{\mathbf{G}_{\parallel}}^{bi}(z)$  vanishes. this gives us a linear equation for the  $C_{ai}$  coefficients.

$$-C_{bi} + \sum_j (D_{ij}^b - E_{nk} O_{ij}^b) \langle \wp^{bj} | f^0 \rangle + \sum_{ejl} (D_{ij}^b - E_{nk} O_{ij}^b) \langle \wp^{bj} | f^{el} \rangle C_{el} = 0 \quad (5.16)$$

Defining

$$X_{bi}^0 \equiv \sum_j (D_{ij}^b - E_{nk} O_{ij}^b) \langle \wp^{bj} | f^0 \rangle \quad (5.17)$$

and

$$X_{bi}^{el} \equiv \sum_j (D_{ij}^b - E_{nk} O_{ij}^b) \langle \wp^{bj} | f^{el} \rangle, \quad (5.18)$$

a linear equation for  $C_{bi}$  coefficients takes of the form:

$$C_{bi} - \sum_{el} X_{bi}^{el} C_{el} = X_{bi}^o \quad (5.19)$$

and this uniquely determines  $\Psi^{II}$  for Bloch states.

$$\begin{aligned} M_{bi,el} &\equiv \delta_{bi,el} - X_{bi}^{el} \\ C_{bi} &= \sum_{el} M_{bi,el}^{-1} X_{el}^o \end{aligned} \quad (5.20)$$

**Region III** In region III, the wave function takes of the form:

$$\tilde{\Psi}_{nk}^{III} = \sqrt{\frac{1}{A}} \sum_{\mathbf{G}_{\parallel}} \chi_{nk\mathbf{G}_{\parallel}}^{III}(z) e^{i(k_{\parallel} + \mathbf{G}_{\parallel}) \cdot r_{\parallel}} \quad (5.21)$$

as discussed before. Equations for  $z \rightarrow \infty$  become dominated by  $\mathbf{G}_{\parallel} = 0$  contribution.

$$\left\{ \frac{-\hbar^2}{2m} \frac{d^2}{dz^2} + \frac{\hbar^2}{2m} (k_{\parallel} + \mathbf{G}_{\parallel})^2 + V_{\infty} - \epsilon_{n\mathbf{k}_{\parallel}\mathbf{k}_{\perp}} \right\} f_{\mathbf{G}_{\parallel}^0}^{III}(z) = 0 \quad (5.22)$$

suppose for  $z > z_N$

$$f_{\mathbf{G}_{\parallel}}^{III}(z) = \sum_{\mathbf{G}_{\parallel}^0} C^{\mathbf{G}_{\parallel}^0} f_{\mathbf{G}_{\parallel}^0}^{\mathbf{G}_{\parallel}}(z) \quad (5.23)$$

where for  $z \rightarrow \infty$ ,  $f_{\mathbf{G}_{\parallel}^0}^{\mathbf{G}_{\parallel}}(z) = e^{-\kappa_{\mathbf{G}_{\parallel}^0} z} \delta_{\mathbf{G}_{\parallel}\mathbf{G}_{\parallel}^0}$  as defined in equation (4.27).

**Matching condition at  $z_N$ :**

$f_{\mathbf{G}_{\parallel}}^{II}(z_N) = \sum_{\mathbf{G}_{\parallel}^0} C^{\mathbf{G}_{\parallel}^0} f_{\mathbf{G}_{\parallel}^0}^{\mathbf{G}_{\parallel}}(z_N)$  and  $f_{\mathbf{G}_{\parallel}}^{III}(z_N) = \sum_{\mathbf{G}_{\parallel}^0} C^{\mathbf{G}_{\parallel}^0} f_{\mathbf{G}_{\parallel}^0}^{\mathbf{G}_{\parallel}'}(z_N)$  Where the ' denotes first derivative with respect to  $z$ .

If there are  $N_{\mathbf{G}_{\parallel}}$  values of  $\mathbf{G}_{\parallel}$ , we have  $N_{\mathbf{G}_{\parallel}}$  unknowns and  $2N_{\mathbf{G}_{\parallel}}$  equations for each Bloch wave. Actually there are at least 2 Bloch waves in region I; one traveling in the direction  $+z$  and a degenerate solution traveling in the direction  $-z$ ; suppose we normalize the solution to the  $+z$  Bloch wave:

$$f_{\mathbf{G}_{\parallel}}^{II+}(z_N) + \mathcal{R}f_{\mathbf{G}_{\parallel}}^{II-}(z_N) = \sum_{\mathbf{G}_{\parallel}^0} C^{\mathbf{G}_{\parallel}^0} f_{\mathbf{G}_{\parallel}^0}^{\mathbf{G}_{\parallel}}(z_N)$$

Now we have  $N_{\mathbf{G}_{\parallel}} + 1$  unknowns. Need to add  $N_{\mathbf{G}_{\parallel}} - 1$  decaying wave solutions at the energy  $E_{nk}$ . These equations can be generalized as follows.

1. choose  $N_{\mathbf{G}_{\parallel}} - 1$  of the grid points  $z_i$ ;  $z_0 < z_q < z_s$
2. solve Schrödinger equations with  $f_{\mathbf{G}_{\parallel}}^{0q}(z)$  with  $f_{\mathbf{G}_{\parallel}}^{0q}(z) \equiv 0$  for  $z < z_q$ ; corresponding behavior for  $f_{\mathbf{G}_{\parallel}}^{ai}(z)$ .

Thus matching condition becomes

$$\begin{aligned} f_{\mathbf{G}_{\parallel}}^{II+}(z_s) + \mathcal{R}f_{\mathbf{G}_{\parallel}}^{II-}(z_s) + \sum_{q=1}^{N_{\mathbf{G}_{\parallel}}-1} D_q f_{\mathbf{G}_{\parallel}}^q(z_s) &= \sum_{\mathbf{G}_{\parallel}^0} C^{\mathbf{G}_{\parallel}^0} f_{\mathbf{G}_{\parallel}^0}^{\mathbf{G}_{\parallel}}(z_s) \\ f_{\mathbf{G}_{\parallel}}^{II'+}(z_s) + \mathcal{R}f_{\mathbf{G}_{\parallel}}^{II'-}(z_s) + \sum_{q=1}^{N_{\mathbf{G}_{\parallel}}-1} D_q f_{\mathbf{G}_{\parallel}}^{\prime q}(z_s) &= \sum_{\mathbf{G}_{\parallel}^0} C^{\mathbf{G}_{\parallel}^0} f_{\mathbf{G}_{\parallel}^0}^{\prime \mathbf{G}_{\parallel}}(z_s) \end{aligned}$$

### Band gap solutions

The band gap solutions are very similar to those discussed in section 4.5.

## 5.2 Methods of integration

We have used two methods to solve the above equations namely, Predictor-Corrector and Green's function formulations.

### 5.2.1 Predictor-corrector

Since we have a special second-order equation of the form of  $y'' = G(x, y)$  in which  $y'$  is not explicitly involved, we can use predictor corrector (PC) method to integrate it inwards. Lets rewrite our equation in the PC form [15].

$$\frac{d^2}{dz^2} f_{\mathbf{G}_{\parallel}}^{G_0}(z) = \left[ (k_{\parallel} + \mathbf{G}_{\parallel})^2 + \frac{2m}{\hbar^2} (V_{\infty} - \epsilon_{nk_{\parallel}k_{\perp}}) \right] f_{\mathbf{G}_{\parallel}}^{\mathbf{G}_{\parallel}^0}(z) + \sum_{\mathbf{G}_{\parallel}'} \bar{V}_{\mathbf{G}_{\parallel} - \mathbf{G}_{\parallel}'}(z) f_{\mathbf{G}_{\parallel}'}^{\mathbf{G}_{\parallel}^0}(z)$$

The Predictor term of PC formalism is as follows:

$$y_i = y_{i+3} + y_{i+1} - y_{i+4} + \frac{h^2}{4} (5y''_{i+3} + 2y''_{i+2} + 5y''_{i+1})$$

and the Corrector term of the PC will be:

$$y_i = 2y_{i+1} - y_{i+2} + \frac{h^2}{12} (y''_{i+2} + 10y''_{i+1} + y''_{i+1})$$

Our regions II and III equations would take of the form:

- Predictor Term

$$\begin{aligned} f_{\mathbf{G}_{\parallel}}(z+h) &= f_{\mathbf{G}_{\parallel}}(z) + f_{\mathbf{G}_{\parallel}}(z-2h) - f_{\mathbf{G}_{\parallel}}(z-3h) \\ &+ \frac{h^2}{4} (5f''_{\mathbf{G}_{\parallel}}(z) + 2f''_{\mathbf{G}_{\parallel}}(z-h) + 5f''_{\mathbf{G}_{\parallel}}(z-2h)) \end{aligned}$$

- Corrector Term

$$\begin{aligned} f_{\mathbf{G}_{\parallel}}(z+h) &= 2f_{\mathbf{G}_{\parallel}}(z) - f_{\mathbf{G}_{\parallel}}(z-h) \\ &+ \frac{h^2}{12} (f''_{\mathbf{G}_{\parallel}}(z+h) + 10f''(z) + f''_{\mathbf{G}_{\parallel}}(z-h)). \end{aligned}$$

In all of these expressions  $f''_{\mathbf{G}_{\parallel}}(z)$  is evaluated by  $M_1(\mathbf{G}_{\parallel}, z)$ . To use the PC we need to know at least four points. For region II these values are taken from the known Bloch functions . In region III, we need to integrate from  $z_{\rho}$  in the vacuum region toward  $z_N$ . The initial inputs are:

$$\chi(0, z_{max-i}) = e^{-\kappa_{G_{11}}^0 * h(z_{max-i})}$$

$$\chi(1 : G_{max}, z_{max-3} : z_{max}) = 0$$

where  $i = 0, 1, 2$  and  $3$ .

### 5.2.2 Green's function method

It is possible also to use Green's function to solve for the wave function in region II. It will take of the form:

$$f_{\mathbf{G}_{\parallel}}(z+h) = f_{\mathbf{G}_{\parallel}}(z) \cos(\varkappa h) + \frac{f'_{\mathbf{G}_{\parallel}}(z)}{\varkappa} \sin(\varkappa h) \quad (5.24)$$

$$+ \frac{1}{\varkappa} \int_0^h \sin(\varkappa(h-z')) \mathcal{G}_{\mathbf{G}_{\parallel}}(z) dz' \quad (5.25)$$

where

$$\mathcal{G}_{\mathbf{G}_{\parallel}}(z) = \frac{2m}{\hbar^2} \sum_{\mathbf{G}_{\parallel}} V_{\mathbf{G}_{\parallel}-\mathbf{G}_{\parallel}'}(z) * f_{\mathbf{G}_{\parallel}}(z) \quad (5.26)$$

$$\varkappa = \sqrt{\frac{2m}{\hbar^2} E - |k_{\parallel} + \mathbf{G}_{\parallel}|^2} \quad (5.27)$$

## 5.3 Some results

This section consites our results for the intermediate wavefunctions using the above discussed methods. Figure (5.3) shows the initial potential used to simulate lithium crystal in the body centered cube (bcc) structure. The solution for the Bloch wavefunction that extends toward the intermediate region expressed in equation (5.12) is shown in Figure (5.4). Predictor-Corrector method was used to integrate the wavefunctions. The  $\mathbf{G}_{\parallel} = (0, 0)$ ,  $\mathbf{G}_{\parallel} = (0, 1)$  and  $\mathbf{G}_{\parallel} = (-1, 0)$  component of the wavefunction are shown. Figure (5.5) shows the solution of the intermediate wavefunction those do not exist in the bulk as expressed in equation (5.15). The  $2s$  and  $2pz$  wavefunction for two lithium atoms and their corresponding atom augmentation sphere are shown. Figure (5.6) show the total intermediate wavefunction computed using equation (5.10) for lithium crystal. This are examples of the well behaved solution. This means that the intermediate wave functions do not diverge at the region-II and region-III boundary. This is due to the fact that we have a very simple surface. We have one atom per unit cell and the atom is centered at the unite cell and no atom got cut buy our boundary. But this method have an issue for complex surfaces, as shown above for the case of diamond.

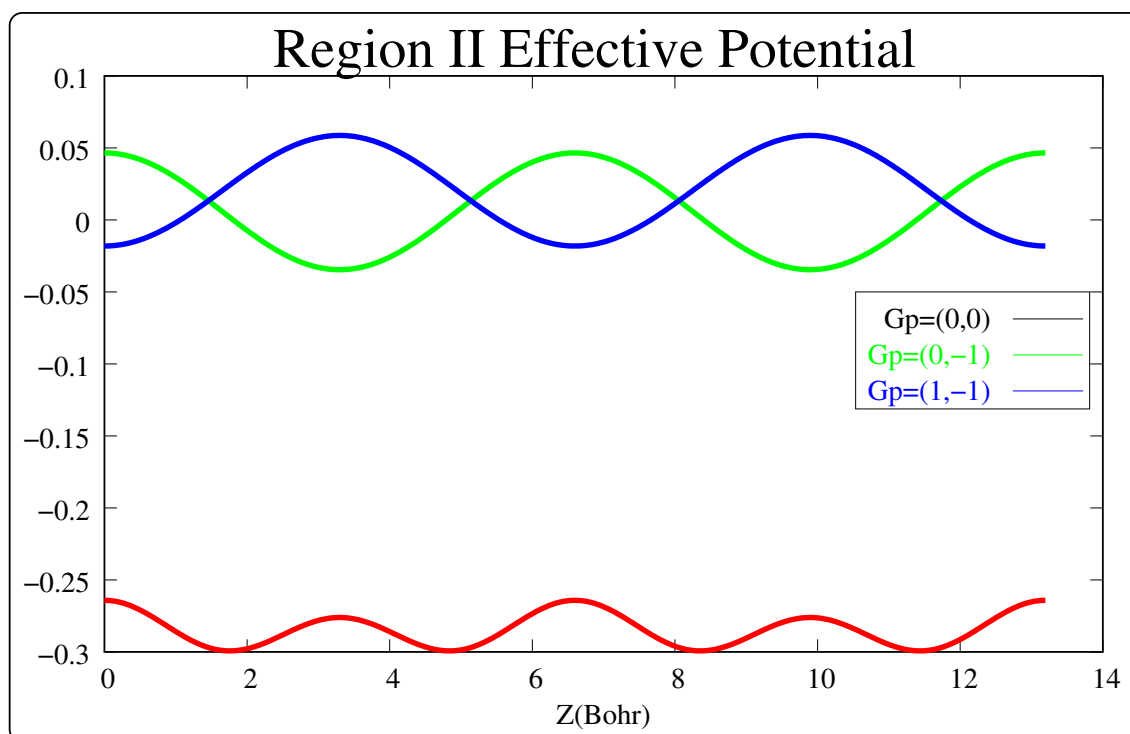


Figure 5.3: Region II effective potential used for Li in bcc structure

Figure (5.7) demonstrates that many different integrating schemes can be used to solve the intermediate wavefunctions. In particular, it shows the result of Predictor-Corrector and Green's function methods for lithium surface in bcc structure for different integrating step size. As can be seen, the results for different integration algorithms agree better for small step size than for larger step sizes.

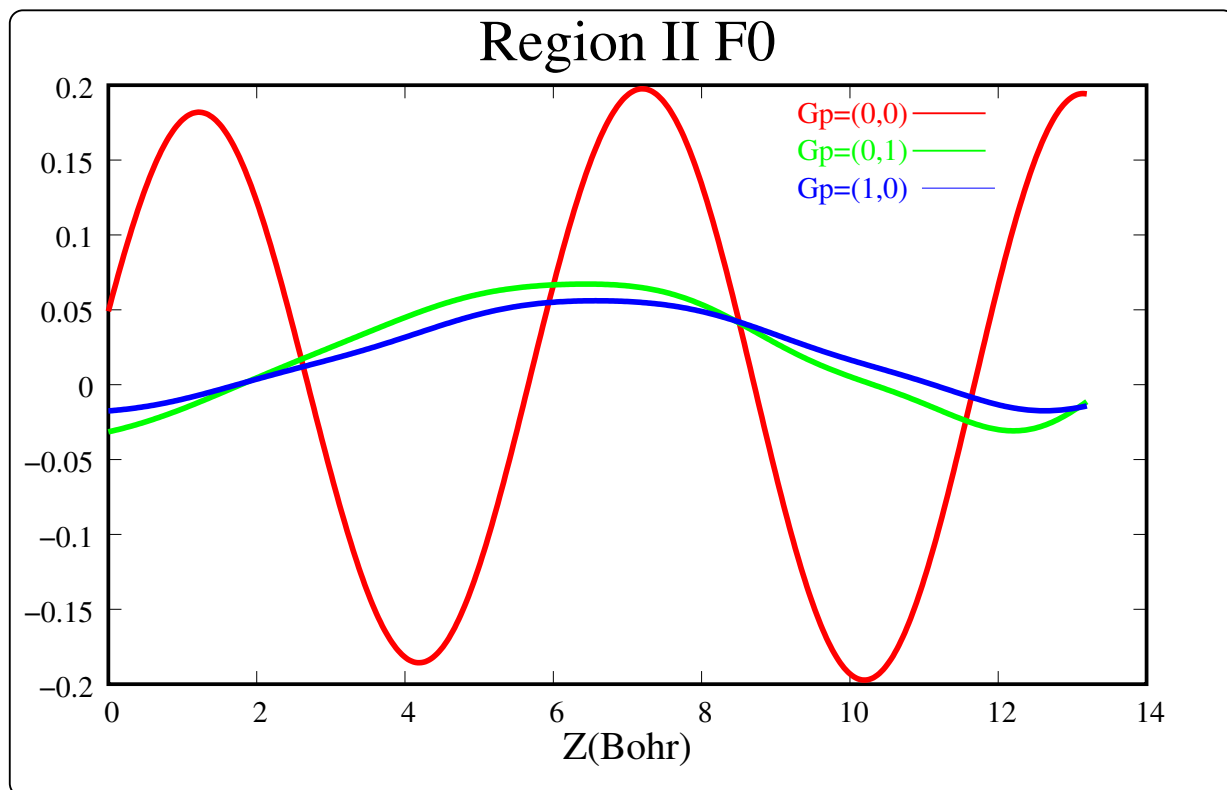


Figure 5.4: Region II  $f_0$  solutions for Li in bcc structure using PC method

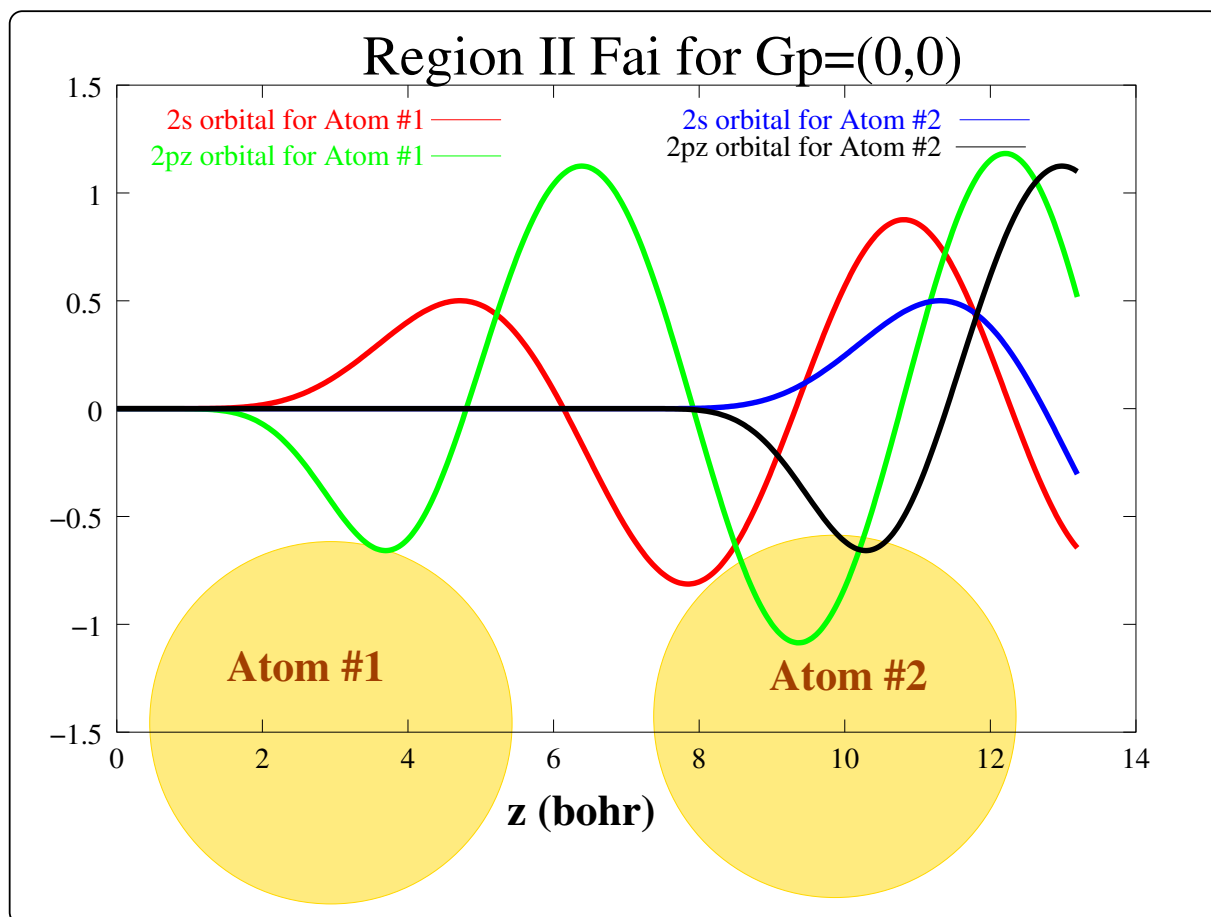


Figure 5.5: Region II  $f_{ai}$  solutions for Li in bcc structure using PC method



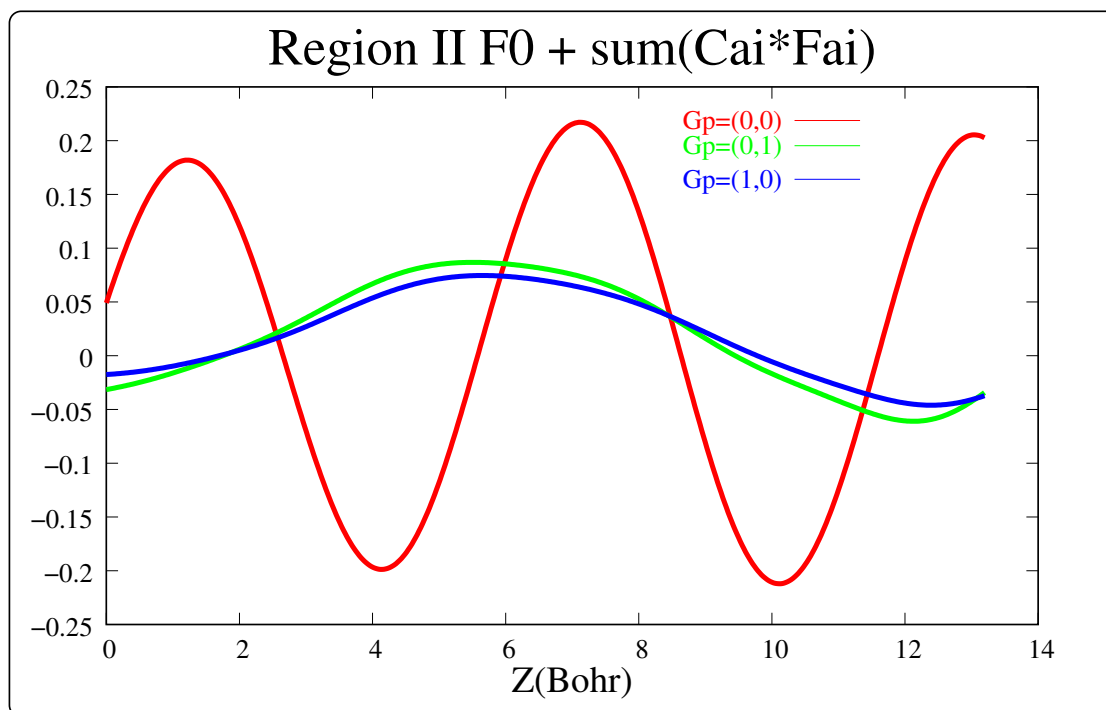


Figure 5.6: Region II  $f_0 + \sum_{ai} C_{ai} f^{ai}$  solutions for Li in bcc structure using PC method

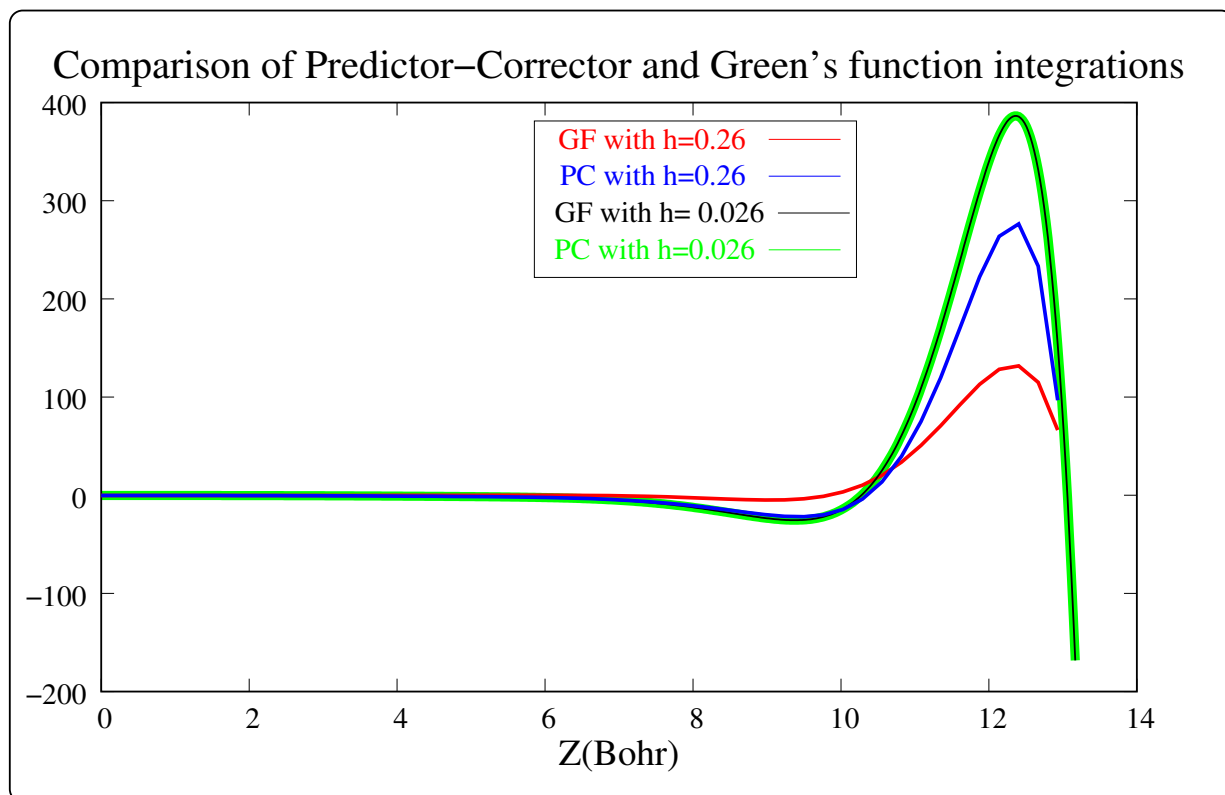


Figure 5.7: Region II  $f_0 + \sum_{ai} C_{ai} f^{ai}$  solutions for Li in bcc structure using PC and Greens function method

# Chapter 6

## User guide

### 6.1 How to run

The “SIPAW” (Semi-Infinite PAW) method is written in Fortran90/95. The main program is called `surfpwpaw`. It depends on PWPAW, GMRES, lapack, blas and fftw libraries. A general Makefile is available that needs only a modification to the library and compiler paths.

After a successful completion, we have a program called `surfpwpaw` and lets say that this binary is saved in the directory `/usr/local/bin`. To run it, give the following command:

```
/usr/local/bin/surfpwpaw bulkDia.paw surfDia.paw
```

Where `bulkDia.paw` and `surfDia.paw` are input filenames for the example described below.

#### 6.1.1 Bulk input

```
-----bulkDia.paw-----
#
# Input file for diamond
#

open Log      'diamond.log'      # Set output files
```

```
Open Error 'diamond.error'  
Open output 'diamond.out'
```

```
Max_AtomTypes 1  
MAX_Specific_Atoms 4
```

```
Max_TotalPsi 60  
MinPsi 40
```

```
Psi_Memory 200  
Proj_Memory 50  
Ylm_Memory 50  
Bloch_Memory 50
```

```
SuperCell          # Define the crystal  
  A (4.74097300545033813, 0.00000000000000000, 0.00000000000000000)  
  B (0.00000000000000000, 4.74097300545033813, 0.00000000000000000)  
  C (0.00000000000000000, 0.00000000000000000, 6.70474832315260166)
```

```
Include '444'  
Include 'diamondsurf.sym'  
  Gauss_Width 0.001  
  BZ_Method GAUSS  
End
```

```
PlaneWave_Cutoffs  
  Gcut_LOW 8  
  Gcut_HIGH 16  
End
```

```
Include '/physp2/natalie/pwpawpaper/atompaw_work/atompaw/C/VNC2/C.atomicdata'
```

```
AtomType_Occupancy C  
  Orbitals_Size 2  
  Valence_Orbitals 1 2  
  Valence_occupancy 1 3  
End
```

```
Atom_List Frac_Position  
  C1 C (-0.50000000000, -0.2500000000, -0.375)
```

```

C2 C      ( 0.000000000000,-0.2500000000,-0.125)
C3 C      ( 0.000000000000, 0.2500000000, 0.125)
C4 C      ( 0.500000000000, 0.2500000000, 0.375)
End

```

```

FORCES_ALWAYS_CALC_H
Mix_Veff
V_NewMix 1.0 0.2
Dij_NewMix 1.0 0.2
Mix_SecondValue 0.2
FORCES_ALWAYS_CALC_H
Store_Lowest_Energy 'diamond'
Set_Name Force_Name 'diamond.forces'
Set_Name Position_Archive_Name 'diamond.positions'

```

```
Initialize_System
```

```
Relax charge 30 1.0E-8
```

```
-----bulkDia.paw-----
```

The detailed instructions on what each keyword means for the bulk input is explained in reference [64]. The main difference is that, in the above case there is no “QUIT” keyword at the end. This keyword sends an exit signal to the main program and terminates the whole program before it processes the surface calculations. The other important keyword is also the “relax charge”. This generates a self-consistent electron wave function for the bulk unit cell. The bulk unit cell should be in surface geometry, that is,  $\mathbf{G}_1$  and  $\mathbf{G}_2$  should be in the  $x - y$  plane while  $\mathbf{G}_3$  should be in the  $z$ -direction.

### 6.1.2 Surface input

```

-----surfDia.paw-----
Solution_method GMRES
Surf_mode AppelbaumBound
Slabinput /physp2/natalie/surface_project/diamond001/SL/4again/Dia8l.ham
RegionIIIsolver Predictor_Corrector
ZSTEP 0.0694071 # it is in bohr scale (not in A)

```

```

NOZSTEPS 211 10 # for region II III
LAMBDA 2.0
ZZERO 0.0000000 # 3.3523748 #we used a/2 = 6.7047496/2
INTERFACEATOMS 4 #a=3.548A= 6.70474832315260165750 bohr
  iC1 C C1 -2.370486502725169 -1.185243251362584 4.190467701970376
  iC2 C C2 0.0000000000000000 -1.185243251362584 5.866654782758526
  iC3 C C3 0.0000000000000000 1.185243251362584 0.838093540394075
  iC4 C C4 2.370486502725169 1.185243251362584 2.514280621182225
END

```

```

MGMRES 1000
iterGMRES 90000
auxiterGMRES 20000
tolGMRES 1.e-5
toldelta 2.e-3
matchpts 120
R3SMALL 1.e-11

```

```
SETINTERFACEPARAMS
```

```
TEST_WAVEGMRES
Quit
```

```
-----surfDia.paw-----
```

The keywords and their default values for this file are as follows. (Note: the keywords are not case sensitive.)

```

INTERFACEATOMS integer:: nodefault

INTERFACEATOMS Specific_atoms_2d
  Name1 Type1 BulkName1 (x1,y1,z1) !Given in Cartesian coordinates
  Name2 Type2 BulkName2 (x2,y2,z2) !and in bohr unit
  .. .. ..
  NameN TypeN BulkNameN (xN,yN,zN)
END

```

Where Name is any specific name for that atom, Type is the type of the atom. It is the atomic symbol from the periodic table. BulkName is the symbolic name given

for that atom in the bulk input file.

```

SURF_MODE          character :: Plan3Bound
  APPELBAUMBOUND
  PLAN3BOUND       Alternative plan I
  PLAN4BOUND       Alternative plan II
  PLAN6BOUND       Alternative plan III
  PLAN8            Alternative plan IV

```

This defines what type of boundary condition at the region I and II interface the user wants to use. All the different methods are explained in previous Chapter.

```

SOLUTION_METHOD   real::      (GMRES)
  GMRES
  LAPACK

```

The solution method applies for the initial value formalism. GMRES is the best to use for practical purpose. The LAPACK option should be used only for small systems as it needs a huge memory.

```

REGIONIIISOLVER   real :: (PREDICTOR_CORRECTOR)
  PREDICTOR_CORRECTOR
  NUMEROV

```

Region III can be solved using two different methods. From our experience the two methods give very close accuracy and performance.

```

ZSTEP            real::      (0.0)
  The spacing between each grid points along
  the z-direction in bohr unit.
NOZSTEPS         real::      (0.0) (0.0)
  It is the number of grid points along the z-direction.
  It takes two arguments. The first one is the number of
  on the interface region and the second one is for the vacuum region.

```

```

LAMBDA           Real::      (no def)
  Damping parameter for initial potential. It is used to change the
  shape of the initial potential at the region II-III interface.

```

SLABINPUT Character:: filename  
 If this is defined, it resets the initial potential for region II-III region by the potential given in file ‘filename’. Usually this potential can be generated from a slab calculation with the same surface geometry as the used wants to simulate in the semi-infinite method.

ZZERO real :: (0.0)  
 Location of bulk-interface plane (z<sub>1</sub>) relative to the origin of bulk cell coordinates.

MGMRES integer (0)  
 restart parameter for GMRES calculation

ITERGMRES integer (0)  
 iterations for each GMRES calculation

AUXITERGMRES integer :: (0)  
 iterations for each auxiliary GMRES calculation

MATCHPTS integer :: (5)  
 number of Plan6 matching pts for Delta

TOLGMRES real :: (1.e-5)  
 tolerance parameter for each GMRES calculation

TOLDELTA real :: (1.e-3)  
 tolerance for iteration phiR

R3SMALL real :: (1.e-6)  
 SVD cut-off used in region three wave function calculation.

SETINTERFACEPARAMS character:: ()  
 a keyword to call the subroutine Set\_Interface\_Params to setup most of the bulk parameters like converting the three dimensional G-points to 2-dimensional G-point sets, bulk density, bulk potential, boundary atoms etc.

INT\_SCRP character :: ()  
 For debugging the 2D-projectors (scrptP)

TEST\_WAVEGMRES character :: ()  
 a keyword to call most of the surface calculation routines. It is kind of the driver program.



## 6.2 Smear plot

To generate the smear diagram, one needs to relax the electron wave functions using similar input as above. Once it converged and the PWPAW program terminated, we need to run the program again but this time instead of “relax charge”, we use “load\_solution” keyword followed by the wave function file name.

```
-----
Load_solution 'CdSe.wfn'
```

```
Set_Eigenmax 0.8
```

```
Calculate Surface_Bands CdSeX 40 1.E-5
-----
```

CdSeX is the input file that contains the k-vector coordinates of the Brillouin zone.

```
-----begin CdSeX-----
0. 0. 1. 20      # Kp vector and n of k perpendicular
      98          # maximum number of bands per k-point
0   0   0        # Gamma point
0.1 0.0 0.0
0.2 0.0 0.0
0.3 0.0 0.0
0.4 0.0 0.0
0.5 0.0 0.0     # XP point
0.5 0.1 0.0
0.5 0.2 0.0
0.5 0.3 0.0
0.5 0.4 0.0
0.5 0.5 0.0     #M
0.4 0.5 0.0
0.3 0.5 0.0
0.2 0.5 0.0
0.1 0.5 0.0
0.0 0.5 0.0     #X
0.0 0.4 0.0
0.0 0.3 0.0
0.0 0.2 0.0
0.0 0.1 0.0
-----end CdSeX-----
```

The first line sets the magnitude of  $\delta\mathbf{k}_\perp = \frac{|\mathbf{G}_\perp|}{n}$ .

Once the pwpaw code finished running, it will produce an output file CdSeX.surfband. CdSeX.surfband contains five columns data. These are,  $k_x, k_y, k_z, E_{min}$  and  $E_{max}$ . Smearplot2000 an IDL program is then used to generate a postscript smear plot diagram. The source code for the smearplot2000 is given in Appendix (B.3).

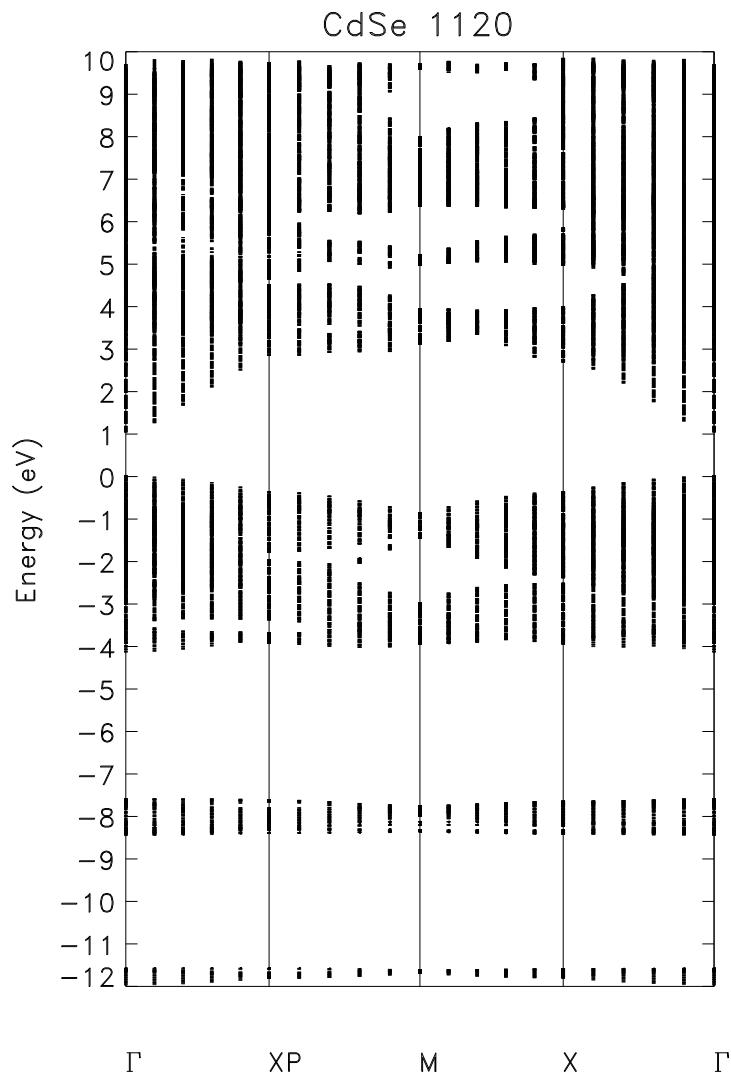


Figure 6.1: Smear diagram of CdSe  $11\bar{2}0$

The Brillouin zone for the wurzite structure used to calculate Figure 6.1 is shown in Figure 6.2.

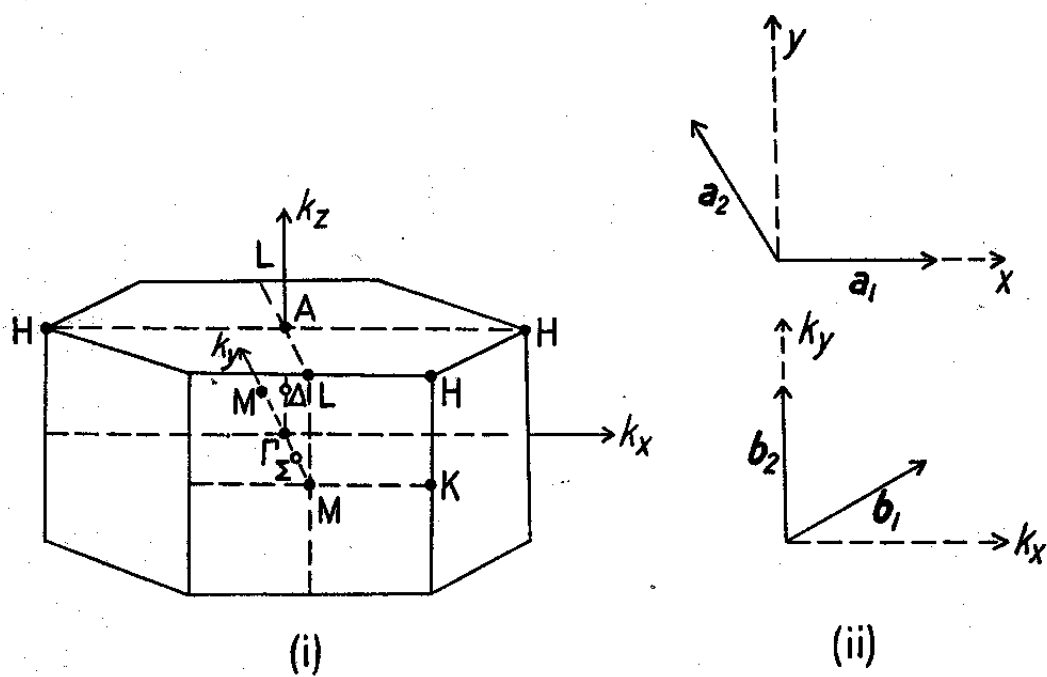


Figure 6.2: Diagram of the Brillouin zones for CdSe  $(11\bar{2}0)$ [30]

Similarly the smear plot for diamond (001) is shown in Figure (6.3) and its corresponding Brillouin zone in Figure (6.4)[53].

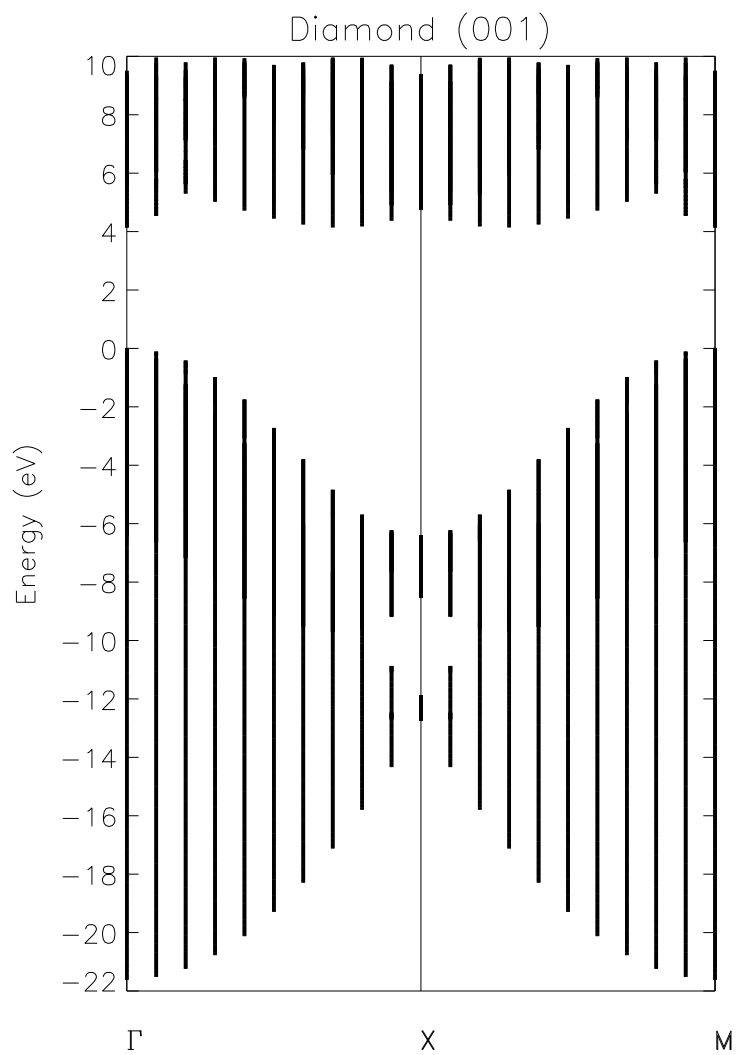


Figure 6.3: Smear diagram for diamond (001)[53]

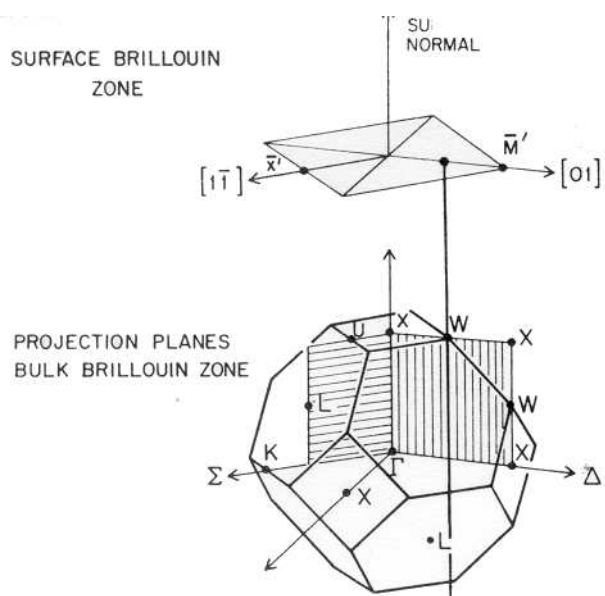


Figure 6.4: Diagram of the Brillouin zones for diamond (001)

## Chapter 7

# Concluding Remarks and Future Work

This project explored ways to understand surface defect states using different experimental and theoretical methods. Experimentally, we have used photoelectron spectroscopy measurements to study the surface states of a CdSe (11 $\bar{2}$ 0) crystal. By using specific crystal properties, such as band gap and photo threshold, we are able to identify and label all the important band edges for our crystal. Auger electron spectroscopy and low-energy electron diffraction methods were also used to characterize our crystal. By damaging the crystal using Argon sputtering and a 2 KeV electron beam from Auger electron spectroscopy, we were able to observe the production of surface defect states.

Theoretically, we have developed a semi-infinite method based on projector augmented wave formalism. We investigated the different numerical problems associated with modelling surface defects. Specially, we show the advantage and disadvantage of an “initial value” formalism versus a “boundary value” formalism of the numerical problem. In the “initial value” formalism, we use information from the bulk wave functions to integrate the differential equations toward the surface. In the “boundary value” formalism, both information from the bulk wave functions and from the physical solutions in the vacuum region are used to set up a full set of linear equations. These equations are conveniently solved using the GMRES algorithm.

Computationally, we have built the foundations for a modern modular FORTRAN90/95 compliant robust package that can use all of the different methods discussed in previous chapters. The code uses keywords to select different options. Since it is modular, it is very simple to extend it to include any new idea of solving the intermediate wavefunction. It is specially designed to interface well with the existing PWPAW code for the bulk calculation. One does not need to run two different codes explicitly; it is done automatically. At the time of this writing, the program is only 4.6MB in size. For diamond (001) with 16 layers of interface region, the run time size was about 340MB which is not too large for modern systems.

For the future, we are in a process of implementing the “generalized Bloch” method that accounts for the degenerate reflected Bloch waves. We think that this will solve most of the shortcomings of the other methods. There is a high hope that the next versions of the code will have some kind of parallel implementation. Specially the projector and wavefunction dot products can be calculated in parallel very easily as each of them are independent.

Good software packages are not good enough if it is not easy for the end user to use it. We are taking the necessary steps to implement a graphical user interface with built in input error checking. The first version will be implemented using ITCL [incr tcl] object oriented language based on tcl. The main reason we choose ITCL is that it is portable across many platform and operating systems. Our ideal vision is to use this interface to set-up the necessary input parameters, and using an ssh or any other method to submit a job to a remote cluster. In addition to this, it could have result visualization modules for monitoring an output of a running or terminated job. A proto type of this interface is shown in Figures (7.1) and (7.2).

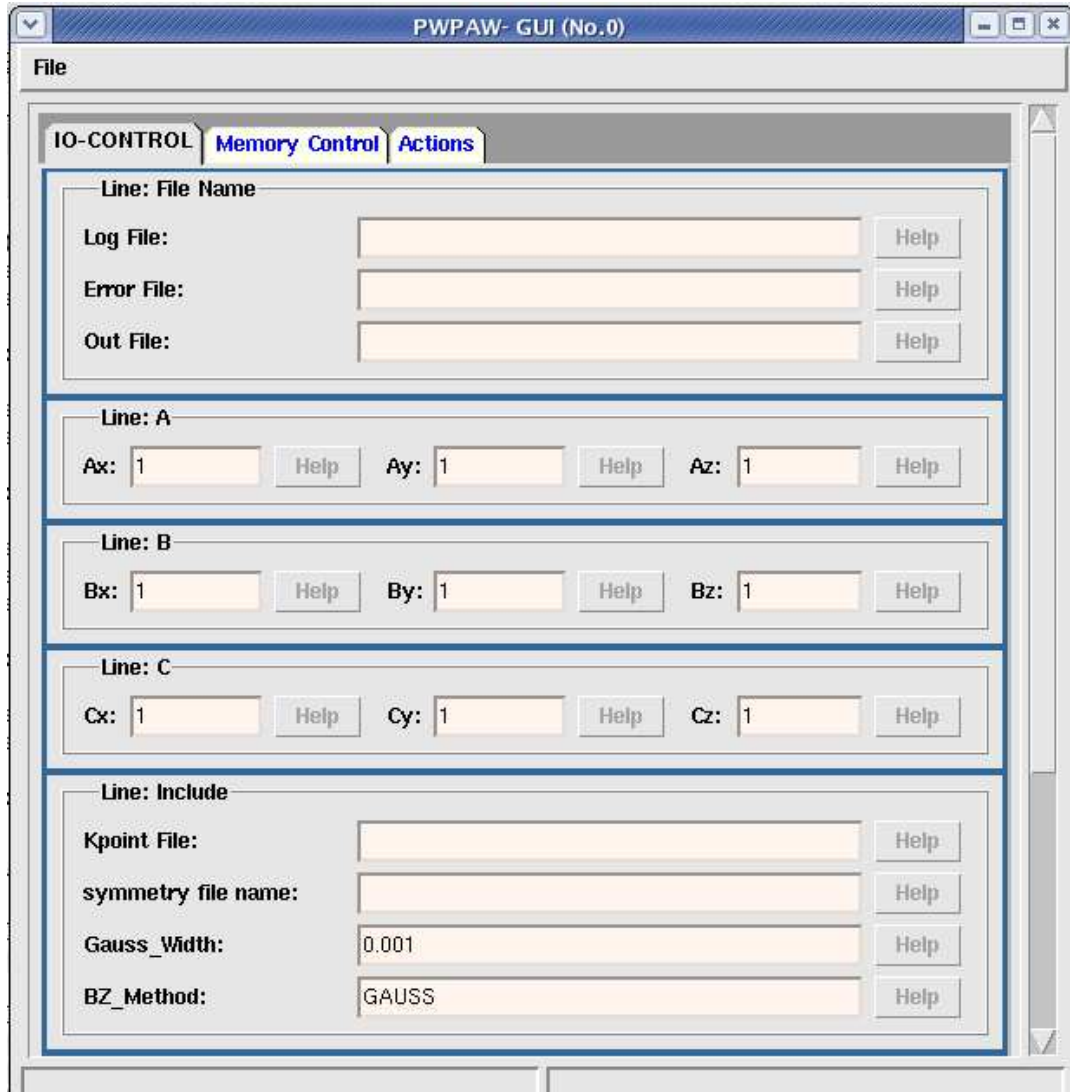


Figure 7.1: A Graphical User Interface showing the input output control tab for PWWAW/SIPAW



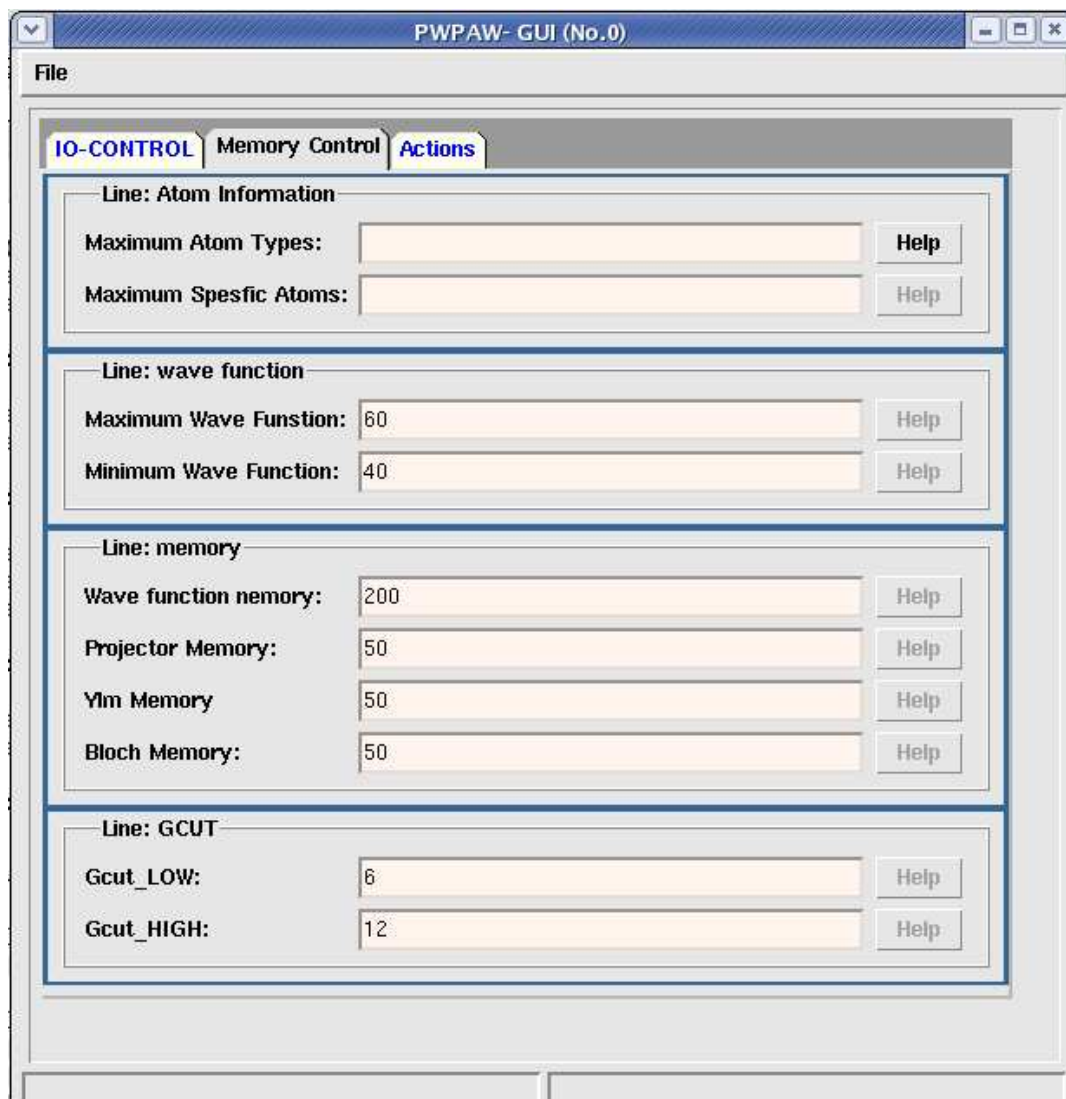


Figure 7.2: A Graphical User Interface showing the memory control tab for PW-PAW/SIPAW

# Bibliography

- [1] Yonas B. Abraham, N. A. W. Holzwarth, R. T. Williams, G. Eric. Matthews, and Alan R. Tackett. The electronic structure of oxygen related defects in  $\text{PbWO}_4$  and  $\text{CaMoO}_4$  crystals. *Physical Review B*, 64:245109, 2001.
- [2] Yonas Beyene Abraham. Optimization with surrogates for electronic-structure calculations. Master's thesis, Wake Forest university, 2004.
- [3] J. A. Appelbaum and D. R. Hamann. Self-consistent electronic structure of solid surfaces. *Phys. Rev. B*, 6:2166–2177, 1972.
- [4] Joel A. Appelbaum and D. R. Hamann. The electronic structure of solid surfaces. *Review of Modern Physics*, 48:479–496, 1976.
- [5] P. Atkins. *Molecular Quantum Mechanics*. Oxford University Press, 1983.
- [6] G. B. Bachelet, D. R. Hamann, and M. Schlter. Pseudopotentials that work: From H to Pu. *Phys. Rev. B*, 26:4199, 1982.
- [7] P. E. Blöchl. Projector augmented-wave method. *Phys. Rev. B*, 50:17953–17979, 1994.
- [8] Hyoung Joon Choi and Jisoon Ihm. Ab initio pseudopotential method for the calculation of conductance in quantum wires. *Phys. Rev. B*, 59(3):2267–2275, 1999.
- [9] M. F. Chung and H. E. Farnsworth. Investigations of surface stability of II-VI wurtzite compounds by LEED. *Surface Science*, 22:93–110, 1970.

- [10] M. L. Cohen and J. C. Chelikowsky. *Electronic Structure and Optical Properties of Semiconductors*. Springer-Verlag, 1989.
- [11] P. Czoschke, Hawoong Hong, L. Basile, and T.-C. Chiang. Quantum oscillations in the layer structure of thin metal films. *Phys. Rev. Lett.*, page 226801, 2003.
- [12] Lawrence E. Davis, 1978. *HandBook of Auger Electron Spectroscopy*.
- [13] Robert Eisberg and Robert Resnick. *Quantum Physics of Atoms, Molecules, Solids, Nuclei, and Particles*. John Wiley and Sons, New York, NY, 2nd edition, 1985.
- [14] Mark Embree. The tortoise and the hare restart GMRES. *SIAM Review*, 45(2):259–266, 2003.
- [15] F.B.Hildebrand. *Introduction to Numerical Analysis*. McGraw-Hill, second edition edition, 1956.
- [16] Ron Fleming. Auger electron spectrometry theory tutorial. on line at <http://www.cea.com>.
- [17] Valérie Frayssé, Luc Giraud, and Serge Gratton ande Julien Langou. A set of GMRES routines for real and complex arithmetics on high performance computers. Technical Report TR/PS/03/3, CERFACS technical Report, 2003.
- [18] V. Frayss, L. Giraud, S. Gratton, and J. Langou. A set of GMRES routines for real and complex arithmetics on high performance computers. Technical report, CERFACS Technical Report TR/PA/03/3, public domain software available on [www.cerfacs/algor/Softs](http://www.cerfacs/algor/Softs), 2003.
- [19] D. R. Hamann, M. Schlüter, and C. Chiang. Norm-conserving pseudopotentials. *Phys. Rev. Lett.*, 43:1494–1497, 1979.
- [20] D. R. Hartree. The wave mechanics of an atom with non-coulmbic central field: parts i, ii, and iii. *Proc. Cambridge Philos. Soc.*, 24:89, 1928.

- [21] D.R. Hartree. *Numerical Analysis*. Oxford University Press, second edition edition, 1958.
- [22] P. Hohenberg and W. Kohn. Inhomogeneous electron gas. *Physical Review*, 136:B864–B871, 1964.
- [23] N. A. W. Holzwarth, J. A. Chervenak, C. J. Kimmer, and Y. Zeng. multilayer-relaxation geometry and electronic structure of a W(111) surface. *Phys. Rev. B*, 48:12136–12145, 1993.
- [24] N. A. W. Holzwarth and M. J. G. Lee. Surface electronic wave functions of a semi-infinite muffin-tin lattice. I. The spherical-wave method. *Phys. Rev. B*, 18:5350–5364, 1978.
- [25] N. A. W. Holzwarth, G. E. Matthews, R. B. Dunning, A. R. Tackett, and Y. Zeng. Comparison of the projector augmented wave, pseudopotential, and linearized augmented plane wave formalisms for density functional calculations of solids. *Phys. Rev. B*, 55:2005–2017, 1997.
- [26] N. A. W. Holzwarth, G. E. Matthews, A. R. Tackett, and R. B. Dunning. Orthogonal polynomial projectors for the projector-augmented-wave (paw) method of electronic-structure calculations. *Phys. Rev. B*, 57:11827–11830, 1998.
- [27] N. A. W. Holzwarth, A. R. Tackett, and G. E. Matthews. A Projector Augmented Wave (PAW) code for electronic structure calculations, Part I: *atom-paw* for generating atom-centered functions. *Computer Physics Communications*, 135:329–347, 2001. Available from the website <http://pwpaw.wfu.edu>.
- [28] D. W. Jepsen, P. M. Marcus, and F. Jona. Low-energy-electron-diffraction spectra from [001] surfaces of face-centered cubic metals: Theory and experiment. *Phys. Rev. B*, 5:3933–3951, 1972.
- [29] J. D. Joannopoulos, Th. Starkloff, and Marc Kastner. Theory of pressure dependence of the density of states and reflectivity of selenium. *Phys. Rev. Lett.*, 38:660–663, 1977.

- [30] H Jones. *The theory of Brillouin zones and electronic states in crystals*. American Elsevier, 1975.
- [31] W. Kohn and L. J. Sham. Self-consistent equations including exchange and correlation effects. *Physical Review*, 140:A1133–A1138, 1965.
- [32] P. Kruger and J. Pollmann. Scattering-theoretical method for semiconductor surfaces: Self-consistent formulation and application to si(001)-(2 × 1). *Physical Review B*, 38(15):10578–10599, November 1988.
- [33] P. Krüger and J. Pollmann. Self-consistent surface electronic structure for semi-infinite semiconductors from scattering theory. *Physica B*, 172:155–166, 1991.
- [34] N. D. Lang and W. Kohn. Theory of metal surface: Charge density and surface energy. *Phys. Rev. B*, 1(12):4555–4568, june 1970.
- [35] N. D. Lang and W. Kohn. Theory of metal surfaces: Charge density and surface energy. *Phys. Rev. B*, 1:4555–4568, 1970.
- [36] N. D. Lang and W. Kohn. Theory of metal surfaces: work function. *Phys. Rev. B*, 3:1871–1223, 1971.
- [37] N. D. Lang and A. R. Williams. Self-consistent theory of the chemisorption of H, Li, and O on a metal surface. *Phys. Rev. Lett.*, 34:531–534, 1975.
- [38] N. D. Lang and A. R. Williams. Theory of atomic chemisorption on simple metals. *Phys. Rev. B*, 18:616–636, 1978.
- [39] M. Leblans. Program written by Marc Leblans.
- [40] M. Leblans, R.K.R. Thoma, J.L. LoPresti, M. Reichling, and R.T. Williams. Femtosecond time-resolved photoelectron spectroscopy of annealed and sputtered GaP (110), ZnTe (110) and ZnSe (110). *Materials science forum*, 239-241:159–162, 1997.

- [41] M. J. G. Lee and N. A. W. Holzwarth. Surface electronic wave functions of a semi-infinite muffin-tin lattice. II. Application to Cu (001) and (110). *Phys. Rev. B*, 18:5365–5368, 1978.
- [42] I.N Levine. *Quantum Chemistry*. Allyn and Bacon, 1983.
- [43] Janice L. Lopresti. *Picosecond and subpicosecond photoelectron spectroscopy of laser excited ZnTe, ZnSe, GaN and GaP*. Experimental Ph.D dissertation, Wake Forest University, 1998.
- [44] K. O. Magnusson and S. A. Flodström. Valence- and conduction-band electronic structure of wurtzite CdSe. *Phys. Rev. B*, 35(5):2556–2559, 1987.
- [45] K. O. Magnusson, U. O. Karlsson, D. Straub, S. A. Flodström, and F. J. Himpsel. Angle-resolved inverse photoelectron spectroscopy studies of CdTe(110), CdS(11 $\bar{2}$ 0), and CdSe(11 $\bar{2}$ 0). *Phys. Rev. B*, 36(12):6566–6573, 1987.
- [46] J.S. Nelson, s.j. Plimpton, and M.P. Sears. Plane-wave electronic-structure calculations on a parallel supercomputer. *Phys. Rev. B*, 47(4):1765–1774, 1993.
- [47] T. Oguchi and T. Sasaki. Density-functional molecular-dynamics method. *Prog. Theo. Phys. Suppl.*, 103:93, 1991.
- [48] Encyclopædia Britannica Online. Orbital, 2004.
- [49] R.G. Parr and W. Yang. *Density-Functional Theory of Atoms and Molecules*. Oxford University Press, 1989.
- [50] M. C. Payne, M. P. Teter, D. C. Allen, T. A. Arias, and J. D. Joannopoulos. Iterative minimization techniques for abinitio total-energy calculations - molecular-dynamics and conjugate gradients. *Rev. Mod. Phys.*, 64:1045, 1992.
- [51] J. B. Pendry. *Low Energy Electron Diffraction*. Academic Press, 1974.
- [52] John P. Perdew and Yue Wang. Accurate and simple analytic representation of the electron-gas correlation energy. *Phys. Rev. B*, 45:13244–13249, 1992.

- [53] E. W. Plummer and W. Eberhardt. Angle-resolved photoemission as a tool for the study of surfaces. In I. Prigogine and S. A. Rice, editors, *Advances in Chemical Physics*, volume 49, pages 533–657. John Wiley and Sons, 1982.
- [54] J. Pollmann, P. Krüger, M. Rohlfing, M. Sabisch, and D. Vogel. Ab initio calculations of structural and electronic properties of prototype surfaces of group IV, III-V, and II-VI semiconductors. *Applied Surface Science*, 104/105:1–16, 1996.
- [55] Johannes Pollmann and Peter Krüger. Green functions in the theory of semiconductor surfaces. *Progress in surface science*, 2003. On line version: doi:10.1016/j.progsurf.2003.08.021.
- [56] Antonio Redondo, III William A. Goddard, and T. C. McGill. Ab initio effective potentials for silicon. *Phys. Rev. B*, 15:5038–5048, 1977.
- [57] Mark W. Rowe. *Picosecond Time-Resolved Photoelectron Spectroscopy of Si (111)  $7 \times 7$ , Si(111):B  $\sqrt{3} \times \sqrt{3}$  R30°, Si(100)  $2 \times 1$ , and Si(111)  $1 \times 1$* . PhD thesis, Wake Forest University. Dept. of Physics., 1991.
- [58] Mark W. Rowe, H.L. Liu, G.P. Williams, and R.T. Williams. Picosecond photoelectron-spectroscopy of excited-states at Si(111)  $\sqrt{3} \times \sqrt{3}$  r30°-B, Si(111) $7 \times 7$ , Si(100)  $2 \times 1$ , and laser-annealed Si(111)  $1 \times 1$  surfaces. *Phys. Rev. B*, 47(4):2048–2064, 1993.
- [59] Y. Saad and M. Schultz. GMRES: A generalized minimal residual algorithm for solving nonsymmetric linear systems. *SIAM J. Sci. Stat. Comput.*, 7:856–869, 1986.
- [60] J.C. Slater. *Quantum Theory of Matter*. McGraw-Hill, 1968.
- [61] T. Starkloff and J.D. Joannopoulos. Local pseudopotential theory for transition metals. *Phys. Rev. B*, 16:5212–5215, 1977.
- [62] M. D. Stiles and D. R. Hamann. Ballistic electron transmission through interfaces. *Phys. Rev. B*, 38:2021–2037, 1988.

- [63] M. D. Stiles and D. R. Hamann. Electron transmission through NiSi<sub>2</sub>-Si interfaces. *Phys. Rev. B*, 40:1349–1352, 1989.
- [64] A. R. Tackett, N. A. W. Holzwarth, and G. E. Matthews. A Projector Augmented Wave (PAW) code for electronic structure calculations, Part II: *pwpaw* for periodic solids in a plane wave basis. *Computer Physics Communications*, 135:348–376, 2001. Available from the website <http://pwpaw.wfu.edu>.
- [65] E.D. Thoma. *Subpicosecond time-resolved absorption spectroscopy of alkali halide crystals / by Eben D. Thoma*. PhD thesis, Wake Forest University. Dept. of Physics., 1997.
- [66] R. K. R. Thoma. *Laser photo electron spectroscopy of defect states in GaP(110) and Ki / by R.K.R. Thoma*. PhD thesis, Wake Forest University. Dept. of Physics., 1996.
- [67] I. Tütto and A. Zawadowski. Quantum theory of local perturbation of the charge-density wave by an impurity: Friedel oscillations. *Phys. Rev. B*, 32(4):2449–2470, 1985.
- [68] David Vanderbilt. Soft self-consistent pseudopotentials in a generalized eigenvalue formalism. *Phys. Rev. B*, 41:7892–7895, 1990.
- [69] Dirk Vogel, Peter Krüger, and Johannes Pollmann. Self-interaction and relaxation-corrected pseudopotentials for II-VI semiconductors. *Phys. Rev. B*, 54:5495–5511, 1996.
- [70] R.C. Weast. *CRC Handbook of Chemistry and Physics*. CRC press inc, 1980.
- [71] C. M. Wei and M. Y. Chou. Theory of quantum size effects in thin Pb(111) films. *Phys. Rev. B*, 66:233408, 2002.
- [72] Masashi Yamada, Jun'ichi Kanasaki, Noriaki Itoh, and Richard T. Williams. Low energy laser photoelectron study of defect states on cleaved Si(111)2 × 1 surfaces. *Surface Science*, 349:L107–L110, 1996.



- [73] Alex Zunger and Marvin L. Cohen. First-principles nonlocal-pseudopotential approach in the density-functional formalism. II. application to electronic and structural properties of solids. *Phys. Rev. B*, 20:4082–4108, 1979.

## Appendix A

Related publication by the author

## Electronic structure of oxygen-related defects in $\text{PbWO}_4$ and $\text{CaMoO}_4$ crystals

Yonas B. Abraham, N. A. W. Holzwarth,\* R. T. Williams, and G. Eric Matthews  
*Department of Physics, Wake Forest University, Winston-Salem, North Carolina 27109*

Alan R. Tackett

*Department of Physics and Astronomy, Vanderbilt University, Nashville, Tennessee 37235*

(Received 19 June 2001; published 4 December 2001)

Several types of defect structures in  $\text{PbWO}_4$  and  $\text{CaMoO}_4$  are studied within the framework of density functional theory. While  $\text{PbWO}_4$  is currently of greater technological interest, we were able to carry out more extensive calculations for  $\text{CaMoO}_4$ , including lattice relaxation, large simulation cells, and more complicated defects. The structural and chemical similarity of the two materials suggests that their defect properties may also be similar. The electronic structure of isolated oxygen vacancies, oxygen and Pb or Ca double vacancies, and substitutional Y are modeled using a supercell approximation. We find that the main effect of oxygen vacancies in  $\text{PbWO}_4$  and  $\text{CaMoO}_4$  is the introduction of states of W or Mo  $d$  character into the band gap. The energies of these defect states are very sensitive to their occupancy. An isolated O vacancy produces a doubly occupied defect state below the conduction band. Removing charge from this defect state lowers its energy and causes additional states of W or Mo  $d$  character to move into the band gap. Large supercell simulations for the Ca and O double vacancy in an unrelaxed or slightly relaxed structure produce an unstable electronic structure suggesting the possibility of more extensive lattice distortion. In addition, we also present preliminary results of simulations of interstitial oxygen atoms in  $\text{CaMoO}_4$ , finding a relatively stable configuration with the interstitial O forming a weak bond between two  $\text{MoO}_4$  clusters.

DOI: 10.1103/PhysRevB.64.245109

PACS number(s): 61.72.Ji, 71.15.Nc, 71.55.Ht, 71.70.Ch

### I. INTRODUCTION

Since the adoption of  $\text{PbWO}_4$  single crystals as part of the scintillation detector system for the Large Hadron Collider at CERN,<sup>1,2</sup> there has been considerable interest in identifying possible defect structures in  $\text{PbWO}_4$  and related crystals. These defects, which can affect the detector performance, may occur during crystal growth and also are likely to be produced by radiation during use. Lead tungstate and related materials have a long legacy of earlier work, some of which is described in Refs. 3–7. New possible applications of these materials have recently been reported, including Cherenkov radiation production,<sup>8</sup> high temperature ionic conductors,<sup>9</sup> and Raman lasers.<sup>10</sup>

There is a large literature of experimental work directed at identifying several types of defects in  $\text{PbWO}_4$  (Ref. 11) and related materials. It is believed that Pb vacancies are often formed during the growth process. On the basis of x-ray and neutron diffraction, an ordered modification of  $\text{PbWO}_4$  has been identified in which 1 out of every 16 Pb atoms are missing.<sup>12</sup> It is apparently difficult to directly control the stoichiometric concentration of Pb. However, it has been found that during the growth process, the addition of materials that can be incorporated as trivalent positive ions such as Y or La at the missing Pb sites can improve the luminescence properties of the resultant crystals.<sup>13,14</sup> The direct observation of O vacancies is difficult, but spectroscopic studies of doped and annealed crystals indicate the presence of isolated oxygen vacancies and oxygen vacancies associated with cation vacancies.<sup>15–18</sup> In addition, studies of  $\text{PbWO}_4$  crystals annealed in an oxygen atmosphere suggest that interstitial oxygen can also contribute to the defect structures.<sup>16,17,19,20</sup>

The purpose of this paper is to survey the electronic struc-

tures of some models of defects in  $\text{PbWO}_4$  and  $\text{CaMoO}_4$  in order to understand their ground state stability and qualitative electronic signatures. The calculations were performed within the framework of density functional theory,<sup>21,22</sup> using a supercell approach. Since density functional theory gives us a variational approximation to the electronic ground state of our defect models, we are able to estimate their energetics and optimal geometries. In addition, from partial densities of states, we obtain qualitative spectroscopic information. For technical reasons, we are able to carry out a more thorough investigation of  $\text{CaMoO}_4$  than of  $\text{PbWO}_4$ . However, the structural and chemical similarity of the two materials suggests that their defect properties are likely to be similar.

Earlier electronic structure studies of perfect crystals of these materials<sup>23</sup> showed that states near the band gap are well described by a molecular orbital picture<sup>24</sup> of the anion group  $[\text{WO}_4]^{-2}$ . Here W (or Mo) is in an approximately tetrahedral site due to the four nearest neighbor oxygen ions and the group has a formal charge of  $-2$ . A simplified version of the molecular orbital diagram is presented in the left panel of Fig. 1, showing the occupied bands of mainly O  $p$  character well separated from the unoccupied bands of mainly W (or Mo)  $d$  character, split by the approximately tetrahedral crystal field and antibonding interactions into lower states of  $e$  symmetry and upper states of  $t_2$  symmetry. Band gap defects could therefore be produced by changes to this anion group such as changes to its charge, geometry, and/or atomic constituents. In addition, since their crystal structure is not closely packed, additional atoms can be introduced into the lattice of these materials, and some of these can introduce new states into the band gap region.

For the purposes of describing the defect configurations simulated in this study we adopt the following notation in

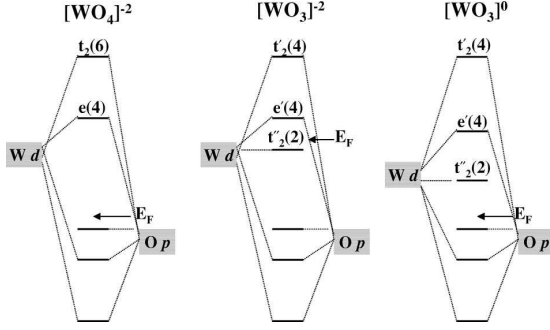


FIG. 1. Simplified molecular orbital diagram for states near band gap for  $[\text{WO}_4]^{-2}$  (left panel),  $[\text{WO}_3]^{-2}$  (middle panel), and  $[\text{WO}_3]^0$  (right panel). The numbers in parentheses represent the degeneracy (including spin) of the orbital; “ $\leftarrow E_F$ ” indicates the approximate location of the Fermi level. The  $[\text{WO}_4]^{-2}$  group is found in the perfect crystal, while the other complexes represent possible defect configurations.

order to identify both the defect stoichiometry and the group dominating the states in the band gap:

$$\{\text{added atoms/removed atoms}\}[\text{BO}_n]^q. \quad (1)$$

Here  $B$  represents the transition metal (only W or Mo in this study),  $n$  represents the number of coordinated O’s (only 3 or 4 in this study), and  $q$  represents the net formal charge associated with the  $\text{BO}_n$  group. As we shall show, a simplified, although useful model of some of these effects are shown in the middle and left panels of Fig. 1.

The outline of the paper is as follows. In Sec. II, we describe the computational details of our simulations. In order to study the effects of geometry optimization in the vicinity of the defect site and to simulate large supercells, we used the PWPAAW code<sup>25</sup> to study some model defects in  $\text{CaMoO}_4$ . In particular, the results of simulations of oxygen vacancies and interstitials, combined oxygen and Ca vacancies, and substitutional Y alone and in combination with O and Ca vacancies in  $\text{CaMoO}_4$  are reported in Sec. III A. In order to extend some of these findings to  $\text{PbWO}_4$ , we used the WIEN97 code<sup>26</sup> which has been implemented for treating relativistic effects that better describe the heavy elements of Pb and W. In Sec. III B, we report results from our study of oxygen vacancies and combined oxygen and Pb vacancies in  $\text{PbWO}_4$  simulated in an idealized geometry in a small supercell. Conclusions are given in Sec. IV, based on the comparison of the calculational results for  $\text{CaMoO}_4$  and  $\text{PbWO}_4$  and on the analysis of the more complete simulations for  $\text{CaMoO}_4$ .

## II. CALCULATIONAL METHODS

### A. Choice of supercells

The scheelite crystal structure is characterized by the body-centered tetragonal space group  $I4_1/a$ . In terms of the conventional unit cell parameters  $a$  and  $c$ , the following lattice vectors were used for the 2 formula unit simulations (“2x”).

TABLE I. Lattice constants used in the simulations.

Material	Ref.	$a$ (Å)	$c$ (Å)
$\text{CaMoO}_4$	27	5.222	11.425
$\text{PbWO}_4$	28	5.456	12.020

$$2 \text{ unit} \begin{cases} \mathbf{A}_2 = \frac{1}{2}(-a\hat{x} + a\hat{y} + c\hat{z}) \\ \mathbf{B}_2 = \frac{1}{2}(+a\hat{x} - a\hat{y} + c\hat{z}) \\ \mathbf{C}_2 = \frac{1}{2}(+a\hat{x} + a\hat{y} - c\hat{z}) \end{cases} \quad (2)$$

This is, in fact, the same unit cell as the perfect crystal. The nearest distance between defects is  $a$ .

For the 8 formula unit simulations (“8x”), the lattice vectors were given by

$$8 \text{ unit} \begin{cases} \mathbf{A}_8 = (a\hat{x} + a\hat{y}), \\ \mathbf{B}_8 = (a\hat{x} - a\hat{y}), \\ \mathbf{C}_8 = c\hat{z}. \end{cases} \quad (3)$$

The nearest distance between defects is  $\sqrt{2}a$ . Coincidentally, this 8 formula unit cell is the same unit cell recently analyzed<sup>12</sup> for the Pb deficient crystal having the stoichiometry  $\text{Pb}_{7.5}\text{W}_8\text{O}_{32}$ , with one of the Pb sites having  $\frac{1}{2}$  occupancy. For all of the simulations, the values of the lattice constants were taken from experiment and are listed in Table I.

### B. PAW calculations of $\text{CaMoO}_4$

In order to efficiently study the energetics and optimal geometry of the defects and to carry out simulations in large (8x) supercell, we used the PWPAAW code<sup>25,29</sup> based on the projector augmented wave (PAW) approach of Blöchl<sup>30</sup> to study the nonrelativistic material,  $\text{CaMoO}_4$ . The local density approximation (LDA) form of Perdew and Wang<sup>31</sup> was used to approximate the exchange-correlation interactions.

The first step of the PAW procedure is to produce the necessary projector and basis functions (analogous the construction of a pseudopotential function in a pseudopotential formalism). This is done using the ATOMPAAW code.<sup>32</sup> Since this material is both highly ionic and covalent, upper core electron states can be important for determining the self-consistent electronic structure. Specifically, we found it necessary to include projector and basis functions for the upper core states together with the valence states of Ca, Y, and Mo. The values of the local potential contributions  $\tilde{v}_{\text{loc}}^a(r)$  were constructed using the squared sinc shape function and aligned so that the pseudopotential basis functions corresponding to the valence  $s$  state of each atom are eigenstates of a purely local pseudo-Hamiltonian as described in Ref. 32. Table II lists the parameters used in this work. In this table, the notation  $\varepsilon$  indicates a continuum function, where the positive energy  $\varepsilon$  is chosen to ensure that the  $\phi_{\varepsilon}^a(r)$  basis

TABLE II. List of parameters used to construct basis and projector functions.

Atom	$Z^a$	$nl$ basis	$r_c^a$ (Bohr)
O	8	$2s, \varepsilon s, 2p, \varepsilon p$	1.4
Ca	20	$3s, 4s, 3p, \varepsilon p, 3d$	1.9
Y	39	$4s, 5s, 4p, \varepsilon p, 4d, \varepsilon d$	1.9
Mo	42	$4s, 5s, 4p, \varepsilon p, 4d, \varepsilon d$	1.9

function has the correct number of nodes in the augmentation region. For representing the valence  $l=1$  states of Ca, Y, and Mo, continuum basis functions  $\phi_{\varepsilon p}^a$  were used instead of the bound  $\phi_{4p}^a$  or  $\phi_{5p}^a$  functions which had nodes inconveniently close to the augmentation radii. For O, in addition to the valence  $\phi_{2s}^0$  and  $\phi_{2p}^0$  functions, continuum basis functions  $\phi_{\varepsilon s}^0$  and  $\phi_{\varepsilon p}^0$  were also used to ensure that the negative ion states would be well represented. In order to optimize the plane wave convergence, the augmentation radii  $r_c^a$  were chosen to be as large as possible without allowing the augmentation spheres to overlap. With this set of parameters, the reciprocal lattice cut off parameters could be taken to be 8 and 10 Bohr<sup>-1</sup> for the plane wave representations of the pseudowavefunctions  $\tilde{\Psi}_{n\mathbf{k}}$  and the pseudodensity  $\tilde{n}$ , respectively.

During the course of the project, several other parameter sets were used, yielding similar results and demonstrating the expected insensitivity of the calculation to these parameters. Both the  $2x$  and  $8x$  defect supercells were studied using the PWPW code. For the  $2x$  supercell, the Brillouin zone integrals were approximated by sampling 8  $\mathbf{k}$  points throughout the Brillouin zone. For the  $8x$  supercell, the Brillouin zone integrals were approximated sampling only the zone center.

The partial densities of states were evaluated using a Gaussian smearing function<sup>33</sup> in the following form:

$$N^a(E) = \frac{2}{\sqrt{\pi}\sigma} \sum_{n\mathbf{k}} C_{n\mathbf{k}}^a W_{\mathbf{k}} e^{-(E-E_{n\mathbf{k}})^2/\sigma^2}. \quad (4)$$

Here the factor of 2 comes from assuming that each distinct band is doubly occupied. The normalized Brillouin zone weight factors are denoted by  $W_{\mathbf{k}}$ . The band index is noted by  $n$ , and  $E_{n\mathbf{k}}$  denotes the band energy. The coefficient  $C_{n\mathbf{k}}^a$  represents the charge contained in a single sphere enclosing atom  $a$ , with radius taken to be the augmentation radius  $r_c^a$ , averaged over similar spheres. The Gaussian smearing parameter was taken to be  $\sigma=0.12$  eV.

For several of the defect systems studied, we were able to optimize the geometry of the atoms around the defect by moving the atoms within the supercell until the forces on them were smaller than a specified tolerance. In addition to obtaining the atomic positions of the optimized geometry, two energy measures could be determined. For each set of atomic positions  $\{\mathbf{R}^a\}$ , the PWPW program calculates the LDA cohesive energy  $E_{\text{coh}}(\{\mathbf{R}^a\})$ , defined to be the total electronic energy of the periodic system subtracted from the sum of the total electronic energies of the corresponding isolated spherical atoms. The ‘‘relaxation energy’’ measures the

energy gained by geometry optimization, relative to the initial atomic positions  $\{\mathbf{R}_0^a\}$ , which, except for the missing atoms, were taken from perfect crystal positions

$$\Delta E \equiv E_{\text{coh}}(\{\mathbf{R}^a\}) - E_{\text{coh}}(\{\mathbf{R}_0^a\}). \quad (5)$$

Also of interest, is an estimate of the formation energy for the defect, whose zero order approximation can be determined from the cohesive energy difference of the perfect and defective crystal simulations  $F^0 \equiv E_{\text{coh}}(\text{crystal}) - E_{\text{coh}}(\text{defect})$ . Two corrections must be considered. First, since our defects involve oxygen, the final or initial state of the system involves molecular oxygen whose dissociation energy can be taken from the experimental value  $D=5.08$  eV.<sup>34</sup> Second, since the spherical atom approximation underestimates the total energy of each atom, the cohesive energies are generally overestimated. For the systems we are considering, these errors are negligible or cancel except for the total energy of one of the O atoms. An approximate correction can be determined from spectroscopic data<sup>35,36</sup> which allows one to calculate the atomic ground state energy relative to the multiplet average which corresponds to the total energy calculated in the LDA results. For O, the multiplet correction energy can be estimated as  $\Delta E_{\text{mult}} \approx 0.94$  eV.<sup>36</sup> Therefore, the formation energies for *neutral* defects can be approximated as

$$F \approx F^0 \pm \left( \frac{1}{2} D + \Delta E_{\text{mult}} \right) \approx F^0 \pm 3.48 \text{ eV}, \quad (6)$$

where the plus or minus signs pertain to interstitial O or O vacancies, respectively.

### C. LAPW calculations of PbWO<sub>4</sub>

For modeling defects in PbWO<sub>4</sub>, where relativistic effects are important, we used the WIEN97 code<sup>26</sup> based on the linearized augmented plane wave (LAPW) (Ref. 37) approach using the local density approximation (LDA) form of Perdew and Wang,<sup>31</sup> as in the PWPW calculations. The calculational parameters were taken to be the same as those used in our previous perfect crystal studies.<sup>23</sup> The defect simulations were performed using the  $2x$  supercell only and the Brillouin zone integrals were approximated by sampling 27  $\mathbf{k}$  points throughout the Brillouin zone.<sup>38</sup> The partial densities of states were evaluated using Eq. (4), with the sphere radius chosen to be the muffin tin sphere radius.<sup>39</sup> The reason for switching codes for the PbWO<sub>4</sub> study is that relativistic effects, which have not yet been implemented in the PWPW code, are available in the WIEN97 code. In previous work,<sup>40,41</sup> we have shown that the PAW and LAPW methods produce essentially identical results for nonrelativistic calculations.

## III. RESULTS AND DISCUSSION

### A. Defects in CaMoO<sub>4</sub>

In order to study large simulation cells, atomic motions about the defect site, and more complicated defects, we carried out several calculations on CaMoO<sub>4</sub> which is structurally and chemically very similar to PbWO<sub>4</sub>. For these simu-

TABLE III. Geometry optimization results for ideal crystal and various defects in  $\text{CaMoO}_4$ . The experimental bond lengths and bond angles are quoted on the first line, in comparison with the calculated optimization results quoted on the second line. The remaining lines summarize the results of defect geometry optimizations using  $(2x)$  and  $(8x)$  supercells, listing the range of bond lengths and angles, the relaxation energies ( $\Delta E$ ) [Eq. (5)], and formation energies ( $F$ ) [Eq. (6)].

System	Case	Mo-O bond lengths ( $\text{\AA}$ )	Mo-O bond angles	$\Delta E$ (eV)	$F$ (eV)
Ideal crystal	Exp. <sup>a</sup>	1.77	$107^\circ, 114^\circ$		
Ideal crystal	Cal.	1.79	$107^\circ, 114^\circ$		
$\{O\}[\text{MoO}_3]^{-2}$	$2x$	1.79–1.83	$105^\circ\text{--}117^\circ$	0.2	7.1
$\{O\}[\text{MoO}_3]^{-2}$	$8x$	1.79–1.81	$106^\circ\text{--}115^\circ$	0.2	7.1
$\{\text{CaO}\}[\text{MoO}_3]^0$	$2x$	1.74–1.83	$103^\circ\text{--}117^\circ$	0.9	15.8
$\{O\}[\text{MoO}_4]^{-2}$	$2x$	1.79–1.84	$102^\circ\text{--}116^\circ$	2.1	0.4

<sup>a</sup>Experimental x-ray results from Ref. 27.

lations, the atomic positions of the perfect crystal were optimized, starting from the crystallographic results<sup>27</sup> finding the results listed in Table III. The calculated optimal Mo-O bond length is found to be slightly longer than the experimental value, as is typical of LDA calculations.<sup>42</sup> The calculated bond angles for Mo-O were found to be essentially identical to the experimental values. Table III also summarizes the geometry optimization results obtained for some of the defect simulations [using the notation defined in Eq. (1)] which are discussed in the following subsections.

### 1. O vacancy

The O vacancy ( $\{O\}[\text{MoO}_3]^{-2}$ ) was studied in both the  $2x$  and  $8x$  supercells. Table III summarizes the results of the geometry optimization. We see that the bond length and angular changes are similar but slightly larger for the  $2x$  supercell compared with that for the  $8x$  supercell. This is understandable since, in the latter case, the relaxation effects are spread over a larger number of sites. In both simulations, the relaxation effects are relatively small—the bond lengths increase by a few hundredths of an angstrom and the angles change by a few degrees, indicating that the  $[\text{MoO}_3]^{-2}$  complex is relatively stable and structurally similar to the  $[\text{MoO}_4]^{-2}$  complex from which it is derived. The calculated energy gained in optimizing the geometry was 0.2 eV and the formation energy for a neutral O vacancy was estimated using Eq. (6) to be 7.1 eV for both  $2x$  and  $8x$  simulations. The two simulations differed by less than 2% and 0.2% for the relaxation energies and formation energies respectively.

The partial densities of states for the  $2x$  and  $8x$  supercell simulations are compared with the partial densities of states of the perfect crystals in the top two panels of Figs. 2 and 3, respectively. The results for the two simulation cells look very similar to each other, with the main differences attributable to the effects of the different  $\mathbf{k}$ -point samplings of the supercell Brillouin zones. The bottom panel of Fig. 3 shows the partial densities of states for the unrelaxed geometry of the O vacancy in the  $8x$  supercell. Comparison

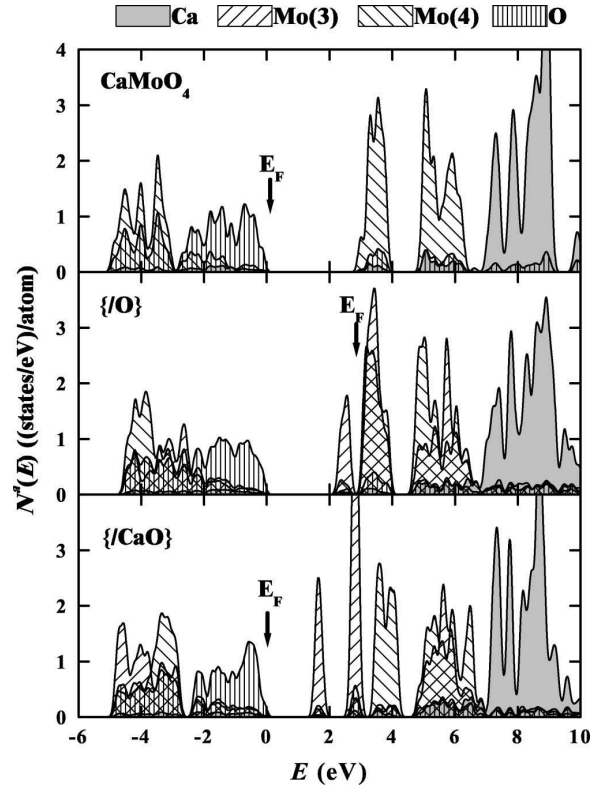


FIG. 2. Partial densities of states for  $2x$  simulation of  $\text{CaMoO}_4$ : perfect crystal (top panel), O vacancy (middle panel), and Ca and O double vacancy (bottom panel). Calculations were done with lattice relaxation. The zero of energy for each plot is adjusted so that the top of the oxygen bands line up with that of the perfect crystal. For the defect plots, the two types of W sites—the threefold coordinated “(3)” and the fourfold coordinated “(4)” are shaded differently. The Fermi level (“ $E_F$ ”) is indicated with an arrow in each plot.

of the two lower panels (with and without geometry optimization) shows that changes in the partial densities of states due to lattice relaxation around the oxygen vacancy are very small. Similarly small lattice relaxation effects were found for the  $2x$  simulation. These results suggest that the  $\{O\}[\text{MoO}_3]^{-2}$  defect in  $\text{CaMoO}_4$  is rather insensitive to small geometry changes and that its effects are spatially localized.

The partial density of states curves for the O vacancy show that an impurity state associated with the  $\text{MoO}_3$  group is introduced below the conduction band. This state is fully occupied because the O vacancy removes six oxygen  $p$  states from the valence band while removing only four valence electrons, leaving two extra electrons which can be accommodated by the  $\text{MoO}_3$  group—as described by the  $\{O\}[\text{MoO}_3]^{-2}$  notation.

In order to further characterize the defect state, it is helpful to examine the charge density contours. In Figs. 4 and 5, plots of charge density contours about the  $[\text{MoO}_3]^{-2}$  site in a plane which contains an Mo-O bond and the missing O site, are shown for the  $8x$  simulation. Figure 4 is a plot for

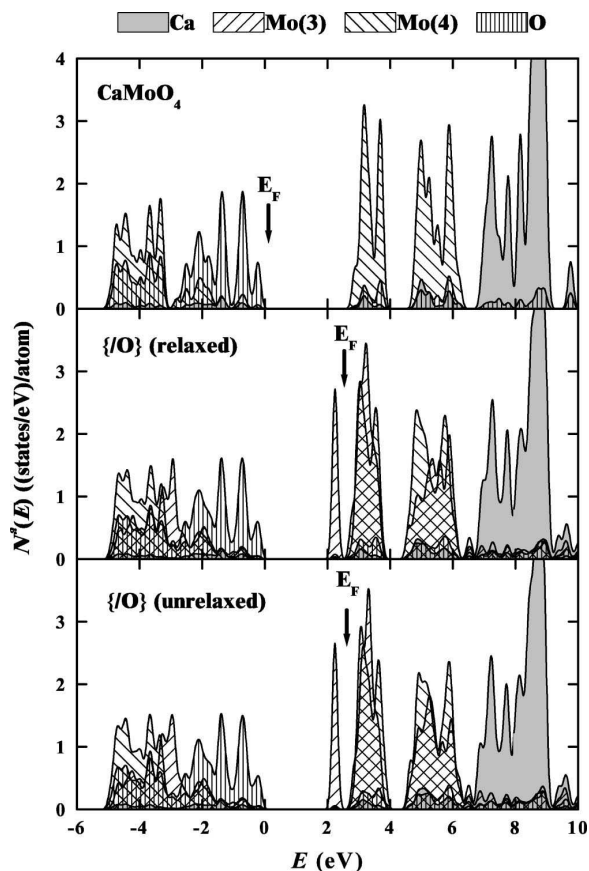


FIG. 3. Partial densities of states for 8x simulation  $\text{CaMoO}_4$ : perfect crystal (top panel) and O vacancy (middle panel), using the same notations as in Fig. 2. These calculations were done with lattice relaxation. For comparison, the bottom panel shows the partial density of states for the unrelaxed O vacancy.

the uppermost occupied defect state near 2.2 eV. These contours illustrate the shape of a distorted Mo 4d orbital which has appreciable density in the vicinity of the missing O and which we label “ $t_2''$ ,” for reasons discussed below. This picture is in marked contrast to that found for states associated with an oxygen vacancy in “simple” oxides such as MgO or CaO,<sup>43–45</sup> which is usually called an “F center.” For the F center, the electrons are confined by the electrostatic potential of the surrounding ions forming an *s*-like ground state,<sup>46</sup> while for the  $\{O\}[\text{MoO}_3]^{-2}$  defect, the electrons occupy a Mo 4d orbital which is lowered in energy by the crystal field of the remaining oxygen ions.

Figure 5 plots the charge density contours about the  $[\text{MoO}_3]^{-2}$  site for the unoccupied states: (a) showing the lower conduction band between the energies 2.5–4.0 eV and (b) showing the upper conduction band starting above 4.0 eV. Since the partial density of states peaks for these two groups of states show (middle panel of in Fig. 3) comparable contributions from both the threefold and fourfold Mo sites, it is not surprising that these two charge contour plots are similar to those of the perfect crystal,<sup>23</sup> where the lower con-

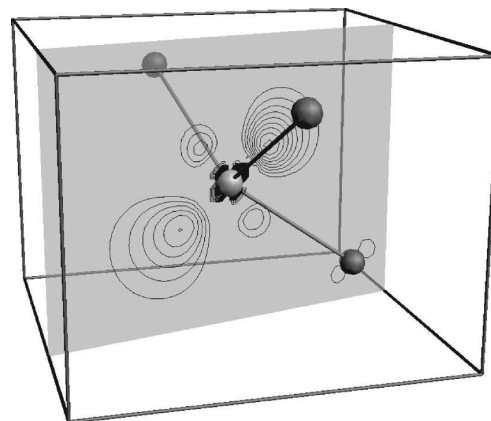


FIG. 4. Ball and stick model and contour plot for the 8x simulation of an O vacancy in  $\text{CaMoO}_4$  at the  $[\text{MoO}_3]^{-2}$  site. The plane on which the contours are drawn passes through the Mo atom, one of its nearest neighbor O atoms, and the plane of the O vacancy. The contour levels are drawn at intervals of 0.2 electrons/ $\text{\AA}^3$ , with the lowest contour level at 0.2 electrons/ $\text{\AA}^3$  and represent the charge density of the occupied defect state.

duction band has *e* symmetry and the upper conduction band has  $t_2$  symmetry. Also apparent in these plots are antibonding contributions from the nearest neighbor O 2p orbitals in the plotting plane.

The appearance of these three contour plots motivates us to analyze the  $[\text{BO}_n]^q$  clusters in greater detail. For the perfect crystal,<sup>23</sup> we showed that the  $[\text{BO}_4]^{-2}$  cluster could be partially explained in terms of crystal field effects of the  $\text{O}^{-\gamma}$  ions on the degenerate *d* states of W or Mo and partially in terms of hybridization between the W or Mo *d* states and the O 2p, summarized by the molecular diagram shown in the left panel of Fig. 1. For the  $[\text{BO}_3]^{-2}$  cluster, the crystal field effects can be analyzed as follows. Idealizing the geometry of the cluster slightly so that  $\text{O}^{-\gamma}$  ions are placed at three of the four ideal tetrahedral positions at a distance *R* from a central W or Mo ion, we find that the leading term in the degenerate perturbation of the W or Mo *d* states can be written in the form

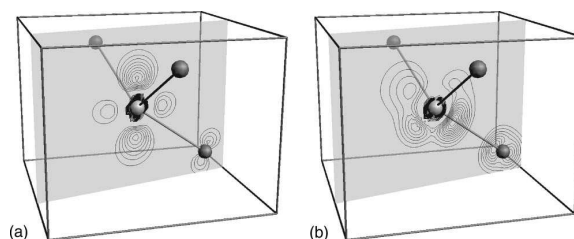


FIG. 5. Ball and stick model and contour plots for the 8x simulation of an O vacancy in  $\text{CaMoO}_4$  at the  $[\text{MoO}_3]^{-2}$  site similar to Fig. 4, but with contour levels representing the charge density associated (if the states had been fully occupied) with the unoccupied lower conduction band states (a) and upper conduction band states (b).

$$\delta V_{mm'} = \frac{\gamma e^2 \langle r_d^2 \rangle}{7R^3} M_{mm'}, \quad (7)$$

where  $M_{mm'}$  is a  $5 \times 5$  matrix with indices  $m$  corresponding to the five azimuthal quantum numbers associated with the degenerate  $d$  ( $l=2$ ) states. Diagonalizing the matrix we find three eigenvalues

$$\delta E = \frac{\gamma e^2 \langle r_d^2 \rangle}{7R^3} \times \begin{cases} 2 & (2) & t'_2, \\ -1 & (2) & e', \\ -2 & (1) & t''_2, \end{cases} \quad (8)$$

where the number in parenthesis denotes the degeneracy and the label on the right indicates the approximate relation to the corresponding state of pure tetrahedral symmetry. The lowest singly degenerate energy state which we have labeled “ $t''_2$ ” has pure  $t_2$  character. The two doubly degenerate states have mixed character, with slightly more  $e$  or  $t_2$  character as indicated by the labels  $e'$  and  $t'_2$ , respectively. We can estimate these energies for  $B = \text{Mo}$ , using  $\langle r_d^2 \rangle \approx 1 \text{ \AA}$ , corresponding to the expectation value of the second power of the radius of the  $d$  orbitals of Mo (estimated from atomic orbitals),  $R \approx 1.79 \text{ \AA}$  corresponds to the Mo-O bond length, and  $\gamma = 2$ , we find the splitting between the extreme eigenvalues to be  $\Delta E_{t'_2} - \Delta E_{t''_2} \approx 2.8 \text{ eV}$ . This is considerably larger than the corresponding crystal field splittings for tetrahedral geometry in the perfect crystal.<sup>23</sup> Interestingly, the partial densities of states for threefold coordinated W and Mo shown in Figs. 2, 3, and 9, as well as the charge density contour plots shown in Figs. 4 and 5 are consistent with this analysis in the sense that the self-consistent electronic structure of all of the defects containing  $[\text{BO}_3]^{-2}$  clusters have three groups of states, the lowest state is occupied and has a single spatial degeneracy while the upper two states are unoccupied and have double spatial degeneracy. In addition to the crystal field analysis, hybridization of the  $d$  states of the  $B$  ion with the  $p$  states of O are also important in determining the electronic structure as illustrated in the middle panel of Fig. 1. Due to the spatial arrangement of the clusters, hybridization affects the  $t'_2$  states more than the others. Extending this analysis to the uncharged cluster  $[\text{BO}_3]^0$ , we might expect the energy diagram to be similar while the occupancies change as illustrated in the right most panel of Fig. 1. However, as we shall show below, the situation becomes considerably more complicated.

### 2. Ca and O double vacancy

Removing both Ca and O atoms changes the charge balance associated with the defect states since the missing Ca removes two valence electrons from the system. We expect the double vacancy defect to be characterized by  $\{\text{CaO}\} \times [\text{MoO}_3]^0$  in our adopted notation. The results of the  $2x$  simulation for the relaxed double vacancy are shown in the bottom panel of Fig. 2 for the partial density of states in Table III for the geometric and energetic results. The effects of geometry optimization are much larger than those of the single O vacancy, adjusting the energies of states associated

with the  $[\text{MoO}_3]^0$  clusters relative to other states of the system. Table III summarizes the relaxed Mo-O bond lengths and angles. In particular, we find the Mo-O bond lengths associated with the  $[\text{MoO}_3]^0$  groups to be shortened by 0.05  $\text{\AA}$ , while those associated with the regular  $\text{MoO}_4^{-2}$  groups are approximately the same length as in the perfect crystal except for one bond which points in the direction of the missing oxygen which is lengthened by 0.04  $\text{\AA}$ . The simple description of this process is that the  $[\text{MoO}_3]^0$  is able to compensate for the loss of charge by contracting its effective volume, thereby increasing the local charge density available for the Mo-O bonds. Correspondingly, the relaxation energy listed in Table III is much larger than for the single O vacancy case. The estimated formation energy is also listed in Table III.

While this explanation of the double vacancy seems reasonable, it apparently is not the whole story. Recognizing that the  $2x$  simulation corresponds to an extremely high concentration of defects and that there are severe geometry restrictions consistent with the assumed supercell, we expect the results for the  $8x$  simulation to be more reliable. Unfortunately, we have no results for the  $\{\text{CaO}\}[\text{MoO}_3]^0$  defect in the  $8x$  simulation cell because we found it *impossible* to stabilize its self-consistency iterations with or without lattice relaxation effects. What appears to be happening in the more realistic simulation is that there is are two or more nearly degenerate configurations of this system. In addition to the  $[\text{MoO}_3]^0([\text{MoO}_4]^{-2})_4$  configuration consistent with the  $2x$  simulations, another configuration of the form  $[\text{MoO}_3]^{-4\epsilon}([\text{MoO}_4]^{-2+\epsilon})_4$  seems to also exist. This second configuration corresponds to the partial transfer of negative charge (denoted by  $\epsilon$ ) to the  $[\text{MoO}_3]^q$  group. This charge comes from the top of the O valence band and is presumably associated with the four nearest neighbor  $[\text{MoO}_4]^{-2}$  groups. Apparently, the energy of the  $[\text{MoO}_3]^q$  group is extremely sensitive to its charge state when  $q$  becomes less negative than  $q = -2$ , as confirmed by simulations with negatively charged supercells (compensated with a uniform positive charge).

### 3. Y substitutional and charge effects

In order to understand these charging effects in more detail and also to study the effects of trivalent substitutional impurities studied in the literature,<sup>14,47</sup> we performed some simulations with Y substituting for one of the Ca atoms ( $\{\text{Y/Ca}\}[\text{MoO}_4]^{-(2+\delta)}$ ). Here  $\delta$  represents the excess electronic charge incorporated into the lower conduction band due to the trivalent substitutional impurity Y. These calculations were done using the  $8x$  supercell but without geometry optimization. Figure 6 (top panel) shows the partial density of states. The results show that Y adds electrons to the conduction band of  $\text{CaMoO}_4$  and introduces new unoccupied states primarily above the second conduction band, but introduces no new states of Y character within the band gap. This is similar to the behavior that we have found for  $\text{PbWO}_4:\text{La}$  simulations.<sup>48</sup> In future work, we hope to study the geometry relaxation of this system, in order to find out whether the model is consistent with the experimental obser-



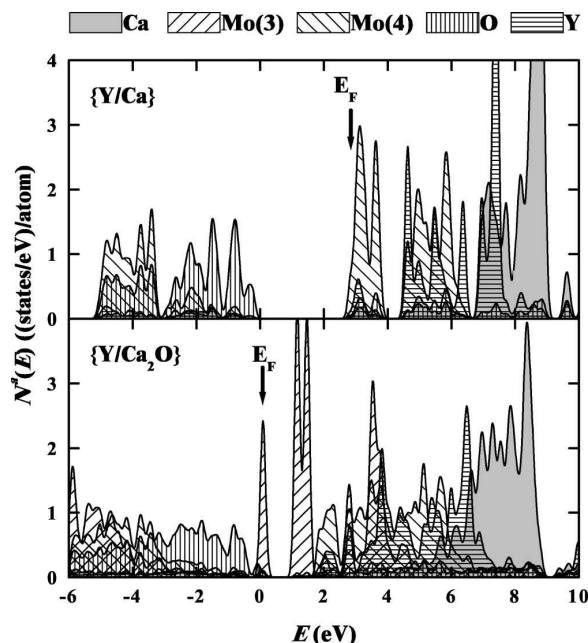


FIG. 6. Partial densities of states for  $8x$  simulation  $\text{CaMoO}_4$  with Y substituting for one Ca alone (top panel) and with a Ca and O vacancy double vacancy (lower panel), using the same notations as in Fig. 2. Calculations were done without lattice relaxation.

vation that excess electrons can localize on one of the molybdate sites to form  $[\text{MoO}_4]^{-3}$  centers. Recently,  $[\text{WO}_4]^{-3}$  and  $[\text{WO}_4]^{-3}\text{-La}^{+3}$  centers have been identified in electron spin resonance studies of La doped  $\text{PbWO}_4$  at low temperature<sup>49,50</sup> with temperature dependences indicating binding energies of 0.05 and 0.27 eV, respectively, below the conduction band energy.

We also considered the effects of Y substitution impurities in conjunction with Ca and O double vacancies ( $\{\text{Y}/\text{Ca}_2\text{O}\}[\text{MoO}_3]^{-1}$ ) using the  $8x$  simulation cell without geometry optimization. The partial density of states are shown in the bottom panel of Fig. 6. Here we see that the extra charge from the trivalent Y is accommodated by the  $\text{MoO}_3$  group. In contrast to the neutral  $\text{CaO}$  double vacancy, the excess charge from Y causes the  $[\text{MoO}_3]^{-1}$  group to be electronically stable with a half-filled defect state (of “ $t_2$ ” character) just above the top of the valence band and an unfilled defect state (of “ $e'$ ” character) below the conduction band.

#### 4. Interstitial O

There is a fair amount of experimental evidence<sup>18–20,51</sup> that interstitial oxygen can be accommodated into the  $\text{PbWO}_4$  lattice. It is therefore of interest to study the corresponding defect in  $\text{CaMoO}_4$ . We have carried out a  $2x$  simulation for an interstitial O atom initially placed between two Ca sites, and finding a stable O site between two  $\text{MoO}_4$  groups. Figure 7 shows the optimized geometry with some of the bond lengths and angles listed in Table III. As seen in the figure, the interstitial O forms a weak bond which bridges

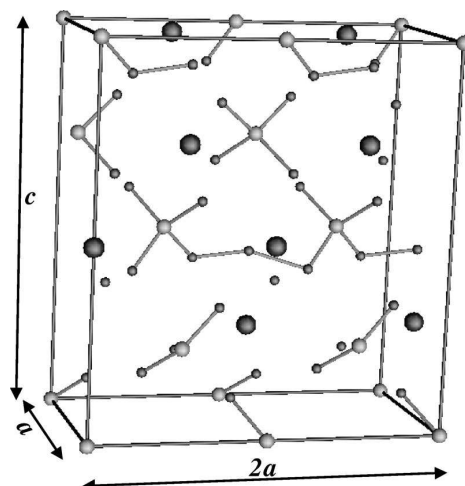


FIG. 7. Ball and stick model of stable configuration of interstitial O in  $\text{CaMoO}_4$  for  $2x$  simulation. Atomic sites are shown with increasing sphere sizes in the order O, Mo, and Ca. Nearest neighbor Mo-O and O-O bonds are also indicated.

two oxygens associated with nearby  $[\text{MoO}_4]^{-2}$  clusters. The O–O bond lengths are found to be 1.8 Å. Since we have not carried out an exhaustive geometry optimization, we believe there may be additional stable interstitial sites, such as found, for example in recent empirical potential simulations.<sup>52</sup> Table III also lists our calculated formation energy for the neutral interstitial O and finds it to be small ( $\approx 0.4$  eV), suggesting that it could be relatively easy to introduce extra neutral O into this lattice.

The partial density of states for our optimized geometry shown in Fig. 8 shows that interstitial O states are energetically aligned close to the O bands of the perfect lattice. By integrating the partial density of state curves in Fig. 8, we estimate that interstitial O’s have a charge very similar to that of tetrahedral O’s. While formally the tetrahedral O’s have a charge of  $-2e$ , molecular bonding reduces the actual charge.

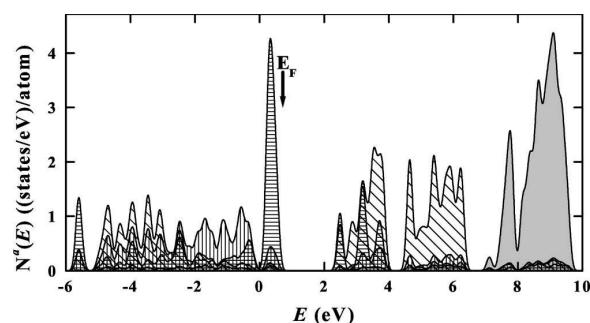


FIG. 8. Partial densities of states for  $2x$  simulation of  $\text{CaMoO}_4$  with an interstitial O atom, at the stable geometry shown in Fig. 7. The shadings of the various partial density of states curves is the same as in Fig. 2 except that the interstitial O states are indicated with horizontal stripes.

Since the simulations were carried out for the  $2x$  supercell, the concentration of extra O in the simulation corresponded to a stoichiometry of  $\text{CaMoO}_{4.5}$ . Experimentally, rather high concentrations of extra O has been achieved. For example, gravimetric analysis of  $\text{PbWO}_4$  annealed in an oxygen atmosphere<sup>19</sup> suggests that it is possible to achieve a stoichiometry of  $\text{PbWO}_{4.1}$ , at least at high temperature.

### B. Defects in $\text{PbWO}_4$

For the two formula unit simulations in  $\text{PbWO}_4$ , including those for the “perfect crystal,” the atomic positions (except for those removed) were taken from the experimental crystallographic results<sup>28</sup> without allowing for optimization of the defect geometry. Two kinds of defects were modeled—an oxygen vacancy and a Pb and O double vacancy.

In Fig. 9, the results for the partial densities of states for the two defect simulations are compared with those of the perfect crystal. The results are very similar to the corresponding results for the  $2x$  simulations of the  $\text{CaMoO}_4$  system shown in Fig. 2. The main differences in the occupied states are that in  $\text{PbWO}_4$  there is a narrow Pb  $6s$  band at approximately 2 eV below the valence band and a corresponding antibonding contribution of Pb  $6s$  states at the top of the valence band. The main differences in the unoccupied states are that for  $\text{CaMoO}_4$ , the crystal field split Mo  $d$  states form two distinct bands of “ $e$ ” and “ $t_2$ ” character separated by nearly 1 eV. In  $\text{PbWO}_4$ , the crystal field split W  $d$  states of “ $e$ ” and “ $t_2$ ” character overlap, but form two distinct peaks. Also  $\text{PbWO}_4$  lacks the equivalent of the high density of states at the top of the transition metal  $d$  states caused by the Ca  $3d$  states in  $\text{CaMoO}_4$ .

What is of interest is the identification of defect states introduced into the band gap. Since we have such a high concentration of the defects, quantitative identification of the valence and conduction band edges are difficult. However, we can make the following qualitative analysis which is very similar to the  $\text{CaMoO}_4$  case. For the O vacancy simulation, a peak associated with the three-fold coordinated W site appears in the band gap, below the conduction band edge. This state is fully occupied in our model crystal because the O vacancy removes six oxygen  $p$  states from the valence band while removing only four valence electrons. Therefore, this defect would be given as  $\{/\text{O}\}[\text{WO}_3]^{-2}$  in our suggested notation. The charge density contours associated with both the filled band gap state and the unfilled states in the conduction band are very similar to those shown in Figs. 4 and 5 for  $\text{CaMoO}_4$ . Since our  $\text{CaMoO}_4$  simulations on the oxygen vacancy showed that our results were insensitive to supercell size and relaxation effects, we expect these results for the O vacancy in  $\text{PbWO}_4$  to be similarly insensitive to supercell and relaxation effects.

For the Pb and O double vacancy, the partial density of states plot (bottom panel of Fig. 9) shows that two peaks associated with the three-fold coordinated W site appear in the band gap. These states are empty because the Pb vacancy does not remove any states from the valence band (other than from the narrow  $6s$  band below the valence band), but re-

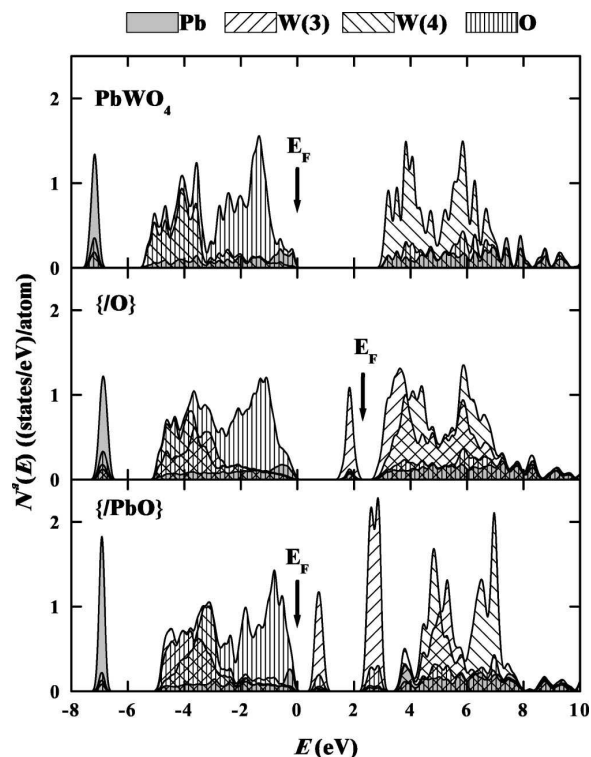


FIG. 9. Partial densities of states for  $\text{PbWO}_4$ , perfect crystal (Ref. 39) (top panel), O vacancy (middle panel), and Pb and O double vacancy (bottom panel), using the same notations as in Fig. 2. Calculations were done without lattice relaxation.

moves two additional valence electrons. Thus this defect would be given as  $\{/PbO\}[\text{WO}_3]^0$  in our suggested notation. Since our  $\text{CaMoO}_4$  simulations on the Ca and O double vacancy could not be extended to the  $8x$  supercell, we expect that the double vacancy in  $\text{PbWO}_4$  to also be more complicated than implied by these unrelaxed  $2x$  simulations.

### IV. SUMMARY

These simulations of oxygen vacancies in  $\text{CaMoO}_4$  and  $\text{PbWO}_4$  focused attention on the ground state electronic structure of the  $[\text{BO}_3]^q$  clusters. In addition to the electronic structure of the  $[\text{BO}_3]^q$  clusters themselves, it is also important to understand the alignment of the cluster states with respect to the other states in the crystal. Our self-consistent calculations indicate that the  $[\text{BO}_3]^q$  clusters are well defined and stable for  $q = -2$  as found in the  $\{/O\}$  simulations and is also stable for  $q = -1$  as found in the  $\{Y/\text{Ca}_2\text{O}\}$  simulations. For less negative values of  $q$ , the electronic balance between the  $[\text{BO}_3]^q$  clusters associated with the O vacancy and the  $[\text{BO}_4]^{-2}$  associated with the regular lattice seems to be very delicate.

In summary, we have shown that the main effect of O vacancies in  $\text{PbWO}_4$  and  $\text{CaMoO}_4$  is the introduction of states of W or Mo  $d$  character into the band gap. The energies of these defect states are very sensitive to their charge.

For a single O vacancy in  $\text{PbWO}_4$  and  $\text{CaMoO}_4$

( $\{O\}[BO_3]^{-2}$ ), based on  $2x$  and  $8x$  simulations with relaxation effects included (for the  $CaMoO_4$  case), we find a well-defined filled defect state below the conduction band, whose symmetry we have analyzed to be  $t_2''$  with density contours shown in Fig. 4. This defect is very insensitive to lattice relaxation and simulation cell size. Since the state is filled with 2 electrons, it cannot act as a trap for excess electrons nor can it be observed by electron spin resonance. Furthermore, since its energy is approximately 0.7 eV below the conduction band minimum, it cannot be an effective electron donor. It might be observable in infrared excitation, but cannot account for visible luminescence. If electrons are removed from the defect, we expect its energy to be lowered and the spectrum to become more complicated.

For a  $PbO$  or  $CaO$  double vacancy in  $PbWO_4$  or  $CaMoO_4(\{AO\}[BO_3]^0)$ , based on  $2x$  simulations, we find two groups of unfilled defect states within the band gap. The lower state is of  $t_2''$  character, while the upper state is of  $e'$  character. Geometric optimization of the  $2x$   $CaMoO_4$  simulation showed that shortened Mo-O bonds for the  $[MoO_3]^0$  cluster are energetically favored. However, our inability to extend these calculations to the  $8x$  supercell simulations suggests that this defect system is electronically metastable or perhaps unstable. Simulations with charged supercells and with substitutional Y described in Sec. III A 3 show that the  $[BO_3]^q$  defect is electronically stabilized with  $q \leq -1$ . In the absence of excess charge, such as provided by the substitutional trivalent Y atom, the lowest  $[BO_3]^0$  state becomes degenerate with the O valence band. The fact that we are unable to stabilize this calculation has led us to speculate that there are at least two nearly degenerate configurations of this system which we have described as involving the  $[BO_3]$  site and its four nearest neighbor  $[BO_4]$  sites in the form  $[MoO_3]^0([MoO_4]^{-2})_4$  and  $[MoO_3]^{-4\epsilon}([MoO_4]^{-2+\epsilon})_4$ . This type of degeneracy usually results in a lattice distortion according to a Jahn-Teller mechanism.<sup>53</sup> This reasoning leads us to suggest that a  $CaO$  double vacancy may result in

a more complicated defect, perhaps involving lattice distortions on several neighboring sites.

A single electron associated with an O vacancy in  $PbWO_4$  has been suggested by Laguta and co-workers<sup>54</sup> as the model for a photoinduced “ $Pb^+-V_O$ ” center observed in electron spin resonance. The electron spin resonance signature is that of an electron interacting primarily with Pb nuclei adjacent the oxygen vacancy, and the authors refer to it as a  $Pb^+$  center perturbed by a bare oxygen vacancy. The puzzle from the perspective of the calculations presented here is that the experiment finds little contribution from  $W 5d$  states. Laguta and co-workers suggest<sup>54,55</sup> that there may be another lattice configuration of this defect, accessible over a thermal barrier, which resembles more closely an electron localized in an  $W 5d$  orbital. This second configuration may perhaps correspond to the  $[WO_3]^{-1}$  center discussed in the present notation. This experiment and analysis suggests that lattice distortion may also be significant for the  $q = -1$  defect. Further computational and experimental work is needed.

We have also presented preliminary simulations of interstitial neutral O introduced into the  $2x$  lattice. These studies identified a possible stable site for the interstitial O and found the corresponding states to be near the crystalline O valence band. This preliminary work suggests that further study of this system, including larger supercell simulations, charging effects, and perhaps simulation of dynamical effects, may be useful.

Missing from this work, is any information about the effects of these defects on luminescence. For this, it is necessary to go beyond the ground state density functional formalism, considered here.

#### ACKNOWLEDGMENTS

This work was supported by NSF Grant No. DMR-9706575 and a SUR grant from IBM. We would like to thank Martin Nikl for very helpful comments.

\*Corresponding author. Electronic address: natalie@wfu.edu; <http://www.wfu.edu/~natalie>

<sup>1</sup>J. P. Peigneux, Nucl. Instrum. Methods Phys. Res. A **351**, 197 (1994).

<sup>2</sup>P. Lecoq *et al.*, Nucl. Instrum. Methods Phys. Res. A **365**, 291 (1995).

<sup>3</sup>F. A. Kröger, *Some Aspects of the Luminescence of Solids* (Elsevier, New York, 1948).

<sup>4</sup>W. V. Loo, Phys. Status Solidi A **28**, 228 (1975).

<sup>5</sup>R. Biederbick, G. Born, A. Hofstaetter, and A. Scharmann, Phys. Status Solidi B **69**, 55 (1975).

<sup>6</sup>R. Grasser, E. Pitt, A. Scharmann, and G. Zimmerer, Phys. Status Solidi B **69**, 359 (1975).

<sup>7</sup>A. Hofstaetter, R. Oeder, A. Scharmann, D. Schwabe, and B. Vitt, Phys. Status Solidi B **89**, 375 (1978).

<sup>8</sup>M. Kobayashi, S. Sugimoto, Y. Yoshimura, Y. Usuki, M. Ishii, N. Senguttuvan, K. Tanji, and M. Nikl, Nucl. Instrum. Methods Phys. Res. A **459**, 482 (2001).

<sup>9</sup>T. Esaka, Solid State Ionics **136-137**, 1 (2000).

<sup>10</sup>A. A. Kaminskii *et al.*, Opt. Commun. **183**, 277 (2000).

<sup>11</sup>M. Nikl, Phys. Status Solidi A **178**, 595 (2000).

<sup>12</sup>J. M. Moreau, R. E. Gladyshevskii, P. Galez, J. P. Peigneux, and M. V. Korzhik, J. Alloys Compd. **284**, 104 (1999).

<sup>13</sup>E. Auffray, P. Lecoq, M. Korzhik, A. Annenkov, O. Jarolimek, M. Nikl, S. Baccaro, A. Cecilia, M. Diemoz, and I. Dafinei, Nucl. Instrum. Methods Phys. Res. A **402**, 75 (1998).

<sup>14</sup>M. Nikl *et al.*, J. Appl. Phys. **87**, 4243 (2000).

<sup>15</sup>A. N. Annenkov *et al.*, Phys. Status Solidi A **156**, 493 (1996).

<sup>16</sup>M. Nikl, K. Nitsch, J. Hybler, J. Chval, and P. Reiche, Phys. Status Solidi B **196**, K7 (1996).

<sup>17</sup>M. Nikl *et al.*, J. Appl. Phys. **82**, 5758 (1997).

<sup>18</sup>A. Annenkov, E. Auffray, M. Korzhik, P. Lecoq, and J. P. Peigneux, Phys. Status Solidi A **170**, 47 (1998).

<sup>19</sup>W. Li, T. B. Tang, and X. Feng, J. Appl. Phys. **87**, 7692 (2000).

<sup>20</sup>C. Shi, Y. Wei, Z. Yang, D. Zhou, C. Guo, J. Liao, and H. Tang, Chem. Phys. Lett. **328**, 1 (2000).

<sup>21</sup>P. Hohenberg and W. Kohn, Phys. Rev. **136**, B864 (1964).

<sup>22</sup>W. Kohn and L. J. Sham, Phys. Rev. **140**, A1133 (1965).

<sup>23</sup>Y. Zhang, N. A. W. Holzwarth, and R. T. Williams, Phys. Rev. B **57**, 12 738 (1998).

- <sup>24</sup>C. J. Ballhausen and A. D. Liehr, *J. Mol. Spectrosc.* **2**, 342 (1958).
- <sup>25</sup>A. R. Tackett, N. A. W. Holzwarth, and G. E. Matthews, *Comput. Phys. Commun.* **135**, 348 (2001).
- <sup>26</sup>P. Blaha, K. Schwarz, and J. Luitz, WIEN97 [Improved and updated Unix version of the original copyrighted WIEN code, which was published by P. Blaha, I. Schwarz, P. Sorantin, and S. B. Trickey, in *Comput. Phys. Commun.* **59**, 399 (1990).], Tech. Rep., Vienna University of Technology, 1997.
- <sup>27</sup>R. M. Hazen, L. W. Finger, and J. W. E. Mariathasan, *J. Phys. Chem. Solids* **46**, 253 (1985).
- <sup>28</sup>J. M. Moreau, P. Galez, J. P. Peigneux, and M. V. Korzhik, *J. Alloys Compd.* **238**, 46 (1996).
- <sup>29</sup>In fact, the CaMoO<sub>4</sub> calculations proved to be a strenuous test case for the PAW method and this project contributed significantly to the development of the PWPW code.
- <sup>30</sup>P. E. Blöchl, *Phys. Rev. B* **50**, 17 953 (1994).
- <sup>31</sup>J. P. Perdew and Y. Wang, *Phys. Rev. B* **45**, 13 244 (1992).
- <sup>32</sup>N. A. W. Holzwarth, A. R. Tackett, and G. E. Matthews, *Comput. Phys. Commun.* **135**, 329 (2001).
- <sup>33</sup>C. L. Fu and K. M. Ho, *Phys. Rev. B* **28**, 5480 (1983).
- <sup>34</sup>G. Herzberg, *Molecular Spectra and Molecular Structure* (D. Van Nostrand Company, New York, 1950).
- <sup>35</sup>N. A. W. Holzwarth and Y. Zeng, *Phys. Rev. B* **49**, 2351 (1994).
- <sup>36</sup>C. E. Moore, *Atomic Energy Levels* (Superintendent of Documents, U. S. Government Printing Office, 1971), NSRDS-NBS 35 – National Standard Reference Data Series, National Bureau of Standards, Washington, DC, SD Catalog No. C13.48:35/V.I.
- <sup>37</sup>O. K. Andersen, *Phys. Rev. B* **12**, 3060 (1975).
- <sup>38</sup>This *k*-point sampling corresponds to that used in Ref. 23. The decision to use a smaller number of **k** points for the CaMoO<sub>4</sub> simulations compared with those of PbWO<sub>4</sub> was made in order to save computer time. It can be somewhat justified on the basis of narrower, less dispersive bands. From our experience with these materials, we expect that the qualitative conclusions are insensitive to this choice.
- <sup>39</sup>In Ref. 23 the partial density of states were incorrectly reduced by a factor of 2. We would like to thank Dr. Peter Blaha for this correction.
- <sup>40</sup>N. A. W. Holzwarth, G. E. Matthews, R. B. Dunning, A. R. Tackett, and Y. Zeng, *Phys. Rev. B* **55**, 2005 (1997).
- <sup>41</sup>N. A. W. Holzwarth, G. E. Matthews, A. R. Tackett, and R. B. Dunning, *Phys. Rev. B* **57**, 11 827 (1998).
- <sup>42</sup>C. A. Daul, K. G. Doclo, and A. C. Stückli, in *Recent Advances in Density Functional Methods Part II*, edited by D. P. Chong (World Scientific, Singapore, 1997), Chap. 4, pp. 61–113.
- <sup>43</sup>A. E. Hughes and B. Henderson, in *Point Defects in Solids*, edited by J. James H. Crawford and L. M. Slifkin (Plenum Press, New York, 1972), Vol. 1, Chap. 7.
- <sup>44</sup>Q. S. Wang and N. A. W. Holzwarth, *Phys. Rev. B* **41**, 3211 (1990).
- <sup>45</sup>E. Scorza, U. Birkenheuer, and C. Pisani, *J. Chem. Phys.* **107**, 9645 (1997).
- <sup>46</sup>*Physics of Color Centers*, edited by W. B. Fowler (Academic Press, 1968).
- <sup>47</sup>A. Annenkov, E. Auffray, A. Borisevich, M. Korzhik, P. Lecoq, and V. Ligun, *Nucl. Instrum. Methods Phys. Res. A* **426**, 486 (1999).
- <sup>48</sup>R. T. Williams, Y. C. Zhang, Y. Abraham, and N. A. W. Holzwarth, in *SCINT99 – Proceedings of The Fifth International Conference on Inorganic Scintillators and Their Applications*, edited by V. Mikhailin (Moscow State University, Russia, 2000), pp. 118–127, August 16–20, 1999.
- <sup>49</sup>V. V. Laguta, J. Rosa, M. I. Zaritskii, M. Nikl, and Y. Usuki, *J. Phys.: Condens. Matter* **10**, 7293 (1998).
- <sup>50</sup>V. V. Laguta, M. Martini, F. Meinardi, A. Vedda, A. Hofstaetter, B. K. Meyer, M. Nikl, E. Mihoková, J. Rosa, and Y. Usuki, *Phys. Rev. B* **62**, 10 109 (2000).
- <sup>51</sup>M. Nikl, K. Nitsch, K. Polak, E. Mihokova, I. Dafinei, E. Auffray, P. Lecoq, P. Reiche, R. Uecker, and G. P. Pazzi, *Phys. Status Solidi B* **195**, 311 (1996).
- <sup>52</sup>Q. Lin, X. Feng, and Z. Man, *Phys. Rev. B* **63**, 134105 (2001).
- <sup>53</sup>H. A. Jahn and E. Teller, *Proc. R. Soc. London, Ser. A* **161**, 220 (1937).
- <sup>54</sup>V. V. Laguta, M. Martini, A. Vedda, M. Nikl, E. Mihoková, P. Boháček, J. Rosa, A. Hofstätter, B. K. Meyer, and Y. Usuki, *Phys. Rev. B* **64**, 165102 (2001).
- <sup>55</sup>M. Nikl (private communication).

## Electronic structure and optical properties of CdMoO<sub>4</sub> and CdWO<sub>4</sub>

Y. Abraham, N. A. W. Holzwarth, and R. T. Williams

*Department of Physics, Wake Forest University, Winston-Salem, North Carolina 27109*

(Received 7 February 2000; revised manuscript received 4 April 2000)

In previous work, we studied the electronic structure of several molybdate and tungstate crystals having the scheelite structure. The wolframite structure is another common form for molybdate and tungstate materials. In this paper, we compare two chemically similar materials that naturally form in the scheelite and wolframite structures—CdMoO<sub>4</sub> and CdWO<sub>4</sub>, respectively. We compare the electronic structure and approximate optical properties of these materials within the framework of density-functional theory. One major difference between the two materials is in their lower conduction bands, which are dominated by the crystal-field-split *d* bands of the transition metal. For CdMoO<sub>4</sub> the Mo ions have an approximately tetrahedral coordination causing the lower conduction band to be twofold degenerate, while for CdWO<sub>4</sub> the W ions have an approximately octahedral coordination causing the lower conduction band to be threefold degenerate.

### I. INTRODUCTION

Cadmium tungstate (CdWO<sub>4</sub>) and cadmium molybdate (CdMoO<sub>4</sub>) are interesting materials from several points of view, including their optical, chemical, and structural properties. Optical properties of CdWO<sub>4</sub> are of interest because this material has been used as a scintillator for detecting x rays and  $\gamma$  rays in medical applications.<sup>1,2</sup> It has advantages over other scintillator materials due to its relatively large x-ray absorption coefficient and scintillation output, although its relatively long response time is disadvantageous for some applications.

Chemical interest is due to possible catalytic activity of mixed CdMo<sub>x</sub>W<sub>1-x</sub>O<sub>4</sub> crystals, which have been recently studied by Daturi and co-workers.<sup>3,4</sup> These authors found increased catalytic activity for values of *x* in the range  $\frac{1}{8} < x < \frac{1}{4}$ .

Structural interest in these materials is due to the fact that CdWO<sub>4</sub> crystallizes in wolframite structure while CdMoO<sub>4</sub> crystallizes in scheelite structure. These two crystal structures have many examples in ternary molybdate, tungstate, and other ABO<sub>4</sub> materials. According to a compilation by Sleight,<sup>5</sup> the wolframite structure is a generally more closely-packed structure, naturally forming in materials with small A<sup>2+</sup> ions while the scheelite structure naturally forms in materials with larger A<sup>2+</sup> ions. For example, ZnMoO<sub>4</sub> and ZnWO<sub>4</sub> have the wolframite structure, while CaMoO<sub>4</sub> and CaWO<sub>4</sub> have the scheelite structure. In contrast, CdWO<sub>4</sub> and CdMoO<sub>4</sub> have different crystal structures—the wolframite material (CdWO<sub>4</sub>) having a slightly larger unit cell volume than that of the scheelite material (CdMoO<sub>4</sub>). Interestingly, under pressure there seems to be a tendency for the scheelite form of CdMoO<sub>4</sub> to transform to the wolframite form<sup>6</sup> and for the wolframite form of CdWO<sub>4</sub> to transform to the scheelite form.<sup>7</sup> In their mixed crystal work, Daturi and co-workers<sup>3,4</sup> found that the 50%-50% alloy ( $x = \frac{1}{2}$ ) takes the scheelite structure, while alloys with smaller Mo concentrations have the wolframite form.

In order to build a basis for understanding some of these unusual properties, we have carried out detailed electronic structure calculations for CdWO<sub>4</sub> and CdMoO<sub>4</sub> within the framework of density-functional theory. In addition to deter-

mining the ground-state electronic density and distribution of one-electron eigenstates, we have also estimated the optical dielectric functions and reflectivity for these materials. In Sec. II, the crystal structure is discussed. The calculational methods are presented in Sec. III. Density-functional results are presented in Sec. IV and compared with results for related materials, especially with our recent study of several tungstate and molybdate scheelite materials.<sup>8</sup> The calculated optical properties are presented in Sec. V and discussed with reference to recent reflectivity measurements of Nagirnyi and co-workers.<sup>9,10</sup> A summary and conclusions are presented in Sec. VI.

### II. CRYSTAL STRUCTURES

#### A. CdMoO<sub>4</sub>—scheelite structure

Cadmium molybdate has the same crystal structure as CaMoO<sub>4</sub>, CaWO<sub>4</sub>, PbMoO<sub>4</sub>, and PbWO<sub>4</sub> whose electronic structures were reported in our previous paper.<sup>8</sup> It belongs to the scheelite-type structure with a space group of *I*4<sub>1</sub>/*a*  $\equiv C_{4h}^6$  which is No. 88 in *The International Tables*.<sup>12</sup> This structure has eight symmetry elements and a body-centered orthorhombic primitive cell that includes two formula units of CdMoO<sub>4</sub>. Each Mo site is surrounded by four equivalent O sites at a bond length of 1.75 Å in approximately tetrahedral symmetry about that site. Each Cd site is surrounded by 8 O sites at bond lengths of 2.40 Å and 2.44 Å in approximately octahedral symmetry. The crystal parameters used in the present paper were taken from the recent measurements of Daturi and co-workers,<sup>4</sup> which are listed in the first column of Table I. For comparison, earlier results are also listed in this table.<sup>11</sup>

#### B. CdWO<sub>4</sub>—wolframite structure

Cadmium tungstate has the wolframite-type structure, which is in the monoclinic class, with one axis not orthogonal to the other two.<sup>3,4</sup> This wolframite structure has a space group of *P*2<sub>1</sub>/*c*  $\equiv C_{2h}^4$ , which corresponds to No. 13 in the *International Tables*.<sup>12</sup> In this structure, each W is surrounded by 6 near O sites in approximately octahedral coordination. There are two distinct oxygen atoms present. Type one (O<sub>1</sub>) forms a bond to one tungsten atom with a very

TABLE I. Compilation of experimental crystal parameters for CdMoO<sub>4</sub>. Atom positions are specified using the same conventions as in Ref. 8.

	Ref. 4			Ref. 11		
$a(\text{\AA})$	5.156			5.17		
$c(\text{\AA})$	11.196			11.19		
$V(\text{\AA}^3)$	148.82			149.55		
	$x$	$y$	$z$	$x$	$y$	$z$
Cd	0.0	0.25	0.625	0.0	0.25	0.625
Mo	0.0	0.25	0.125	0.0	0.25	0.125
O	0.24	0.091	0.0421	0.25	0.11	0.03

short bond length (1.78 Å) and to two cadmium atoms with longer bond lengths (2.41 and 2.27 Å). Type two (O<sub>2</sub>) connects to two different W atoms with longer bond lengths (1.91 and 2.15 Å) and to Cd with a bond length of 2.20 Å. The unit cell contains two formula units of CdWO<sub>4</sub>. Table II lists the measured lattice constants  $a$ ,  $b$ , and  $c$ , as well as the nonorthogonal angle  $\beta$ . In this paper, we used the parameters of Daturi and coworkers.<sup>3</sup> Table II also lists other crystallography data for comparison.<sup>4,7,13</sup> The crystal volume of CdWO<sub>4</sub> is apparently less than 1% larger than that of CdMoO<sub>4</sub>, and there is considerable variation in the experimental results.

### III. CALCULATIONAL METHODS

The computations were performed using the linearized augmented plane wave method using the WIEN97 code,<sup>14</sup> using the same calculational parameters (muffin-tin radii, reciprocal space truncations, and convergence tolerances) as in our previous calculations on the Ca and Pb molybdates and tungstates in the scheelite structure.<sup>8</sup> Specifically, the muffin-tin radius was chosen to be 1.65 bohr for O, Mo, and W, and 1.90 bohr for Cd. The RKMAX parameter was taken to be 10 and the GMAX parameter was taken to be 14 bohr<sup>-1</sup>. All relativistic effects including the spin-orbit interaction were taken into account. The exchange-correlation functional was taken within the local-density approximation using the form developed by Perdew and Wang.<sup>15</sup> Brillouin-zone integrations within the self-consistency cycles were performed us-

ing a tetrahedron method<sup>16</sup> using 12 and 16 inequivalent  $\mathbf{k}$  points corresponding to 64 and 48  $\mathbf{k}$  points throughout the Brillouin zone for the scheelite and wolframite structures, respectively. For calculating the density-of-states and the imaginary part of the dielectric tensor, a denser sampling of the Brillouin zone was needed. For these, we used 35 and 63 inequivalent  $\mathbf{k}$  points corresponding to 216 and 252  $\mathbf{k}$  points throughout the Brillouin zone for the scheelite and wolframite structures, respectively. The larger number of inequivalent  $\mathbf{k}$  points for the wolframite structure are necessary because of its lower symmetry. We checked the convergence of the  $\mathbf{k}$ -point sampling and found nearly identical results with variations in the number of  $\mathbf{k}$  points of about 15%.

In Sec. IV A, results for the total and partial one-electron density-of-states are presented. In order to avoid the sharp spikes of the tetrahedron method,<sup>16</sup> these are calculated using a Gaussian smearing function<sup>17</sup> of the form:

$$N^x(E) = \sum_{n\mathbf{k}} f_{n\mathbf{k}}^x w_{\mathbf{k}} \frac{e^{-(E-E_{n\mathbf{k}})^2/\sigma^2}}{\sqrt{\pi}\sigma}. \quad (1)$$

In this equation,  $w_{\mathbf{k}}$  denotes the Brillouin-zone sampling weight factor while  $f_{n\mathbf{k}}^x$  denotes the partial density-of-states weight factor. For the total density-of-states  $N^T$ , the  $f_{n\mathbf{k}}^T$  factor is equal to the degeneracy of the state, while for atomic partial density-of-states the  $f_{n\mathbf{k}}^a$  factor is the degeneracy of the state times the charge within the muffin-tin sphere for atom  $a$ , averaged over all spheres of that type. The Gaussian

TABLE II. Compilation of experimental crystal parameters for CdWO<sub>4</sub>. Cd sites are located at the fractional positions  $\pm(1/2, y_{Cd}, 3/4)$ , W sites are located at the fractional positions  $\pm(0, y_W, 1/4)$ , and the O<sub>1</sub> and O<sub>2</sub> sites are located at the fractional positions  $\pm(x_i, y_i, z_i)$  and  $\pm(x_i, -y_i, z_i + 1/2)$ , where  $i=1$  or 2.

	Ref. 3			Ref. 4			Ref. 7			Ref. 13		
$a(\text{\AA})$	5.0289			5.026			5.028			5.02		
$b(\text{\AA})$	5.8596			5.867			5.862			5.85		
$c(\text{\AA})$	5.0715			5.078			5.067			5.07		
$\beta(\text{deg})$	91.519			91.47			91.50			91.5		
$V(\text{\AA}^3)$	149.39			149.69			149.3			148.84		
	$x$	$y$	$z$	$x$	$y$	$z$	$x$	$y$	$z$	$x$	$y$	$z$
Cd	0.5	0.3027	0.75	0.5	0.3020	0.75	0.5	0.3023	0.75	0.5	0.308	0.75
W	0.0	0.17847	0.25	0.0	0.1784	0.25	0.0	0.1785	0.25	0.0	0.180	0.25
O <sub>1</sub>	0.242	0.372	0.384	0.250	0.360	0.393	0.242	0.372	0.383	0.240	0.380	0.380
O <sub>2</sub>	0.202	0.096	0.951	0.189	0.099	0.954	0.203	0.098	0.949	0.210	0.10	0.960

smearing parameter was chosen to be  $\sigma=0.05$  eV. In all of the density-of-states plots and also in presentation of the band dispersions (Sec. IV B), the zero of energy is taken at the top of the valence band.

In Sec. V, results for components of the dielectric tensor and for the reflectivity are presented. In fact, calculation of the optical properties of materials is beyond the scope of density-functional theory, which is rigorously a ground-state formalism. However, there has recently been considerable progress toward developing methods for calculating optical properties from first principles, using density-functional results as the starting point.<sup>18,19</sup> As a first step toward investigating the optical properties of CdMoO<sub>4</sub> and CdWO<sub>4</sub>, we have calculated the imaginary part of the dielectric tensor from the LAPW one-electron eigenvalues  $E_{n\mathbf{k}}$  and corresponding wave functions  $\Psi_{n\mathbf{k}}(\mathbf{r})$  using the approach of Sole and Giralda<sup>18</sup> and the code developed by Ambrosch-Draxl and Abt.<sup>20</sup> In this approximation, the imaginary part of the dielectric tensor is given by a sum of all transitions between occupied “initial” bands  $n_i\mathbf{k}$  and unoccupied “final” bands  $n_f\mathbf{k}$ , integrated over the Brillouin zone:

$$\varepsilon_2^{\alpha\beta}(h\nu) = \left( \frac{2\pi\hbar e}{m(h\nu - \Delta)} \right)^2 \sum_{n_i n_f} \int \frac{d^3k}{(2\pi)^3} M_{n_i n_f}^{\alpha\beta}(\mathbf{k}) \times \delta(E_{n_i\mathbf{k}} - E_{n_f\mathbf{k}} + \Delta - h\nu). \quad (2)$$

This expression depends upon momentum matrix elements in the  $\alpha$  and  $\beta$  directions between occupied and unoccupied states according to

$$M_{n_i n_f}^{\alpha\beta}(\mathbf{k}) \equiv \text{Re}[\langle \Psi_{n_i\mathbf{k}} | p_\alpha | \Psi_{n_f\mathbf{k}} \rangle \langle \Psi_{n_f\mathbf{k}} | p_\beta | \Psi_{n_i\mathbf{k}} \rangle]. \quad (3)$$

The so called “self-energy” parameter  $\Delta$  is a type of “scissors operator,”<sup>21,18,20</sup> which approximates the leading correction to the infamous band-gap underestimation problem of density-functional theory.<sup>22</sup> In the present paper, the value of  $\Delta$  is estimated from experiment. The Brillouin-zone integration in Eq. (2) is approximated using a modified tetrahedron method.<sup>16,20</sup> The real part of the dielectric tensor is determined by numerically evaluating the Kramers-Kronig relations

$$\varepsilon_1^{\alpha\beta}(h\nu) \approx \delta_{\alpha\beta} + \frac{2}{\pi} \mathcal{P} \int_{\nu_{\min}}^{\nu_{\max}} \frac{\nu' \varepsilon_2^{\alpha\beta}(h\nu')}{\nu'^2 - \nu^2} d\nu', \quad (4)$$

where  $\delta_{\alpha\beta}$  indicates the Kronecker  $\delta$  function in the directional indices  $\alpha$  and  $\beta$ .

Strictly speaking, the equality of Eq. (4) holds only when the integration includes the entire frequency range. However, the integration must exclude part of the low-frequency range because we have only included electronic (no vibrational) contributions to  $\varepsilon_2$ , and it must exclude part of the high-frequency range because we have only calculated electronic transitions over a 30-eV range. From the form of the Kramers-Kronig transform (4), for  $h\nu_{\min} \leq h\nu \leq h\nu_{\max}$ , one can reasonably argue that the neglected integration in the low-frequency range will contribute a slowly varying negative value, while the neglected integration in the high-frequency range will contribute a slowly varying positive value. These corrections affect the calculation of the reflectivity and will be discussed further in Sec. V.

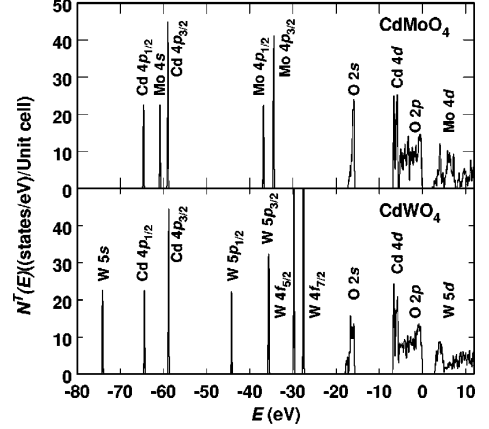


FIG. 1. Total density-of-states of CdMoO<sub>4</sub> and CdWO<sub>4</sub> including upper core, valence, conduction-band states. The zero of energy is placed at the top of the valence band. Labels represent dominant atomic character of spectral peaks.

tivity and will be discussed further in Sec. V. When the electric-field direction  $\alpha$  coincides with an optic axis of the crystal, the corresponding normal incidence reflectivity can then be estimated from the complex components of the dielectric tensor:

$$R_N^\alpha = \left| \frac{(\varepsilon^{\alpha\alpha})^{1/2} - 1}{(\varepsilon^{\alpha\alpha})^{1/2} + 1} \right|^2. \quad (5)$$

This can be conveniently evaluated using the following form:

$$R_N^\alpha = \frac{U^\alpha + 1 - V^\alpha}{U^\alpha + 1 + V^\alpha}, \quad (6)$$

where,

$$U^\alpha \equiv \sqrt{(\varepsilon_1^{\alpha\alpha})^2 + (\varepsilon_2^{\alpha\alpha})^2} \quad \text{and} \\ V^\alpha \equiv \sqrt{2(\sqrt{(\varepsilon_1^{\alpha\alpha})^2 + (\varepsilon_2^{\alpha\alpha})^2} + \varepsilon_1^{\alpha\alpha})}. \quad (7)$$

In Sec. V we will also discuss the calculation of the reflectivity for other geometries in order to compare with experimental data.

## IV. ELECTRONIC STRUCTURE RESULTS

### A. Density-of-states

Figure 1 compares the total density-of-states for CdMoO<sub>4</sub> and CdWO<sub>4</sub> ranging between  $-80$  eV below the top of the valence band to  $+12$  eV above the conduction band. The distribution of the Mo and W core states for these materials is very similar to their distribution in the scheelite molybdates and tungstates studied in our earlier work.<sup>8</sup> The Cd  $4p$  core states are located close to the Mo  $4s$  states in CdMoO<sub>4</sub> and  $10$  eV above the W  $5s$  states in CdWO<sub>4</sub>. For both materials the Cd  $4d$  states are concentrated near the bottom of the valence band which, as we will see below, has largely O  $2p$  character.

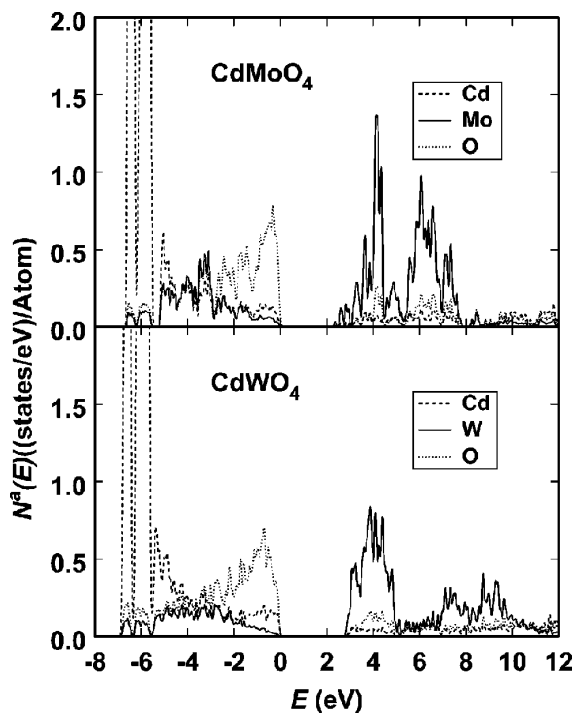


FIG. 2. Partial density-of-states for valence and conduction bands of CdMoO<sub>4</sub> and CdWO<sub>4</sub>, indicating Cd, Mo or W, and O contributions with dashed, solid, and dotted lines, respectively.

Figure 2 shows the partial density-of-states for CdMoO<sub>4</sub> and CdWO<sub>4</sub> in a 20-eV energy range starting at 8 eV below the top of the valence bands, comparing the spectral contributions from the Cd, W, Mo, and O muffin-tin spheres. Comparing the partial density-of-states plots of these two materials, we see that the main features are similar. One finds the density-of-states features for CdWO<sub>4</sub> are generally not as highly peaked as for CdMoO<sub>4</sub>, due to the lower local symmetry and wider distribution of ligand bond lengths in the wolframite CdWO<sub>4</sub> compared with that of the scheelite CdMoO<sub>4</sub>.

The contributions of the Cd 4*d* states are concentrated in double peaks (due to spin-orbit splitting) of approximate width 1 eV at the bottom of the valence bands of both materials and hybridize to a small extent throughout the valence bands.

The O 2*p* states dominate the upper part of the valence bands and have significant contributions throughout the main portion of the valence bands. From analysis of the electron-density contours, the O 2*p* contributions to the lower and upper valence-band states are primarily  $\sigma$  and  $\pi$  states, respectively, relative to their nearest neighbor Mo or W bonds. For CdWO<sub>4</sub>, the separation of the  $\sigma$  and  $\pi$  contributions of the O 2*p* states is less well-defined because of the different W-O bond lengths in this structure.

The Mo 4*d* states contribute to a small extent near the bottom of the main valence band in CdMoO<sub>4</sub>, and dominate the lower conduction bands. As in other scheelite materials, the Mo 4*d* states are split by the tetrahedral crystal field into two groups of states, which will be discussed further below. For CdWO<sub>4</sub>, the W 5*d* states contribute to a small extent to

the valence bands, with a larger contribution near the bottom of the bands. The dominant contributions of the W 5*d* states occur in the lower portion of the conduction bands where they are split by the approximately octahedral crystal field into two main groups of states.

For the lower portion of the conduction band, contributions associated with the W 5*d* states span more than 7 eV in CdWO<sub>4</sub>, while those associated with the Mo 4*d* states span less than 6 eV in CdMoO<sub>4</sub>. For both of these materials the crystal-field splitting of the *d* states by the approximate octahedral or tetrahedral ligand geometries can be described by twofold degenerate *e* and threefold degenerate *t*<sub>2</sub> states. For CdWO<sub>4</sub>, the lower peak in the conduction-band partial density-of-states is associated with the *t*<sub>2</sub> states, while the upper peaks are associated with *e* states, which are actually split into two peaks due to deviations from octahedral symmetry at the W site. For CdMoO<sub>4</sub>, the lower peak in the conduction-band partial density-of-states is associated with the *e* states while the upper peak is associated with the *t*<sub>2</sub> states. Figure 2 shows a very small contribution to the partial density-of-states in the upper conduction-band energy range near 12 eV, although the total density-of-states at these energies is significant. This implies that the states in this energy range are spatially diffuse so that they have very small contributions inside the muffin-tin spheres used for the partial density-of-states analysis.

## B. Energy-band dispersions

The Brillouin zones for the scheelite and wolframite structures are shown in Fig. 3. The energy dispersion curves calculated for CdMoO<sub>4</sub> and CdWO<sub>4</sub> are shown in Fig. 4. In both cases the dispersion curves are plotted along three different symmetry directions. Both materials show a group of narrow bands between -6.5 and -5.5 eV corresponding to the Cd 4*d*-like states, although other features of the band dispersions are quite different from each other.

For CdMoO<sub>4</sub>, the minimum band gap of 2.4 eV is located at the  $\Gamma$  point at the center of the Brillouin zone. The valence-band dispersion is similar to that of the scheelite materials CaMoO<sub>4</sub> and CaWO<sub>4</sub> studied previously.<sup>8</sup> The conduction bands of CdMoO<sub>4</sub> are much more dispersive than the corresponding conduction bands of both CaMoO<sub>4</sub> and CaWO<sub>4</sub>. In particular, the Ca materials are characterized by a small band gap between the lower and upper conduction bands that correspond to the crystal-field split states of Mo 4*d* and W 5*d* character, while for CdMoO<sub>4</sub> the crystal-field split 4*d* Mo states are not separated by a well-defined band gap.

By contrast, the minimum band gap of 2.9 eV for CdWO<sub>4</sub> does not occur at the  $\Gamma$  point, but at Y, which is located at the center of the Brillouin-zone boundary plane perpendicular to the *b* crystal axis. The valence-band width of 5.3 eV is slightly larger (by 0.3 eV) than the valence band width of CdMoO<sub>4</sub>. The conduction band of CdWO<sub>4</sub> is generally less dispersive than that of CdMoO<sub>4</sub>.

## C. Electron-density maps

In order to further understand the electronic states in greater detail, we have constructed contour plots of the elec-



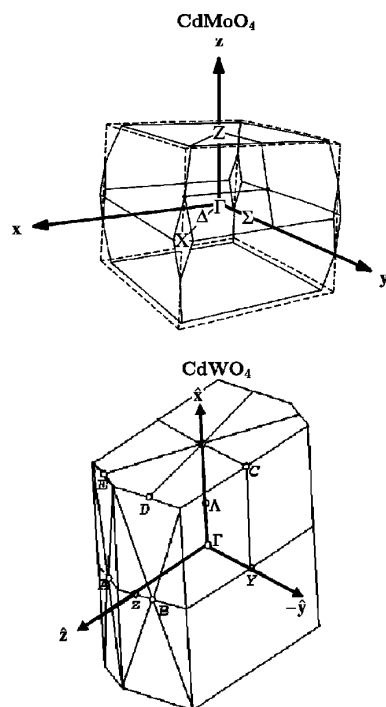


FIG. 3. Diagram of the Brillouin zones for  $\text{CdMoO}_4$  and  $\text{CdWO}_4$ .

tron density associated with selected states. The results for  $\text{CdMoO}_4$  in the scheelite structure were very similar to those of  $\text{CaMoO}_4$  presented in our earlier paper<sup>8</sup> and therefore are not presented here.

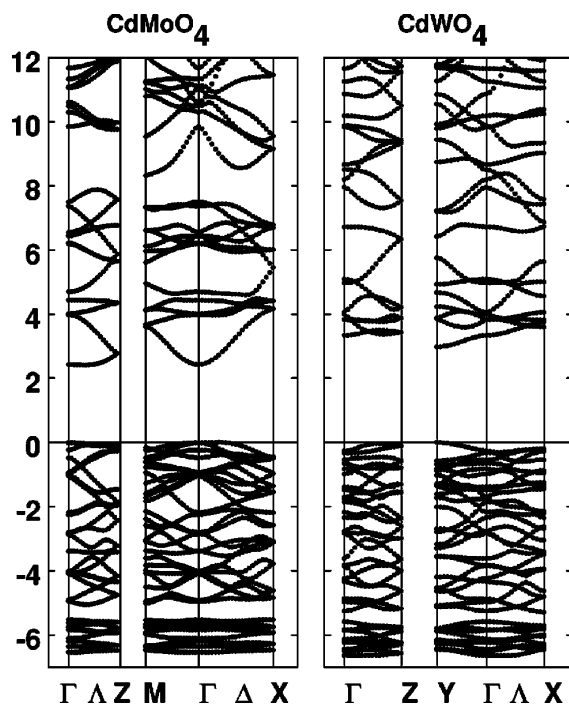


FIG. 4. Energy-band dispersions for  $\text{CdMoO}_4$  and  $\text{CdWO}_4$  plotting along Brillouin-zone directions indicated in Fig. 3.

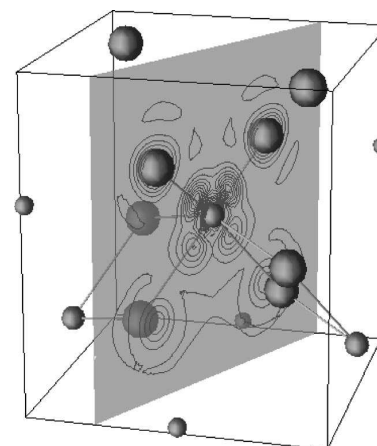


FIG. 5. A perspective drawing of the crystal structure of  $\text{CdWO}_4$ . The spheres represent O, W, and Cd positions using large, medium, and small sizes, respectively. The bonds represent the near-neighbor W-O interactions. The shaded plane is drawn to pass through a W atom and its nearest-neighbor O atoms. This is the plane that is used to construct the two-dimensional electron contour plots described below. The contours superimposed on this diagram correspond to the upper-conduction-band states presented in Fig. 6(f).

For the electron density of  $\text{CdWO}_4$ , we chose to construct contour plots in a plane that passes through a W site and its nearest-neighbor O sites. Figure 5 shows the drawing of the atoms contained in a unit cell of  $\text{CdWO}_4$  and of the plane used for plotting the contours. From this figure, we can see the approximate octahedral symmetry about the W site. For perfect octahedral symmetry, the W site would be surrounded by six equidistant O atoms, with four in a plane and two along an axis perpendicular to that plane. In  $\text{CdWO}_4$ , we see that only two O atoms are in the plane, while another two are close to that plane at a larger bond distance. Bonds from the W to the remaining two O atoms have an intermediate length and make an angle with the plane that is only approximately  $90^\circ$ .

Figures 6(a)–6(f) show contour plots of the electron density for various energy ranges of states of  $\text{CdWO}_4$  in the plane defined in Fig. 5. The contours in Fig. 6(a) correspond to the energy range dominated by the Cd  $4d$  states and thus show a very small contribution to the electron density in the W-O plane shown. Plots 6(b) and 6(c) show O  $2p\sigma$  orbitals hybridizing with the W  $5d$  orbitals, representing the middle portion of the valence band. Plot 6(d) shows the O  $2p\pi$  states that comprise the upper portion of the valence band, with very little contribution from the W states.

Plots 6(e) and 6(f) show the electron-density contours for the lower and upper conduction band states, respectively. These plots clearly show the crystal-field split  $5d$  states of W. If one compares the shapes of these contours with those of the conduction bands of the scheelite materials plotted in a similar way,<sup>8</sup> one finds that they look very similar. In both structures, the bottom conduction-band state has W  $5d$  orbitals that have peak densities in the nonbonding directions and that hybridize with the  $\pi$  states of the nearest-neighbor O atoms. The upper conduction-band state has W  $5d$  orbitals that have peak densities along the bond directions, making antibonding hybrid states with the  $\sigma$  states of the nearest-

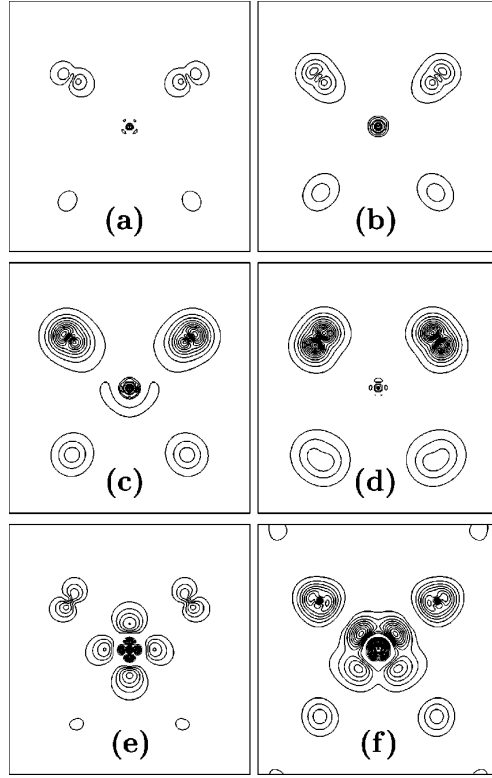


FIG. 6. Contours of electronic charge density for various states of  $\text{CdWO}_4$  plotted in the plane shown in Fig. 5 with contour levels uniformly spaced at intervals of  $0.5 e/\text{\AA}^3$ , starting at  $0.5 e/\text{\AA}^3$ . The one-electron energy ranges for these plots are  $-7.2$  eV to  $-5.6$  eV for (a), and  $-5.6$  eV to  $-4.0$  eV for (b),  $-4.0$  eV to  $-2.0$  eV for (c),  $-1.8$  eV to  $0$  eV for (d),  $2.5$  eV to  $5.1$  eV for (e), and  $5.1$  eV to  $11.9$  eV for (f). For plots (e) and (f), the electron density was calculated supposing full occupancy of these unoccupied bands.

neighbor O atoms. There is one important difference between the wolframite and scheelite conduction bands, however. In the wolframite structure, the local symmetry about the W site is approximately octahedral and the lower band is threefold degenerate with  $t_2$  symmetry while the upper band has  $e$  symmetry. As shown in Fig. 2, the twofold degenerate  $e$  states are split by approximately 2 eV by deviations from octahedral symmetry. In the scheelite structure, the local symmetry about the Mo site is approximately tetrahedral and the lower band is twofold degenerate having  $e$  symmetry, while the upper band is threefold degenerate having  $t_2$  symmetry.

## V. OPTICAL PROPERTIES

As described in Sec. III, in order to calculate the imaginary part of the dielectric tensor from the density-functional results, it is necessary to estimate a self-energy correction  $\Delta$ . A rough estimate of  $\Delta$  is the difference between the experimental band gap and the value determined from our results calculated within the local-density approximation (LDA). Unfortunately, the experimental values of  $E_{\text{gap}}$  have not been precisely measured. Table III lists the LDA values of  $E_{\text{gap}}$  compared with several literature results. For  $\text{CdMoO}_4$ , if we take the reference band gap to be 3.8 eV, the average of the two experimental values, the self-energy correction can be taken to be  $\Delta = 1.4$  eV. Measurements of the absorption edge in  $\text{CdWO}_4$  lead to estimates of  $E_{\text{gap}} = 3.8$  to 4.09 eV.<sup>23,24,26,27</sup> Yochum and Williams<sup>25</sup> have measured the two-photon absorption spectrum of  $\text{CdWO}_4$  using a 200 fs pulse of 420-nm light and white-light continuum of similar duration. The spectrum covers final-state energies from 4.5 to 5.5 eV. The absorption rises from a finite value at 4.5 eV to a plateau at approximately 4.7 eV. Taking the published linear absorption edge in bulk crystals as a definite lower limit for the band gap and the two-photon absorption plateau at 4.7 eV as a definite upper bound, and finally influenced by measured reflectivity spectra,<sup>9,10</sup> we estimate an interband edge of  $4.4 \pm 0.3$  eV for  $\text{CdWO}_4$ . The value of the self-energy correction,  $\Delta = 1.4$  eV, used in the present paper corresponds to the choice of  $E_{\text{gap}} = 4.3$  eV.

Since  $\text{CdMoO}_4$  has orthorhombic symmetry, it has two distinct optic axes. The corresponding dielectric tensor components are  $\epsilon^{xx} \equiv \epsilon^{yy}$ , corresponding to the electric field oriented along one of the  $a$  axes and  $\epsilon^{zz}$ , corresponding to the electric field oriented along the  $c$  axis. The calculated values of  $\epsilon_2^{xx}$  and  $\epsilon_2^{zz}$  and of  $\epsilon_1^{xx}$  and  $\epsilon_1^{zz}$  are shown in Figs. 7 and 8, respectively. The  $\epsilon_2$  results indicate that the dominant transitions occur within approximately 8 eV above the band gap with two main peaks due to transitions between the O valence band and the crystal-field split Mo 4d conduction bands. A small peak near 10 eV is due to transitions from the Cd 4d states. The average of the calculated values of  $\epsilon_1$  is close the experimental measurements in the transparent region,<sup>28</sup> although the calculated birefringence is considerably larger than experiment. As discussed in Sec. III there are some systematic errors due to truncation error in the Kramer's-Kronig integral (4) used to calculate  $\epsilon_1^{\alpha\alpha}$ . Since  $\epsilon_2^{\alpha\alpha}$  is not zero at  $\nu_{\text{max}}$ , we expect our calculated  $\epsilon_1^{\alpha\alpha}(\nu)$  to be underestimated. The fact that  $\epsilon_1^{xx}$  is larger than experiment in the visible range suggests that either the neglected

TABLE III. Estimates of energy-band gaps.

Material	$E_{\text{gap}}$ (eV)	Reference
$\text{CdMoO}_4$	2.43	LDA (present paper)
	3.96	Excitation energy Ref. 23
	3.72	Absorption edge Ref. 24
$\text{CdWO}_4$	2.94	LDA (present paper)
	$4.5 \pm 0.2$	Two-photon absorption Ref. 25
	3.8	Absorption edge Refs. 26 and 27
	4.09	Absorption edge Ref. 24

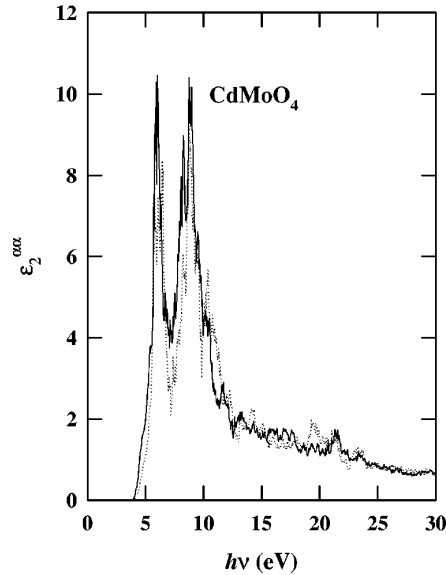


FIG. 7. Calculated values of  $\epsilon_2^{xx}$  (solid line) and  $\epsilon_2^{zz}$  (dotted line) for  $\text{CdMoO}_4$ .

vibrational contributions of  $\epsilon_2^{xx}$  in the Kramer's-Kronig integral are appreciable, or that our calculations generally overestimate the value of  $\epsilon_2^{xx}$ .

Using the calculated values of the dielectric tensor components shown for  $\text{CaMoO}_4$  in Figs. 7 and 8 and Eq. (5), results for the normal-incidence reflectivity are shown in Fig. 9. The calculated reflectivity spectrum shows two main peaks, similar to the spectral form of  $\epsilon_2$ . Unfortunately, we do not know of any reflectivity data available for comparison.

Although the crystallographic  $b$  and  $c$  axes of  $\text{CdWO}_4$  are mutually orthogonal, the  $a$  axis makes an angle of  $91.519^\circ$

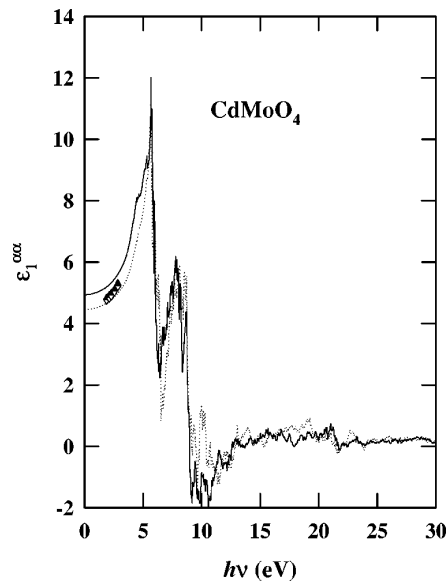


FIG. 8. Calculated values of  $\epsilon_1^{xx}$  (solid line) and  $\epsilon_1^{zz}$  (dotted line) for  $\text{CdMoO}_4$ . Experimental values from Ref. 28 are plotted with filled and open triangles corresponding to  $\epsilon_1^{xx}$  and  $\epsilon_1^{zz}$ , respectively.

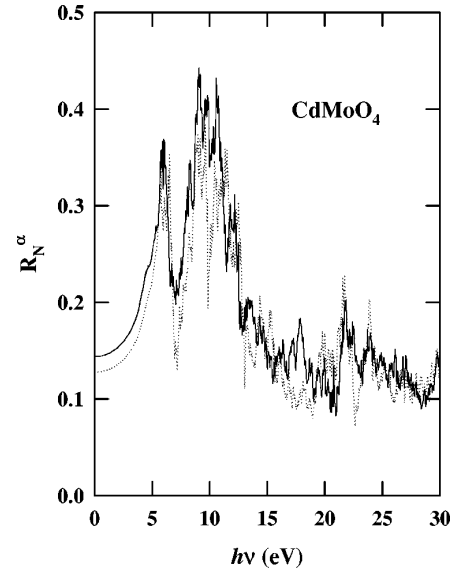


FIG. 9. Calculated values of normal incidence  $R_N^x$  (solid line) and  $R_N^z$  (dotted line) for  $\text{CdMoO}_4$ .

with respect to the  $c$  axis in the  $a$ - $c$  plane. The principal axis system of the dielectric tensor has been determined experimentally in the transparency region. This axis system includes the crystallographic  $b$  axis and two perpendicular axes in the  $a$ - $c$  plane. One of those axes is oriented at an angle of  $13.5^\circ$  (Ref. 29) or  $16^\circ$  (Ref. 30) relative to the crystallographic  $c$  axis at  $\lambda = 633$  nm, and does not rotate appreciably within the transparency region. However, throughout the 30-eV range addressed in the present paper, the principal axes of the dielectric tensor could vary considerably. To facilitate comparisons between theory and experiment referenced approximately to the crystallographic axes, we have adopted a fixed orthogonal coordinate system with the  $y$  axis along the crystallographic  $b$  axis and the  $z$  axis along the crystallographic  $c$  axis. The  $x$  axis then lies in the  $a$ - $c$  plane and makes an angle of  $1.519^\circ$  with the crystallographic  $a$  axis. The dielectric tensor expressed in this coordinate system thus has four nontrivial components:  $\epsilon^{xx}, \epsilon^{yy}, \epsilon^{zz}$  and  $\epsilon^{xz} \equiv \epsilon^{zx}$ . The remaining elements are zero. These are shown in Figs. 10 and 11 for the imaginary and real parts, respectively. The  $\epsilon_2^{\alpha\alpha}$  spectra for  $\text{CdWO}_4$  are similar to those of  $\text{CdMoO}_4$ , although the upper-energy peak is smaller and broader than the lower-energy peak. The off-diagonal component  $\epsilon_2^{xz}$  is much smaller than the diagonal components. The real parts of the dielectric tensor presented in Fig. 11 are compared with experimental points<sup>29,30</sup> in the transparent region. As for  $\text{CdMoO}_4$ , we find that the average calculated real part of the dielectric tensor is close to the experimental average in the transparent range, although the dispersion and birefringence differ. In addition, one of the principal axes of the dielectric tensor calculated in our results makes a much smaller angle with the  $z$  axis than  $13.5^\circ$  or  $16^\circ$  measured by experiment.<sup>29,30</sup> This suggests that our calculated diagonal components of  $\epsilon_1^{\alpha\alpha}$  are comparable or larger than experiment while the calculated off-diagonal  $\epsilon_1^{xz}$  is smaller than experiment in the visible spectral region. These discrepancies are partly due to the truncation error in the Kramer's-Kronig

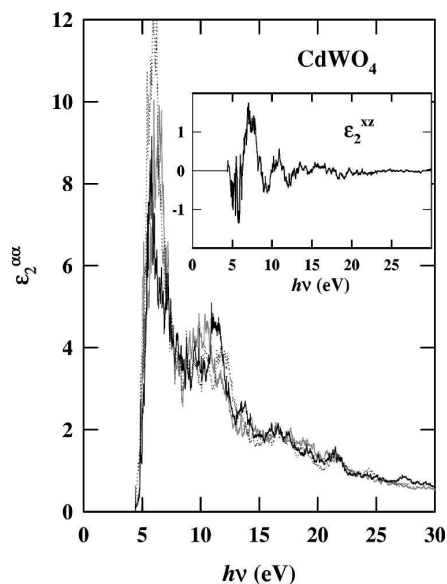


FIG. 10. Calculated values of  $\epsilon_2^{yy}$  (solid-black line),  $\epsilon_2^{zz}$  (dotted line), and  $\epsilon_2^{xx}$  (gray line) for  $\text{CdWO}_4$ . Inset shows off-diagonal element  $\epsilon_2^{xz}$ .

transform discussed above and in Sec. III.

Normal-incidence reflectivity, calculated with the electric field oriented along the  $y$  axis can be calculated from Eq. (5), while other orientations are more complicated. Since the magnitude of the off-diagonal matrix element  $\epsilon^{xz}$  is generally less than 10% of that of the corresponding diagonal components, it is also reasonable to use Eq. (5) to approximate the normal-incidence reflectivity for the electric field oriented along the  $x$  and  $z$  axes. Figure 12 shows the normal-

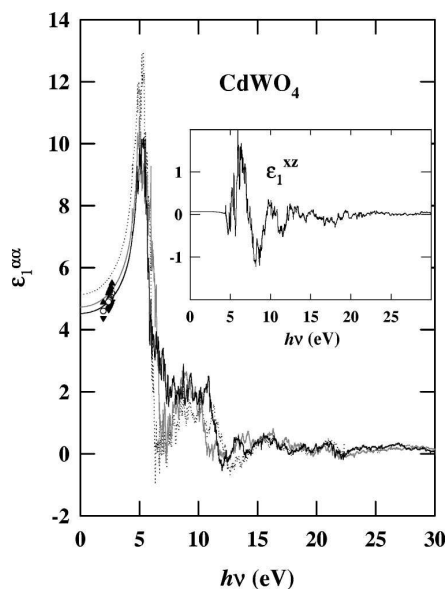


FIG. 11. Calculated values of  $\epsilon_1^{yy}$  (solid black line),  $\epsilon_1^{zz}$  (dotted line), and  $\epsilon_1^{xx}$  (grey line) for  $\text{CdWO}_4$ . Experimental values from Ref. 29 are plotted with filled triangles and open circles corresponding to the three eigenvalues of  $\epsilon_1^{\alpha\beta}$  in the transparent region. Inset shows off-diagonal element  $\epsilon_1^{xz}$ .

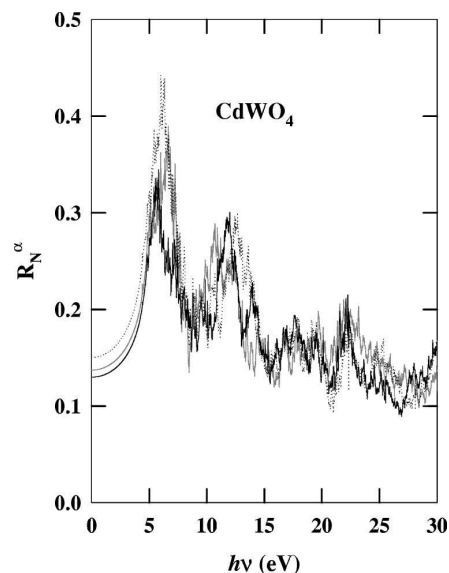


FIG. 12. Values of normal incidence reflectivity for  $\text{CdWO}_4$ :  $R_N^y$  (solid-black line),  $R_N^z$  (gray line) and  $R_N^x$  (dotted line), calculated from Eq. (5), neglecting off-diagonal dielectric contributions.

incidence reflectivity spectra calculated in this way from the uncorrected dielectric tensor components.

Nagimyi and co-workers<sup>9,10</sup> have measured the reflectivity spectrum of a single-crystal sample of  $\text{CdWO}_4$ , cleaved in the  $x$ - $z$  ( or  $a$ - $c$ ) plane. The incident photon beam was oriented with  $p$ -polarization at an angle of  $\theta=45^\circ$  relative to the normal direction. Assuming that the off-diagonal dielectric contributions can again be neglected, the corresponding calculated  $p$ -polarized reflectivity for an incidence angle of  $\theta$  and for the electric field in the  $y$ - $\alpha$  plane (where  $\alpha$  represents either  $x$  or  $z$ ) can be determined from the complex

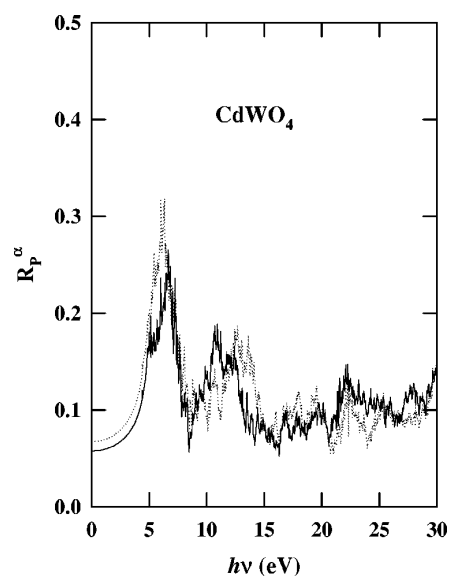


FIG. 13. Values of reflectivity for the  $z$ - $x$  ( $c$ - $a$ ) face of  $\text{CdWO}_4$  for  $p$ -polarization at incidence angle  $\theta=45^\circ$ :  $R_p^z$  (solid black line) and  $R_p^x$  (dotted line), calculated from Eq. (8), neglecting off-diagonal dielectric contributions.

dielectric tensor components according to the equation:

$$R_p^\alpha = \left| \frac{(\epsilon^{yy} - \sin^2 \theta)^{1/2} - (\epsilon^{yy} \epsilon^{\alpha\alpha})^{1/2} \cos \theta}{(\epsilon^{yy} - \sin^2 \theta)^{1/2} + (\epsilon^{yy} \epsilon^{\alpha\alpha})^{1/2} \cos \theta} \right|^2. \quad (8)$$

Results for  $\theta=45^\circ$  are plotted in Fig. 13. The shape of the  $p$ -polarized reflectivity spectrum is similar to that at normal incidence, although its magnitude is reduced. Recent preliminary reflectivity measurements of Nagirnyi and co-workers<sup>9,10</sup> demonstrate that the spectra change with crystal orientation. Their data show a two-peak structure below 12 eV, which is qualitatively similar to the results shown in Fig. 13, although features in the spectra at higher energy differ from our calculations. Detailed comparisons will be done in the future.

## VI. SUMMARY AND CONCLUSIONS

We have carried out detailed electronic structure calculations for CdMoO<sub>4</sub> and CdWO<sub>4</sub>. The electronic structure of CdMoO<sub>4</sub> is similar to that of other scheelite materials, especially to that of CaMoO<sub>4</sub>. Differences are due to the fact that the CdMoO<sub>4</sub> crystal is more compact than other scheelite materials, resulting in larger band widths. In addition, the Cd ions introduce a narrow band of  $3d$  character at the bottom of the valence band.

Despite the fact that CdWO<sub>4</sub> has the lower-symmetry wolframite structure, there are more similarities than differences of its electronic structure compared with that of CdMoO<sub>4</sub>. In both materials, the lower-conduction bands are controlled by the crystal-field-split  $d$  bands of the transition metal. In the case of CdMoO<sub>4</sub>, the Mo ions have an approximately tetrahedral environment that causes the lowest-conduction band to be composed of doubly degenerate  $4d-e$  states. In the case of CdWO<sub>4</sub>, the W ions have an approximately octahedral environment, which caused the lowest-conduction band to be composed of triply degenerate  $5d-t_2$  states. The optical spectra of the two materials are effected by these differences. The calculated imaginary components of the dielectric tensor for CdMoO<sub>4</sub> show two peaks of similar strength, while those for CdWO<sub>4</sub> show a larger peak near threshold and a smaller peak at higher energy. Detailed comparison of the present results with experiment will be possible as soon as single-crystal optical measurements are completed.<sup>10</sup>

This paper was supported by NSF Grant Nos. DMR-9403009, DMR-9706575, and DMR-9732023. We would also like to thank Y. C. Zhang, P. Blaha, and C. Ambrosch-Draxl for help with the WIEN97 code, Z. Burshtein for helpful comments on the refractive index of CdWO<sub>4</sub>, and V. Nagirnyi for sharing his preliminary reflectivity data on CdWO<sub>4</sub>.

- <sup>1</sup>M. Ishii and M. Kobayashi, *Prog. Cryst. Growth Charact.* **23**, 245 (1991).
- <sup>2</sup>S. Chernov, R. Deych, L. Grigorjeva, and D. Millers, *Mater. Sci. Forum* **239-241**, 299 (1997).
- <sup>3</sup>M. Daturi, M. M. Borel, A. Leclaire, L. Savary, G. Costentin, J. C. Lavalley, and B. Raveau, *J. Chim. Phys.* **93**, 2043 (1996).
- <sup>4</sup>M. Daturi, G. Basca, M. M. Borel, A. Leclaire, and P. Paiggio, *J. Phys. Chem. B* **101**, 4358 (1997).
- <sup>5</sup>A. W. Sleight, *Acta Crystallogr., Sect. B: Struct. Crystallogr. Cryst. Chem.* **B28**, 2899 (1972).
- <sup>6</sup>S. R. Shieh, L. C. Ming, and A. Jayaraman, *J. Phys. Chem. Solids* **57**, 205 (1996).
- <sup>7</sup>J. Macavei and H. Schulz, *Z. Kristallogr.* **207**, 193 (1993).
- <sup>8</sup>Y. Zhang, N. A. W. Holzwarth, and R. T. Williams, *Phys. Rev. B* **57**, 12 738 (1998).
- <sup>9</sup>V. Nagirnyi, E. Feldbach, L. Jónsson, M. Kirm, A. Kotlov, A. Luchchik, L. L. Nagomaya, V. D. Ryzhikov, G. Svensson, I. A. Tupitsina, and M. Åsberg-Dahlborg, in *Tungstate Crystals: Proceedings of the International Workshop on Tungstate Crystals, Rome, October 12-14, 1998*, edited by S. Baccaro, B. Borgia, I. Dafinei, and E. Longo (Università degli Studi La Sapienza, Rome, 1999), pp. 155–159.
- <sup>10</sup>V. Nagirnyi, 1999 (private communication).
- <sup>11</sup>A. V. Chichagov, L. N. Dem'yanets, V. V. Ilyukhin, and N. V. Belov, *Kristallografiya* **11**, 686 (1966) [*Sov. Phys. Crystallogr.* **11**, 588 (1966)].
- <sup>12</sup>*International Tables for Crystallography*, Vol. A, edited by T. Hahn (D. Reidel, Boston, 1987).
- <sup>13</sup>A. P. Chichagov, V. V. Ilyukhin, and N. V. Belov, *Dokl. Akad. Nauk (SSSR)*, **166**, 87 (1966) [*Sov. Phys. Dokl.* **11**, 11 (1966)].
- <sup>14</sup>P. Blaha, K. Schwarz, and J. Luitz (1997), WIEN97, Vienna University of Technology. (Improved and updated Unix version of the original copyrighted WIEN code, which was published by P. Blaha, K. Schwarz, P. Sorantin, and S. B. Trickey, *Comput. Phys. Commun.* **59**, 399 (1990).
- <sup>15</sup>J. P. Perdew and Y. Wang, *Phys. Rev. B* **45**, 13 244 (1992).
- <sup>16</sup>P. E. Blöchl, O. Jepsen, and O. K. Andersen, *Phys. Rev. B* **49**, 16 223 (1994).
- <sup>17</sup>C. L. Fu and K. M. Ho, *Phys. Rev. B* **28**, 5480 (1983).
- <sup>18</sup>R. D. Sole and R. Giralda, *Phys. Rev. B* **48**, 11 789 (1994).
- <sup>19</sup>M. Rohlfing and S. G. Louie, *Phys. Rev. Lett.* **81**, 2312 (1998).
- <sup>20</sup>C. Ambrosch-Draxl and R. Abt, *Synth. Met.* **85**, 1099 (1997).
- <sup>21</sup>Z. H. Levine and D. C. Allan, *Phys. Rev. Lett.* **63**, 1719 (1989).
- <sup>22</sup>R. W. Godby, M. Schlüter, and L. J. Sham, *Phys. Rev. B* **37**, 10 159 (1988).
- <sup>23</sup>H. J. Zhang, P. Boutinaud, A. Garcia, J. P. Charminade, and C. Fouassier, *Solid State Commun.* **85**, 1031 (1993).
- <sup>24</sup>F. A. Kröger, *Some Aspects of the Luminescence of Solids* (Elsevier, New York, 1948).
- <sup>25</sup>H. Yochum and R. T. Williams, 1999 (private communication); based on two-photon absorption spectral measurements for CdWO<sub>4</sub>.
- <sup>26</sup>K. Tanaka, T. Miyajima, N. Shirai, Q. Zhuang, and R. Nakata, *J. Appl. Phys.* **77**, 6581 (1995).
- <sup>27</sup>R. H. Gillette, *Rev. Sci. Instrum.* **21**, 294 (1950).
- <sup>28</sup>G. F. Bakhshieva and A. M. Morozov, *Opt. Mekh. Prom.* **44**, 31 (1977) [*Sov. J. Opt. Technol.* **44**, 542 (1977)].
- <sup>29</sup>H. Lotem and Z. Burshtein, *Opt. Lett.* **12**, 561 (1987).
- <sup>30</sup>Z. Burshtein, S. Morgan, D. O. Henderson, and E. Silberman, *J. Phys. Chem. Solids* **49**, 1295 (1988).





```

OPEN (UNIT=22, FILE='nphotons.out', IOSTAT=ios)
nf = nff
do ii = 1, nf
call getarg(ii,fname)
OPEN (UNIT=20, STATUS='Old', FILE=fname, IOSTAT=ios)
do k = 1, 17
read(20,*)
end do
i=1
do
read(20,*,iostat=errr) x(i),y(i,ii)
if(errr.LT.0)exit
if(errr.GT.0)exit
i= i+1
end do
end do
c by now we know that we have x(ndata) and y(ndata,nf)
do j = 1, ndata
do k = 1, nff
lc(k) = y(j,k)
end do
call fit(od,lc,nff,aa,bb)
a(j) = -aa
end do
c now lets output to fill 22
do j = 1, ndata
write (22,*) x(j), a(j)
end do
stop
end
c*****
c* the subroutne fit, takes two real arrays and their size and *

```



```

c* returns slope and intersept *
c*****
SUBROUTINE FIT(X,F,N,A,B)
DIMENSION X(N),F(N)
C1 = 0.0
C2 = 0.0
C3 = 0.0
C4 = 0.0
DO 100 I = 1, N
C1 = C1 + X(I)
C2 = C2 + X(I)*X(I)
C3 = C3 + F(I)
C4 = C4 + F(I)*X(I)
100 CONTINUE
C = C1*C1-C2*N
A = (C1*C3-C4*N)/C
B = (C1*C4-C2*C3)/C
return
end

```

## B.2 Photovoltage calculation (readdata.f)

Listing B.1: a program readdata.f90

```

c*****
c By Yonas Abraham
c On June 2001
c For Voltage Bias Correction
c*****
program readdata

```

```

real x(1000), y(1000)
integer i, errr, j, EB
character(len=11) fname
i=1
call getarg(1, fname)
OPEN (UNIT=20, STATUS='Old', FILE=fname, IOSTAT=ios)
OPEN (UNIT=22, FILE='all.dat', IOSTAT=ios)
do k = 1, 13
read(20,*)
end do

read(20,10)EB
10  format(21X, I3)
write(*,*) EB
read(20,*)
read(20,*)
read(20,*)

do
read(20,*, iostat=errr) x(i), y(i)
if(errr.lt.0) exit
if(errr.gt.0) exit
i = i+1
end do

do
read(22,*, iostat=errr)
if(errr.ne. 0) exit
end do

```

```
k = maxl(y, i)
write(22,*)EB, x(k)

stop
end

integer function maxl(a,n)
integer n
real a(n)

real temp
integer tempi, i

temp = a(1)
tempi = 1

do i = 1, n
  if(temp.LT.a(i)) then
    temp = a(i)
    tempi = i
  end if
end do

maxl = tempi
return
end
```

### B.3 IDL smear plot program (SmearPlot2000.pro)

Listing B.2: a program SmearPlot2000.pro

```

;*****
;By Yonas Abraham
;On: Dec 2000
;For: plotting smear plot in IDL
;*****
pro SmearPlot2000
print , 'input_Vector_filename_'
vecfilename='trick'
kvsefilename='trick'
outf='trick'
devicestuff='ps'
gs='trick'
crynam='trick'
read , vecfilename
print , 'input_your_crystal_name'
read , crynam
print , 'Enter_Fermi_Level_(in_Ry)'
read , fermi
openr , 2 , vecfilename
d=fltarr(3,3)
d0=1.0
d1=1.0
d2=1.0
for i=0,2 do begin
readf , 2 , format='(a5,3e20.12)' , gs , d0 , d1 , d2
d(0,i)=d0
d(1,i)=d1
d(2,i)=d2
endfor

```

```

npanel=0
print , 'Input K vs energy file '
read , kvsefilename
print , 'input number of panels '
read , npanel

;read the knames from the user
;in to kname(i). NOTE, for npanels there are npanel+1 name
kname=strarr(npanel+1)
print , 'kname' ,kname
bb='irick'
for i=0, npanel do begin
print , 'input the ' ,i , 'th k-point name Eg. !7C stands for Gamma and !5M f
read , bb
kname(i)=bb
endfor

;following are k0 and kf in three by npnel dim
k0=fltarr(npanel,3)
kf=fltarr(npanel,3)
kdiff=fltarr(npanel,3)
length=fltarr(npanel)
l1=fltarr(3)

;folloing are the initial for the k0(x,y,z)
k0x=1.0
k0y=1.0
k0z=1.0
kfx=1.0
kfy=1.0

```

```

kfz=1.0

;now input the k0 and kf matrix
for i=0, npanel-1 do begin

print , 'Input starting k point in x,y,z format for the ', i+1, 'th panel'
read , k0x , k0y , k0z
k0(i,0)=k0x
k0(i,1)=k0y
k0(i,2)=k0z

print , 'Input end k point in x,y,z format for the ', i+1, 'th panel'
read , kfx , kfy , kfz
kf(i,0)=kfx
kf(i,1)=kfy
kf(i,2)=kfz

;calculate the length of each panel
kdiff=kf-k0
l1=d##kdiff[i,*]
length(i)=sqrt(transpose(l1)##l1)
endfor
;total length
totallength=total(length)
;scale each panel length to fit 7in width

for j=0,npanel-1 do begin
length(j)=6.5*length(j)/totallength
endfor

```

```

; initialize some parameters
k1=1.0
k2=1.0
k3=1.0
ev11=1.
ev22=1.
emin=1.0
emax=1.0
ev1=fltarr(1)
ev2=fltarr(1)
k=fltarr(3)
dl1=fltarr(3)
dl=0.0
dl2=0.0
inde=0
print, 'input  $\epsilon_{min}$ ,  $\epsilon_{max}$ , and  $\Delta_{interval}$  in eV'
read, emin, emax, eval
shift=0.0
v=fltarr(3)
cv=fltarr(3)
v2=fltarr(3)
cdir=fltarr(3)
ymin=0.
ymax=total(length)
titleline=crynam

for j=0,npnl-1 do begin
openr, 3, kvsefilename
v2=kf[j,*]-k0[j,*]

```

```
cdir=(d##v2)/(length(j)*totallength/6.5)
```

```
WHILE NOT EOF(3) DO BEGIN
```

```
READF,3 ,format='(5f10.5) ',k1 ,k2 ,k3 ,ev11 ,ev22
```

```
k(0)=k1
```

```
k(1)=k2
```

```
k(2)=k3
```

```
ev1(0)=(ev11-fermi)*13.6057
```

```
ev2(0)=(ev22-fermi)*13.6057
```

```
v=transpose(k)-k0[j ,*]
```

```
cv=d##v
```

```
dl=sqrt(transpose(cv##cv)
```

```
dl2=transpose(cdir##cv
```

```
xdiff=dl[0]-dl2[0]
```

```
if(abs(xdiff) lt 1.0E-7) then begin
```

```
dl=dl*6.5/totallength +shift
```

```
nne=1
```

```
nne=(emax-emin)/eval
```

```
nne=fix(nne)
```

```
eev=findgen(nne+1)
```

```
eev=emin+eev*eval
```

```
xx=7.0
```

```
yy=9.5
```

```
xo=0.5
```

```
yo=0.5
```

```
set_plot , 'ps'
```

```
device ,/portrait ,font_size=20
```

```
device ,/helvetica ,/bold
```

```
device ,/inches ,xsize=xx ,ysize=yy ,xoffset=xo ,yoffset=yo
```

```
inde=inde+1
```



```

if (inde eq 1) then begin
plot , dl , ev1 , psym=3, xstyle=1, ystyle=1, yrange=[emin , emax] , $
    xrange=[ymin , ymax] , xticks=1, xtickn=['_ ' , '_ ' ] , xminor=-1, $
    title=titleline , yminor=-1, yticks=nne , ytickv=eev , $
    ytitle='_Energy_(eV)_ '
endif
if((ev1 [0] le emax) and (ev2 [0] le emax) and $
    (ev1 [0] ge emin) and (ev2 [0] ge emin)) then begin
oplot , [ dl , dl ] , [ ev1 , ev2 ] , thick=8
endif

;plot the vertical line to seperate the panels

endif

ENDWHILE
close , 3
oplot , [ length(j)+shift , length(j)+shift ] , [ emin , emax ]
shift=shift+length(j)
endfor

;for i=0, npanel-1 do begin
;endfor

;write the knames on the plot
bib=fltarr(npanel+1)
bib(0)=0.0

for i=1, npanel do begin

```

```
bib(i)=bib(i-1)+length(i-1)
endfor

for i=0, npanel do begin
xyouts , bib(i) , emin - 2.0 , kname(i) , / data
endfor

close , 2
device , / close
end
```